Semi-classical and Quantum Modeling of Low Dimensional Devices and Sensors

Thesis Submitted

by

SHARMISTHA SHEE KANRAR

Doctor of Philosophy(Engineering)

Electronics and Telecommunication Engineering Department,

Faculty Council of Engineering & Technology

Jadavpur University Kolkata,
India

2025

JADAVPURUNIVERSITY

KOLKATA– 700032

Index No. **108/19/E**

1. **Title of the thesis**:

Semi-Classical and Quantum Modeling of Low Dimensional Devices and Sensors

2. **Name & Dept. of the Supervisor**:

Prof. Subir Kumar Sarkar,
Department of Electronics and Telecommunication Engineering,
Jadavpur University, Jadavpur, Kolkata-700032, India

3. List of publication (Related to thesis)

Journals

I. **Sharmistha Shee Kanrar** and Subir Kumar Sarkar, "Non-equilibrium Green's function analysis of charge plasma-based source-drain electrode P-type MoTe2 MOSFET for high sensitivity hydrogen sensing," Micro and nanostructures, pp. 207823–207823, Mar. 2024, doi: https://doi.org/10.1016/j.micrna.2024.207823.

II. **Sharmistha Shee Kanrar** and Subir Kumar Sarkar, "Deep insight of inter-channel coupling in AlGaN/GaN double channel HEMT and its application in C-ERB2 sensing," *Physica Scripta*, vol. 99, no. 8, pp. 085037–085037, Jul. 2024, doi: https://doi.org/10.1088/1402-4896/ad6047.

III. **Sharmistha Shee Kanrar** and S. K. Sarkar, "Analytical modeling of subband quantization and quantum transport in very Low-dimensional dual metal double gate TFET," Superlattices and Microstructures, vol. 160, p. 107063, Dec. 2021, doi: https://doi.org/10.1016/j.spmi.2021.107063.

IV. **Sharmistha Shee Kanrar**., Jana, A., De, A. et al. NEGF-based investigation of electrically doped few layer MoTe2 H2 gas sensor. J Comput Electron 25, 6 (2026). https://doi.org/10.1007/s10825-025-02449-5

V. **Sharmistha Shee Kanrar** and Subir Kumar Sarkar, "Impact of Bohm Quantum Potential on SiGe-Based Heterojunction Tunnel FET Biosensors: Modeling and Comparative Analysis", *communicated*.

VI. Abir Jana**, Sharmistha Shee Kanrar**, A. K. De, Komal Kumari, B. Gupta, and Subir Kumar Sarkar, "A crossbar architecture based system (CAS) as hydrogen gas sensing platform," Nanotechnology, Aug. 2023, doi: https://doi.org/10.1088/1361-6528/acf29e.

VII. A. De, **S. Shee Kanrar,** and S. K. Sarkar, "Investigation into MoTe2 Based Dielectric Modulated AMFET Biosensor for Label-Free Detection of DNA Including Electric Variational Effects," Silicon, Oct. 2021, doi: https://doi.org/10.1007/s12633-021-01423-7.

VIII. A. K. De, **Sharmistha Shee Kanrar**, and Subir Kumar Sarkar, "Noise analysis of MoTe2-based dual-cavity MOSFET as a pH sensor," Semiconductor Science and Technology, vol. 37, no. 10, pp. 105015–105015, Sep. 2022, doi: https://doi.org/10.1088/1361-6641/ac8c68.

IX. Komal Kumari, **Sharmistha Shee Kanrar** , Abir Jana and Subir Kumar Sarkar, "Graded SiGe channel Dielectric Modulated Tunnel FET BioSensor: Proposal and comparative analysis" NanotechnologyPerceptions20No.S15(2024)4126-4141.

X. D. Sen, A. De, B. Goswami, **Sharmistha Shee Kanrar**, and S. K. Sarkar, "Noise immune dielectric modulated dual trench transparent gate engineered MOSFET as a label free biosensor: proposal and investigation," Journal of Computational Electronics, vol. 20, no. 6, pp. 2594–2603, Sep. 2021, doi: https://doi.org/10.1007/s10825-021-01780-x

Conferences

I. **Sharmistha Shee Kanrar** and Subir Kumar Sarkar, "Optimization and Simulation of $In_{(1-x)}Ga_xAsyP_{(1-y)}/InP$ wideband Multi-Well Photodetectors for Communication Systems using k.p Method" in ETMN 2024.

II. **Sharmistha Shee Kanrar**, A. De, and Subir Kumar Sarkar, "Sensitivity Analysis of HEMT Biosensor for Variation in Alx Ga1-xN Layer Alloy Composition, Bulk Trap and Doping," Jan. 2024, doi: https://doi.org/10.1109/ciec59440.2024.10468245.

III. **Sharmistha Shee Kanrar** and Subir Kumar Sarkar, "Influence of Interface Trap on Sensitivity of Doping-Less MoTe2 Hydrogen Sensor," Dec. 2023, doi: https://doi.org/10.1109/codec60112.2023.10466174.

IV. **Sharmistha Shee Kanrar**, Dinesh Kumar Dash, and Subir Kumar Sarkar, "Comparative Study of Threshold Characteristics in Low-Dimensional TFET with Quantum Confinement," Springer eBooks, pp. 407–413, Jan. 2021, doi: https://doi.org/10.1007/978-981-15-8366-7_60.

V. **Sharmistha Shee Kanrar**, Shib Sankar Das, Abir Jana and Subir Kumar Sarkar "Impact of Hole Gas in O_2 sensing Applications in Ge Core Si Shell Nanowires: Quantum Simulation Study" in EDKCON 2024.

VI. **Sharmistha Shee Kanrar**, Shib Sankar Das and Subir Kumar Sarkar, "Graded SiGe channel Dielectric Modulated Tunnel FET BioSensor: Proposal and comparative analysis" communicated to International Conference on Computer, Electrical & Communication Engineering 2025 (Conference ID #61355).

VII. A. Jana, S. S. Kanrar, B. Gupta and S. K. Sarkar, "A Study on Axially Graded $Si_{(1-x)}Ge_{(x)}$ Nanowire Solar Cell with Monte Carlo Simulation," 2024 IEEE International Conference of Electron Devices Society Kolkata Chapter (EDKCON), Kolkata, India, 2024, pp. 506-511, doi: 10.1109/EDKCON62339.2024.10870757.

Book Chapter

Sharmistha Shee Kanrar, Shib Sankar Das and Subir Kumar Sarkar, “Classical to Semi-classical Transport in Field Effect Transistors” in CRC Press Book Entitled "Classical to Quantum Transport in Multi-Dimensional Field Effect Transistors”, *accepted*.

4. **List of Patents : Nil**

5. **List of Presentations in National/International/Conferences/Workshops :**

Oral Presentation:

I. **Sharmistha Shee Kanrar**, A. De, and Subir Kumar Sarkar, “Sensitivity Analysis of HEMT Biosensor for Variation in Alx Ga1-xN Layer Alloy Composition, Bulk Trap and Doping in The 8 th International Conference on Computers and Devices for Communication (CODEC) held on 14th-16th December, 2023.

II. **Sharmistha Shee Kanrar** and Subir Kumar Sarkar, “Influence of Interface Trap on Sensitivity of Doping-Less MoTe2 Hydrogen Sensor,” in 2024 3rd International Conference on Control, Instrumentation, Energy & Communication (CIEC) in January 25 - January 27, 2024

Poster Presentation:

I. **Sharmistha Shee Kanrar** and Subir Kumar sarkar, "A Novel Application of Source Engineering to Ease Quantum Confinement Effects in Very Low-Dimensional Tunnel FETs" International Conference on Nano Science and Technology, March 5-7, 2020, Venue: Biswa Bangla Convention Centre, New Town, Kolkata

PROFORMA–1

“Statement of Originality”

I, **Sharmistha Shee Kanrar**, registered on **06-06-2019** do hereby declare that this thesis entitled “**Semi-classical and Quantum Modeling of Low Dimensional Devices and Sensors**” contains literature survey and original research work done by the undersigned candidate as part of Doctoral studies.

All information in this thesis have been obtained and presented in accordance with existing academic rules and ethical conduct. I declare that, as required by these rules and conduct, I have fully cited and referred all materials and results that are not original to this work.

I also declare that I have checked this thesis as per the “Policy on Anti Plagiarism, Jadavpur University, 2019”, and the level of similarity as checked by iThenticate software **is 2 %.**

Signature of Candidate: Sharmistha Shee Kanrar.

Date : 07/11/25

Certified by Supervisor: (Signature with date, seal)

07.11.2025

Dr. Subir Kumar Sarkar
Professor and Former Head, Dept. of Electronics
& Telecommunication Engg.
Jadavpur University, Kolkata-32

PROFORMA-2

CERTIFICATEFROMTHESUPERVISOR

This is to certify that the thesis entitled **"Semi-classical and Quantum Modeling of Low Dimensional Devices and Sensors"** submitted by Shri/Smt **Sharmistha Shee Kanrar** who got his/her name registered on 06-06-2019for the award of Ph.D.(Engg./Pharmacy) degree of Jadavpur University is absolutely based upon his/her own work under the supervision of **Prof. Subir Kumar Sarkar** and that neither his/her thesis nor any part of the thesis has been submitted for any degree/diploma or any other academic award anywhere before.

Signature of the Supervisor

And date with Office Seal

07.11.2025

Dr. Subir Kumar Sarkar
Professor and Former Head, Dept. of Electronics & Telecommunication Engg.
Jadavpur University, Kolkata-32

Dedicated to-

My parents, Sister and in-laws

For their love and support

My Husband

Mr. Arnab Kanrar

For his motivation and co-operation

Acknowledgement

I would like to extend my sincere appreciation and profound gratitude to my supervisor Prof. Subir Kumar Sarkar of Electronics and Telecommunication Engineering Department, Jadavpur University, for his invaluable guidance and constant encouragement in carrying out my research. I was allowed to enjoy all the necessary freedom in carrying out the research work and at the same time the intense supervision by my supervisor helped me in significant enhancement of the quality of the research. This work could not have reached this stage without profiting from his expertise, encouragement and valuable criticisms. I would also like to express my sincere gratefulness towards him for his invaluable guidance not only towards my research, but also for his active role in helping me with my overall personal and professional development.

I also take this opportunity to thank Faculty Council of Engineering and Technology and Department of Electronics and Telecommunication Engineering, Jadavpur University for allowing me to carry on my research work and sourcing me with various inputs and guidance, as and when I required them.

My gratitude extends to respected teachers, Prof. Bhaskar Gupta, Prof. Sudhabindu Ray, Prof. Manotosh Biswas, Prof. P. Venkateswaran, Prof. Sheli Sinha Chaudhuri, Dr. Chandrima Mondal, Dr. Sayan Chatterjee for their advice, useful suggestions and encouragement in carrying out the research work.

I would like to acknowledge my senior Dr. Dinesh Kumar Dash and Mr. Arpan De as I would always remain indebted to them for their constant support, suggestion and help in my PhD journey. I would extend special thanks to my fellow research scholars Mr. Abir Jana, Mrs. Komal Kumari, Mr. Shiv Shankar Das for providing their continuous emotional support and for making the laboratory an interesting place to work.

I would like to particularly mention the name of my husband Mr. Arnab Kanrar for his love and immense support during this PhD journey. I would also express my heartfelt gratitude towards him for providing me with the necessary impetus and positive mindset to reach to the present stage of my doctoral degree.

I am also glad to thank my sister Dr. Shrestha Shee for being with me and sharing countless smiles and providing moral support all the way.

I would express my love and respect towards my parents for their sacrifice, love, belief, never ending support and encouragement during this entire journey. Without the incessant effort, support and blessings of my parents and my in-laws, this work could never have been completed successfully.

Finally, as it is impossible to mention everybody by name, I would like to convey my thanks to all who have contributed in one way or another, in making this work reach the present stage.

Date: 07/11/25

Place : Kolkata.

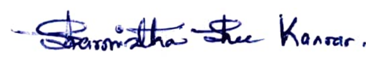

Sharmistha Shee Kanrar

CONTENTS

Chapter 1: Introduction and Organization of the Thesis **1-13**

1.1 Introduction and Motivation
1.2 Organization of the Thesis

Chapter 2: Introduction to Semi-classical and Quantum Transport in Nano-scaled Devices **14-45**

2.1 Overview of Nano-scaled Devices
2.2 Importance of carrier Transport Phenomena
2.3 Classical Transport Models and their limitations
2.4 Semi-classical and Quantum Transport
2.5 Literature Study
2.6 Conclusion

Chapter 3: Quantum Transport (NEGF) in Low-Dimensional MOSFETs **46-77**

3.1 Introduction to Low-Dimensional MOSFETs
3.2 Quantum Transport in MOSFETs based on NEGF: Theoretical Analysis
3.3 Charge Plasma Engineering and its application
3.4 Gas sensing application of TMD based FET
3.5 Non-Equilibrium Green's Function Analysis of Charge Plasma-Based Source- Drain Electrode P-type MoTe2 MOSFET for High Sensitivity Hydrogen Sensing
3.6 Conclusion and Future Work

Chapter 4: Density Gradient : DG (Quantum Moments Model) of High-Electron-Mobility Transistors for Biosensing Applications **78-110**

4.1 Introduction to HEMTs & Double-Channel HEMT
4.2 DG (Quantum Moments Model) in HEMT
4.3 Bio sensor application of HEMT
4.4 Deep insight of inter-channel coupling in AlGaN/GaNDouble Channel HEMT and its application inC-ERB2 sensing
4.5 Conclusion and Future Work

Chapter 5: Analytical and BQP (Bohm Quamtm Potential) based Quantum Analysis Tunnel Field-Effect Transistors **111-155**

5.1 Introduction to TFETs
5.2 Quantum Effects in TFETs
5.3 Quantum Analytical Modeling of Very Low-Dimensional Dual Metal Double Gate TFET
5.4 Impact of Bohm Quantum Potential on SiGe-Based Heterojunction Tunnel FET Biosensors: Modeling and Comparative Analysis
5.5 Conclusion and Future Work

Chapter 6: Parabolic Quantum Well Model and Quantum correction models **156-179**

6.1 Introduction to Parabolic Quantum Well Model and Multi-Well Photodetectors
6.2 Device structure, Simulation of In(1-x)GaxAsyP(1-y)/InP wideband Multi-Well Photodetectors using k.p Method
6.3 Other Quantum correction models
6.4 Conclusion and Future Work

Chapter 7: Conclusion and Future Work **180-184**

7.1 Conclusion
7.2 Future Work

Bibliography **185-212**

Preface

The continuous scaling of electronic devices has been the cornerstone of technological advancement for over half a century. As the dimensions of transistors and sensors approach the nanometer regime, classical models of carrier transport cease to adequately describe their physical behavior. In this regime, phenomena such as quantum confinement, tunneling, and subband formation begin to dominate, demanding modeling frameworks that can capture the intricate interplay between classical drift-diffusion transport and quantum-mechanical effects. This thesis, titled *"Semi-classical and Quantum Modeling of Low-Dimensional Devices and Sensors,"* is motivated by the growing necessity to develop, understand, and validate transport models that bridge the gap between traditional and quantum approaches across different device architectures and material systems.

The work presented here is the result of several years of research dedicated to exploring the transition from classical to quantum transport in nanoscale electronic devices and their applications in sensing. The primary objective of this thesis is to systematically study, compare, and integrate semiclassical and quantum transport methodologies to analyze the electrical and sensing characteristics of low-dimensional devices such as MOSFETs, HEMTs, TFETs, and quantum-well-based structures. The motivation arises from the recognition that, although extensive progress has been made in modeling nanoscale devices, a unified cross-platform understanding of transport phenomena that spans semiclassical and quantum regimes is still lacking.

Traditionally, the drift-diffusion (DD) and hydrodynamic models have served as the foundation of semiconductor device simulation due to their computational efficiency and simplicity. However, as device lengths approach and fall below 10 nm, these classical models fail to capture confinement effects and quantum tunneling that critically influence device performance. On the other hand, fully quantum approaches such as the Non-Equilibrium Green's Function (NEGF) formalism offer highly accurate predictions but at the cost of significant computational overhead and device-specific implementation complexity. This dichotomy presents an important research challenge: how to link the simplicity of

semiclassical approaches with the accuracy of quantum models in a scalable and physically consistent manner across multiple device geometries and material platforms.

In addition to transistor applications, this challenge becomes even more pronounced in the domain of sensors, where charge transport is inherently modulated by external physical, chemical, or biological stimuli. In the case of nanoscale FET-based sensors, for instance, the response is highly sensitive to small variations in surface potential, charge distribution, and interface states—all of which are profoundly affected by quantum phenomena. However, most sensor modeling efforts continue to rely on classical electrostatic approximations, neglecting crucial effects such as discrete energy subbands, wavefunction penetration, charge quantization, and carrier localization. This inadequacy not only limits the accuracy of predictive modeling but also constrains the design and optimization of high-performance sensors.

Therefore, this thesis aims to bridge this modeling gap by exploring how semiclassical correction schemes and fully quantum frameworks can complement each other in analyzing low-dimensional transistors and sensors. The study systematically evaluates the computational cost, physical fidelity, and scalability of different modeling paradigms—ranging from the density-gradient (DG) and Bohm Quantum Potential (BQP) models to the rigorous NEGF formalism—and establishes their relative merits and limitations for device and sensor applications. The emphasis is on understanding how these transport models influence device metrics such as current–voltage characteristics, energy band profiles, transmission spectra, and, in the context of sensors, the sensitivity and selectivity under quantum confinement.

Each chapter of this thesis builds upon this central theme of cross-model exploration. The early chapters introduce the fundamental transport equations and the evolution of device scaling, highlighting the gradual breakdown of classical assumptions as device dimensions shrink. Subsequent chapters delve into specific modeling frameworks: the NEGF-based treatment of quantum transport, the DG-based semiclassical correction schemes, and the BQP formulation for approximating quantum confinement within drift-diffusion frameworks. The modeling is extended to quantum wells, where carrier transport is

governed by discrete subband energies, and quantum corrections are necessary to predict the actual charge distribution and energy landscape.

The later part of the thesis transitions from transistor modeling to sensor-oriented analysis. Here, the impact of quantum transport on sensing mechanisms is explored through examples such as electrically doped tunnel FET biosensors, AlGaN/GaN HEMT hydrogen sensors, and $MoTe_2$-based gas sensors. These case studies illustrate how quantum phenomena such as tunneling probability, density of states modification, and surface potential variation directly affect the sensitivity and detection capability of nanosensors. By comparing semiclassical and quantum-corrected simulations, the thesis provides a deeper insight into the interplay between transport modeling, material properties, and sensor architecture.

The research presented also integrates device structural engineering strategies that enhance or exploit quantum effects. Techniques such as channel material grading, interchannel coupling, and charge-plasma-based doping are analyzed alongside transport models to evaluate their combined influence on electrical and sensing performance. These engineering methods are essential for optimizing devices at dimensions where conventional doping and electrostatic control become less effective. The study emphasizes that the true potential of nanoscale sensors can only be realized through a combined understanding of quantum transport and advanced device engineering.

The materials explored in this thesis—such as $MoTe_2$, SiGe, and AlGaN/GaN heterostructures—were selected due to their distinct quantum characteristics and technological relevance. $MoTe_2$, as a layered transition metal dichalcogenide (TMD), offers tunable band alignment and a high surface-to-volume ratio, making it a strong candidate for hydrogen sensing. AlGaN/GaN HEMTs exhibit strong polarization-induced charge accumulation, which can be effectively modeled using quantum-corrected frameworks to predict high electron mobility and enhanced sensitivity. Similarly, SiGe-based TFETs and quantum-well photodetectors showcase the intricate role of tunneling and subband quantization, both of which are essential for accurate modeling and design. By studying these diverse material systems under different transport regimes, the thesis contributes to

establishing a broader, unified understanding of semiclassical-to-quantum transition phenomena.

In essence, this thesis is both an analytical and methodological journey—an attempt to unify different modeling paradigms under a consistent physical framework that remains relevant across low-dimensional devices and sensors. It demonstrates that semiclassical models, when equipped with appropriate quantum correction schemes, can capture much of the essential physics at a fraction of the computational cost of fully quantum simulations. Conversely, it also shows where semiclassical approximations fail and why a full quantum approach becomes indispensable. This comparative and integrative perspective is what distinguishes the present work from many existing studies focused on isolated devices or single modeling methods.

The broader motivation of this research extends beyond academic inquiry. As the world moves toward pervasive sensing, intelligent systems, and ultra-scaled electronics, the demand for accurate, physics-based modeling grows ever more critical. Understanding transport phenomena at the quantum scale is fundamental not only for predicting device behavior but also for guiding experimental design and material innovation. The insights gained through this thesis are intended to contribute to this ongoing evolution—bridging the gap between theoretical modeling and practical device engineering.

In conclusion, this thesis reflects a concerted effort to explore, understand, and unify semiclassical and quantum transport frameworks for nanoscale devices and sensors. It seeks to provide clarity on when, why, and how different modeling approaches should be applied and what their implications are for performance prediction and sensor design. By addressing the limitations of existing models and highlighting the interplay between transport mechanisms, material properties, and structural engineering, the thesis aims to contribute meaningfully to the field of nanoscale device physics and sensor technology.

List of Figures

Figure No.	Description	Page No
1.1	Industrial roadmap guided by the IRDS 2022.	2
1.2	Accuracy cost trade-off of classical, semi-classical and quantum models.	4
2.1	Basic Structure of MOSFET	18
2.2	Schematic of TFET Structure	20
2.3	General HEMT Structure	21
2.4	Schematic representation of Quantum Well	23
3.1	(a) A diagram of the proposed device shows charge-plasma (CP) metals. The device thickness is considered to be 5, 7, and 9 nm. (b) The gas adsorption mechanism on the Palladium (Pd) surface which causes dipole generation, translating to work function change of the metal. (c,d) TCAD simulation setup calibration with experimental.	65
3.2	Lateral variation of energy band at different channel thickness (a)=5nm, (b)=7nm and (c)=9 nm, and pressure of H_2 i.e.,P1(initial) = 10^{-14} Torr, P2 = 10^{-12} Torr and P 3= 10^{-10} Torr to illustrate the band bending under various conditions.	68
3.3	Lateral variation of potentail at different channel thickness (a)=5nm, (b)=7nm and (c)=9 nm, and pressure of H_2i.e., P1(initial) = 10^{-14} Torr, P2 = 10^{-12} Torr and P 3= 10^{-10} Torr to illustrate the change in potential under various conditions.	69
3.4	Lateral variation of electron and hole concentratiion at different channel thickness (a)=5nm, (b)=7nm and (c)=9 nm, and pressure of H_2i.e., P1(initial) = 10^{-14} Torr, P2 = 10^{-12} Torr and P 3= 10^{-10} Torr.	72
3.5	Spatial distribution of hole concentration at different channel thickness (a)=5nm, (b)=7nm and (c)=9 nm, and pressure of H_2i.e., P1 (initial)= 10^{-14} Torr, P2 = 10^{-12} Torr and P 3= 10^{-10} Torr.	73
3.6	Transfer Characteristics at different channel thickness (5, 6, 7, 8, 9, 10 nm) and pressure of H_2i.e., P1(initial) = 10^{-14} Torr, P2 = 10^{-12} Torr and P 3= 10^{-10} Torr.	73
3.7	Drain current Sensitivity at different channel thickness (5, 6, 7, 8, 9, 10 nm) and pressure of H_2i.e., P1 (initial)= 10^{-14} Torr, P2 = 10^{-12} Torr and P 3= 10^{-10} Torr.	74
4.1	(a). Schematic of the DCHEMT used in this study. (b) Charges at interfaces according to charge neutrality model.	93

4.2	a.Alignment of the models (lines) with the corresponding experimental results (marks) , b. Process flow diagram for potential device fabrication and analyzing sensitivity .	**94**
4.3	Plot of energy band diagram along device thickness forx_u=0.1, 0.3, 0.5, each plot corresponds to change in x_l=0.1, 0.3, 0.5.	**101**
4.4	(a-c) Distribution of electron concentration profiles across the device's thickness illustrating the impact of different mole fractions (d) Comparison of maximum carrier concentration in upper and lower channels of the AlGaN/GaN double-channel HEMT obtained from analytical calculation (with and without Density Gradient correction) and numerical simulation.	**103**
4.5	Comparison of drain current vs. drain-source voltage (Id-Vds) characteristics. Marker for no biomarker condition (Iref), c-erB-2 concentration 4 µg/ml, 6 µg/ml, 9µg/ml, 13 µg/ml.	**104**
4.6	Comparison of Sensing Current for increasing both channel mole fraction. Solid lines and dotted lines indicate Sensing Current c-erB-2 concentration 4 µg/ml (indicating healthy condition) and c-erB-2 concentration 13 µg/ml(indicating diseased condition) for x_u=0.1, 0.3, 0.5, with each plot corresponding to variations in x_l=0.1, 0.3, 0.5.	**106**
4.7	The sensitivity of drain current is analyzed for different values of x_u =0.1, 0.3, 0.5andx_l =0.1 , 0.3, 0.5.	**107**
5.1	Device structure of the Dual Material Double Gate tunnel FET.	**119**
5.2	Surface potential profile along the channel with Vds = 0.5 V and varying Vgs.= 0.5V, 0.7V and 1.0V. Symbols: Simulation values from ATLAS	**121**
5.3	(a) Formation of potential well and potential barrier along the channel at on state (b) Approximated rectangular potential well under M_1 with perturbation. (c) Quantum transport of electron from region1(channel $0<z<L_1$) to region2(drain) through potential barrier (channel $L_1 < z < L_2$).	**122**
5.4	Electric Field along the channel with Vgs =0.1V and 0.5V at Vds = 0.5 V. Symbols: ATLAS.	**129**
5.5	Current density vs gate voltage with scaling (L_1) at Vds=0.5V. Q: Quantum, C: Classical, Marks: Simulation.	**130**
5.6	An exploratory comparison of transmission coefficientT(E)-vs engergy between classical tunneling and quantum tunneling.	**131**
5.7	(a) Quantum transmission coefficient of an electron, having energy (E), tunneling through potential barrier (V_0) under M_2, (a) Linear, (b) semi-log	**131**
5.8	Current density against gate voltage with varying work function difference (dW= ϕ_{M2}-ϕ_{M1}) in gate materials.	**132**

5.9	Transconductance against gate length for Vgs =1V to 1.05V and Vds =0.75V. Q: Quantum, C: Classical, Marks: Simulation.	133
5.10	Heterojunction TFET with (a)SiGe Source, Si Channel, and Si Drain , (b) Ge Source, SiGe Channel and Si Drain configurations (c) Si source SiGe Pocket Si channel and Si drain	137
5.11	Contour plots illustrating the classical potential profiles for the three TFET architectures: (i) SiGe Source-Si Channel-Si Drain, (ii) Ge Source-SiGe Channel-Si Drain, and (iii) Si Source-SiGe Pocket-Si Channel-Si Drain.	144
5.12	(a) electron quantum potential and (b) overall potential for the three TFET architectures: (i) Ge Source-SiGe Channel-Si Drain, (ii) SiGe Source-Si Channel-Si Drain, and (ii) Si Source-SiGe Pocket-Si Channel-Si Drain with and without quantum effects.	146
5.13	Energy band diagrams for (i) Ge Source-SiGe Channel-Si Drain, (ii) Si Source-SiGe Pocket-Si Channel-Si Drain, and (iii) SiGe Source-Si Channel-Si Drain configurations with and without quantum effects.	147
5.14	BTBT for (i) Ge Source-SiGe Channel-Si Drain, (ii) Si Source-SiGe Pocket-Si Channel-Si Drain, and (iii) SiGe Source-Si Channel-Si Drain configurations with and without quantum effects.	148
5.15	Id-Vg for (a) Ge Source-SiGe Channel-Si Drain, (b) SiGe Source-Si Channel-Si Drain and (c) Si Source-SiGe Pocket-Si Channel-Si Drain configurations with and without quantum effects (d) Drain current vs Gate Voltage Characteristics for Different TFET Configurations comparing the analytical model(calc.) and simulation results(Sim.).	150
5.16	On state current sensitivity for (i) Ge Source-SiGe Channel-Si Drain, (ii) SiGe Source-Si Channel-Si Drain and (iii) Si Source-SiGe Pocket-Si Channel-Si Drain configurations with and without quantum effects	151
5.17	Threshold voltage sensitivity for (i) Ge Source-SiGe Channel-Si Drain, (ii) SiGe Source-Si Channel-Si Drain and (iii) Si Source-SiGe Pocket-Si Channel-Si Drain configurations with and without quantum effects.	152
6.1	Schematic of the device used in simulation.	162
6.2	Impact of varying As mole fraction in $In_{(1-x)}Ga_xAs_yP_{(1-y)}$ /InP MQW structure on electron concentration (a) contour plot , (b) line plot.	168
6.3	Impact of varying As mole fraction in $In_{(1-x)}Ga_xAs_yP_{(1-y)}$ /InP MQW structure on dark current.	169
6.4	Impact of varying As mole fraction in $In_{(1-x)}Ga_xAs_yP_{(1-y)}$/InP MQW structure on photocurrent.	170
6.5	Power Spectral Density at (a) y=0.24 (b) y=0.42 and (c) y=0.69.	172

List of Tables

Table No.	Description	Page No
1.1	Technological advancements guided by the IRDS 2022.	1
2.1	Comparison of Devices at Nanoscale	17
2.2	Comparison of transport models.	35
3.1	Poisson Equation Solution Steps	52
3.2	Steps for NEGF and Poisson Coupling	56
4.1	Dimensions of the device taken into account in this modeling	95
4.2	Characterization of Interface Charges Associated with C-ERB2 Biomolecules Investigated in the Current Study	99
4.3	Comparison of the sensitivity data with the double channel HEMTs used for other sensing applications.	108
5.1	Typical Parameter Values	119
5.2	Comparison of selectivity data between classical and quantum models	153
6.1	Key Differences of Single and Multiple Qunatum Well	160
6.2	Summary of models used in the Qunatum Well simulation	164
6.3	Summary of Comparison of quantum correction models	177

List of Abbreviations

2DEG	Two-Dimensional Electron Gas
Al	Aluminum
AlGaN	Aluminum Gallium Nitride
BQP	Bohm Quantum Potential
BTBT	Band-to-Band Tunneling
BTE	Boltzmann Transport Equation
C-erbB2	Human Epidermal Growth Factor Receptor 2 (HER2) Biomarker
CB	Conduction Band
CMOS	Complementary Metal–Oxide–Semiconductor
DC	Direct Current
DC-HEMT	Double Channel High Electron Mobility Transistor
DD	Drift–Diffusion Model
DG	Density Gradient
DIBL	Drain-Induced Barrier Lowering
DMDG-TFET	Dual Metal Double Gate Tunnel Field-Effect Transistor
DOS	Density of States
EF	Electric Field
FEM	Finite Element Method
FET	Field-Effect Transistor
GaN	Gallium Nitride
HEMT	High Electron Mobility Transistor
H_2	Hydrogen Gas
Id–Vg	Drain Current vs Gate Voltage Characteristics
InGaAsP	Indium Gallium Arsenide Phosphide
InP	Indium Phosphide
I–V	Current–Voltage Characteristics
MB	Miniband (in Superlattice Structures)
MBE	Molecular Beam Epitaxy
MOCVD	Metalorganic Chemical Vapor Deposition
MOSFET	Metal–Oxide–Semiconductor Field-Effect Transistor

MQW	Multi Quantum Well
$MoTe_2$	Molybdenum Ditelluride
N_2	Nitrogen
NEGF	Non-Equilibrium Green's Function
Pd	Palladium
QCE	Quantum Confinement Effect
QW	Quantum Well
QWIP	Quantum Well Infrared Photodetector
RF	Radio Frequency
SC-HEMT	Single Channel High Electron Mobility Transistor
SCE	Short Channel Effect
SE-BQP	Strain-Engineered Bohm Quantum Potential
SLATT	Superlattice Transport Model
SP	Schrödinger–Poisson (Self-consistent Solver)
SRH	Shockley–Read–Hall Recombination
STE	Stress Transfer Efficiency
TCAD	Technology Computer-Aided Design
TE	Transverse Electric Polarization
TFET	Tunnel Field-Effect Transistor
TM	Transverse Magnetic Polarization
WF	Work Function

List of Symbols

Symbol	Meaning / Description	Unit
A	Spectral Function	—
α, γ	Quantum Correction Parameters in BQP Model	—
a_{Si}, a_{Ge}	Lattice Constants of Si and Ge	Å or nm
β	Beta Parameter in Van Dort Model	—
χ	Electron Affinity	eV
Csi	Silicon Body Capacitance	F/cm^2
Cox	Oxide Capacitance	F/cm^2
Cox(f,b)	Front and Back Oxide Capacitance	F/cm^2
Dn	Diffusion Coefficient for Electrons	cm^2/s
Dp	Diffusion Coefficient for Holes	cm^2/s
Dn	2-D Density of States	$cm^{-2}\cdot eV^{-1}$
DOS	Density of States	—
ΔEc	Conduction Band Offset / Energy Difference	eV
ΔE	Energy Shift / Change in Bandgap	eV
ΔEg	Bandgap Energy Shift	eV
ΔEv	Valence Band Shift	eV
E	Energy	eV
Ec	Conduction Band Edge Energy	eV
Ef	Fermi Level / Energy	eV
EF_{max}	Maximum Electric Field	V/cm
ε	Permittivity / Strain Tensor	F/cm or —
ε_0	Vacuum Permittivity	F/cm
ε_{si}	Permittivity of Silicon	F/cm
Ev	Valence Band Edge Energy	eV
f_S, f_D	Fermi-Dirac Distribution (Source & Drain)	—
Φ_{M1}, Φ_{M2}	Work Functions of Gate Metals 1 & 2	eV
φ	Potential	V
γ	Fitting Factor	—
Γ	Broadening Function	—
g_m	Transconductance	S or A/V
g(y)	Function in Van Dort Model	—
G	Retarded Green's Function	—
G^A	Advanced Green's Function	—
$G^<$	Lesser Green's Function	—
ħ	Reduced Planck's Constant (h/2π)	J•s
H_2	Hydrogen Gas	—

Symbol	**Meaning / Description**	**Unit**
Id	Drain Current	A
Ip	Hole Current	A
I	Current	A
J	Current Density	A/cm^2
J_T	Tunneling Current Density	A/cm^2
k	Wavevector	m^{-1}
kB	Boltzmann Constant	J/K
k•p	Momentum–Matrix Perturbation	—
L	Channel Length	nm
Λ_{DG}	DG Correction Potential	V
m	Carrier Effective Mass	kg
m*	Effective Mass of Electron / Charge Carrier	kg
n_{2D}	Two-Dimensional Electron Density	cm^{-2}
n, p	Electron and Hole Concentrations	cm^{-3}
n_{buff}	Carrier Concentration in Buffer	cm^{-3}
N, N_A, N_D	Doping Concentrations	cm^{-3}
Nch	Channel Doping Concentration	cm^{-3}
Nc, Nv	Effective Density of States	cm^{-3}
n_i	Intrinsic Carrier Concentration	cm^{-3}
Ψ	Wave Function	—
Ψi*	Complex Conjugate of Wave Function	—
Qg	Gate Charge	C
φ_{BQP}	Effective Potential with BQP	eV
ρ	Charge Density	C/cm^3
Σ	Self-energy (NEGF Formalism)	—
Σ_S, Σ_D	Source and Drain Self-Energies	—
σ	Bound Sheet Charge	C/m^2
T	Temperature	K
T(E)	Transmission Coefficient	—
t_{ox}	Oxide Thickness	nm
t_{oxf}, t_{oxb}	Front/Back Gate Oxide Thickness	nm
t_{si}	Silicon Film Thickness	nm
τ	mean free time	s
V	Applied Bias Voltage	V
VB	Valence Band	—
Vd	Drain Voltage	V
V_{FB}	Flat-Band Voltage	V

Symbol	Meaning / Description	Unit
Vg	Gate Voltage	V
Vgs	Gate–Source Voltage	V
Vs	Source Voltage	V
λ_{BQP}	Bohm Quantum Potential Scaling Factor	—
(v_p)	Hole drift velocity	m/s
(v_n)	Electron drift velocity	m/s
(q)	Electron/hole charge	C (Coulomb)
(τ_p)	Hole scattering time / relaxation time	s (seconds)
(τ_n)	Electron scattering time / relaxation time	s (seconds)
(m^*_p)	Effective mass of hole	kg
(m^*_n)	Effective mass of electron	kg
(EF)	Electric field	V/m
(μ_p)	Hole mobility	$m^2/(V\cdot s)$
(μ_n)	Electron mobility	$m^2/(V\cdot s)$
(μ_{phonon})	Mobility limited by phonon scattering	$m^2/(V\cdot s)$
(μ_{imp})	Mobility limited by ionized impurity scattering	$m^2/(V\cdot s)$
(T)	Temperature	K (Kelvin)
(N_{imp})	Impurity concentration	m^{-3} / cm^{-3}
(λ_D)	Debye screening length	m
(μ_{net})	Net carrier mobility combining phonon and impurity scattering	$m^2/(V\cdot s)$
(R_p)	Net rate of holes moving	s^{-1}
(R_n)	Net rate of electrons moving	s^{-1}
(N_p)	Hole concentration	m^{-3} / cm^{-3}
(N_n)	Electron concentration	m^{-3} / cm^{-3}
(dN_p/dx)	Hole concentration gradient	m^{-4} / cm^4
(dN_n/dx)	Electron concentration gradient	m^{-4} / cm^4

Chapter 1: Introduction and Organization of the Thesis

1.1. Introduction and Motivation
1.2. Organization of the Thesis

1.1 Introduction and Motivation

Introduction

The relentless advancements in semiconductor technology have fundamentally transformed modern electronics, enabling the development of compact, efficient, and high-performance devices. This evolution has been guided by Moore's Law, which predicts the exponential scaling of transistor density on integrated circuits[1], [2]. However, as device dimensions continue to shrink to the nanometer scale, traditional device physics encounters significant challenges, necessitating a paradigm shift in the modeling and analysis of charge transport mechanisms. This thesis addresses these challenges by exploring the realm of semi-classical and quantum transport phenomena, focusing on their implications for low-dimensional devices and sensors.

Year of production	**2022**	**2025**	**2028**	**2031**	**2034**	**2037**
Logic industry "Node range" Labeling	3 nm	2 nm	1.5 nm	1.0 nm	0.7 nm	0.5 nm
Logic device for logic	funFET	LGAA	LGAA CFET-SRAM	LGAA CFET-3D CFET SRAM 3D	LGAA CFET-3D CFET SRAM 3D	LGAA CFET-3D CFET SRAM 3D
Mx Pitch (nm)	32	24	20	16	16	16
Gate pitch (nm)	48	45	42	40	38	38
Lg: Gate length – HP(nm)	16	14	12	12	12	12

Table 1.1. Technological advancements guided by the IRDS 2022[3].

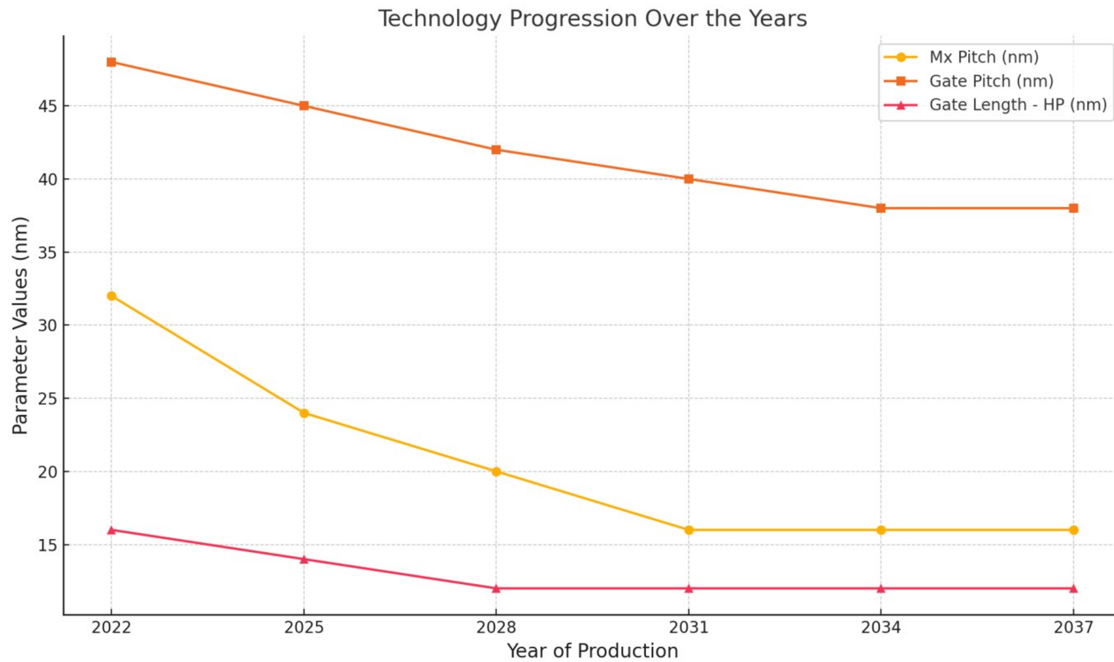

Figure 1.1. Industrial roadmap guided by the IRDS 2022.

The demand for smaller, faster, and more energy-efficient devices has driven the semiconductor industry to push the boundaries of scaling. Scaling not only modifies electrical behavior but also changes material parameters. The effective mass, bandgap, and density of states become dimension-dependent due to quantum confinement. As a result, new design trade-offs emerge between electrostatic control, leakage current, and mobility degradation. Short-channel effects, gate-induced drain leakage, and direct source-to-drain tunneling are manifestations of this scale-dependent physics. These phenomena necessitate a shift from classical device modeling toward semiclassical and fully quantum mechanical approaches that can accurately describe charge transport under confined geometries. The transition from classical to nanoscale dimensions introduces phenomena that are profoundly influenced by quantum mechanics. While classical models, such as the drift-diffusion and hydrodynamic model have successfully described carrier transport in bulk devices, they fail to capture quantum effects such as tunneling, quantum confinement, and wave interference, which dominate at nanoscale dimensions[4], [5], [6]. This necessitates the development and application of advanced transport models that integrate quantum mechanics and semi-classical principles to accurately predict device behavior. Semiclassical models provide an essential bridge

between classical drift-diffusion theories and quantum mechanical transport formalisms. In these models, quantum corrections are introduced into classical equations to account for carrier confinement, tunneling, and non-local effects without fully abandoning the particle-based description. Techniques such as the Density Gradient (DG) method, Bohm Quantum Potential (BQP) model, and quantum correction models (QCM) extend the conventional Poisson and continuity equations by embedding quantum potential terms derived from the wavefunction curvature or the carrier density gradient. These semiclassical methods preserve computational efficiency while enhancing physical accuracy, making them particularly attractive for device-scale simulations. They enable a self-consistent description of carrier distributions, potential profiles, and electrostatics in ultra-thin body devices, nanowires, and multi-gate FETs. For example, in double-gate or gate-all-around structures, the quantum confinement of carriers modifies threshold voltage and charge centroid, which can be effectively captured using semiclassical quantum correction models. Similarly, the BQP model helps approximate the impact of quantum confinement on carrier density and potential energy, ensuring that simulations remain tractable yet physically meaningful. While semiclassical models suffice for many nanoscale devices, they fall short when quantum coherence, tunneling, or interference effects dominate transport. In such regimes, a fully quantum mechanical framework is essential to describe electron flow accurately. The Non-Equilibrium Green's Function (NEGF) formalism has emerged as a powerful tool to model carrier transport in low-dimensional systems. Unlike semiclassical models, NEGF captures the wave nature of electrons, quantum tunneling, and energy-dependent transmission under non-equilibrium bias conditions. NEGF allows the inclusion of realistic scattering processes—such as electron-phonon and impurity interactions—through self-energy terms, making it highly versatile for studying transport in nanowires, quantum wells, and 2D material-based transistors. The formulation enables the computation of transmission spectra, local density of states (LDOS), and quantum current densities, which are critical for understanding and optimizing nanoscale device performance. Moreover, NEGF seamlessly bridges the gap between ballistic and diffusive regimes, making it indispensable for analyzing ultra-scaled transistors and tunneling-based devices such as Tunnel FETs .

Besides, Low-dimensional semiconductor structures have become the cornerstone of next-generation nanoelectronics. For instance, 2D materials like MoS_2 and $MoTe_2$ exhibit high carrier mobility, strong electrostatic control, and excellent mechanical flexibility, making them ideal candidates for applications in sensors, transistors, and optoelectronic devices[7, p. 222], [8], [9], [10]. Similarly, nanowires [11], [12], [13], [14], [15] and quantum wells [16], [17], [18] provide opportunities for engineering band structures and enhancing device performance through quantum effects.

Beyond logic and memory devices, low-dimensional structures have revolutionized the field of sensing. As devices scale down, their surface-to-volume ratio increases dramatically, making them highly sensitive to external perturbations such as gas molecules, biomolecules, or photons. This sensitivity, coupled with the ability to tune electronic properties through quantum confinement, allows low-dimensional FETs to function as precise and selective sensors [19], [20], [21]. For example, hydrogen sensors based on transition metal dichalcogenides (TMDs) leverage quantum confinement and surface interactions to achieve high sensitivity and rapid response times[22]. Likewise, biosensors utilizing tunneling field-effect transistors (TFETs) exploit quantum tunneling to detect biomolecules with exceptional precision [23].

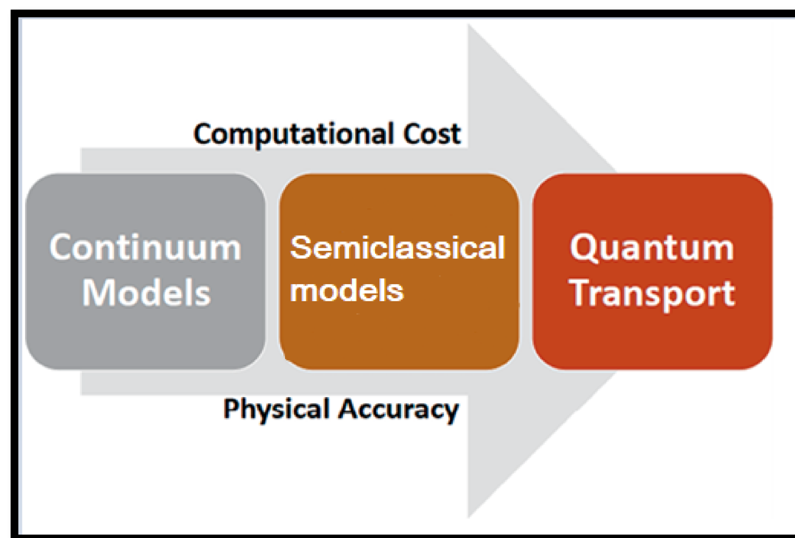

Figure 1.2: Accuracy cost trade-off of classical, semi-classical and quantum models. [24-31]

Despite their potential, the design and optimization of low-dimensional sensors pose significant challenges. Accurate modeling of charge transport is critical for understanding device behavior and predicting performance [24], [25], [26], [27] [28], [29], [30] [31].

Research Gap

Although extensive progress has been made in modeling nanoscale electronic devices, there remains a substantial gap in establishing a unified, cross-platform understanding of transport phenomena that bridges semiclassical and quantum regimes. Most existing studies either focus on classical drift-diffusion and hydrodynamic models, which are computationally efficient but inadequate in capturing confinement and tunneling at sub-10 nm scales, or on fully quantum mechanical approaches such as the Non-Equilibrium Green's Function (NEGF) formalism, which, though highly accurate, are computationally intensive and often restricted to specific device types. This dichotomy leaves a persistent gap in systematically linking model complexity with physical accuracy across various device architectures—such as MOSFETs, HEMTs, TFETs, and quantum-well-based structures—where carrier behavior is strongly influenced by dimensionality, confinement, and potential fluctuations.

In the sensor domain, despite rapid developments in nano-FET-based biosensors and gas sensors, most analyses continue to rely heavily on classical electrostatics, neglecting crucial quantum effects like discrete subband formation, charge quantization, and wavefunction overlap that directly impact sensitivity, selectivity, and linearity of response. A detailed and comparative study that integrates different material systems (Si, III–V, and 2D materials), device configurations (planar, double-gate, tunnel-based, and quantum-well structures), and corresponding transport frameworks (semiclassical drift-diffusion, density-gradient, and NEGF-based quantum models) remains largely unexplored. Specifically, the impact of transport modeling accuracy on the predicted sensitivity and signal transduction efficiency of nanoscale sensors has not been systematically evaluated, even though it critically determines device performance under strong quantum confinement.

Moreover, the structural and material engineering strategies—such as dielectric grading, charge plasma doping, inter-channel coupling, and barrier modulation—required to maintain device functionality and sensing precision in such low-dimensional regimes have not yet been comprehensively addressed. Therefore, a significant research gap exists in (i) developing scalable and physically consistent transport models that adapt across device geometries and materials, (ii) benchmarking semiclassical corrections against quantum transport predictions for balanced accuracy–cost trade-offs, (iii) examining how these models influence sensor response characteristics, and (iv) identifying structural and material design principles suitable for robust operation under quantum-dominated conditions. Addressing these gaps is crucial to accurately predict, design, and optimize the performance of emerging low-dimensional nanoelectronic and sensor devices that operate at or beyond the classical limit.

Motivation

This thesis is motivated by the growing necessity to comprehensively investigate semiclassical and quantum transport mechanisms in low-dimensional electronic devices and sensors, where classical descriptions of charge transport begin to fail. As device dimensions approach the nanometer regime, phenomena such as quantum confinement, tunneling, and discrete subband formation become dominant, demanding a deeper integration of physics-based models that transcend traditional drift-diffusion or hydrodynamic formulations. The work presented here builds upon prior studies of quantum transport in hydrogen sensors, inter-channel coupling effects in double-channel HEMTs, and quantum-mechanical behavior in TFETs and photodetectors—each contributing to a more complete understanding of carrier dynamics and sensing at the quantum scale.

- The primary motivation for this thesis arises from the evident limitations of existing transport models in accurately capturing the physical behavior of nanoscale devices used in sensing applications. While classical and semiclassical models have proven effective for micro-scale device analysis, their predictive power diminishes in sub-10 nm structures, where electron–wave interactions, tunneling, and charge quantization substantially modify current flow and

sensitivity. Despite extensive literature on device-level modeling, the direct correlation between transport framework accuracy and sensor response characteristics remains insufficiently explored. This work is thus driven by the need to bridge semiclassical and quantum transport frameworks—establishing a continuum of understanding that can predict electronic and sensing behavior across different architectures, including MOSFETs, HEMTs, TFETs, and quantum-well-based devices.

- A second motivation stems from the emerging demand for advanced, miniaturized sensors capable of precise operation under diverse and harsh environments. The next generation of nanosensors requires not only high sensitivity and selectivity but also stable performance governed by structural engineering techniques compatible with quantum-scale operation. Techniques such as charge-plasma-based electrical doping, inter-channel coupling, dielectric and material grading, and multi-layer quantum confinement offer promising routes to tune electrostatics and carrier transport. However, their effective implementation requires a strong theoretical foundation that links these engineering strategies to the underlying transport mechanisms. This thesis aims to address this gap by integrating semiclassical and quantum modeling approaches with structural and material design principles to formulate optimized sensor architectures.
- The third motivation lies in exploring and utilizing material diversity to enhance both electronic and sensing functionalities at low dimensions. Novel materials such as $MoTe_2$, AlGaN/GaN, and SiGe provide distinct advantages due to their tunable band structures, high carrier mobility, and strong confinement effects. For instance, $MoTe_2$ exhibits exceptional hydrogen adsorption properties owing to its high surface-to-volume ratio, while AlGaN/GaN heterostructures enable high electron mobility and superior confinement—ideal for high-frequency and sensing devices. Similarly, graded SiGe structures enable band alignment tuning and improved charge control for biosensing applications. By coupling such materials with appropriate transport modeling frameworks, this thesis seeks to derive predictive insights into how material parameters, device geometry, and quantum effects collectively influence sensitivity, linearity, and noise performance in nanosensors.

In summary, this thesis is driven by the urgent need to unify transport modeling and sensor physics under a comprehensive, cross-platform framework applicable to low-dimensional systems. By systematically integrating semiclassical corrections and quantum transport methodologies, it aims to overcome the limitations of conventional models, quantify their impact on sensor sensitivity and performance, and guide the structural and material design of future nanoscale devices. The outcomes of this study are expected to contribute significantly to the understanding and advancement of next-generation nanoelectronic and sensor technologies, with potential implications for biosensing, gas detection, photodetection, and emerging quantum devices.

1.2. Organization of the Thesis

The organization of the thesis reflects these motivations, with each chapter addressing a specific structural engineering approach integrated with a suitable transport phenomenon (semiclassical or quantum) to explore the electrostatics and enhance the sensing capabilities of the devices. The first chapter provides an introduction to the thesis, outlining the motivations, objectives, and scope of the work. Subsequent chapters delve into the modeling and analysis of specific device types, including MOSFETs, HEMTs, TFETs, and photodetectors, highlighting the role of semi-classical and quantum transport in their operation. The thesis concludes with a discussion of emerging trends and future directions in the field, emphasizing the importance of continued research in nanoscale transport phenomena. Below is a detailed description of the chapters and their contents:

Chapter 2: Introduction to Semi-classical and Quantum Transport in Nano-scaled Devices

This chapter serves as a foundational introduction to the key concepts and frameworks essential for understanding the transport phenomena in nano-scaled devices.

2.1 Overview of Nano-scaled Devices

This section provides an overview of the technological evolution of nano-scaled devices and their significance in the context of modern electronics and sensors.

2.2 Importance of Carrier Transport Phenomena

Carrier transport is critical to the functioning of semiconductor devices. This section emphasizes the role of charge carriers in device performance, focusing on how phenomena such as drift, diffusion, and quantum effects influence current flow and response characteristics.

2.3 Classical Transport Models and their Limitations

Classical transport models, like the drift-diffusion and hydrodynamic models, are reviewed, highlighting their applicability to larger devices but also their limitations in accurately predicting behavior at the nano scale.

2.4 Semi-classical and Quantum Transport

A deeper discussion on semi-classical and quantum transport models is provided. These models, including the Non-Equilibrium Green's Function (NEGF) approach and quantum correction methods, are contrasted with classical approaches.

2.5 Literature Study

This section reviews existing research in semiclaasical and quantum transport, with an emphasis on their application to nano-scaled devices.

2.6 Conclusion

The chapter concludes by summarizing the key points.

Chapter 3: Quantum Transport (NEGF) in Low-Dimensional MOSFETs

Chapter 3 delves into the application of quantum transport in low-dimensional MOSFETs, focusing on the use of the NEGF approach for accurate modeling of carrier transport in nanoscale MOSFETs.

3.1 Introduction to Low-Dimensional MOSFETs

This section provides an overview of the design, structure, and significance of low-dimensional MOSFETs.

3.2 Quantum Transport in MOSFETs based on NEGF: Theoretical Analysis

A theoretical study of quantum transport in MOSFETs using the NEGF formalism is provided along with reviews on significant existing research .

3.3 Charge Plasma Engineering and it's Application

This section explores charge plasma engineering, an advanced technique that manipulates the carrier concentration profile to improve device performance and focus on its application on low dimensional devices.

3.4 Gas Sensing Application of TMD-Based FETs

The use of Transition Metal Dichalcogenide (TMD)-based FETs in sensing applications is discussed focusing on gas densing application.

3.5 Non-Equilibrium Green's Function Analysis of Charge Plasma-Based Source-Drain Electrode P-type $MoTe_2$ MOSFET for High-Sensitivity Hydrogen Sensing

In this section, a research on NEGF transport in $MoTe_2$-based MOSFET is explored. The focus is on modeling p and n type $MoTe_2$ device for hydrogen sensing using charge plasma engineering.

3.6 Conclusion and Future Work

The chapter concludes with a summary of the main findings, emphasizing the importance of NEGF in simulating quantum transport in low-dimensional MOSFETs.

Chapter 4: Density Gradient: DG (Quantum Moments Model) of High-Electron-Mobility Transistors for Biosensing Applications

This chapter is focused on the use of the Density Gradient (DG) model, which is part of the quantum moments approach, for simulating High-Electron-Mobility Transistors (HEMTs), with an emphasis on their biosensing applications.

4.1 Introduction to HEMTs & Double-Channel HEMTs

An overview of HEMTs is presented, covering their structure, operating principle, and key advantages, followed by a discussion of the limitations of single-channel HEMTs. The concept of double-channel HEMTs (DCHEMT) is then introduced.

4.2 DG (Density Gradient -Quantum Moments Model) in HEMT: Theoretical Analysis and literature survey

This section presents a detailed theoretical analysis of the DG model in general along with reported researches and applications of DG model.

4.3 Biosensor Application of HEMTs

HEMTs are explored for their potential in biosensing, with a focus on detecting crucial biological molecules.

4.4 Deep Insight into Inter-Channel Coupling in AlGaN/GaN Double Channel HEMT and its Application in C-ERB2 Sensing

AlGaN/GaN Double Channel HEMT is investigated in details, with emphasis on interchannel coupling and the role of mole fraction variation. This section discusses how quantum effects influence the device performance, particularly in biosensing applications like C-ERB2 sensing for cancer diagnostics.

4.5 Conclusion and Future Work

The chapter concludes by summarizing the role of the DG model in modeling HEMTs for biosensing application with compoarison with other transport models.

Chapter 5: Analytical and BQP (Bohm Quantum Potential) Based Quantum Analysis of Tunnel Field-Effect Transistors

Chapter 5 focuses on the application of Bohm Quantum Potential (BQP) in modeling Tunnel Field-Effect Transistors (TFETs).

5.1 Introduction to TFETs

This section introduces TFETs, detailing their working principle, advantages, and challenges.

5.2 Quantum Effects in TFETs

A theoretical study and literature survey of quantum effects in TFETs is provided.

5.3 Comprehensive Quantum Analytical Modeling of Very Low-Dimensional Dual Metal Double Gate TFET

This section presents a modeling approach for very low-dimensional TFETs using quantum analytical methods. The impact of dual-metal double gates on device performance is examined. The role of quantum tunneling, the impact of the gate material are discussed in detail.

5.4 Impact of Bohm Quantum Potential on SiGe-Based Heterojunction Tunnel FET Biosensors: Modeling and Comparative Analysis

The BQP is incorporated into the modeling of SiGe-based heterojunction TFETs, with a focus on their application in biosensing.

5.5 Conclusion and Future Work

The chapter concludes with a summary of the key findings, emphasizing the role of semiclasical and quantum transport models in idetermiming the electrostatic and sensing performance in TFETs.

Chapter 6: Quantum Correction Models and Parabolic Quantum Well Model

Chapter 6 focuses on the use of quantum correction models and the Parabolic Quantum Well (PQW) model in device simulation.

6.1 Introduction to Parabolic Quantum Well Model and Multi-Well Photodetectors

This section introduces the PQW model, which is used to describe the quantum mechanical behavior of carriers confined within a potential well.

6.2 Device Structure, Simulation of $In_{(1-x)}Ga_xAs_yP_{(1-y)}$/InP Wideband Multi-Well Photodetectors using k·p Method

This section discusses the simulation of multi-well photodetectors using the k·p method.

6.3. Other Quantum correction models

The section provides an overview of various quantum correction models applicable for quantum well based photodetectors.

6.4 Conclusion and Future Work

The chapter concludes with a summary of the quantum correction models and the PQW model's application in device simulation.

Chapter 7: Conclusion and future work

7.1 Conclusion

Compartive analysis of transport mechanisms in low-dimensional semiconductor devices using NEGF, DG, BQP, and related models. Optimization models to find suitability for transport model for nanoscale sensing performance.

7.2 Future Work

Future work may incorporate scattering, defects, and temperature effects to enhance physical accuracy along with exploring experimental validation of advance practical nanoscale sensor design.

Chapter 2:

Introduction to Semi-classical and Quantum Transport in Nano-scaled Devices

2.1. Overview of Nano-scaled Devices

2.2. Importance of carrier Transport Phenomena

2.3. Classical Transport Models and their limitations

2.4. Semi-classical and Quantum Transport

2.5. Literature Study

2.6. Conclusion

2.1 Overview of Nano-Scaled Devices

The rapid evolution of semiconductor technology has led to the continuous scaling of device dimensions deep into the nanometer regime, enabling faster, smaller, and more energy-efficient electronic systems. This miniaturization, guided by Moore's law for decades, has redefined not only the performance benchmarks but also the fundamental physics governing device operation. As the characteristic dimensions of transistors approach the atomic scale, classical electrostatic and material approximations become inadequate, and quantum mechanical effects start to influence even the most conventional device architectures. Phenomena such as quantum confinement, tunneling, and discrete energy quantization have transitioned from being secondary considerations to primary design constraints in modern nanoelectronic systems.

Within this landscape, various device architectures have been developed to sustain performance, reliability, and scalability as the industry moves deep into the nanometer regime. Among these, the Metal-Oxide-Semiconductor Field-Effect Transistor (MOSFET) continues to be the cornerstone of digital electronics. Its working principle is based on controlling the conductivity of a semiconductor channel through the electric field applied at the gate terminal. In the planar MOSFET, a gate voltage modulates the surface potential to create an inversion layer of carriers beneath the oxide, enabling current flow between the source and drain. However, as the channel length is reduced below tens of nanometers, short-channel effects (SCEs) such as Drain-Induced Barrier Lowering (DIBL), threshold voltage roll-off, and subthreshold leakage become prominent due to weakened gate control. To counter these challenges, advanced multi-gate configurations have been introduced. These architectures enhance gate coupling and reduce electrostatic interference from the drain, thereby improving the device's scalability and switching performance. Despite their success, the fabrication complexity and sensitivity to quantum confinement and interface states in ultra-thin channels remain critical limitations in nanoscale MOSFETs.

To address the fundamental subthreshold limit of 60 mV/decade inherent in thermionic emission-based transistors, the Tunnel Field-Effect Transistor (TFET) was proposed as an alternative device concept. TFETs operate on the principle of band-to-band tunneling (BTBT), where carriers quantum-mechanically tunnel through a potential barrier between the valence band of the source and the conduction band of the channel. This tunneling mechanism enables TFETs to achieve extremely low leakage currents and steep subthreshold slopes, making them ideal candidates for ultra-low power and energy-efficient applications. However, their main disadvantage lies in the low ON-current, which arises from limited tunneling probability and high sensitivity to material properties and interface quality. To enhance performance, heterojunction designs, graded bandgap materials, and Double-Material Double-Gate (DMDG) configurations have been explored, which also provide better control over electrostatics and channel potential at nanoscale dimensions.

In contrast, High Electron Mobility Transistors (HEMTs) leverage heterostructure engineering to achieve high-speed operation and superior current drive. By forming a two-dimensional electron gas (2DEG) at the interface of two semiconductors with

different bandgaps—typically AlGaN/GaN or AlGaAs/GaAs systems—HEMTs provide a high-density, high-mobility channel without intentional doping. The absence of impurity scattering in the conduction path enables very high electron mobility, resulting in excellent transconductance and frequency performance.

Nevertheless, at the nanoscale, challenges such as polarization-induced charge imbalance, thermal management, and short-gate effects become critical, requiring careful optimization of barrier thickness, gate design, and interface quality.

Beyond transistors, Quantum Well (QW) and Multiple Quantum Well (MQW) devices represent the frontier of optoelectronic nanostructures, where charge carrier behavior is dominated by quantum confinement in one or more spatial dimensions. In a quantum well, a thin semiconductor layer with a smaller bandgap is sandwiched between higher bandgap materials, creating a potential well that confines electrons and holes in discrete energy subbands. This quantization enhances carrier recombination efficiency and allows precise wavelength tunability, making QWs and MQWs the foundational structures in lasers, LEDs, and photodetectors. The advantages of these devices lie in their enhanced optical gain, reduced threshold current, and superior spectral control, while disadvantages include fabrication sensitivity, strain accumulation in multi-layer stacks, and carrier leakage due to thermal and tunneling effects. At nanoscale thicknesses, the design and optimization of QW structures require precise control of well width, barrier composition, and interface abruptness, as even small variations can drastically affect energy levels and device performance.

Collectively, these device architectures exemplify the technological and physical innovations required to sustain the progress of nanoelectronics. Each class of device demonstrates a distinct approach to overcoming the scaling-induced limitations of conventional transistors—whether through enhanced electrostatic control (MOSFETs), quantum tunneling mechanisms (TFETs), heterostructure-induced high mobility (HEMTs), or quantum confinement-enhanced optoelectronic efficiency (QWs/MQWs). As scaling continues, the interplay between quantum effects, material engineering, and structural design becomes the defining factor in the performance and functionality of next-generation nanoscale devices.

Device	Key Mechanism	Strengths	Challenges
MOSFET	Gate-controlled conductivity	Scalability, integration	Short-channel effects, leakage currents
TFET	Quantum tunneling	Ultra-low power, steep switching	Low drive current, fabrication complexity
HEMT	High electron mobility	High-speed, high-power operation	Thermal management, material cost
Quantum Wells	Carrier confinement	Tunable properties, optical efficiency	Precision fabrication, defect control

Table 2.1.Comparison of Devices at Nanoscale

2.2. Importance of Carrier Transport Phenomena

Carrier transport phenomena represent a cornerstone in the study and development of electronic, optoelectronic, and nanoscale devices. The behavior of charge carriers such as electrons and holes within a material determines its electrical, thermal, and optical properties, shaping the functionality and efficiency of devices ranging from transistors to photovoltaic cells. At the nanoscale, where quantum effects become prominent, understanding and accurately modeling carrier transport phenomena becomes increasingly critical. This section delves into the significance of carrier transport in nanoscale devices, elucidating the fundamental principles, mechanisms, and implications for device performance and technology advancement.:

The field of nanotechnology encompasses the manipulation, design, and engineering of materials at dimensions typically ranging from 1 to 100 nanometers. At this scale, materials exhibit unique physical and chemical properties that differ significantly from their bulk counterparts. The emergence of nano-scaled devices has been driven by advancements in various scientific disciplines. These devices hold the potential to revolutionize industries ranging from electronics to medicine, offering innovative solutions to complex challenges faced in traditional applications.

The continuous miniaturization of semiconductor devices, driven by Moore's law and the demand for enhanced performance, has led to the emergence of nano-scaled transistors where classical transport assumptions gradually lose validity. At nanometer dimensions, carrier behavior becomes governed by a combination of quantum mechanical and semi-classical effects. Among the key representatives of modern nanoelectronic devices are Metal–Oxide–Semiconductor Field-Effect Transistors (MOSFETs), Tunnel Field-Effect Transistors (TFETs), High Electron Mobility Transistors (HEMTs), and Quantum Well (QW) devices. Each of these structures exploits distinct physical mechanisms to achieve superior control over charge transport, energy efficiency, and scalability. The impact of extensive scaling on these devices are explained below:

MOSFET (Metal-Oxide-Semiconductor Field-Effect Transistor) [32]

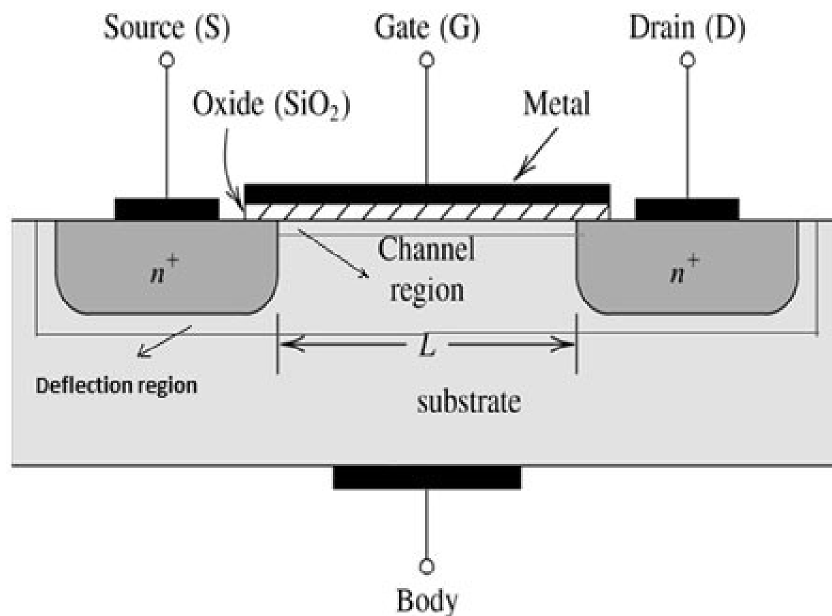

Figure 2.1. Basic Structure of MOSFET

MOSFETs are fundamental building blocks of modern electronics. Scaled MOSFET devices under the 10 nm regime showcase significant advancements in semiconductor technology, driven by the demand for higher performance and reduced power consumption. In the case of MOSFETs, the device operation is fundamentally governed by the modulation of the surface potential and the formation of an inversion layer in the semiconductor channel under the influence of the gate voltage. As device geometries shrink to the sub-10 nm scale, the conventional drift-diffusion approximation becomes insufficient to capture the complete transport picture. At such dimensions, the carrier motion is no longer continuous, and quantum mechanical effects begin to dominate the electrostatics and carrier dynamics within the device. In ultra-thin silicon channels or two-dimensional material-based MOSFETs, quantum confinement along the vertical direction leads to discrete energy subbands, altering the density of states and redistributing charge carriers in the inversion layer. This energy quantization results in a shift in the threshold voltage, reduction in gate capacitance, and a modification of effective mobility due to altered scattering probabilities and carrier degeneracy.

Furthermore, quantum tunneling becomes increasingly relevant in ultra-scaled oxide and channel regions. Carriers can penetrate potential barriers, giving rise to gate leakage currents and source-to-drain tunneling, which limit further downscaling of the gate oxide thickness and channel length. These tunneling currents, coupled with wavefunction penetration into gate dielectrics, redefine the electrostatic boundary conditions and necessitate a quantum-corrected potential formulation.

Transition metal dichalcogenide (TMD)-based field-effect transistors (FETs) have emerged as promising candidates for next-generation electronic and optoelectronic devices due to the unique properties of TMD materials like MoS_2, WS_2, $MoSe_2$, and $MoTe_2$. These atomically thin semiconductors exhibit tunable bandgaps, high on/off current ratios, and excellent electrostatic control due to their reduced dimensionality. The intrinsic two-dimensional nature of TMDs minimizes short-channel effects, making them ideal for scaling down to nanometer regimes. To modle Transition metal dichalcogenide (TMD)-based field-effect transistors (FETs), advanced modeling frameworks employ self-consistent Schrödinger–Poisson (SP) solvers or quantum correction models, which extend beyond the limitations of classical models.

Alongside these quantum phenomena, traditional short-channel effects (SCEs)—such as Drain-Induced Barrier Lowering (DIBL), velocity saturation, and channel length modulation—remain critical. To mitigate these and preserve electrostatic control, advanced structural innovations such as high-κ gate dielectrics, strained channels, and multi-gate geometries have been developed. These architectures enhance gate coupling and effectively confine carriers, making them inherently more sensitive to quantum confinement and tunneling effects. Thus, as MOSFETs enter the quantum-dominated regime, understanding and modeling carrier transport requires a seamless transition from classical to semi-classical and fully quantum transport formulations, which will be explored in the subsequent sections.

TFET (Tunnel Field-Effect Transistor)[33]

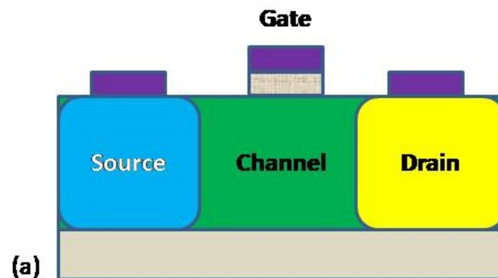

Figure 2.2. Schematic of TFET Structure

Nanoscale Tunnel Field-Effect Transistors (TFETs) are emerging as promising candidates for low-power electronics due to their ability to achieve sub-60 mV/decade subthreshold swing, making them ideal for ultra-low-voltage operation. Unlike conventional MOSFETs, TFETs rely on band-to-band tunneling (BTBT) for carrier injection, enabling superior energy efficiency.

In the case of Tunnel Field-Effect Transistors (TFETs), the device operation is fundamentally driven by band-to-band tunneling (BTBT)—a purely quantum mechanical process—which enables carriers to traverse the energy barrier between the valence band of the p-type source and the conduction band of the channel under the

influence of gate bias. Unlike MOSFETs, where thermionic emission over a potential barrier dominates, TFETs rely on tunneling through the barrier, enabling subthreshold swings well below the Boltzmann limit of 60 mV/decade. This characteristic makes TFETs exceptionally promising for ultra-low-power logic and sensing applications, especially as devices continue to scale into the nanometer regime.

At such scales, quantum confinement effects and wavefunction coupling between source and channel regions play a decisive role in determining the device's electrical behavior. The effective barrier width and height, which dictate the tunneling probability, become highly sensitive to local electrostatics, gate dielectric configuration, and channel thickness apecialaly in multi gate advanced structures like Double gate (DG) and Dual MetalDouble-Gate (DMDG) TFETs.

To accurately model these nanoscale quantum phenomena, conventional drift-diffusion prove inadequate. Instead, quantum-corrected frameworks must be employed that captures essential quantum confinement effects—including wavefunction penetration and carrier localization—without the computational complexity of full quantum transport solvers. This makes it particularly useful for simulating DG and DMDG-TFETs, where localized potential variations and material heterogeneity strongly influence tunneling and charge distribution.

HEMT (High Electron Mobility Transistor)[34]

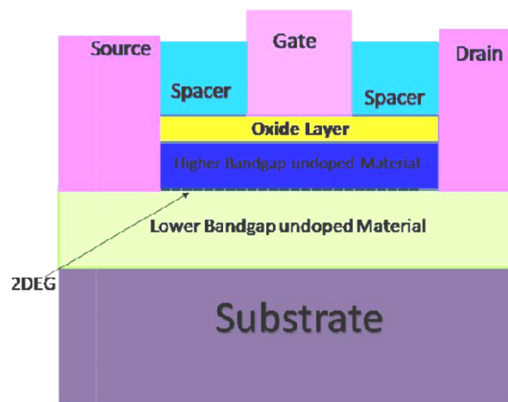

Figure 2.3. General HEMT Structure

In the case of High Electron Mobility Transistors (HEMTs), carrier transport is primarily governed by two-dimensional electron gas (2DEG) formation at the heterojunction interface of dissimilar semiconductor materials —typically III-V systems. The lattice mismatch and bandgap discontinuity between the barrier and channel layers create a strong built-in electric field, leading to quantum confinement of electrons in a narrow potential well at the interface. This confinement results in the formation of discrete quantized energy subbands, within which carriers exhibit extremely high mobility due to spatial separation from ionized impurities. Consequently, As the device dimensions are scaled further into the nanoscale regime, quantum mechanical effects increasingly influence the electrostatic and transport behavior of the 2DEG channel. The subband energy levels, carrier density, and sheet charge distribution within the quantum well become strongly dependent on the interface potential profile, polarization charge, and barrier thickness. Traditional drift-diffusion models fail to account for these effects, as they assume a continuous carrier distribution and neglect the quantized nature of the energy states. Therefore, a more sophisticated approach—one that inherently captures quantum confinement, tunneling, and carrier redistribution—is necessary to describe HEMT behavior accurately at these dimensions.

One of the most effective ways to incorporate such quantum effects within a semi-classical framework is through the self-consistent solution of the Poisson and DG-corrected transport equations that allows for a more accurate evaluation of subband populations and electrostatic potential profiles without the full computational complexity of solving the Schrödinger equation. This balance between physical rigor and numerical efficiency makes the Density Gradient method particularly suitable for simulating quantum-confined HEMT structures, where both polarization-induced charges and quantum corrections dictate carrier transport.

Quantum Well Devices [35]

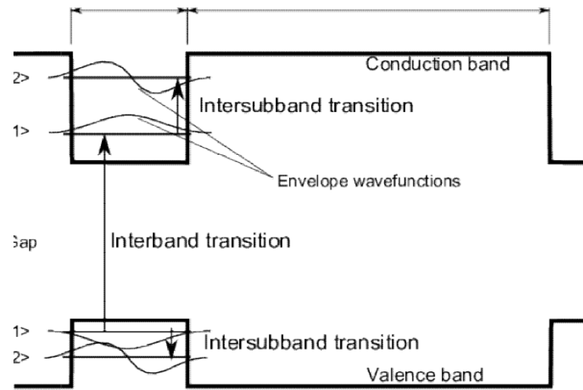

Figure 2.4. Schematic representation of Quantum Well [36] .

Quantum wells are structures where charge carriers are confined in one dimension, allowing motion in the other two dimensions. This confinement leads to discrete energy levels and enhanced control over electronic and optical properties. In the case of Quantum Well (QW) devices, carrier transport and optical behavior are dominated by quantum confinement effects that arise when charge carriers are restricted in one dimension to a potential well of nanometer-scale thickness. Such confinement leads to the formation of discrete quantized energy subbands, fundamentally altering the electronic density of states and modifying carrier transport, optical absorption, and emission properties. A quantum well typically consists of a low bandgap semiconductor layer (the well) sandwiched between higher bandgap materials (the barriers), creating a potential profile where carriers—electrons and holes—are confined in the well region but remain free to move in the other two dimensions. This two-dimensional quantization forms the foundation for a broad class of optoelectronic devices including quantum well lasers, photodetectors, light-emitting diodes (LEDs), and modulators.

As device architectures evolve toward multiple quantum well (MQW) configurations, quantum mechanical interactions between adjacent wells further complicate carrier dynamics. In MQW structures, wavefunction coupling between wells leads to miniband formation, enabling resonant tunneling and coherent carrier transport across the potential barriers. The energy level alignment, barrier thickness, and well width thus critically determine the carrier transmission probability, optical gain, and recombination efficiency. Furthermore, quantum tunneling and carrier escape

mechanisms play essential roles in defining the high-speed and efficiency characteristics of MQW devices. These effects cannot be captured by classical transport equations and require a fully quantum-mechanical treatment to describe accurately.

To model such behavior, the Schrödinger–Poisson (SP) framework is often employed to determine subband energies and spatial charge distributions self-consistently. However, for devices involving carrier injection, tunneling, and transmission he Quantum Transmitting Boundary Method (QTBM) provides a more rigorous and computationally tractable approach. The QTBM extends the traditional Schrödinger equation by incorporating open boundary conditions, allowing wavefunctions to transmit and reflect across interfaces without artificial confinement.

2.3. Classical Transport Models and their limitations

In the classical era, understanding electron behavior in materials relied on classical physics principles. For instance, the Free Electron Model depicted electrons as free agents darting about a material, blissfully ignoring the atomic lattice [37] [38]. This model was akin to treating electrons as marbles rolling around in a box, helping us grasp concepts like electrical conductivity and other macroscopic properties. Building on this, Paul Drude's 1900 model applied classical physics to elucidate electrical and thermal conductivity by envisioning electrons as classical particles with an effective mass, offering valuable insights into material transport properties. Then, in 1900, Max Planck introduced a revolutionary idea: thermal radiation is emitted in discrete packets of energy known as quanta [39]. In 1905, and Albert Einstein leveraged this concept to shed light on the photoelectric effect, suggesting that light behaves more like energetic particles than a smooth, undulating wave. This particle-like behavior also played a pivotal role in explaining the Compton effect. In 1924, Louis de Broglie brought a fresh perspective, proposing that if waves could act like particles, then particles should display wave-like properties [40]. The Heisenberg uncertainty principle, unveiled in 1927, took this idea further by stating that we can't precisely measure both the position and momentum of a tiny particle simultaneously [41]. Rather than tracking electrons the probability functions are used to estimate where they might be. In 1926, Erwin Schrödinger introduced wave mechanics, blending Planck's quantum ideas with de Broglie's wave-particle duality [42]. His equation enabled the calculation of energy

levels and wavefunctions of electrons in a crystal, crucial for deciphering band structures. Before delving into the semiclassical and quantum transport phenomena [43]. [44]. [45] [46], [47], [48] [49] [50] , it is important to understand the limitations of classical models in this section.

Conventional transport frameworks serve as the foundation for analyzing charge carrier behavior in semiconductor technologies. Methods such as drift-diffusion and hydrodynamic models employ principles of classical mechanics alongside the Boltzmann Transport Equation (BTE) to characterize carrier movement influenced by electric fields, scattering events, and thermal interactions. Although effective for large-scale devices, these approaches rely on a continuum assumption and neglect quantum mechanical phenomena, which become increasingly relevant as device dimensions approach the nanoscale. This drawback limits their precision in capturing effects like quantum confinement, tunneling, and the dual nature of particles and waves that dominate in low-dimensional systems. The advent of ultra-scaled transistors and devices featuring intricate material interfaces underscores the need for re-examining classical approaches and creating new paradigms to seamlessly integrate classical and quantum transport regimes.

Classically, when an electric field (EF) is applied to a semiconductor, it exerts a force on charge carriers, prompting them to accelerate and move [51]. For this motion to occur, energy states in the conduction and valence bands must be available, akin to steps on a ladder for carriers to transition. As a hole within the crystal accelerates under the influence of the electric field, its velocity increases. However, periodic collisions with lattice atoms interrupt this acceleration, causing the hole to lose most or all of its acquired energy. It then resumes accelerating until the next scattering event. This cycle of acceleration and scattering continues repeatedly. The average time between collisions in a semiconductor is referred to as the "mean free time" (τ). During this interval, charged particles such as electrons or holes gain energy from the applied electric field as they accelerate. Upon colliding with atoms, they lose most of their energy, and the acceleration process recommences. Consequently, the mean peak velocity (v_{p}) achieved just prior to a collision is defined as follows [52], [53]

$v_p(\ \ oles) = \left[\frac{q\tau_p}{m*_p}\right] EF$

$v_p(electron) = -\left[\frac{q\tau_n}{m*_n}\right] EF$ (2.1)

Throughout the thesis, subscripts p and n are used to represent holes and electrons, respectively, in all relevant notations and equations.

$v_p = \mu_p EF$

$v_n = -\mu_n EF$ (2.2)

Where q is the electron/hole charge, $m*_p$, $m*_n$ are respective effective mass of hole and electron , μ_p and μ_n are the proportionality factor defined as 'hole and electron mobility ' respectively.

the rate of scattering due to phonons can be derived using Fermi's Golden Rule and is directly proportional to the phonon population. The mobility (μ), assuming phonon scattering as the sole mechanism, exhibits a decline with rising temperature (T), since the phonon population increases with temperature, leading to diminished mobility. The mobility (μ) can be estimated as:

$\mu_{phonon} \propto T^{-3/2}$ (2.3)

conversely, the mobility limited by ionized impurity scattering $\mu_{impurity}$, is time and again described by Brooks-Herring or Conwell-Weisskopf model and it increases with temperature (T) and can be approximated by

$\mu_{impurity} \propto \frac{T^{3/2}}{N_{impurity}}$ (2.4)

where $N_{impurity}$ represents the impurity concentration. At reduced temperatures, impurity scattering becomes predominant as phonon scattering decreases. The degree of ionized impurity scattering can be mitigated through screening, a process where other carriers in the semiconductor shield the moving carriers from the full influence of the impurity's Coulombic field. The effectiveness of this shielding is quantified by the Debye screening length, which indicates how efficiently carriers are screened within the material. Elevated carrier concentrations enhance screening, thereby diminishing the scattering effects of the impurity's electric field.

When these two scattering mechanisms are assumed to be independent, the probability of a scattering event occurring in a short time interval is the sum of the probabilities for each individual process. This additive principle extends to the overall mobility as well, where the total mobility (μ_{net}) is calculated by combining the contributions from both scattering mechanisms [54]

$$\frac{1}{\mu_{net}} = \frac{1}{\mu_{phonon}} + \frac{1}{\mu_{impurity}} \tag{2.5}$$

For particles moving from an area where they're crowded (high concentration) to a place where there's more space (low concentration). Now, if those gas molecules are charged, this movement creates what we call a diffusion current.

For our calculations, we'll assume the temperature is consistent throughout, meaning the average speed of the electrons doesn't change based on their position (x). To find the current, we'll focus on how many electrons are flowing across a specific area at a given time, particularly at the point. The net rate of electrons (R_n) and holes (R_p) flowing in a set direction is obtained by Taylor series expansion and is given by

$$R_p = -v_p l_p \frac{dN_p}{dx}$$
$$R_n = -v_n l_n \frac{dN_n}{dx} \tag{2.6}$$

Where l_p, l_n are the distance travelled by hole and electron before collisions with velocity v_p and v_n, $\frac{dN_p}{dx}$ and $\frac{dN_n}{dx}$ being the density gradient over distancerespectively.

So, the diffusion current is

$$J_p{}^{diff} = qR_p = -qv_p l_p \frac{dN_p}{dx} = -qD_p \frac{dN_p}{dx}$$
$$J_n{}^{diff} = -qR_n = qv_n l_n \frac{dN_n}{dx} = qD_n \frac{dN_n}{dx} \tag{2.7}$$

D_p and D_n are the hole and the electron diffusion coefficients respectively, both positive, having unit of cm^2/s.

Through these interactions, the hole reaches an average drift velocity. Notably, at low electric field strengths, this drift velocity exhibits a direct proportionality to the applied

electric field, implying that a stronger electric field results in a faster movement of the particle.
Similarly, electrons demonstrate a comparable behavior. Their average drift velocity also increases linearly with the electric field at lower field intensities. However, due to their negative charge, electrons move in the direction opposite to the applied electric field.

The drift current density for hole and electron (J_p^{drift} and J_n^{drift}) at volume charge density (N_p and N_n) now can be expressed as

$$J_p^{drift} = qN_p v_p = qN_p \mu_p F$$

$$J_n^{drift} = -qN_n v_n = qN_n \mu_n F \qquad (2.8)$$

The net drift current density (J) is

$$J = J_p^{drift} + J_n^{drift} = qN_p \mu_p F + qN_n \mu_n F = \sigma F \qquad (2.9)$$

σ being the conductivity having unit $(\Omega\text{-cm})^{-1}$ and its reciprocal is the resistivity.
The conductivity and resistivity of an extrinsic semiconductor are mainly determined by the properties of the majority carriers and temperature. At moderate temperatures (the extrinsic range), the semiconductor's dopant atoms are entirely ionized, meaning the number of majority carriers (electrons or holes) stays fairly constant. However, the mobility of these carriers, which influences how easily they move through the material, relies on temperature, causing changes in overall conductivity.
As temperature rises, the inherent carrier concentration (carriers generated thermally) rises and begins to dominate the semiconductor's behavior, impacting both the carrier concentration and the conductivity. In contrast, at low temperatures, a process called freeze-out occurs, where the carriers become trapped, reducing both the electron concentration and the material's conductivity.

It was assumed that the mobility of charge carriers remains constant and that drift velocity is a linear function of electric field. In simpler terms, as we increase the electric field, the drift velocity of the electrons as well as holes increases proportionally—up to a certain point.Now, in reality, things get more interesting at high

electric fields. The total velocity of a particle combines both the random thermal velocity and the drift velocity. At small electric fields, the relationship between drift velocity and the electric field is linear. However, as the electric field becomes stronger, this linear relationship breaks down, and the drift velocity approaches a saturation velocity.

An electron's movement in a lattice is quite different from how it behaves in free space. Here, it's not just the external forces at play but also internal forces within the crystal—like the tug-of-war between positively charged ions and electrons—that influence its motion. Here comes the concept of the **effective mass (*m**)**, which accounts not only for the electron's actual mass but also the impact of these internal forces.

The energy-k diagram essentially captures both internal and external forces acting on the electron within a crystal. This allows us to link the effective mass of the electron to the contour of the E-versus-k curve (will be discussed in details in subsequent sections).

$$E = \frac{p^2}{2m*} = \frac{\hbar^2 k^2}{2m*} \tag{2.10}$$

As the electric field increases, it gives electrons more energy, and eventually, they get scattered into higher energy states, known as upper valleys in the conduction band. The effective mass of electrons in these valleys is higher, meaning they become harder to move, and thus, their mobility decreases. This phenomenon, called intervalley scattering, explains the non-linear relationship between mobility and electric field at high values.

Thus, the entire current density now can be expressed as:-

$$J^{total} = J_p^{\ total} + J_n^{\ total} = J_p^{\ drift} + J_p^{\ diff} + J_n^{\ drift} + J_n^{\ diff} = qN_p\mu_p E + qN_n\mu_n E - qD_p\frac{dN_p}{dx} + qD_n\frac{dN_n}{dx}$$

(2.11)

Continuity Equation ensures the conservation of the charge and is given separately for electrons and holes as [12]:-

$$\frac{\partial N_p}{\partial t} = -\frac{1}{q}\nabla . J_p^{\ total} + G_p - R_p$$

$$\frac{\partial N_n}{\partial t} = \frac{1}{q}\nabla . J_n^{\ total} + G_n - R_n$$

(2.12)

Where G_p and G_n : generation rates, R_p and R_n : recombination rates for holes and electrons respectively.

The Poisson equation relates the electric potential φ to the charge distribution within the semiconductor as:

$$\nabla \cdot (\varepsilon \nabla \varphi) = -q(N_p - N_n + N_D{}^+ - N_A{}^-)$$

(2.13)

Where ε : permittivity, $N_A{}^-$ and $N_D{}^+$: ionized acceptor and donor concentrations respectively. Other terms bear identical meaning as in section 1.

The DD model has been extensively used in the analysis and design of various types of FETs, including Metal-Oxide-Semiconductor FETs (MOSFETs) [55], FinFETs [56], and Tunnel FETs (TFETs) [57]. It predicts the current-voltage characteristics, threshold voltage, subthreshold behavior, and short-channel effects. The model is valuable in analyzing how alterations in parameters like channel length, oxide thickness, and doping levels impact the overall performance of a device. The DD model is heavily utilised in optimizing FET designs for specific applications. For instance, it helps in tuning the doping profiles and gate work functions to achieve the desired trade-off between drive current and leakage current in low-power applications.

Limitations of Classical Transport Models in Field-Effect Transistors (FETs)

The classical transport model has been a fundamental tool for understanding the operation of field-effect transistors (FETs), providing insights into the movement of charge carriers under applied electric fields. However, as FETs are scaled down to nanoscale dimensions, these models face several limitations that affect their ability to accurately predict device performance. These limitations arise primarily because classical models were developed under assumptions that are increasingly invalid in modern ultra-scaled devices.

***1.** Quantum Effects[58]*

One of the most significant limitations of classical transport models is their inability to account for quantum mechanical phenomena. Classical models treat electrons as

particles moving under the influence of electric fields and collisions with impurities or lattice vibrations. However, at nanoscale dimensions, electrons exhibit wave-particle duality, and their behavior is influenced by quantum effects.

For instance, quantum tunneling becomes a critical factor in nanoscale FETs. In this phenomenon, electrons can penetrate and pass through energy barriers that they would not overcome in a purely classical framework. Tunneling leads to increased leakage currents, especially in thin gate dielectrics, which classical models fail to predict. Additionally, quantum confinement in narrow channels modifies the density of states and energy dispersion, further challenging the applicability of classical assumptions.

2. *Ballistic Transport* ***[59]***

Classical transport models rely on the assumption that charge carriers undergo frequent scattering events with impurities, phonons, or other carriers, leading to a diffusive transport regime. However, as FET channel lengths approach the mean free path of electrons, ballistic transport becomes dominant. In ballistic transport, carriers traverse the channel without scattering, resulting in minimal resistance and faster switching speeds.

3. *Short-Channel Effects* ***[60]***

Short-channel effects (SCEs) pose another challenge to classical transport models. In nanoscale FETs, the control of the gate over the channel weakens, allowing undesirable interactions between the source and drain regions. Phenomena such as drain-induced barrier lowering (DIBL) and increased subthreshold leakage currents become more pronounced.

4. *Surface and Interface Scattering* ***[61]***

At nanoscale dimensions, the influence of surfaces and interfaces on carrier transport becomes significant. Surface roughness, defects, and interface states can strongly affect carrier mobility and introduce variability in device performance. Classical models, which often treat scattering in a bulk-like manner, fail to capture the nuances of surface and interface scattering.

5.** Non-Uniform Electric Fields **[62]

Classical transport models typically assume a uniform electric field across the channel. This assumption holds for large-scale devices but breaks down at the nanoscale, where electric fields can vary significantly due to non-uniform doping profiles, structural asymmetries, and material inhomogeneities [63]**.**

2.4. Semi-classical and Quantum Transport

The rapid miniaturization of semiconductor devices, as foreseen by the Semiconductor Industry Association (SIA), has brought forth a multitude of challenges in device modeling and simulation. Modern semiconductor devices such as High Electron Mobility Transistors (HEMTs), Metal-Oxide-Semiconductor Field-Effect Transistors (MOSFETs), and Resonant Tunneling Diodes (RTDs) operate on the decanano length scale (below 50 nm), where quantum mechanical effects become significant . This miniaturization has necessitated the inclusion of quantum mechanical phenomena, such as confinement, tunneling, and quantum charge transport, which classical models are unable to account for adequately. Quantum corrections to classical models provide a pathway to bridge the gap between classical descriptions and quantum mechanical behavior, ensuring that simulations remain computationally efficient while incorporating essential quantum effects.

However, as devices have shrunk to nanometer scales, this model faces limitations. In particular, the DD model assumes a continuum of charge carriers, neglecting quantum effects such as wave-like behavior and quantum confinement in the inversion layers of MOSFETs or tunneling through potential barriers. To address these deficiencies, quantum corrections are necessary, allowing the inclusion of quantum effects into otherwise classical models.

- When the dimensions of the device become comparable to the de Broglie wavelength of charge carriers, the carriers are confined in potential wells, such as the inversion layer in MOSFETs. This results in the quantization of energy levels, which cannot be captured by classical models.
- At very small gate oxide thicknesses (on the order of a few nanometers), electrons can tunnel through the oxide barrier in MOSFETs, leading to gate

leakage. This quantum tunneling is ignored by classical models but has significant implications for device reliability.

- The transport of charge carriers is no longer dominated purely by drift and diffusion mechanisms but involves quantum mechanical interference and phase coherence effects. Classical models fail to describe such behavior.

The quantum effects models used in simulations, such as those in Atlas, are indispensable tools for understanding the behavior of nanoscale devices. Each model addresses specific aspects of quantum phenomena, particularly confinement effects, and operates independently, meaning they should not be combined. Below is a detailed exploration of these models and their unique functionalities.

1. Self-Consistent Coupled Schrödinger-Poisson Model [64]

This model integrates the solutions of Schrödinger's equation and Poisson's equation to provide a detailed self-consistent representation of electrostatic potential, quantum states, bound energies, and carrier wavefunctions in a device. It is highly effective in analyzing quantum confinement and electrostatics, making it ideal for understanding the behavior of charge carriers in confined systems. However, this model is not suited for carrier transport simulations. It is commonly employed for accurately predicting bound state properties in devices such as quantum wells and nanostructures.

2. Density Gradient (Quantum Moments) Model [65]

The density gradient model extends classical transport models by introducing quantum corrections derived from the Wigner function's equations of motion. It provides a quantum-corrected carrier distribution and is particularly useful for simulating transport phenomena while maintaining consistency with results from the Schrödinger-Poisson model. Despite its utility in transport scenarios, the model does not yield detailed information about bound state energies or carrier wavefunctions, limiting its application to cases requiring precise quantum state analysis.

3. Bohm Quantum Potential (BQP) Model [31]

The Bohm quantum potential model addresses quantum mechanical effects in transport by constructing a potential based on Bohmian mechanics. It improves upon the density gradient model in terms of calibration and computational convergence, making it a

preferred choice for simulating devices where capturing subtle quantum effects in transport is critical. Its ability to model quantum influences on carrier dynamics enhances its application in nanoscale device simulations.

4. Quantum Correction Models [66]

These phenomenological models, including those by Van Dort and Hansch, specifically address quantum confinement effects in MOSFET inversion layers. They refine conventional modeling approaches by correcting carrier densities and mobilities to account for quantum confinement effects. These corrections significantly improve the predictive accuracy of classical models in nanoscale MOSFETs, making them a valuable addition to the modeling toolkit.

5. Parabolic Quantum Well Model [16], [35], [67]

This model is tailored for devices with quantum wells, such as light-emitting diodes (LEDs) and lasers. It uses the Schrödinger equation to calculate bound state energies and wavefunctions critical for analyzing recombination and gain mechanisms. Additionally, the model employs a capture-escape framework to determine Fermi level positions, providing insights into the electronic properties of quantum well structures. This makes it a powerful tool for designing optical devices.

6. Non-Equilibrium Green's Function (NEGF) Approach [68]

The NEGF model offers a comprehensive quantum transport framework, especially for devices with strong transverse confinement. It accurately predicts eigen energies, wavefunctions, quantum carrier density, current densities, and ballistic current-voltage characteristics. This method is essential for nanoscale device simulations, where traditional transport models fall short in capturing the full scope of quantum mechanical behaviors.

These quantum effects models collectively enable a nuanced understanding of the electronic and optical properties of nanoscale devices. By addressing the limitations of classical approaches and incorporating quantum principles, they provide the foundation for designing and optimizing the next generation of semiconductor technologies.

Model	Type	Assumptions	Applications	Limitations
Drift–Diffusion (DD)	Classical	Assumes near thermal equilibrium; neglects quantum confinement and tunneling; mobility is field-independent.	Bulk semiconductors, long-channel MOSFETs, low-field operation analysis.	Fails for sub-20 nm devices; cannot capture quantum effects or non-equilibrium carrier distributions.
Density Gradient (DG)	Semi-classical	Quantum effects represented through carrier density gradient terms; based on modified potential energy expression.	Quantum corrections in nanoscale MOSFETs, HEMTs, and nanowire devices.	Approximate; lacks full wavefunction information; limited accuracy under strong confinement.
Bohm Quantum Potential (BQP)	Semi-classical	Introduces a quantum potential term derived from the Bohmian interpretation of quantum mechanics; modifies classical potential landscape.	Quantum-corrected simulations of double-gate MOSFETs, TFETs, and nanoscale sensors.	Requires calibration; semi-empirical; does not fully solve Schrödinger’s equation or handle strong tunneling.
Quantum Transmitting Boundary Method (QTBM)	Quantum	Solves Schrödinger’s equation with open boundary conditions allowing for carrier transmission and reflection; assumes coherent transport.	Modeling quantum wells, resonant tunneling diodes (RTDs), and multiple quantum well (MQW) lasers.	Ignores incoherent scattering; computationally intensive for complex or large 3D systems.
Non-Equilibrium Green’s Function (NEGF)	Quantum	Treats transport as quantum mechanical and possibly non-coherent; includes scattering via self-energy functions.	Simulation of nanoscale FETs, 2D materials, molecular and thermoelectric devices.	High computational cost and mathematical complexity; requires detailed material and scattering parameters.

Table 2.2. Comparison of transport models.

2.5. Literature Survey

The Drift-Diffusion (DD) model remains a cornerstone in the simulation and analysis of charge transport in semiconductor devices. Initially grounded in classical mechanics, it offers a simplified yet effective framework for understanding carrier dynamics, particularly in macroscopic systems.

Sano et al. (2002) investigated the physical implications of atomistic dopants in DD simulations, offering insights into discrete random dopant effects on electric potential [69]. Similarly, Pinnau (2002) reviewed the quantum drift-diffusion model, highlighting its ability to capture generation-recombination processes and transient carrier dynamics in quantum regimes [70]. While the DD approximation has proven successful in modeling macroscopic devices, its validity for nanoscale simulations, particularly for photodiode characteristics, has been critically assessed by Konno et al. (2004) [71].

As outlined by De Falco et al. (2005), the model serves as a generalization of classical transport equations, incorporating the influence of electric fields and scattering mechanisms to describe carrier motion. Advances in this domain have led to quantum-corrected versions, such as the Schrödinger-Poisson–drift-diffusion and quantum drift-diffusion models, which address the limitations of classical assumptions in nanoscale devices [72].

Nonequilibrium extensions, such as the kinetic drift-diffusion (kDD) model proposed by Felekidis et al. (2016), address the computational challenges of simulating devices under dynamic conditions. Similarly, Liu and Shu (2016) analyzed local discontinuous Galerkin methods, emphasizing their effectiveness in handling convection and diffusion terms in one-dimensional systems [73].

Rossi et al. (2019) developed a multiparticle drift-diffusion (mp-DD) framework, enabling the examination of transport phenomena in both organic and inorganic electronic devices. Moreover, Nagy et al. (2019) compared DD and Monte Carlo simulations, demonstrating the limitations of QC-DD in predicting on-current variability in nanowire FETs [74] [75]. Wang et al. (1998) extended this model with an inversion layer quantization approach, enhancing its computational efficiency while addressing

quantum confinement effects in MOSFETs [76]. Bufler et al. (2003) highlighted the limitations of drift-diffusion and HD models in scaled double-gate MOSFETs, emphasizing the need for refined parameters to achieve accuracy [77] [78] [79]. [80], [81]. By the 1990s, NEGF had emerged as a practical transport tool for nanoscale electronics. A landmark contribution came in 1992, when Meir and Wingreen derived a Landauer-like formula for current through interacting regions using the Keldysh approach, firmly establishing NEGF as a cornerstone of quantum transport theory[82].

By the 1990s, NEGF had emerged as a practical transport tool for nanoscale electronics. A landmark contribution came in 1992, when Meir and Wingreen derived a Landauer-like formula for current through interacting regions using the Keldysh approach, firmly establishing NEGF as a cornerstone of quantum transport theory[82]. In the early 2000s, the formalism extended beyond electronic systems, with atomistic Green's function (AGF) and harmonic NEGF (h-NEGF) approaches applied to phonons[83]. Notably, Mingo and Yang (2003) presented one of the first atomistic studies of phonon transport in nanowires, revealing how surface disorder and amorphous coatings dramatically affect phonon transmission and thermal conductivity[84]. This was followed in 2006 by Yamamoto and Watanabe, who formulated a nonequilibrium phonon Green's function method to study defective carbon nanotubes, highlighting the robustness of quantized conductance[85]. Through the mid-to-late 2000s, AGF techniques matured and broadened, with significant methodological advances in treating interfaces, strained films, and heterostructures, alongside improvements in surface Green's function algorithms and numerical stability. Influential contributions from Zhang, Fisher, Mingo, and collaborators further solidified AGF as a powerful framework for phonon transport studies[86].

Between 2005 and 2009, significant advancements in the application of the Non-Equilibrium Green's Function (NEGF) formalism were made to model nanoscale devices. Early works such as Ravishankar et al. (2005) compared NEGF with Monte Carlo simulations in double-gate MOSFETs, highlighting the strengths of NEGF in capturing quantum transport [87]. Martinez et al. (2007) introduced a full 3D real-space NEGF simulator for nano-MOSFETs, enabling the study of nonperturbative effects [88], while Neophytou et al. (2007) applied NEGF to investigate vacancy defects in carbon nanotubes [89]. By 2008, NEGF had expanded to FinFET modeling (Khan et al.) and

strain effects in double-gate MOSFETs (Kalna et al.), demonstrating its versatility in different device architectures [90]. Parallel efforts combined DFT with NEGF to study molecular-scale transport (Ganji et al., 2008) and basis set effects in nanotubes (Abadir et al., 2009), bridging atomistic and device-level simulations [91]. Further, Munteanu et al. (2009) used NEGF to probe electron transport through high-κ dielectrics [92], while Seoane et al. (2009) employed 3D NEGF to quantify current variability due to dopant randomness in nanowire MOSFETs [93]. Collectively, these studies established NEGF as a cornerstone for quantum transport modeling in nanoscale transistors and molecular devices, capturing effects beyond the scope of semiclassical approaches.

From 2011 to 2015, the NEGF framework evolved into a versatile tool for nanoscale device modeling across diverse material systems and applications. Early efforts, such as Dastjerdy et al. (2011), demonstrated 3D NEGF-based simulations of silicon nanowire MOSFETs, setting a foundation for quantum transport studies in confined geometries [94]. Martinez et al. (2012) and Georgiev et al. (2013) extended this to junctionless and dopant-engineered Si nanowire transistors, emphasizing variability and atomic-scale effects. Ji et al. (2013) applied DFT–NEGF to metal–graphene contacts, linking contact resistance to injection and lateral transport processes [95]. In parallel, Wang et al. (2014) investigated CNTFET performance via gate and channel engineering within NEGF quantum kinetics [96]. The method's conceptual underpinnings were further clarified in Datta's 2015 perspective, while Syaputra et al. (2015) expanded its reach to silicene transport [97] and Farhana et al. (2015) explored CNTFET behavior [98]. Collectively, these studies established NEGF as a unifying quantum transport framework for transistors, low-dimensional materials, and molecular-scale sensors.

In recent years, the coupling of density functional theory (DFT) with non-equilibrium Green's function (NEGF) methods has become a central approach for exploring quantum transport in low-dimensional materials and nanoscale devices. Pang et al. (2017) applied DFT+NEGF to phosphorene for ultra-sensitive detection of HCN and HNC gases, highlighting its distinct current–voltage responses under doping [99]. Extending this approach, Zhou et al. (2018) investigated black phosphorene-type GaTeCl as a novel 2D channel materiall [100], while Akhavan et al. (2018) optimized HgCdTe nBn infrared photodetectors using NEGF-Poisson simulations, emphasizing ballistic transport characteristics [101]. Complementarily, Wilson et al. (2019) employed DFT+NEGF to

analyze discrete dopants in Si/III–V FETs [102], while Pala and Esseni (2019) introduced empirical pseudopotential and mode-space NEGF models for efficient full-band device simulations, later extended to nanowire transistors [103]. On the scattering front, Martinez et al. (2016) explored phonon-limited transport in Si, GaAs, and InGaAs nanowires and FinFETs via NEGF [104].

From 2020 onwards, NEGF applications have expanded significantly. Hu et al. (2020) combined DFT with NEGF to study 2D $SbSiTe_3$, reporting tunable electronic properties and strong ballistic transport [105]. In 2021, Polanco reviewed NEGF in vibrational energy transport (h-NEGF and a-NEGF) [83], while Stegmann and Stefanucci provided concise introductions to NEGF theory for electron transport and real-time simulations, respectively—establishing a theoretical foundation for new researchers [106]. The methodologydocumented and matured further in 2022, when Verma & Singh emphasized its many-body perturbation theory (MBPT) basis for nanoscale MOS devices [107]. In 2023, Thakur & Sarkar published a stepwise tutorial on NEGF for devices and defective materials, bridging pedagogy with practical applications [108]. Most recently, in 2024, Poobalan et al. studied bilayer graphene transport via tight-binding NEGF simulations [109], and Agrawal et al. analyzed doped graphene nanoribbon interconnects with DFT+NEGF, underscoring NEGF's role in next-generation nanoelectronics [110].

Recent developments in DFT–NEGF simulations have expanded their applicability across sensors, transistors, thermoelectrics, spintronics, and molecular devices. Zhu and Wang (2025) demonstrated the potential of GeS monolayers as heavy-metal sensors, where adsorption of Cu, As, and Pb notably influenced electronic transport [111]. Munna and Alam (2025) explored bismuthene nanoribbon TFETs, highlighting their promise for low-power topological electronics. In the domain of thermoelectric transport [112], Balaji et al. (2025) applied NEGF to GeTe/antimonene and GeTe/arsenene vdW heterostructures, showing how interface engineering can significantly boost performance [113]. In device-level studies, Acharya et al. (2025) quantified the sensitivity of GaAs/AlGaAs resonant tunneling diodes to barrier and well variations [114], while Raman et al. (2025) analyzed SiGe–Ge–Si junctionless nanowire FETs, focusing on quantum effects from heterostructure engineering [115]. At the scaling frontier, Afzalian (2025) provided a roadmap for CNT- and 2D-material

MOSFETs, benchmarking their limits under hybrid-functional DFT–NEGF frameworks [116]. Complementarily, Wu and Jiang (2025) integrated DFT–NEGF with microkinetic modeling to design polythiophene-based gas sensors, achieving high selectivity for NO_2 and SO_3 [117]. Collectively, these studies illustrate the versatility of NEGF, bridging fundamental quantum transport with applied nanoscale device engineering.

The Density-Gradient (DG) quantum correction model emerged as a bridge between fully quantum mechanical approaches (like the Schrödinger–Poisson and Non-Equilibrium Green's Function (NEGF) formalisms) and classical drift–diffusion simulations. It enables the incorporation of quantum confinement and tunnelling effects within a semiclassical framework while maintaining computational efficiency. The theoretical foundations of the DG model were rigorously established by Ancona and Tiersten, and its application to semiconductor devices was further expanded in the early 2000s. Ancona et al. (2000) applied the DG formalism to analyze MOS tunnelling phenomena, demonstrating that the quantum correction effectively smoothens carrier density discontinuities and refines potential distributions in ultra-thin oxides [118]. The landmark implementation of the DG model on unstructured grids was reported by Wettstein, Schenk, and Fichtner (2001), who integrated DG corrections into general-purpose device simulators, enabling its application to arbitrary device geometries such as HEMTs and SOI structures. They demonstrated that the DG potential successfully mimics the quantum confinement potential obtained from Schrödinger–Poisson calculations, thereby validating the method as a computationally efficient alternative for complex devices [119]. Following this, Asenov et al. (2003) calibrated DG corrections in three-dimensional drift–diffusion frameworks for decananometer MOSFETs, highlighting the model's ability to capture quantum mechanical charge redistribution in scaled channels. They reported improved consistency between DG-corrected and Schrödinger–Poisson models in sub-100 nm devices [120] . For nonlocal and hydrodynamic transport, Jin, Park, and Min (2004) developed a Hydrodynamic Density-Gradient (HDG) model, incorporating both nonlocal transport and quantum mechanical corrections. This advancement enabled the study of high-field transport in nanometer-scale devices while maintaining quantum consistency [121]. To address energy transport and quantum heating, Chen and Liu (2006) combined DG corrections with the energy-transport model, thereby forming a quantum-corrected hydrodynamic

framework suitable for nanoscale high-speed devices [122]. In the context of III–V and heterostructure devices, Hu et al. (2006) applied the DG model to GaN-based metal-oxide HEMTs, studying self-heating and carrier confinement in two-dimensional electron gas (2DEG) channels. Their results showed that DG correction effectively captures the electrostatic coupling between the barrier and channel regions [123]. Morris and Limon (2006) developed a multilevel solver for the DG equation, improving convergence efficiency and robustness for quantum-corrected drift-diffusion simulations. Their paper presented an iterative numerical approach capable of solving the nonlinear DG equation efficiently, an essential step toward 3D implementation [124].In the same year, Bufler, Hudé, and Erlebach (2006) introduced an accurate quantum correction technique for Monte Carlo (MC) simulations, which reconstructed the quantum mechanical density via DG potentials. Their Journal of Computational Electronics article demonstrated that incorporating DG corrections in MC frameworks successfully reproduces quantum confinement effects in channel regions [125]. The boundary condition problem for DG-corrected MC simulations was systematically addressed by Riddet, Brown, Roy, and Asenov (2008), who proposed a method to ensure physical consistency of DG potentials at Ohmic contacts and heterointerfaces [126]. To strengthen theoretical underpinnings, Baccarani, Gnani, Gnudi, and Reggiani (2008) provided a rigorous analysis of quantum drift–diffusion and DG models within Bohm's quantum potential framework [127]. Wu et al. (2009) extended DG concepts beyond semiconductor devices, developing a Density-Gradient-Corrected Embedded Atom Method for quantum mechanical modeling of metallic systems. Their paper demonstrated that the inclusion of DG corrections improves the accuracy of potential energy surfaces as the density gradient increases [128]. A key comparative study by Brown, Martinez, Seoane, and Asenov (2009) evaluated DG versus NEGF quantum correction schemes for 3D nanowire MOSFETs, concluding that DG corrections reproduce the main features of NEGF-calculated charge distributions while being significantly faster computationally [129]. Building on these frameworks, Brown, Watling, Roy, and Riddet (2010) analyzed the role of DG quantum corrections in the simulation of statistical variability in MOSFETs. Their work demonstrated that the DG model accurately captures device-to-device variations in sub-30 nm transistors by reflecting quantum mechanical charge spreading and threshold voltage shifts induced by discrete dopants [130]. Garcia-Loureiro, Seoane and coauthors presented an

implementation of DG quantum corrections for full 3-D multigate nanoscaled transistor simulation. Their work focused on algorithmic integration, finite-element discretization, and practical aspects for multigate devices (DG coupling into Poisson/continuity, solver coupling and performance) [131]. Researchers worked on DG calibration strategies for realistic 3-D geometries. Pons, Triozon, Jaud et al. studied density-gradient calibration for 2-D quantum confinement applied to Tri-Gate SOI transistors, presenting SISPAD results that quantify how DG parameters should be tuned against Schrödinger–Poisson solutions for complex cross-sections [132].The use of the density-gradient (DG) quantum correction in device simulation has evolved from purely electrostatics-based modelling toward performance optimization and compact model integration in recent years. For example, Gaurav, Gill, Kaur and Rattan (2016) applied a DG-augmented drift-diffusion simulator together with artificial neural network (ANN) and genetic algorithm (GA) techniques to optimize triangular trigate bulk FinFETs with 20 nm gate length. They reported improvements in key metrics by incorporating DG quantum corrections in the simulation loop of the ANN/GA optimization [133]. Beyond device-level optimization, the DG formalism has been embedded into compact-model frameworks: Hong (2019) developed a compact charge model for double-gate MOSFETs that explicitly includes the DG equation with realistic boundary conditions, yielding analytical expressions for parameter extraction and charge-voltage behaviour [134]. At the same time, more fundamental theoretical works addressed gradient corrections in quantum materials and their relevance for device-scale modelling: Moldabekov et al. (2017) derived gradient correction pre-factors (γ_D) for two- and one-dimensional electron gases at finite temperature, establishing that the prefactor equals 1/3 in high-temperature limit, thereby refining the DG coefficient calibration for device contexts. Collectively, these works reflect a maturation of DG methods: from incorporation into drift-diffusion/TCAD simulators toward full integration into performance-driven design (via ANN/GA) and compact modelling disciplines, bridging the gap between numerical simulation and circuit-level/variability-aware device design. Quantum confinement and carrier transport modeling have evolved significantly with the integration of density-gradient (DG) quantum corrections into drift-diffusion (DD) and Monte Carlo frameworks. Dutta et al. (2021) developed a 3D DG-based quantum-corrected drift-diffusion simulator that effectively captured confinement effects in ultra-scaled MOSFETs. Their anisotropic DG approach improved the prediction accuracy of channel

charge distribution and threshold voltage, validating the model's compatibility with TCAD tools [135]. Similarly, Soares et al. (2024) presented a quantum-corrected Monte Carlo simulator combining the DG correction with the Bohm Quantum Potential (BQP) method. Comparative analysis revealed that the DG model offered better numerical stability and convergence for nanoscale FinFET simulations [136] . On the theoretical front, Rhee et al. (2020) extended the DG model to second-order quantum corrections, improving accuracy in modeling single-charge effects and discrete dopant fluctuations in sub-10 nm MOS devices. This higher-order formulation enhanced quantum confinement representation in ultra-thin-body MOSFETs [137]. Li et al. (2024) integrated DG equations with Poisson's equation to explore oxide reliability degradation in nanosheet GAA FETs. Their work emphasized DG's relevance beyond electronic transport, extending its applicability to electrothermal and reliability analyses [138].

The concept of the Bohm Quantum Potential (BQP) originates from the causal interpretation of quantum mechanics proposed by David Bohm (1952), where the wavefunction is expressed in polar form to derive a quantum-corrected Hamilton–Jacobi equation that includes an additional potential term, now known as the *Bohm potential* [139]. This potential represents the influence of the quantum wave nature of particles and provides a deterministic yet nonlocal description of quantum phenomena, bridging the gap between classical and quantum mechanics. Subsequent works by Bohm and Hiley (1984) expanded this interpretation, showing that the quantum potential could consistently explain measurement processes and relativistic quantum field theories within the same framework.

The physical interpretation of the BQP has evolved significantly over time. Aharonov and Bohm (1961) emphasized the significance of electromagnetic potentials in quantum theory, illustrating that potentials, not just fields, have observable quantum mechanical effects [140]. Later, Dennis et al. (2015) demonstrated that the BQP could be viewed as a form of *internal energy* associated with context-dependent energy redistribution within quantum systems[141]. In plasma physics, Moldabekov et al. (2015) extended the concept to quantum plasmas, linking the BQP to statically screened ion potentials and showing its relevance in both Bose and Fermi systems [142].

More recently, Hojman et al. (2021) reaffirmed the measurable reality of the Bohm potential, demonstrating its physical consequences in optical and wave-based quantum systems [143]. The ongoing refinement of the BQP framework, as seen in the covariant

non-local formulation by Mauri and Giona (2023), underscores its versatility in describing nonlocal quantum correlations and thermodynamic consistency under isothermal conditions [144]. Collectively, these foundational and contemporary studies establish the BQP as a unifying construct that captures the nonclassical behavior of carriers in nanoscale systems. In the context of semiconductor devices such as TFETs, this formulation allows quantum confinement, tunneling, and wavefunction curvature effects to be modeled self-consistently within semi-classical transport equations, thereby providing a bridge between drift-diffusion and Schrödinger–Poisson frameworks .

Gusmeroli and Spinelli (2006) applied QBTM in the analysis of ballistic double-gate devices, integrating it with Poisson–Schrödinger solvers to simulate carrier injection and extraction, thereby demonstrating its relevance in high-speed nanoscale devices. Gao Cheng-Zhi and Liu Jin-Liang (2003) explored discretization and interface approximation techniques in quantum wells, wires, and dots, highlighting the importance of accurate interface modeling for QBS simulations. Dutta (2014) studied alternative channel material MOSFETs with undoped InGaAs/InP quantum wells, emphasizing the role of quantum confinement on device characteristics through coupled Poisson–Schrödinger simulations. Nemnes et al. (2016) further advanced time-dependent electron transport studies by introducing transparent boundary conditions in the R-matrix method [145], Kosik et al. (2021) investigated open boundary conditions for the Wigner transport equation, applying them to a GaAs/AlGaAs quantum well structure and validating QBTM-like methods for open quantum systems [146]. Several studies have focused on understanding quantum transport and quasi-bound states (QBS) in III-V semiconductor quantum wells, emphasizing both analytical and numerical methods. Nimje and Mahajan (2023) provided an analytical estimation of the lifetime of QBS in III-V quantum wells, extending previous calculations for infinite triangular wells and employing the Quantum Transmitting Boundary Method (QBTM) to evaluate the width and lifetime of these states, which are critical for tunneling-based devices [147], enabling accurate modeling of coherent transport in nanostructured interfaces. Collectively, these works highlight the centrality of QBTM and advanced boundary condition treatments in predicting quasi-bound state behavior, quantum confinement effects, and overall nanoscale device performance, forming a robust foundation for the analysis and simulation of III-V semiconductor quantum wells in

modern electronic and optoelectronic devices.

2.6. Conclusion

Chapter 2 delves into the critical aspects of carrier transport phenomena in nano-scaled devices, laying the groundwork for understanding how transport mechanisms evolve at reduced dimensions. The chapter begins with an overview of nano-scaled devices, emphasizing their unique features and the challenges they present. It highlights the pivotal role of carrier transport phenomena in determining the performance and efficiency of these devices. The limitations of classical transport models, which rely on continuum approximations and neglect quantum effects, are thoroughly examined. These models, while effective for bulk-scale devices, fail to capture the discrete energy states, tunneling phenomena, and wave-particle duality that dominate at the nanoscale. This realization necessitates the use of semi-classical and quantum transport models, which integrate quantum mechanical principles to provide a more accurate representation of carrier dynamics. The discussion on semi-classical models bridges the gap between classical and quantum approaches by incorporating effects like energy quantization and scattering into carrier transport equations. Quantum transport models, such as the Non-Equilibrium Green's Function (NEGF) framework, are introduced as indispensable tools for understanding nanoscale behavior, enabling accurate simulations of phenomena like tunneling and quantum interference. The literature study provides a detailed review of advancements in transport modeling and highlights the contributions of various researchers in this field. This analysis underscores the growing importance of these models in addressing real-world challenges in nano-electronic device design and optimization. In conclusion, this chapter underscores the necessity of semi-classical and quantum transport frameworks in modern nano-electronics, bridging the gap left by classical approaches. The insights gained here are essential for exploring advanced transport mechanisms and applying them to the design of next-generation devices. This sets the stage for subsequent chapters to delve deeper into specific transport phenomena, methodologies, and their applications in cutting-edge technologies.

Chapter 3:

Quantum Transport (NEGF) in Low-Dimensional MOSFETs

3.1. Introduction to Low-Dimensional MOSFETs

3.2. Quantum Transport in MOSFETs based on NEGF: Theoretical Analysis

3.3. Charge Plasma Engineering and its application

3.4. Gas sensing application of TMD based FET

3.5. Non-Equilibrium Green's Function Analysis of Charge Plasma-Based Source-Drain Electrode P-type $MoTe_2$ MOSFET for High Sensitivity Hydrogen Sensing

3.6. Conclusion and Future Work

3.1. Introduction to Low-Dimensional MOSFETs

Metal-Oxide-Semiconductor Field-Effect Transistors (MOSFETs) are the cornerstone of modern electronics, serving as the fundamental building blocks for a wide variety of devices, including integrated circuits (ICs), processors, memory devices, and communication systems. Over the decades, the MOSFET has evolved significantly, with advancements in materials, device structures, and fabrication techniques.

MOSFETs are semiconductor devices that control the flow of charge carriers between two regions (called the source and drain) using an electric field applied to a gate terminal. The main components of a MOSFET include the source, drain, gate, and channel. The gate terminal is separated from the semiconductor channel by a thin insulating layer, often made of silicon dioxide (SiO_2). By applying a voltage to the gate, an electric field is created, which modulates the conductivity of the semiconductor channel and controls the flow of current between the source and drain.

The MOSFET operates in three distinct regions:

1. **Cut-off region**: The gate voltage is below the threshold voltage, and no current flows through the channel.
2. **Linear (or triode) region**: The gate voltage is above the threshold, and the MOSFET operates as a resistor, allowing current to flow from the source to the drain.
3. **Saturation region**: The gate voltage is sufficiently high to form a conducting channel, but the drain voltage is high enough that the channel near the drain is pinched off, leading to a constant current flow.

The performance of a MOSFET is typically described by key parameters such as threshold voltage, transconductance, on-current, and subthreshold swing. As devices shrink in size, these parameters are affected by the scaling laws, and new physical phenomena begin to influence device behavior.

As the demand for faster and more efficient electronics has increased, the semiconductor industry has pursued the miniaturization of MOSFETs to improve speed and reduce power consumption. This is in line with Moore's Law, which predicts that the number of transistors on an integrated circuit will double approximately every two years, enabling greater computational power and functionality [148]. However, when scaling down MOSFETs to the nanometer regime, several fundamental challenges arise. Traditional MOSFETs, based on bulk silicon, experience performance degradation due to short-channel effects (SCEs). These effects include threshold voltage roll-off, drain-induced barrier lowering (DIBL), and subthreshold leakage, which degrade the device's ability to switch on and off efficiently as the channel length becomes shorter. To

mitigate these issues, researchers have turned to low-dimensional structures, where the channel dimensions are reduced to the point where quantum effects become significant.

Since the invention of the MOSFET, continuous device scaling — as described by Moore's Law — has been the primary driver of electronic technology. Reducing the channel length, oxide thickness, and supply voltage has allowed for faster switching speeds, lower power consumption, and higher packing densities. However, as dimensions entered the nanometer regime (below ~30 nm), classical models that once described device operation with high accuracy began to fail. This breakdown originates from two major fronts: electrostatic short-channel effects (SCEs) and quantum mechanical confinement.

In long-channel MOSFETs, the gate terminal effectively controls the channel potential and hence the flow of carriers between the source and drain. But as the channel length shrinks, the control of the gate weakens due to fringing electric fields and drain-induced barrier lowering (DIBL). These phenomena, collectively known as short-channel effects, result in higher off-state leakage, threshold voltage roll-off, and degraded subthreshold performance.
Classically, SCEs are treated using the Poisson's equation with charge density approximations derived from drift-diffusion or hydrodynamic models. While these capture electrostatic coupling and mobility degradation, they ignore the discrete nature of energy states and the quantum confinement that arises in ultrathin films and nanowires.

When the MOSFET channel body thickness or channel cross-section approaches the de Broglie wavelength of electrons (~10 nm), carrier motion perpendicular to the current flow becomes confined. This confinement quantizes the energy levels into subbands, leading to a redistribution of charge away from the oxide interface.

To handle nanometer-scale effects while retaining computational simplicity, semi-classical models such as the density-gradient (DG) method or quantum correction potential (QCP) approaches were introduced. These models add a quantum potential term to the classical drift-diffusion equations, allowing partial inclusion of confinement

effects and charge quantization without explicitly solving Schrödinger's equation. However, semiclassical models assume local equilibrium and continuum energy distributions, which makes them inadequate for describing quantum tunneling, interference, and ballistic transport that dominate when the mean free path becomes comparable to the channel length (< 20 nm). In such ultra-scaled regimes, the current is determined not by scattering-limited drift but by wave transmission through potential barriers, demanding a fully quantum mechanical treatment.

The limitations of semiclassical frameworks led to the adoption of the Quantum Transport approach, where the wave nature of electrons, phase coherence, and non-local effects are explicitly included. Among these, the Non-Equilibrium Green's Function (NEGF) formalism provides a unified and rigorous methodology for describing carrier transport under both equilibrium and bias conditions.

These transport models tackle short-channel effects (SCEs) by integrating the wave-like nature of electrons, offering a level of accuracy beyond that of semiclassical approaches when the device dimensions approach the electron's de Broglie wavelength. The Non-Equilibrium Green's Function (NEGF) framework serves as the central formalism, as it inherently captures quantum phenomena such as tunneling and carrier confinement, which play key roles in SCE manifestation.

In ultra-scaled channels, the drain electric field can distort the potential barrier near the source, enabling charge carriers to flow even when the transistor is intended to remain off. In severe situations, known as punch-through, the depletion regions of the source and drain overlap completely. Through a self-consistent solution of the transport and Poisson equations, the NEGF formalism explicitly reproduces the two-dimensional electrostatic potential distribution responsible for such barrier lowering. By accurately computing the potential profile across the channel, NEGF-based simulations can precisely quantify drain-induced barrier lowering (DIBL) and its impact on device characteristics.

As both the gate oxide thickness and channel length are reduced to a few nanometers, quantum tunneling becomes a dominant conduction mechanism, allowing electrons to penetrate potential barriers instead of surmounting them. This process substantially

increases the off-state leakage current, a behavior intrinsically described by the NEGF method. Within this framework, Green's functions represent electron propagation while inherently including their wave characteristics, such as transmission through barriers. Consequently, the tunneling current arises naturally from the NEGF formulation, enabling accurate prediction of leakage variations as the device scales down.

In multi-gate MOSFET architectures, the ultrathin channel regions restrict carrier motion in one or more spatial directions, leading to quantized energy levels and changes in the local density of states (LDOS). This quantization modifies both the threshold voltage and the carrier spatial distribution. By coupling the Schrödinger and Poisson equations self-consistently, the NEGF approach directly captures these discrete energy states and their impact on electronic transport. This feature is vital, as quantum confinement can sometimes intensify SCEs—a phenomenon that purely classical transport models fail to represent.

There are several key types of low-dimensional MOSFETs, each of which exploits the reduced dimensionality of the active channel to achieve superior performance [149] [13] [150] among which in this chapter the MOSFET based on Transition Metal Dichalcogenide (TMD) materal has been explored for sensing application [151], [152]

Molybdenum ditelluride ($MoTe_2$) is one of the promising 2D material that belongs to the TMD family used as channel material in low dimensional MOSFETs [153], [154] [149]. $MoTe_2$ exhibits a tunable bandgap and high electron mobility, which makes it suitable for high-performance transistors. $MoTe_2$ also stands out for its unique metallic-to-semiconducting transition depending on the number of layers, allowing for further tunability in device characteristics. Moreover, $MoTe_2$ has shown potential in quantum transport applications due to its ability to support topological states, which could lead to enhanced performance in quantum computing and sensing devices. As with other TMDs, $MoTe_2$ faces challenges related to synthesis, scalability, and interface control with other materials, particularly for integration into mainstream semiconductor technologies.

In this context, a $MoTe_2$-based MOSFET structure has been explored for gas sensing applications, leveraging its intrinsic surface sensitivity and high carrier mobility. Which has been elaborated in subseqyuuent sections.

3.2. Quantum Transport in MOSFETs based on NEGF: Theoretical Analysis

The Non-Equilibrium Green's Function (NEGF) formalism is a powerful tool for simulating quantum transport in nanoscale devices [68], [155], [156], [157]. It provides a self-consistent way to solve for the charge transport and potential distribution in a system under non-equilibrium conditions, where classical methods fail to account for quantum effects like tunneling, interference, and confinement. NEGF handles these effects by combining the Schrödinger equation for quantum mechanics and the Poisson equation for electrostatics into a self-consistent framework.

In NEGF, the quantum transport problem is described using Retarded Green's Function (G). the derived functions allow us to compute quantities like:

- Electron density at each point in the device.
- Current density through the device.
- Potential distribution due to the electrostatic effects.

The NEGF formalism works by solving a set of coupled equations:

1. The Schrödinger equation, which describes the quantum state of electrons.
2. The Poisson equation, which describes the electrostatic potential due to the charge distribution.

The solution involves an iterative procedure to achieve self-consistency between the quantum transport and electrostatic potential. Below are the stepwise details:

Step 1: Initialize Device Parameters

Define the device geometry, material properties, and boundary conditions. These include:

- Device dimensions (e.g., channel length, thickness).
- Material parameters (e.g., bandgap, dielectric constant).
- Contact potentials and boundary conditions (e.g., source and drain voltages).

Step 2: Solve the Poisson Equation for Initial Potential

The **Poisson equation** relates the electrostatic potential (φ) to the charge density (ρ):

$$\nabla^2 \varphi(x) = -\frac{\rho(x)}{\varepsilon}$$

Where:

- φ is the electrostatic potential.
- ρ(x) is the charge density (to be updated iteratively).
- ε is the permittivity of the material.

Step	Action	Details
1	Discretize the domain	Use a grid (e.g., finite difference or finite element) for the device geometry.
2	Apply boundary conditions	Set potential values at the source, drain, and gate terminals.
3	Solve using iterative methods	Use techniques like Gauss-Seidel or Successive Over-Relaxation (SOR).
4	Output initial potential distribution	The result serves as input for quantum transport calculation.

Table 3.1. **Poisson Equation Solution Steps**

Step 3: Solve the Schrödinger Equation for Green's Functions

The **Schrödinger equation** is solved in each slice of the device to find the eigenenergies and wavefunctions:

$$H\psi = E\psi \tag{3.1}$$

Where:

- H is the Hamiltonian matrix (including potential from Poisson solution).
- Ψ is the wavefunction.
- E is the energy eigenvalue.

The electrostatic potential shifts the local band edges. In the (effective-mass) Schrödinger equation include that shift as a potential energy

$$V(\mathrm{x},\mathrm{y}) = E_{c0} - V_{offset}(x,y) + q\varphi(x,y) \tag{3.2}$$

where E_{c0} is a reference conduction-band edge (material-dependent) and V_{offset} accounts for band offsets and Quantum corrections, φ(x,y) is the two dimensionl potential profile.

$$[-\frac{\hbar^2}{2}\nabla.\left(\frac{\nabla}{m*(\mathrm{x},\mathrm{y})}\right) + V(x,y)]\Psi(\mathrm{x},\mathrm{y}) = E\Psi(x,y) \tag{3.3}$$

Continuous 1D effective-mass Schrödinger in the directioj of quantization i.e., along the thickness of the device ‘y’

$$[-\frac{\hbar^2}{2}\nabla.\left(\frac{\nabla}{m*(\mathrm{y})}\right) + V(y)]\Psi(y) = E\Psi(y) \tag{3.4}$$

It is to be mentioned that in NEGF, both the directions are taken as direction of quantization, so along the length of the device ‘x’ we have

$$[-\frac{\hbar^2}{2}\nabla.\left(\frac{\nabla}{m*(x)}\right) + V(x)]\Psi(x) = E\Psi(x) \tag{3.5}$$

For the analytical solution , we discretize (finite-difference) in one direction initially grid x_i, spacing Δx upto N points. For constant m∗ use central difference

$$-\frac{\hbar^2}{2m*}\frac{\Psi(x)_{i+1} - 2\Psi(x)_i + \Psi(x)_{i-1}}{\Delta x^2} + V(x)\Psi(x)_i = E\Psi(x)_i \tag{3.6}$$

This builds the tridiagonal eigenproblem

$$H\Psi(x)_i = E\Psi(x)_i$$

To form the Hamiltonian , we obtain the elements as

$$H_{ii} = 2t + V_i$$
$$H_{i,i\pm1} = -t$$
$$t = \frac{\hbar^2}{2m^*(\Delta x)^2}$$

(3.7)

$$H=\begin{bmatrix} E_{c0}+2t+\varphi(x_1) & -t & 0 & \ldots & 0 \\ -t & E_{c0}+2t+\varphi(x_2) & -t & \ldots & 0 \\ 0 & -t & E_{c0}+2t+\varphi(x_3) & \ldots & 0 \\ \ldots & \ldots & \ldots & \ldots & \ldots \\ \ldots & \ldots & \ldots & -t & E_{c0}+2t+\varphi(x_N) \end{bmatrix}$$

(3.8)

It is to be noted that theboundary elements do not have preceeding and fowling elements at both the ends and hence the the incorporation of the said wave functions at the left, right contact is given in literature as self energy functions that are defined as

$$\Sigma_S=\begin{bmatrix} -t\exp(ik_1a) & 0 & 0 & \ldots & 0 \\ 0 & 0 & 0 & \ldots & 0 \\ 0 & 0 & 0 & \ldots & 0 \\ \ldots & \ldots & \ldots & \ldots & \ldots \\ \ldots & \ldots & \ldots & 0 & 0 \end{bmatrix}$$

(3.8)

$$\Sigma_D=\begin{bmatrix} 0 & 0 & 0 & \ldots & 0 \\ 0 & 0 & 0 & \ldots & 0 \\ 0 & 0 & 0 & \ldots & 0 \\ \ldots & \ldots & \ldots & \ldots & \ldots \\ \ldots & \ldots & \ldots & 0 & -t\exp(ik_2a) \end{bmatrix}$$

From this, the Retarded Green's Function is calculated:

$$G=[EI-H-\Sigma_S-\Sigma_D]^{-1} \quad (3.9)$$

If scattering is considered the Retarded Green's Function includes stacttering matrix $\Sigma_{scatter}$ that takes into account internal scatterting

$$G=[EI-H-\Sigma_S-\Sigma_D-\Sigma_{scatter}]^{-1}$$

The broadening functions $\Gamma_\mathbf{S}$ and $\Gamma_\mathbf{D}$

$\Gamma_S = i(\Sigma_S - \Sigma_S^*)$ (3.10)

$\Gamma_D = i(\Sigma_D - \Sigma_D^*)$ (3.11)

The transmission coefficient is

$T(E) = Trace[\Gamma_S\, G\, \Gamma_D\, G^A]$ (3.12)

Where G^A, advanced green function, is the adjoint (conjugate transpose) of G.

The lesser Green's function describes the occupation of these available states by electrons and plays a vital role in determining the electron density within the device region and, consequently, the overall current flowing through it. This electron density is fundamental to the self-consistent coupling with the Poisson equation, which governs the electrostatic potential distribution across the channel.

The self-energy due to source and drain has the lesser compenent defined as

$\Sigma_S^< = i\, \Gamma_S\, f_S$

$\Sigma_D^< = i\, \Gamma_D\, f_D$ (3.13)

f_S or f_D denotes fermi distributions at surce drain end given by

The total lesser self-energy from source and drain

$\Sigma^< = \Sigma_S^< + \Sigma_D^<$ (3.14)

The lesser Green's function that describes the occupation of available states by electrons is given by

$G^< = G\, \Sigma^< G^A$ (3.15)

G is used to determine where the energy states are and $G^<$ is used to determine how many electrons occupy them under non-equilibrium bias conditions. Both are necessary to accurately model a MOSFET using the NEGF formalism.

Step 4: Calculate the Charge Density

Electron density at a position $\rho(x)$ is an energy integral over the diagonal components of $G^<$

Step 5: Update the Poisson Equation

Using the updated charge density $\rho(x)$, the Poisson equation is solved again to update the potential (φ) in step 2. This process ensures that the electrostatic potential is consistent with the quantum charge distribution.

Step 6: Iterate Until Convergence

Steps 3–5 are repeated until the solutions for the Schrödinger and Poisson equations converge. Convergence is typically defined by:

- A small change in potential (Δφ).
- Consistent charge density ($\rho(x)$) across iterations.

Step 7: Compute Transport Properties

Once convergence is achieved, the following transport properties are calculated:

- Current density (J): Derived from Green's functions.
- Channel potential: Analyzed for sensing and switching behavior.
- Device performance metrics: Like on/off ratio, subthreshold slope, and sensitivity (for gas sensing applications).

Step	Process	Outcome
1	Initialize parameters	Define geometry, materials, and boundary values.
2	Solve Poisson equation	Initial potential distribution (φ).
3	Solve Schrödinger equation	Green's functions (G, G^A).
4	Calculate charge density (ρ)	Update ρ based on Green's functions.
5	Update Poisson equation	Adjust φ for new charge density.
6	Iterate until convergence	Consistent ϕ, ρ, and G.
7	Analyze transport properties	Extract I-V characteristics and sensitivities.

Table 3.2. **Steps for NEGF and Poisson Coupling**

By integrating NEGF with the Schrödinger-Poisson framework, this study provides an accurate depiction of the quantum transport mechanisms in the $MoTe_2$-based MOSFET, particularly for sensing applications like hydrogen detection.

3.3. Charge Plasma Engineering and its application

Charge Plasma Engineering (CPE) is an innovative approach that represents a departure from traditional doping techniques in semiconductor devices, particularly field-effect transistors (FETs) [158], [159], [160], [161], [162]. This technique leverages electrostatic gating and electric field modulation to create a charge plasma in the device, eliminating the need for doping, which can introduce various performance-limiting factors such as scattering and fluctuations due to random dopants .

Charge Plasma Engineering operates on the premise of utilizing the inherent electrostatic properties of materials to control charge transport. The key aspects include dopingless techniques where, by utilizing metal electrodes with tailored work functions, CPE can generate a charge plasma without the physical doping of semiconductor materials. This helps mitigate issues associated with excessive doping, such as reduced carrier mobility and increased series resistance. Beside, the application of electric fields can modulate carrier concentrations effectively throughout the channel, facilitating better control over device performance. By carefully managing the Debye length and channel thickness, optimal performance can be achieved.

The charge transfer mechanism in scaled semiconductor devices arises from the interaction between the metal contacts and the semiconductor channel. At equilibrium, when the device is at rest, the metal and semiconductor regions are connected, and charge transfer occurs due to energy band alignment disparities between the metal and the semiconductor. The Fermi level in the metal and the semiconductor initially do not align, leading to the migration of electrons from the metal into the semiconductor, filling lower energy states.

This transfer leads to a net movement of negative charge from the metal to the semiconductor. This process creates a charge plasma at the interface between the metal

and the semiconductor, influencing the carrier distribution and potential profile across the device. The formation of this charge plasma is crucial for controlling the threshold voltage and ensuring proper switching behavior. In the case of $MoTe_2$-based MOSFETs, the narrow bandgap and tunable electronic properties of the material further influence the way charge is transferred across the interface, providing a unique opportunity for designing advanced transistors that can operate efficiently at the nanoscale.

The interface between the metal contacts and the semiconductor material is one of the most critical regions in terms of charge plasma engineering. In conventional MOSFETs, this interface is often dominated by the metal Fermi level pinning, which leads to undesirable effects such as increased contact resistance and threshold voltage shifts. Metal Fermi level pinning occurs when the metal's Fermi level becomes fixed at a specific value due to the interaction with the semiconductor material, leading to poor electrostatic control and inefficiency in the device.

In the case of $MoTe_2$ and other 2D materials, the issue of Fermi level pinning can be alleviated using advanced interface engineering techniques. A common method involves the use of ultra-thin insulating layers, such as Al_2O_3, at the metal-semiconductor interface. The metal-Al_2O_3-semiconductor structure has been shown to effectively eliminate Fermi level pinning, providing better control over the electrostatic properties and carrier injection into the semiconductor channel. This approach ensures that the Fermi level in the metal and the semiconductor are able to align more naturally, facilitating efficient charge transfer and reducing contact resistance, which is crucial in scaled devices where every nanometer matters.

As MOSFETs scale down, the dimensions of the device become smaller, and the charge plasma formed at the metal-semiconductor interface becomes more significant. This plasma, which consists of electrons and holes that are created due to the energy band alignment disparities, is responsible for the overall carrier distribution and device performance. The narrower the channel and the smaller the dimensions of the metal-semiconductor overlap, the more pronounced the effects of charge plasma formation become.

As the device is scaled down, the length of the charge-plasma region becomes a critical factor in controlling threshold voltage and subthreshold slope. Shorter charge-plasma regions enable better electrostatic control over the channel, reducing short-channel effects and improving switching behavior. However, if the charge-plasma region is too short, it may lead to a reduced charge transfer efficiency, which would degrade the device's overall performance.

The engineering of charge plasma in scaled MOSFETs impacts several key performance metrics, including threshold voltage, on-current, subthreshold slope, and switching speed. By optimizing the charge plasma formation and the metal-semiconductor interface, the following benefits can be realized:

- Reduced Contact Resistance: Effective charge plasma formation leads to better contact between the metal and semiconductor, reducing contact resistance and ensuring efficient current injection into the channel.
- Improved Electrostatic Control: The gate dielectric, along with the charge plasma region, helps to maintain effective electrostatic control over the channel, reducing short-channel effects and ensuring that the device operates at lower voltages.
- Increased Current Drive: Proper charge plasma engineering results in higher on-current and saturation current, which improves the device's switching performance and makes it suitable for high-speed applications.
- Reduced Leakage Currents: The use of an insulating layer such as Al_2O_3 helps to minimize gate leakage and other forms of off-state current,

Charge plasma formation at the metal-semiconductor interface is governed by the difference between the metal's work function (Wm) and the semiconductor's electron affinity (χ). The induced charge carrier density is determined by the barrier height ϕ_{BN}, given by:

$$\phi_{BN} = W_m - \chi \tag{3.16}$$

For a high work-function metal (W_m), $\phi_{BN}>0$, leading to electron depletion (forming a P + region). Conversely, for a low W_m , $\phi_{BN}<0$, forming an N+ region.

The equilibrium carrier concentration (p for holes or nfor electrons) in the plasma region is expressed as:

$$p = N_v exp(-\frac{q\phi_{BN}}{k_B T})$$
$$n = N_c exp(\frac{q\phi_{BN}}{k_B T}) \quad (3.17)$$

CPE holds promise for the next generation of nanoelectronics, offering scalable, efficient solutions. Advancements in work function engineering, material selection, and hybrid device structures will drive its adoption in diverse applications.

Charge plasma can be intelligently implemented for H_2 sensing by leveraging the unique properties of materials such as palladium (Pd), which is used in the source and drain regions of the device. Palladium has the ability to adsorb and dissociate hydrogen molecules on its surface, leading to the formation of atomic hydrogen that diffuses into the metal. This diffusion causes a shift in the work function of the palladium electrode, resulting in the formation of dipoles at the metal-semiconductor interface. As hydrogen gas interacts with the palladium, the work function of the metal changes, which in turn alters the charge distribution at the source and drain regions, creating virtual P+ regions in these areas. This change in the charge plasma due to hydrogen adsorption modulates the channel potential and current density, thereby affecting the overall performance of the device. The charge transfer mechanism through energy band alignment ensures that the shift in the work function influences the electron density and hole concentration in the semiconductor, enhancing the sensitivity of the device to hydrogen gas. By carefully controlling the conditions under which charge plasma is generated—such as optimizing the metal work function, semiconductor properties, and interface layer thickness—this effect can be harnessed for highly sensitive H_2 detection in gas sensing applications.

3.4. Gas sensing application of TMD based FET

Hydrogen gas (H_2) is widely used in various industrial applications, such as fuel cells, chemical synthesis, and metal refining [163] [164] [165] , [166], [167] [168]. A report by NITI Aayog, the policy think tank of the Government of India, outlines the vision and roadmap for harnessing green hydrogen in India. However, H_2 is also highly flammable and explosive, posing a serious safety risk if leaked. It is reported that hydrogen has a wide flammability range of 4–75% in air and a low ignition energy of 0.02 mJ, making it prone to accidental ignition and explosion [169]. The critical need for sensitive, selective, and dependable H_2 sensors is evident due to their role in detecting and preventing hydrogen leakage, leading to the exploration of diverse sensor types based on varied mechanisms like include electrochemical, resistance-based, catalytic, and optical sensors as well as acoustic sensors [170]. Among various types of H_2 sensors, metal-oxide-semiconductor field-effect transistor (MOSFET) sensors have attracted considerable attention due to low power consumption, high sensitivity, fast response, and easy integration with complementary metal-oxide-semiconductor (CMOS) technology [171], [172], [173].

Smart gas sensors devices require the development of CMOS technology based sensors to reach operating temperatures up to 400°C [174]. The CMOS technology requires n-type and p-type transistors to be paired. Though much study has been done on the sensing capability of n-type $MoTe_2$ sensor, it is highly required to evaluate the performance of the p-type counterpart. In literature it is reported that the p-type MOS exhibits superior surface reactivity and gas adsorption properties compared to the n-type MOS, making it suitable for designing high-performance gas sensors with low humidity dependence, high selectivity [175]. The study by Ahmed et al. provided an overview of various synthesis techniques used for producing p-type nanostructured materials employed in gas sensing applications [176]. Gu et al. successfully fabricated a short-channel p-type Gate-All-Around Silicon Nanowire Field-Effect Transistor (GAA Si NW FET) with a channel size of approximately 16 nanometers [177]. Qin et. al proposed an efficient co-doping approach to enhance the gas-sensing capabilities of p-type MOS devices [178]. Using Au@PdO, Yang et al illustrated that the conduction model of p-type MOS (Metal Oxide Semiconductor) can be improved [179]. Luan et. al showed that

incorporation of noble metal enhances the response and recovery time, sensitivity, selectivity, sensing response, and optimizes the operating temperature of Au/p-type MOS-based sensors [180].

Gas detection using transition metal dichalcogenide (TMD)-based field-effect transistors (FETs) has attracted considerable interest due to the distinctive electrical and chemical characteristics of TMD materials [181]. These traits, such as substantial surface area, electron mobility, adjustable bandgap, and sensitivity to environmental changes, make TMDs excellent candidates for cutting-edge gas detection applications. Transition metal dichalcogenides, including MoS_2, $MoSe_2$, WS_2, and $MoTe_2$, are two-dimensional (2D) layered materials with semiconducting behavior [182], [183].

Lower-dimensional materials offer high sensitivity with size compatibility [184] but the scaling imposes challenges due to high fabrication cost, introduction of severe interface defects, and uncontrollable bandgap [185], [186]. Two-dimensional layered material transition-metal dichalcogenides (TMDs), such as Molybdenum ditelluride($MoTe_2$), are known for their excellent scalability, ultra-thin structure, superior electrostatics, and capacity for large-scale integration. Their unique features, including a higher surface-to-volume ratio, denser surface sites, and the ability to tune electronic properties based on the number of layers, make TMDs promising candidates for various applications [187], [188].

For $MoTe_2$ based sensors, different doping types have been explored to modify the properties of $MoTe_2$ materials for diverse applications. Feng et al. demonstrated light-induced p-type doping in $MoTe_2$ field effect transistors, while Wu et al. focused on ultraviolet-induced p-type doping in p-type $MoTe_2$ [189], [190], [191]. Liu et al. employed cluster doping, specifically with transition metals (Pd, Pt, Ag, Au), to influence the electronic behavior of $MoTe_2$ [192]. Cao et al. introduced nickel (Ni) doping in $MoTe_2$, and Szary ei al. utilized P-block doping in monolayers of $MoTe_2$ [193], [194].

TMD-based FETs represent a promising technology for gas detection applications, but doping in field-effect transistors (FETs) based on transition metal dichalcogenides (TMDs) poses considerable challenges due to the distinctive characteristics of two-dimensional materials—namely, their weak electrostatic screening, high defect sensitivity, and difficulties in achieving stable and uniform doping. These limitations

hinder precise control of charge carrier concentration and often result in high contact resistance, both of which are critical parameters for realizing high-performance devices. The weak electrostatic screening in TMDs causes dopant energy levels to lie deep within the bandgap, functioning as "deep-level" defects with large ionization energies. Consequently, at room temperature, the thermal activation of these dopants is limited, yielding low effective carrier concentrations even at high doping densities.

3.5. Non-Equilibrium Green's Function Analysis of Charge Plasma-Based Source-Drain Electrode P-type $MoTe_2$ MOSFET for High Sensitivity Hydrogen Sensing

To overcome the aforementioned limitations associated with conventional doping in transition metal dichalcogenide (TMD)-based field-effect transistors, this work introduces the alternative approach based on charge plasma engineering as discussed in section 3.3. Instead of introducing impurities into the lattice, charge plasma doping utilizes metals with appropriate work functions at the source and drain regions to induce electron or hole accumulation in the intrinsic TMD channel, thereby forming *n-type* or *p-type* regions without physical doping. This approach effectively eliminates lattice damage, deep-level traps, and non-uniform dopant distribution, while maintaining the structural and electronic integrity of the ultrathin TMD layer.

Building upon this concept, we have investigated a Non-Equilibrium Green's Function (NEGF) based analysis of a charge plasma-engineered P-type $MoTe_2$ MOSFET designed for high-sensitivity hydrogen sensing [195], [196] [155], [157], [197]. In this study, palladium (Pd), with its suitable work function, is employed at the source and drain contacts to induce hole-rich regions (P^+) in the undoped $MoTe_2$ channel. These Pd electrodes simultaneously serve as the active sensing surfaces, enabling enhanced interaction with hydrogen molecules.

The NEGF framework has been employed to capture the quantum transport phenomena governing carrier motion within the ultrathin $MoTe_2$ channel. This approach allows for a detailed understanding of carrier confinement, tunneling, and potential modulation

under hydrogen exposure, providing a rigorous quantum-level insight into the sensing mechanism. The methodology and findings of this investigation are elaborated in the following sections.

The work presents a novel P-type molybdenum ditelluride ($MoTe_2$) Metal-Oxide-Semiconductor Field-Effect Transistor (MOSFET) designed for high sensitivity hydrogen sensing applications. Through the utilization of palladium at the source-drain charge plasma electrode, P+ regions at both ends are generated, obviating the necessity for low-dimensional $MoTe_2$ doping. Simultaneously, the inclusion of palladium on both regions act as the sensing area, resulting in notably heightened sensitivity. The study employs Non-Equilibrium Green's Function (NEGF) formalism to investigate the carrier transport properties of the device. The results provide valuable insights into less explored area of p-type MOSFET performance as Hydrogen(H_2) gas sensor and its potential.

Device Structure

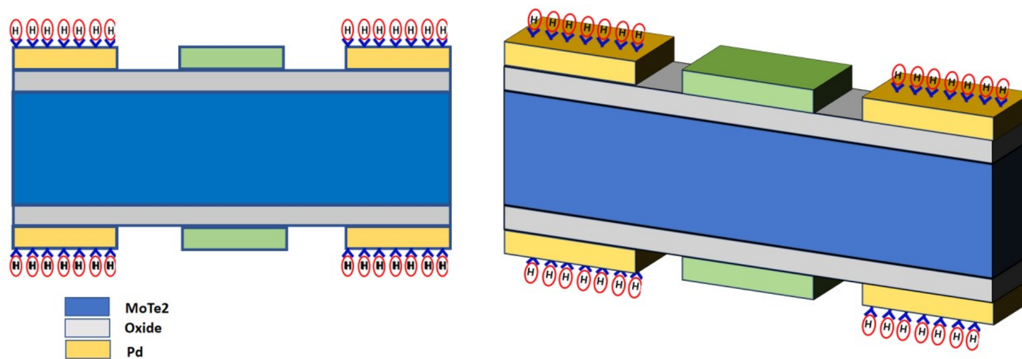

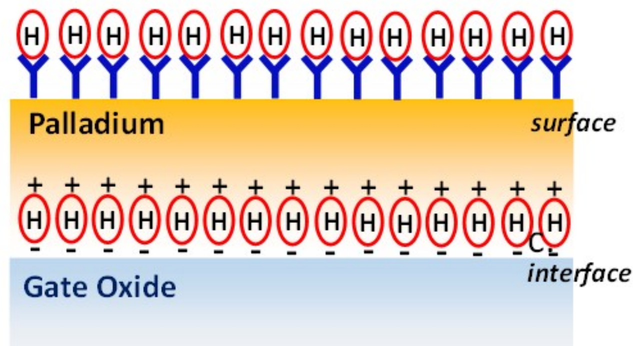

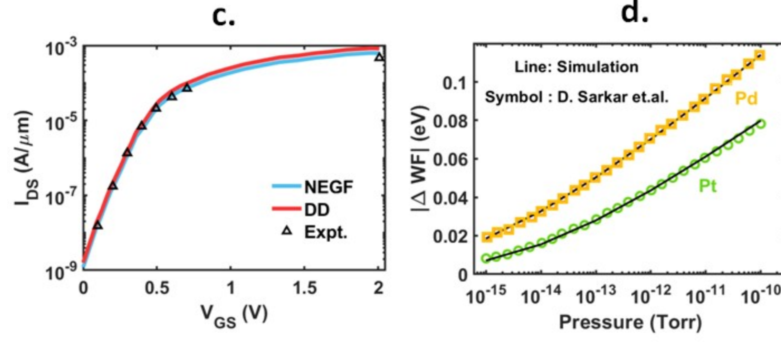

Fig. 3.1. (a) A diagram of the proposed device shows charge-plasma (CP) metals. The device thickness is considered to be 5, 7, and 9 nm. (b) The gas adsorption mechanism on the Palladium (Pd) surface which causes dipole generation, translating to work function change of the metal. (c,d) TCAD simulation setup calibration with experimental.

Figure 3.1 depicts the device structure where the regions of charge-plasma metal overlap at source and drain side each measure 10 nm, while the gate region is also 10 nm. The thickness of the device (t_{CH}) is considered to be 5, 7 and 9 nm. All data taken at tch/2, Lg=10nm, Vd=-0.5, P1=initial, P2=10^{-12} Torr, P3=10^{-14} Torr. The generation of charge plasma is achieved through the application of a high work function metal on the source-drain region. The thin insulator layer between channel and gate as well as between channel and CP is capable of withstanding the potential difference but remains susceptible to the movement of electrons. Due to alignment of energy bands and the Fermi level between the metal and semiconductor, electrons shift from the semiconductor to the metal, occupying lower energy states. Consequently, there is a net transfer of negative charge from the semiconductor to the metal, establishing a region in the semiconductor with a positive charge. This phenomenon can be theoretically comprehended through the provided equation [35-36].

$$p_0 = Nv \exp\left[\frac{q\phi_{BN}}{kT}\right] \tag{3.18}$$

where, $$q\phi_{BN} = qW_{s,d} - q\chi \tag{3.19}$$

$q\phi_{BN}$, $qW_{s,d}$ and $q\chi$ illustrating the barrier height, metal work function, and semiconductor electron affinity, the variation in the source and drain ends emerges as a consequence of the applied electric field, attributed to the barrier lowering effect. In

this work, effective P+ concentration in source and drain regions are achieved using metals with palladium, satisfying the above condition for charge plasma formation.

The presence of palladium enables the device to sense at source and drain charge plasma electrodes. The hydrogen gas sensing mechanism entails the adsorption and dissociation of hydrogen molecules on the Palladium electrode [186]. This process causes atomic hydrogen to diffuse into the metal, resulting in the formation of dipoles at the interface. As analytically established, depending on the initial value of heat of adsorption, coverage ratio at adsorption sites with respect to gas flux, dipole constant and permittivity, the work function of the metal undergoes a change which in turn changes the source drain hole concentration. These virtual P+ regions modulate the channel potential and current by changing its density and thickness in response to H_2 adsorption.

Simulation Methodology

The solution of Schrodinger's equation gives a quantized description of the density of states in the presence of quantum mechanical confining potential variations. As the quantum confinement is in one dimension (along Y axis), the calculation of the quantum electron density relies upon a solution of a 1D Schrodinger equation solved for eigen state energies and wavefunctions at each slice perpendicular to the X axis. We have set the P.SCHRO parameter in the MODELS statement to apply the Schrodinger-Poisson model for holes. P.SCHRODING Computes the self consistent Schrodinger Poisson for holes.Atlas2D solves Schrodinger equation in 1D slices or 2D plane. By specifying the NEGF_MS and SCHRODINGER options on the MODELS statement, we have launched an Non Equilibrium Green's Function (NEGF) solver to model ballistic quantum transport in the proposed device [198]. This fully quantum method treats such effects as source-to-drain tunneling, ballistic transport, quantum confinement on equal footing. A Mode Space (MS) approach is used where Schrodinger equation is first solved in each slice of the device to find eigen energies and eigen functions. Then, a transport equation of electrons moving in the sub-bands is solved. Because only a few lowest eigen sub-bands are occupied and the upper sub-bands can be safely neglected, the size of the problem is reduced. Von Neumann Boundary Conditions (BC) for potential in a contact has been applied by setting the REFLECT parameter on the CONTACT statement.

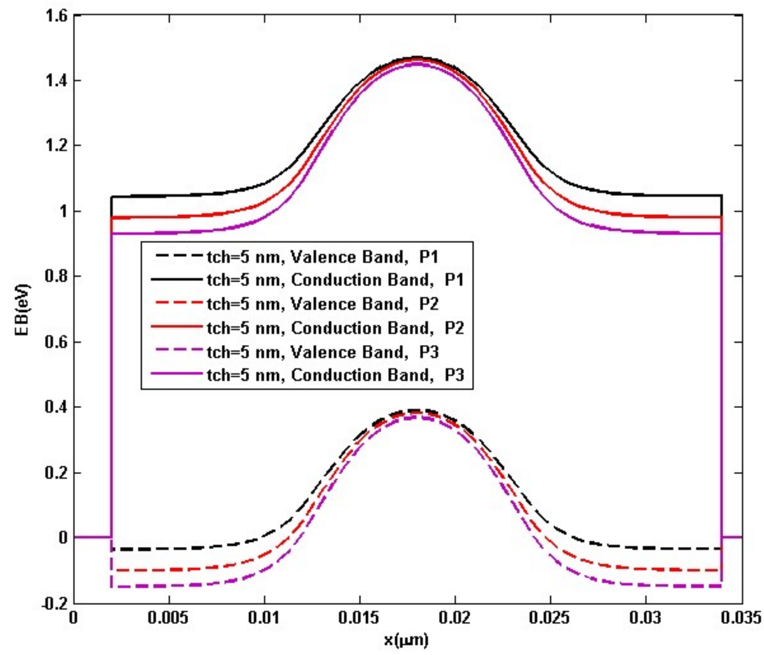

(a)

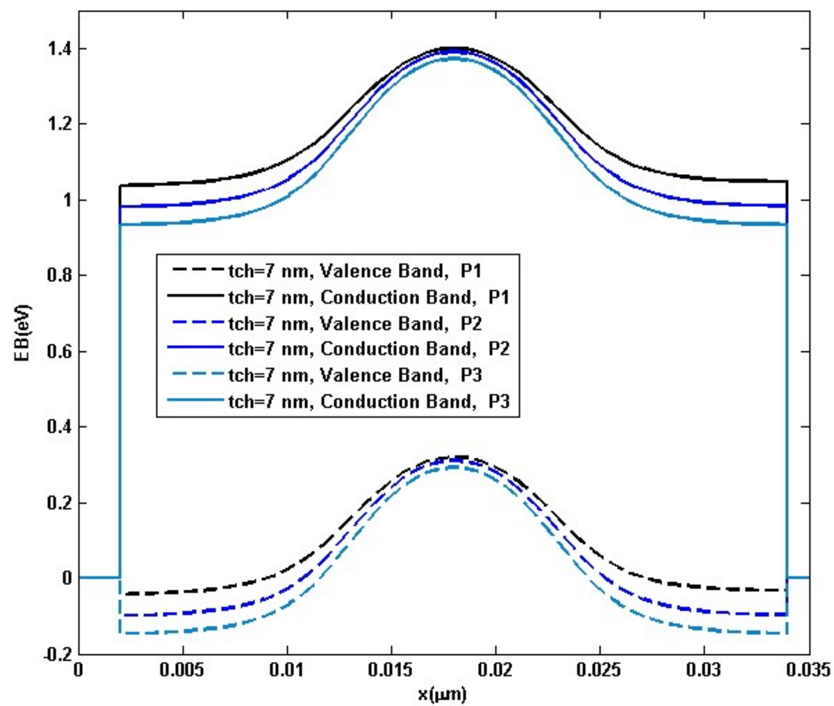

(b)

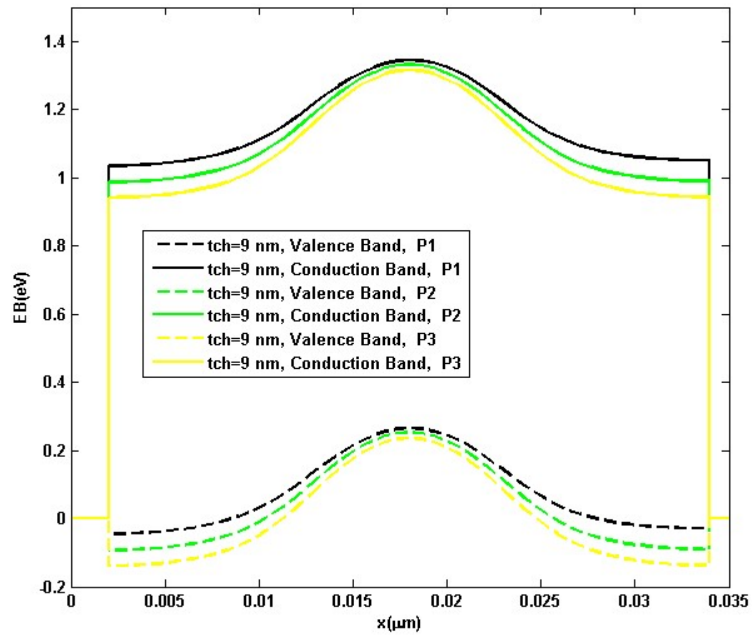

(c)

Fig. 3.2. Lateral variation of energy band at different channel thickness (a)=5nm, (b)=7nm and (c)=9 nm, and pressure of H_2 i.e.,P1(initial) = 10^{-14} Torr, P2 = 10^{-12} Torr and P 3= 10^{-10} Torr to illustrate the band bending under various conditions.

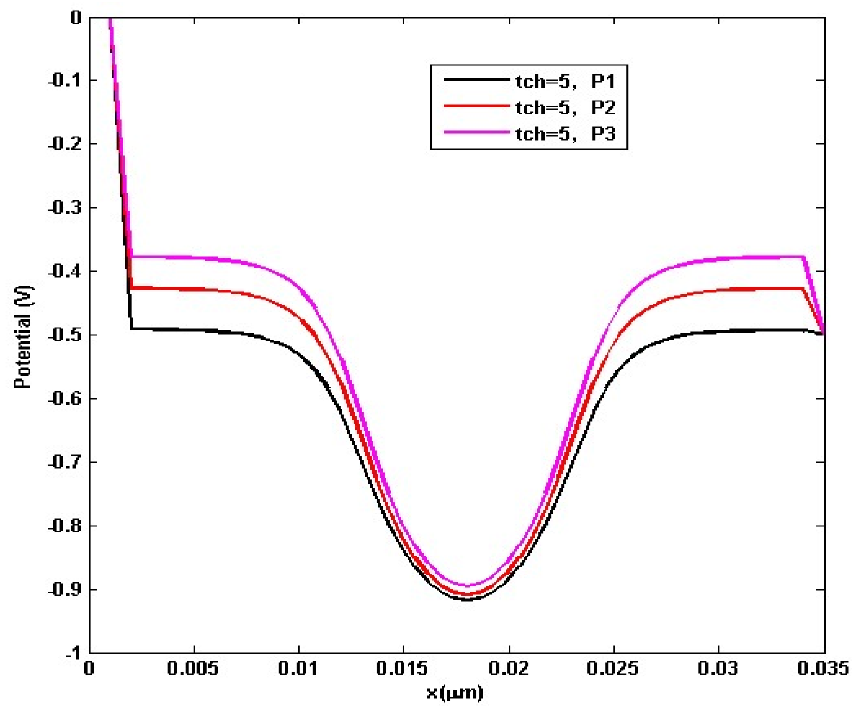

(a)

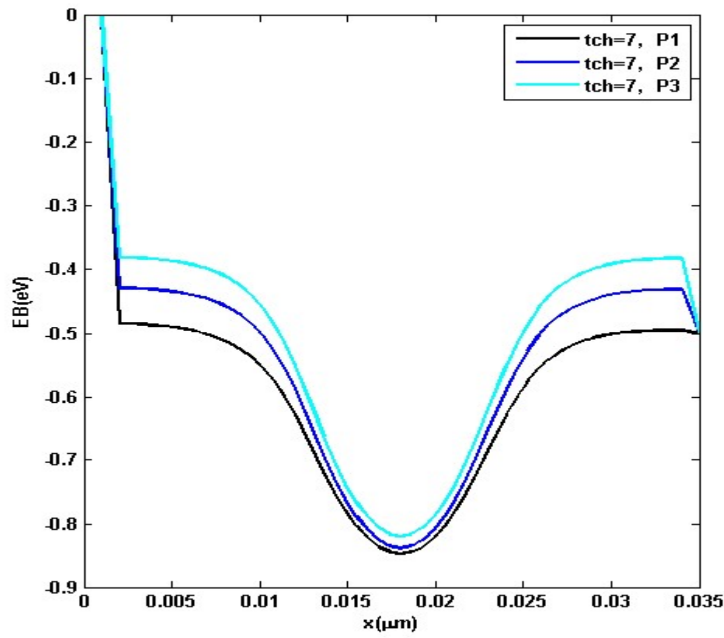

(b)

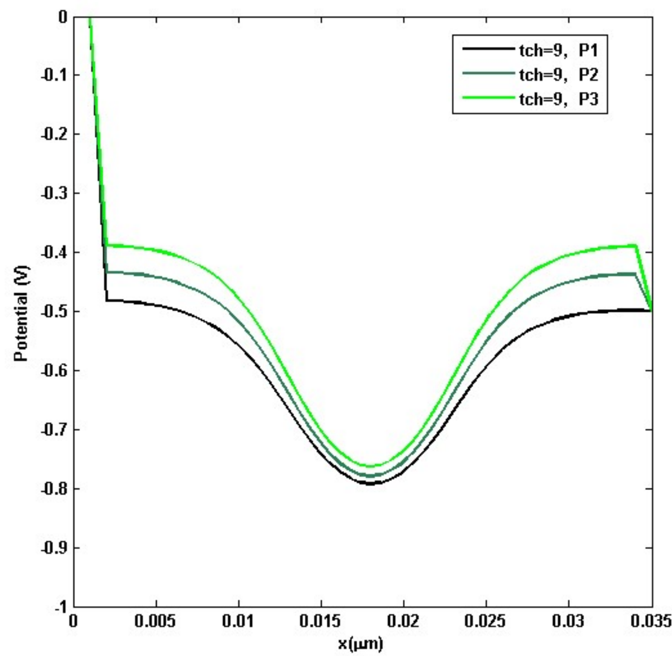

(c)

Fig. 3.3. Lateral variation of potentail at different channel thickness (a)=5nm, (b)=7nm and (c)=9 nm, and pressure of H_2i.e., P1(initial) = 10^{-14} Torr, P2 = 10^{-12} Torr and P 3= 10^{-10} Torr to illustrate the change in potential under various conditions.

Figure 3.2 illustrates the lateral variation of the energy band along a channel with different channel thicknesses focusing on the energy bands at the source and drain ends. As the metal (palladium) with higher work function (5.22eV) than semiconductor is brought into contact with oxide layer, energy level alignment leads to barrier formation at the semiconductor interface and flow of electron from metal to semiconductor, leaving holes in the semiconductor.

On application of H_2 gas, work function of the charge plasma metal decreases according to the adsorption and dissociation of hydrogen model as discussed in section II. As a result, Fermi level of the metal moves closer to the conduction band of the semiconductor that brings down the conduction and valance band at both source and drain ends.

In Fig. 3.3, the surface potential variation along channel position for different source drain work function (i.e., different gas pressure) as the channel thickness is varied with 5nm, 7nm, 9nm. It is evident that as the gas pressure increases from P1=10^{--14} Torr to P3=10^{-10} Torr, potential at the source and drain ends rises. This can be attributed to the fact that as the energy bands shift downward with an increase in pressure (as shown in Figure 3.2), it indicates a decrease in the energy levels for electrons within the material. This results in electrons possessing lower potential energy.

As a result, the potential energy of the material increases, because the electrons have less negative potential energy. This leads to a higher potential energy under the metal gate in the semiconductor. Moreover, with increase in channel thickness, the device loses gate controllability over the channel and, hence, exhibits flatter surface potential profile.

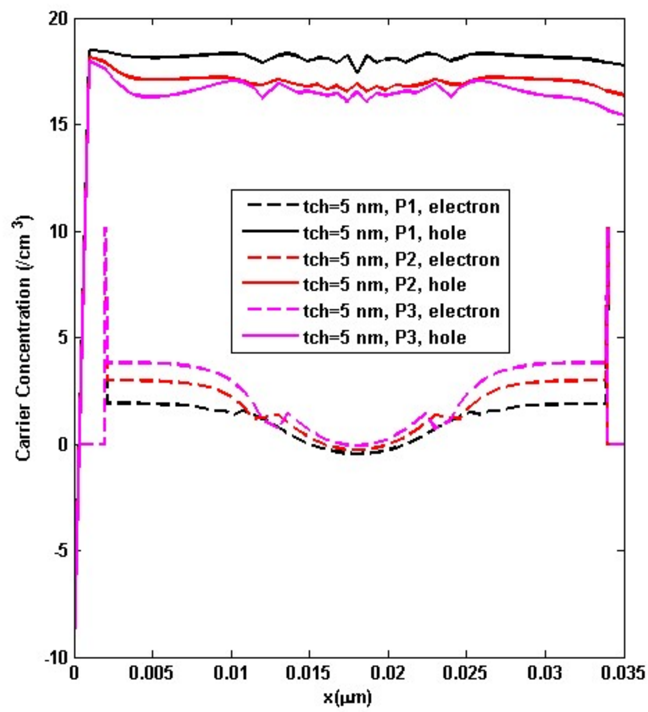

(a)

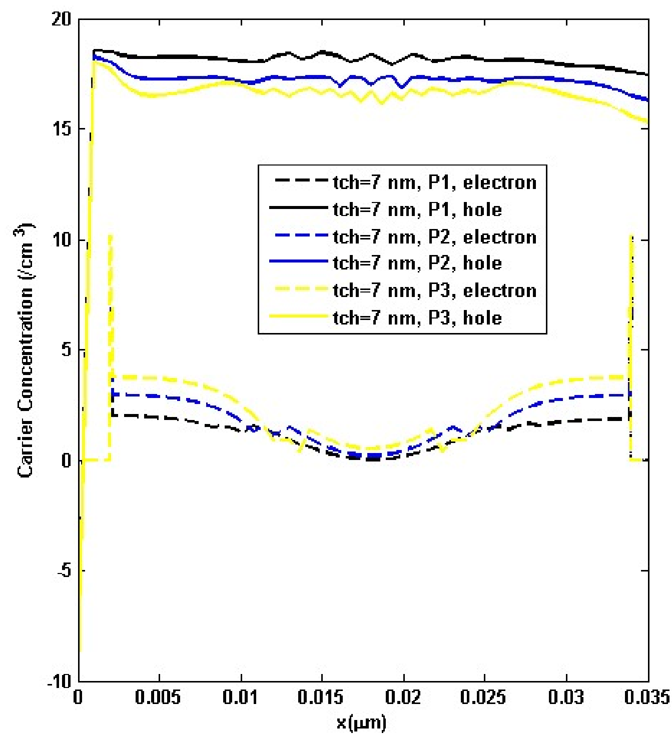

(b)

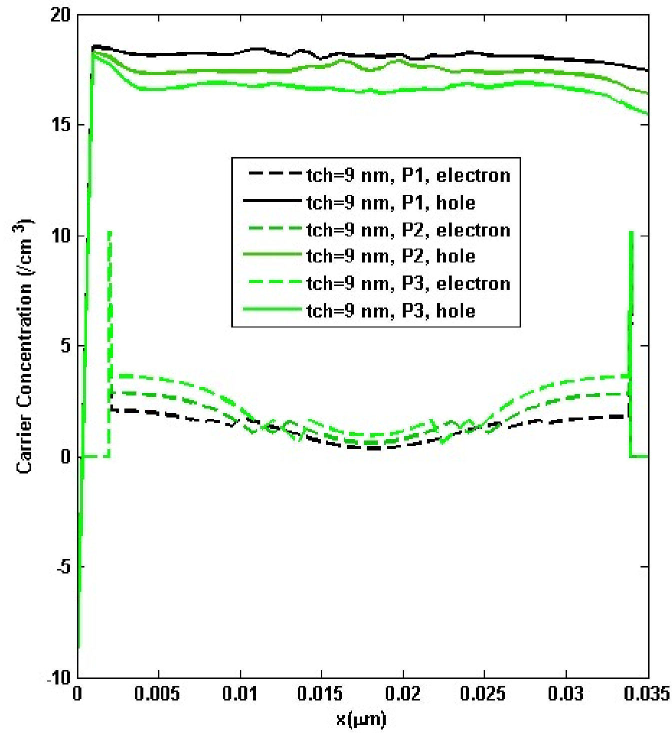

(c)

Fig. 3.4. Lateral variation of electron and hole concentratiion at different channel thickness (a)=5nm, (b)=7nm and (c)=9 nm, and pressure of H_2i.e., P1(initial) = 10^{-14} Torr, P2 = 10^{-12} Torr and P 3= 10^{-10} Torr.

Figure 3.4 illustrates the reduction in hole concentration as the pressure in increased. As explained previously, when work function of the metal reduces following application of a gas (according to the gas sensor model), the barrier height lowers leading to lesser flow of electrons from semiconductor. This makes the source and drain lesser P type . Hence, the hole concentration decreases while electron concentration increases. The spatial distribution of hole concentration in the $MoTe_2$ slab is further explained in figure 3.5.

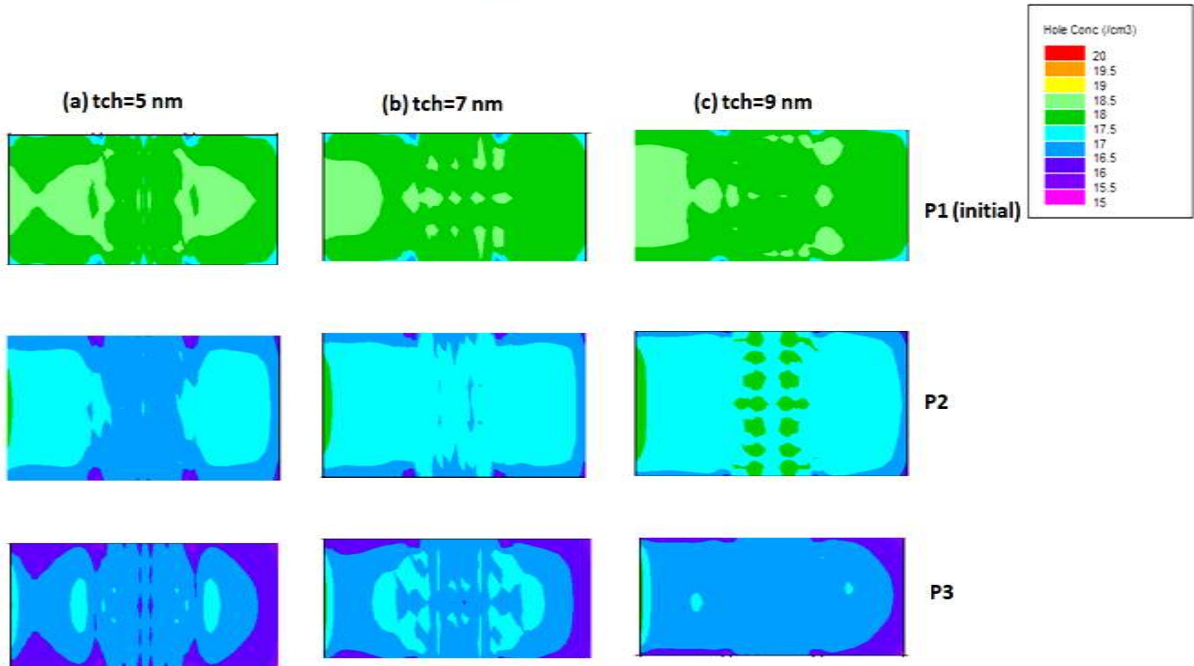

Fig. 3.5. Spatial distribution of hole concentration at different channel thickness (a)=5nm, (b)=7nm and (c)=9 nm, and pressure of H_2i.e., P1 (initial)= 10^{-14} Torr, P2 = 10^{-12} Torr and P 3= 10^{-10} Torr.

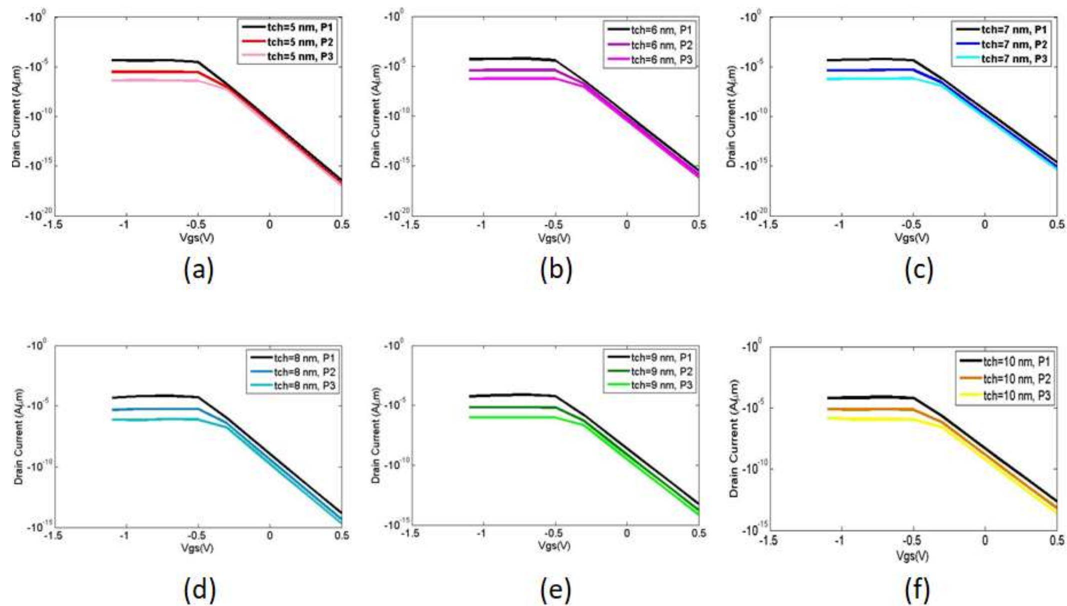

Fig. 3.6. Transfer Characteristics at different channel thickness (5, 6, 7, 8, 9, 10 nm) and pressure of H_2i.e., P1(initial) = 10^{-14} Torr, P2 = 10^{-12} Torr and P 3= 10^{-10} Torr.

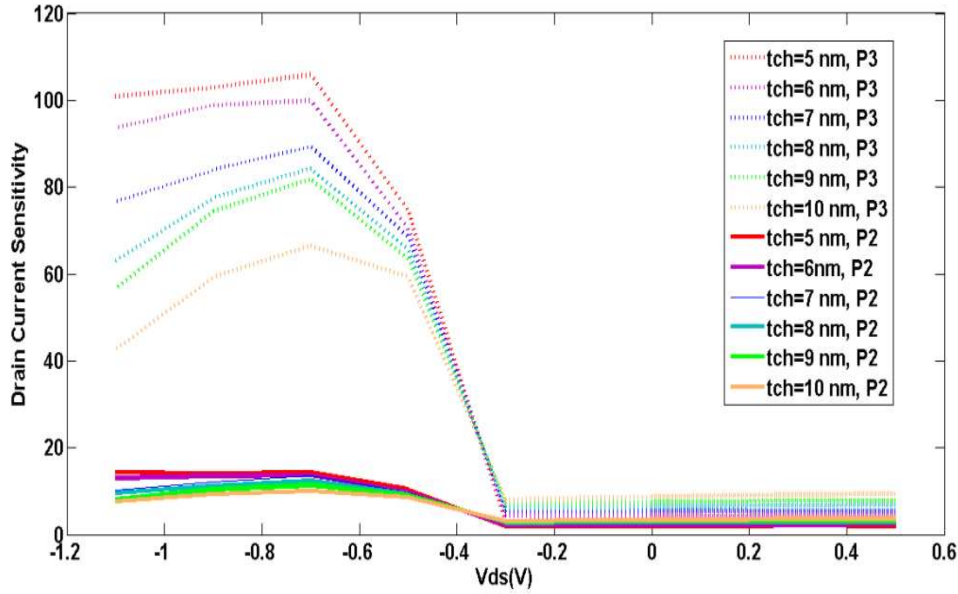

Fig. 3.7. Drain current Sensitivity at different channel thickness (5, 6, 7, 8, 9, 10 nm) and pressure of H_2i.e., P1 (initial)= 10^{-14} Torr, P2 = 10^{-12} Torr and P 3= 10^{-10} Torr.

The reduction in hole concentration directly influences the hole current, lowering it as pressure increases, which has been depicted in figure 3.6. This behavior holds true across various channel thicknesses, across 5 nm to 10 nm. Notably, the change in current within the off region (positive gate voltage) is minor due to the relatively lower impact of alterations in source-drain doping on hole barrier height. However, during the on state, the level of on-current is determined by the difference in the relative energy band height experienced by the holes between the channel and the source-drain. Consequently, an asymmetric dependence on gas pressure is evident between on-current and off-current.

The drain current sensitivity has been defined as the ratio of drain current at H_2 pressure P1 to that at H_2 pressure P2 and/or P3, under varying drain-source voltage across different channel thicknesses (5 nm, 6 nm, 7 nm, 8 nm, 9 nm, 10 nm) and hydrogen gas pressures (P2 and P3) in Figure 3.7. At a constant gate-to-source voltage, sensitivity progressively increases with lower negative drain voltage and subsequently decreases at higher negative drain voltage values. The highest sensitivity is observed in the subthreshold region, where even slight alterations in gas pressure lead to significant

changes in drain current, amplifying sensitivity. Conversely, in the presence of positive drain voltage, drain current sensitivity decreases due to increased control exerted by the drain over charge carrier flow. The MOSFET sensitivity surpasses 100 with lower channel thickness due to positive impacts of enhanced gate capacitance coupling, a stronger electric field, and increased hole concentration in source/drain regions. Sensitivity further amplifies with rising gas pressure, attributed to reduced hole generation enhancing sensitivity. The drain current diminishes with rising gas pressure due to lower hole generation, consequently leading to increased sensitivity with elevated gas pressure.

In contrast to documented sensitivities of H_2 gas sensors utilizing InGaAs CGNWFET and Silicon CGNWFET technologies (7.30 and 7.08 at a work function difference of 50meV, 39.51 and 36.26 at a work function difference of 100meV, respectively), our investigation showcases significantly higher sensitivities. Specifically, our approach achieves a sensitivity of 18 at a work function difference of 70meV and 109 at a work function difference of 120meV, indicating an approximate enhancement of 300% [38] at a channel thickness of 5 nm.

3.6. Conclusion and Future Work

In conclusion, the study proposes a novel approach for highly sensitive ultrathin $MoTe_2$ PMOS FET H_2 sensors, utilizing charge plasma-based electrodes. The application of Non-Equilibrium Green's Function (NEGF) analysis yields insights into its quantum transport behavior for ultra scaled device below 10 nm. The creation of Charge Plasma using Palladium at both the Source and Drain regions has proven highly effective in elevating sensitivity. This enhancement is achieved by expanding the sensing area at both ends while avoiding the need for physical doping in $MoTe_2$. This study also emphasizes the significance of device dimension scaling to realize optimum sensing capabilities. The outcomes of this research provide a foundational understanding for further development and refinement of CMOS-based TMD hydrogen sensors.

In this chapter, we explored the application of Quantum Transport using the Non-Equilibrium Green's Function (NEGF) approach in the analysis of low-dimensional Metal-Oxide-Semiconductor Field-Effect Transistors (MOSFETs), specifically focusing on

charge plasma-based source-drain electrode P-type $MoTe_2$ MOSFETs for high-sensitivity hydrogen sensing. The NEGF formalism provided a comprehensive framework for investigating quantum transport phenomena in low-dimensional systems, where traditional classical models fall short in capturing the intricacies of carrier behavior at the nanoscale.

Through the detailed analysis of charge transport mechanisms in $MoTe_2$ MOSFETs, we demonstrated how the integration of charge plasma engineering at the source-drain interface can significantly enhance the sensitivity and performance of hydrogen sensors. The P-type $MoTe_2$ material, with its unique band structure and electrostatic properties, proved to be a promising candidate for next-generation sensing devices due to its low power operation, high sensitivity to hydrogen gas, and tunable electronic properties.

We also highlighted the critical role of quantum effects, including electron tunneling, in governing the transport characteristics of these low-dimensional devices, which was effectively captured by the NEGF approach. This analysis is vital for the development of future gas sensors that require high sensitivity, fast response times, and low power consumption.

While the current study has provided valuable insights into the potential of $MoTe_2$-based MOSFETs for hydrogen sensing, several avenues remain for future exploration:

1. **Material Optimization**: Further studies should focus on optimizing the $MoTe_2$ material itself, including exploring different synthesis techniques to enhance its crystallinity, reduce defects, and improve its stability under operating conditions. Additionally, the exploration of other 2D materials like WS2 or MoS2 in combination with $MoTe_2$ could provide a deeper understanding of material synergy and enhance sensor performance.
2. **Enhanced Quantum Modeling**: The NEGF approach can be further refined by considering more complex interactions, such as electron-phonon coupling and quantum capacitance effects, which could influence the transport properties at the nanoscale. Additionally, multi-dimensional simulations can be conducted to explore the full potential of charge plasma engineering in different device architectures.

3. **Integration with Advanced Fabrication Techniques**: To bridge the gap between theoretical analysis and practical implementation, future work should focus on the integration of charge plasma-based MOSFETs into real-world sensor platforms. This will require advanced fabrication techniques that can control the material properties at the atomic scale, ensuring consistent performance across large-scale devices.
4. **Exploring Other Gas Sensing Applications**: Beyond hydrogen detection, the principles discussed in this chapter can be extended to the sensing of other gases, including volatile organic compounds (VOCs), CO_2, or NO_2, which are critical in environmental monitoring and healthcare. The versatility of $MoTe_2$-based sensors can open new frontiers in multi-gas detection.
5. **Low Power and Flexible Sensors**: Future research could also investigate the integration of flexible, low-power sensor devices that utilize $MoTe_2$-based MOSFETs, offering the potential for wearable or portable hydrogen detection systems. Developing energy-efficient devices with fast response and recovery times will be crucial for real-time monitoring applications.
6. **Quantum Transport in Other Low-Dimensional Structures**: Expanding the NEGF analysis to other low-dimensional systems such as nanowires, nanosheets, or tunnel FETs could provide a broader understanding of the quantum transport mechanisms in gas sensors and lead to the design of even more efficient devices for various applications.

In summary, the exploration of quantum transport phenomena in low-dimensional MOSFETs using NEGF offers a solid foundation for developing high-performance sensors. With continued advancements in material science, quantum modeling, and fabrication techniques, charge plasma-based MOSFETs, especially $MoTe_2$-based devices, hold significant promise for revolutionizing the future of gas sensing technology.

Chapter 4:

Density Gradient : DG (Quantum Moments Model) of High-Electron-Mobility Transistors for Biosensing Applications

4.1. ***Introduction to HEMTs & Double-Channel HEMT***

4.2. ***DG (Quantum Moments Model) in HEMT***

4.3. ***Bio sensor application of HEMT***

4.4. ***Deep insight of inter-channel coupling in AlGaN/GaNDouble Channel HEMT and its application inC-ERB2 sensing***

4.5. ***Conclusion and Future Work***

4.1. Introduction to HEMTs & Double-Channel HEMT

Introduction to High-Electron-Mobility Transistors (HEMTs)

High-Electron-Mobility Transistors (HEMTs) are a specialized class of field-effect transistors (FETs) that leverage the high electron mobility enabled by the presence of a two-dimensional electron gas (2DEG) formed at the heterointerface of materials with different bandgaps. These transistors are extensively used in high-speed, high-frequency, and power applications due to their remarkable electron mobility, efficiency, and thermal stability. HEMTs are integral to RF and

microwave electronics, power amplifiers, low-noise amplifiers (LNAs), and satellite communication systems.

AlGaN/GaN-based HEMTs have garnered significant interest in sensor technology, attributed to their high electron mobility, wide bandgap, excellent thermal stability, and strong intrinsic polarization [199], [200]. Their superior chemical stability, even in aqueous environments, enhances reliability for biosensing applications. The unique heterojunction structure of GaN HEMTs supports an undoped channel, enabling improved performance and heightened sensitivity [201], [202]. The 2DEG at the AlGaN/GaN interface facilitates the creation of highly sensitive sensors, capable of detecting subtle environmental changes [203].

The operational principle of HEMTs is centered on the formation of a 2DEG at the heterojunction of a wide-bandgap material like Gallium Nitride (GaN) and a narrow-bandgap material such as Aluminum Gallium Nitride (AlGaN). This conduction channel, where electron transport occurs, is heavily influenced by the material properties and the applied gate voltage, leading to enhanced electron mobility and overall device performance.

Structure of HEMTs

The fundamental structure of a conventional HEMT consists of several key components:

- **Source and Drain**: These are the electrodes through which current is injected into and drawn from the channel. The source is typically at a lower potential, while the drain is at a higher potential.
- **Channel**: The active region of the transistor where the electron gas exists. The channel is created at the interface of a heterostructure material. A commonly used combination is AlGaN/GaN, where a high electron density is accumulated at the interface.
- **Gate**: The gate electrode controls the channel conductivity by modulating the 2DEG's density in response to the applied voltage. The gate controls the electron flow, turning the transistor on or off, or modulating its conductivity for amplification.

- **Buffer Layer**: A layer of material that is often inserted between the substrate and the epitaxial layers. This buffer helps improve the quality of the heterojunction and reduce defects.

The 2DEG forms due to the difference in the bandgaps between the two materials at the heterointerface. In AlGaN/GaN HEMTs, a high polarization charge in the AlGaN layer generates the 2DEG in the GaN layer, giving rise to the transistor's high electron mobility.

Advantages of HEMTs

HEMTs offer several unique advantages over traditional silicon-based devices, including high electron mobility, which enhances speed and current-driving capability, resulting in faster switching speeds and higher frequency operation. The wide bandgap materials, such as GaN, enable HEMTs to operate at higher voltages, making them ideal for high-power and high-voltage applications. Their high mobility and efficiency in the 2DEG also provide excellent power efficiency, particularly useful in power electronics and RF amplification. Furthermore, GaN-based HEMTs exhibit high thermal stability, allowing them to perform efficiently at elevated temperatures, unlike silicon-based materials. Additionally, HEMTs are known for their low noise characteristics, making them perfect for low-noise amplifiers (LNAs) and sensitive communication systems.

These attributes make HEMTs ideal for various sensing applications, including chemical and biological detection, imaging, and optoelectronic devices [204], [205], [206], [207], [208], [208].

Double-Channel HEMTs

While traditional HEMTs rely on a single 2DEG for current conduction, Double-Channel HEMTs (DCHEMTs) introduce an additional channel, effectively enhancing the overall device performance. The concept of Double-Channel HEMTs arises from the need to improve the device's current drive capability, reduce on-resistance, and increase the speed of operation by leveraging two parallel conducting channels. In a Double-Channel HEMT, two distinct channels are formed within the

same device. These channels are typically created by modifying the heterostructure of the HEMT or by introducing additional layers of semiconductor material.

Recently, Double Channel High Electron Mobility Transistor (DCHEMT) biosensors have gained prominence due to their enhanced power and current-carrying capacity [202]. This enhancement is attributed to the higher 2DEG density across two 2DEG channels by the incorporation of a lower barrier [209], [210], [211]. In addition to the aforementioned advantages, double-channel HEMTs offer higher mobility owing to a wider distribution of carrier concentration, resulting in an enhanced response to changes. It has been reported that DCHEMT enhances sensitivity from 62% to 136% for given biomarker and investigation conditions compared with single-channel HEMT [212]. The enhancement of electrostatic performance is attributed to two factors: the presence of two high carrier concentration channels and the upper-to-lower channel coupling. Additionally, the higher mobility in the lower channel results from its physical separation from the surface [213]. There are various approaches to creating double-channel HEMTs, including:

- **Dual-Gate Structure**: One of the most common approaches to constructing DCHEMTs involves using two gate electrodes. Each gate can independently control a separate channel, with one channel formed by the usual heterostructure, and the second formed through a different material or heterojunction.
- **Parallel Channel Design**: In some designs, two parallel 2DEGs are created in different layers, allowing current to flow through both channels simultaneously. This structure can be used to increase the current-carrying capacity of the device and improve its efficiency.
- **Double-Channel Modulation**: By applying distinct voltages to the two channels, a more complex control over the device's current can be achieved. This dual-channel configuration allows for fine-tuned modulation of the current flow and better optimization of the device's electrical characteristics.

Double-Channel HEMTs offer several advantages over traditional single-channel HEMTs, including increased current drive capability due to the use of two channels, which enhances current density

.

Additionally, these devices exhibit improved speed by enhancing electron mobility and reducing carrier transit time, which results in higher operational speeds. Double-Channel HEMTs also demonstrate better linearity, higher efficiency, enhanced current-carrying capacity and lower on-resistance,.

Double-Channel HEMTs can be particularly advantageous in the various applications. With increased current drive capability and reduced on-resistance, DCHEMTs are ideal for use in high-power amplifiers, particularly in RF and microwave communication systems. The higher efficiency and lower power losses of Double-Channel HEMTs make them ideal candidates for use in power electronics, such as motor control and power conversion systems.: The dual-channel configuration allows for faster switching speeds, making DCHEMTs suitable for high-speed circuits in areas like signal processing and digital communication. As communication systems evolve to higher frequencies, Double-Channel HEMTs offer a promising solution for future 5G and beyond, where high power, low noise, and high-speed performance are essential.

While Double-Channel HEMTs offer many advantages, several challenges remain, particularly in terms of fabrication complexity, material selection, and integration with existing technologies. Some of the key challenges include:

- **Material and Structural Engineering**: The need for highly precise fabrication techniques and the ability to create stable heterojunctions with low defect densities is crucial for the performance of Double-Channel HEMTs. Advances in material science, particularly in the development of new 2D materials, will play a key role in overcoming these challenges.
- **Thermal Management**: As the current drive increases, thermal management becomes more critical. The higher current density in Double-Channel HEMTs can lead to increased heat generation, which must be effectively managed to prevent device failure.
- **Device Reliability**: The long-term reliability of Double-Channel HEMTs, particularly under high-power or high-frequency conditions, is an area that requires further investigation.

- Research into device degradation mechanisms and the development of more robust materials is essential.
- Despite the presence of multiple channels, the increase in 2DEG density is constrained and does not proportionally multiply with the number of channels [214], [215], [216], [217]. Inter-channel coupling refers to the interaction between two 2DEGs formed at the AlGaN and GaN channels [218], [219], [220]. Zhang et al. studied the correlation between coupling in AlGaN/GaN double channel heterostructures grown through MOCVD and found that pronounced coupling influences the distribution of the 2DEG such that the lower channel resembles the upper channel. The coupling has been demonstrated to be an effective function of channel thickness and was observed to be more definite with a reduced thickness in the upper channel [218]. Lu et al. presented the AlN/GaN/InGaN 'Coupling-Channel high electron mobility transistor' (CC-HEMT), which exhibited consistent transconductance, reduced transconductance derivatives, and stable dynamic source resistance. This was due to the robust channel-to-channel coupling effect compared to an AlN/GaN HEMT [220].
- It has also been uncovered that the coupling effect results in a significant improvement in the gate voltage swing, delivering admirable linearity in both DC and RF conditions [221]. The strength of this coupling depends on factors such as the separation distance between the channels, the composition and thickness of the barrier layers, and the device's operational conditions. Managing and controlling inter-channel coupling is crucial for optimizing the transistor's performance and achieving specific characteristics.

High-Electron-Mobility Transistors (HEMTs) have revolutionized the fields of microwave and RF electronics, power electronics, and communication systems. By leveraging the unique properties of wide-bandgap materials, HEMTs offer unmatched performance in terms of electron mobility, power efficiency, and thermal stability. The introduction of Double-Channel HEMTs has further enhanced these advantages by providing increased current drive capability, reduced on-resistance, and improved device speed. With continued advancements in material science, fabrication techniques, and device design, Double-Channel HEMTs are poised to play a key role in the development of next-generation electronic systems, particularly in high-power, high-speed,

and high-frequency applications. The continued exploration of these devices, including their integration with emerging 2D materials, will further expand their potential in future electronics.

4.2. DG (Quantum Moments Model) in HEMT

Quantum transport models are essential for analyzing HEMTs because they account for the quantum effects that dominate carrier behavior in low-dimensional, high-performance semiconductor devices like those used in HEMTs. At the nanoscale, conventional classical transport models fail to accurately describe phenomena such as quantum confinement, tunneling, and wave-particle duality. These effects become increasingly significant as the dimensions of the channel shrink, especially in high-speed devices where electron mobility and precise control over current flow are critical. Quantum transport models leads to better prediction of device performance, helping to optimize HEMT design for applications in high-frequency, high-power, and low-noise environments.

The Density Gradient (DG) Quantum Moments Model is highly effective for analyzing transport in low-dimensional HEMTs due to its ability to capture quantum effects that significantly influence carrier dynamics in confined structures like 2DEGs. In these devices, where quantum confinement, tunneling, and non-equilibrium effects are prominent, the DG model accounts for quantum corrections to charge distribution, improving the accuracy of transport simulations. By incorporating higher moments of the charge distribution, such as velocity and energy, the DG model provides a more precise understanding of electron behavior under high electric fields and at nanoscale dimensions. This allows for better prediction of key device characteristics like current-voltage performance, efficiency, and scalability, making it a valuable tool for designing and optimizing low-dimensional HEMTs.

The Density Gradient (DG) Model, also referred to as the Quantum Moments Model, is a crucial quantum transport model used to describe the behavior of carriers (electrons and holes) in low-dimensional semiconductor devices, especially when quantum effects such as confinement, tunneling, and wave-function interactions become significant. It is widely applied to model and analyze systems like High Electron Mobility Transistors (HEMTs), MESFETs, and heterojunction

diodes, where the electron distribution is strongly influenced by quantum mechanical effects. This model addresses the carrier transport in these devices by incorporating quantum corrections that arise due to the spatial variation of the local potential on the scale of the electron wave functions.

In the DG Model, the carrier transport equations are extended from classical models like drift-diffusion to include quantum mechanical effects, enabling accurate modeling of electron dynamics in low-dimensional channels such as those in HEMTs. Specifically, the DG model applies quantum corrections to the carrier temperatures, modifying the carrier current and energy flux equations to account for quantum effects. The model uses the Wigner function to describe the statistical behavior of carriers, with the moments of this function providing the necessary quantum corrections.

The key feature of the DG Model is its ability to handle quantum confinement, which occurs when carriers are restricted in low-dimensional structures (such as thin layers, quantum wells, or narrow channels) where classical models fail to describe the transport behavior accurately. The quantum correction potential (Λ) is introduced to account for the effects of quantum confinement, ensuring that the model properly describes the distribution of carriers and their transport characteristics under these conditions.

The density gradient model can be implemented in simulation tools like ATLAS, which can calculate the quantum potential using expressions based on the carrier concentration, effective mass, and quantum correction factors. These corrections are crucial for accurately predicting the current-voltage (I-V) characteristics, threshold voltage, and switching behavior of low-dimensional devices, especially at smaller dimensions where quantum effects dominate. The general analytical Expressions for the DG Model could be based on :-

1. **Electron Current Equation (Quantum Correction)**: The current for electrons in the DG model is modified by a quantum correction term that accounts for the local variation of the carrier concentration. The electron current density expression becomes:

$$J_n = qD_n \nabla_n - qn\mu_n \nabla(\varphi - \Lambda_{DG}) \quad (4.1)$$

where:

- J_n is the electron current density.
- q is the elementary charge.
- D_n is the diffusion coefficient for electrons.
- n is the carrier concentration (electron concentration).
- μ_n is the electron mobility.
- $\nabla(\varphi - \Lambda_{DG})$ represents the gradient of the electrostatic potential (φ :classical potential Λ_{DG} : quantum correction potential).

2. **Hole Current Equation (Quantum Correction)**: Similarly, the hole current density in the DG model is given by:

$$J_p = qD_p\nabla_p - qp\mu_p\nabla(\varphi - \Lambda_{DG}) \tag{4.2}$$

where:

- J_p is the hole current density.
- D_p is the diffusion coefficient for holes.
- p is the hole concentration.
- μ_p is the hole mobility.

3. **Quantum Potential Λ**: The quantum potential Λ is the central term that incorporates quantum corrections to the transport equations. It is calculated based on carrier concentration n and carrier effective mass m, and can be given by:

$$\Lambda_{DG} = -\gamma \frac{h^2\nabla^2\sqrt{n,p}}{6m\sqrt{n,p}} \tag{4.3}$$

where:

- γ is a fitting factor.
- h is the Planck constant.

- m is the carrier effective mass.
- $\nabla^2 n,p$ represents the second spatial derivative of the carrier concentration.

In AlGaN/GaN HEMTs the 2-dimensional electron gas (2DEG) at the heterointerface experiences strong quantum confinement (triangular quantum well) and high sheet carrier density, which lead to deviations from classical drift-diffusion assumptions. For example, the electron distribution maximum is found several angstroms into the GaN channel rather than right at the interface when solved via Schrödinger–Poisson methods. In such a regime, the DG model introduces a quantum correction potential term — derived from the carrier density gradient — that modifies the effective electrostatic potential and replicates confinement effects without the full computational burden of a Schrödinger solver. Because HEMTs typically have extremely narrow quantum wells and high sheet densities ($\sim 10^{13}$ cm^{-2}), modelling these quantum effects is essential for accurately capturing charge distribution, subband occupancy, and effective mobility. The DG approach thus provides a numerically efficient way to include confinement corrections in device simulation of HEMTs, improving accuracy of threshold voltage prediction, transconductance, and channel charge modelling.

When extending from single-channel to double-channel HEMTs, inter-channel coupling becomes a significant factor: the electrostatic fields, quantum well separations, and mutual channel screening influence how each 2DEG sheet responds to gate or surface perturbations. For instance, dual-channel GaN HEMTs have been shown to suppress surface-state induced gate-lag by using the upper 2DEG as an equipotential plane that screens surface fluctuations. In such architectures, the coupling modifies the potential landscape in both channels and thus the charge sharing, tunnelling between wells, and confinement become more complex. The DG model is particularly suited for this scenario because its correction potential term inherently depends on density gradients and can capture the altered quantum confinement environment across multiple sheets. By enabling effective inclusion of quantum coupling and screening in coupled 2DEG systems, DG modelling facilitates realistic simulation of double-channel HEMTs, allowing prediction of how changes in channel spacing, barrier composition, or surface perturbation (as in biosensing) will shift sheet charge, transconductance or sensitivity.

4.3. Bio sensor application of HEMT

Sensors have earned significant research attention over the past decade, leading to the rapid development of semiconductor-based sensing systems. Among these, field-effect transistors (FETs) for temperature sensing, biosensing, optoelectronic, and chemical sensing applications have emerged as cost-effective and easily integrable options [222], [223], [224], [225]. Silicon-based FET biosensing technologies face challenges, such as the degradation of device electrostatic properties as oxide layer erodes in aqueous environment [226]. Additionally, these FETs suffer from impurity scattering as well as self-heating effects, which cause reliability issues [227]. Moreover, silicon is susceptible to chemical and biological reactions, which leads to metallization of the gate and increases the sensing area to channel distance, resulting in lower sensitivity [228].

HEMT-based biosensors exploit the remarkable attributes of High-Electron-Mobility Transistors (HEMTs) to deliver exceptional sensitivity, swift response times, and enhanced capabilities in detecting molecular interactions. These sensors harness the superior electrical properties of HEMTs, such as high electron mobility and minimal noise, which are essential for identifying trace biomolecular concentrations.

Components of HEMT-Based Biosensors

Typically, HEMT-based biosensors include the following integral parts:

1. Substrate: The foundation, often made of materials such as silicon, sapphire, or GaN, offers mechanical support. The substrate material significantly impacts the sensor's overall efficiency.

2. Heterostructure: The core of the biosensor comprises a heterojunction that forms a two-dimensional electron gas (2DEG). This structure is crucial for enhancing electron mobility and facilitating efficient current flow.

3. Gate Electrode: This electrode controls the movement of charge carriers by applying an electrical voltage. It is selected to optimize interaction with the biomolecules of interest.

4. Biorecognition Layer: A surface layer, composed of biomolecules like antibodies, enzymes, or DNA probes, is immobilized to capture the target analytes, which leads to changes in channel conductivity.

Working Principle of HEMT-Based Biosensors

HEMT-based biosensors operate through electrical signal transduction. When target biomolecules, such as antigens or DNA, bind to the biorecognition layer, they cause changes in surface charge density or potential. This interaction leads to a modulation of the 2DEG concentration within the channel. These surface potential changes result in alterations to the current flowing through the HEMT, which can be detected as variations in the drain current. This directly correlates with the concentration of the target biomolecule in the sample. Due to the high electron mobility in the 2DEG, HEMT-based biosensors can detect biomolecules at extremely low concentrations, offering unparalleled sensitivity.

Advantages of HEMT-Based Biosensors

HEMT-based biosensors offer several key benefits. HEMTs feature high gain and low noise, enabling the detection of biomolecules even at low concentrations. Surface functionalization can further enhance specificity for particular analytes. HEMT devices respond rapidly, enabling real-time monitoring and analysis of biomolecular interactions, which is crucial for diagnostic and environmental sensing.These biosensors operate efficiently at room temperature with minimal power requirements, making them ideal for portable and battery-operated devices. HEMT technology's compatibility with standard semiconductor fabrication processes allows seamless integration into electronic circuits, supporting the development of compact and multifunctional sensing platforms.

Applications of HEMT-Based Biosensors

HEMT-based biosensors are used in a wide range of applications. These biosensors are utilized for detecting disease biomarkers, such as those related to cancer, diabetes, and infectious diseases. Functionalized antibodies can be used to identify specific biomarkers, enabling early disease

detection. HEMT biosensors help track environmental pollutants and toxins, ensuring compliance with safety standards and environmental regulations. In food safety, HEMT biosensors are employed to identify contaminants like bacterial pathogens or chemical residues, contributing to food quality and safety. These biosensors are valuable in biodefense applications, providing rapid detection of potential biological threats.

C-erbB-2, also known as Human EGF Receptor 2 (HER2), HER2/neu, or Human Epidermal Growth Factor Receptor 2, is a protein expressed in various cancer cells, with breast, ovarian, bladder, stomach, and esophageal cancers [229]. To describe its importance, breast cancer screening has become increasingly prevalent, with the World Health Organization (WHO) reporting two million new cases and 626,700 deaths in 2020 [230]. Periodical screening every three months has shown a 96% improvement in survival rates, while optimal interventions have reduced the mortality rate by 50% [231]. As a result, there is a rising need for low-priced, user-friendly, specific, and reliable sensors, which is impeded by the minute effective interface charge exhibited by c-erbB-2 [225] , [232], [166].

Despit their advantages, HEMT-based biosensors face several challenges [233]. Achieving stable and uniform functionalization of the biosensor surface is a significant hurdle, influencing both sensitivity and specificity. Non-specific binding of biomolecules can lead to false positives, affecting the accuracy of the sensor. Advances in surface chemistry are needed to address this challenge.: Although HEMT technology shows great promise, scaling up fabrication techniques for large-scale production remains a challenge.

Future research is focusing on refining surface modification methods, integrating advanced nanomaterials to enhance sensitivity, and leveraging machine learning for sophisticated data analysis to better interpret sensor outputs.

HEMT-based biosensors represent cutting-edge technology that harnesses the unique properties of HEMTs to provide highly sensitive, real-time biochemical detection. As research advances, these sensors have the potential to revolutionize diagnostics, environmental monitoring, and food safety. The ongoing innovation in HEMT-based biosensors promises new opportunities in the

realm of molecular sensing, ensuring progress in both practical applications and scientific understanding.

Thus, AlGaN/GaN HEMT-based biosensors have drawn extensive attention in sensing application. However, most existing studies focus on single-channel HEMTs, where the sensing mechanism is primarily governed by the surface potential modulation in a single 2DEG sheet. This architecture often suffers from limited transconductance tunability, weaker electrostatic control, and sensitivity degradation under high ionic strength environments.

The Double-Channel AlGaN/GaN HEMT (DC-HEMT) provides a promising route to overcome these limitations by introducing an inter-channel coupling mechanism that enhances charge modulation and signal amplification. Understanding this coupling is crucial for biosensing applications, especially when detecting low-concentration biomarkers like C-erbB2, where minute surface charge variations must induce measurable electrical responses. Despite numerous works on quantum-corrected transport using the Density Gradient (DG) method in various device contexts and the broad exploration of HEMTs for biosensing, a collaborative study combining inter-channel coupling physics with DG-based quantum transport modeling for biosensing remains unexplored.

Despite extensive research on Density Gradient (DG) quantum transport models across various device applications and numerous studies on AlGaN/GaN HEMTs for biosensing, a collaborative understanding of inter-channel coupling phenomena in double-channel architectures remains largely unexplored. The inter-channel interaction in such structures can significantly influence carrier confinement, charge modulation, and ultimately, biosensing sensitivity. To address this gap, the present work investigates the inter-channel coupling in AlGaN/GaN Double-Channel HEMTs using both analytical and simulation-based approaches within the Density Gradient transport framework. This model enables accurate inclusion of quantum confinement effects, essential for closely spaced 2DEG channels. The objective is to provide a deep physical insight into coupling-induced transport behavior and to optimize device performance for enhanced C-erbB-2 biomarker detection, paving the way for next-generation quantum-enhanced biosensing platforms.

The following work addresses this research gap by providing a deep physical and computational

insight into how inter-channel coupling affects charge transport, electrostatics, and sensitivity in AlGaN/GaN DC-HEMTs. By incorporating the DG quantum correction within the drift–diffusion framework, this study captures nanoscale quantum confinement effects accurately, enabling better prediction and optimization of biosensing performance. The outcome bridges the missing link between semiclassical transport modeling and biosensor design, paving the way for highly sensitive and reliable next-generation GaN-based biosensors for cancer biomarker detection.

4.4. Deep insight of inter-channel coupling in AlGaN/GaNDouble Channel HEMT and its application inC-ERB2 sensing

AlGaN/GaN Double Channel High Electron Mobility Transistors (DCHEMTs) have emerged as promising biosensors, leveraging the unique properties of inter-channel coupling. In the context of AlGaN/GaN-based DCHEMT sensors, inter-channel coupling by alterations in the Al composition at both upper and lower layers may be highly effective. Induced variations can be quantified by adjustments in energy level alignment resulting from modifications in the Al composition of the respective layers. However, to the best of our knowledge, the potential of inter-channel coupling in DC HEMTs for varying the barrier layer composition has not been assessed in the sensing application of HEMTs.

This work investigates the influence of mole fraction variations in the AlGaN layer on inter-channel coupling and explores its implications for C-ERB2 biosensing. The study reveals the potential of inter-channel coupling to enhance sensitivity in biosensing applications, particularly for detecting C-ERB2, a crucial protein associated with various cancers. The device architecture, simulation models, electrostatics, and sensitivity analysis are comprehensively examined. The findings underscore the significance of inter-channel coupling in optimizing biosensor performance, offering valuable insights for the advancement of biosensing technologies.

Device and Simulation Approach

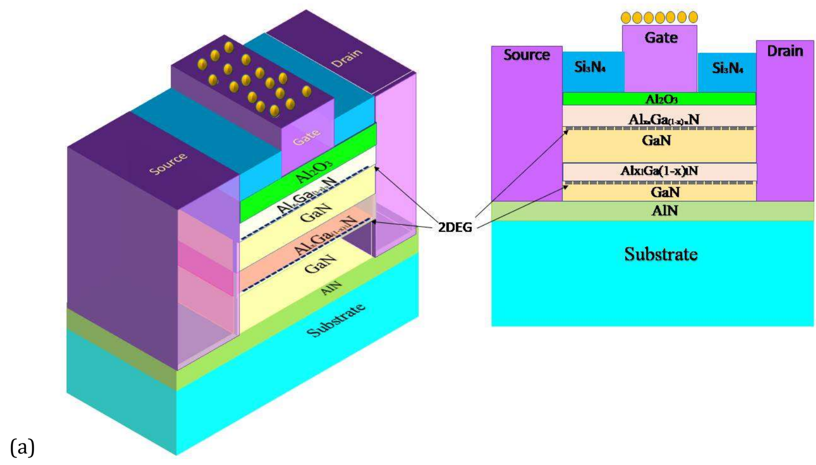

(a)

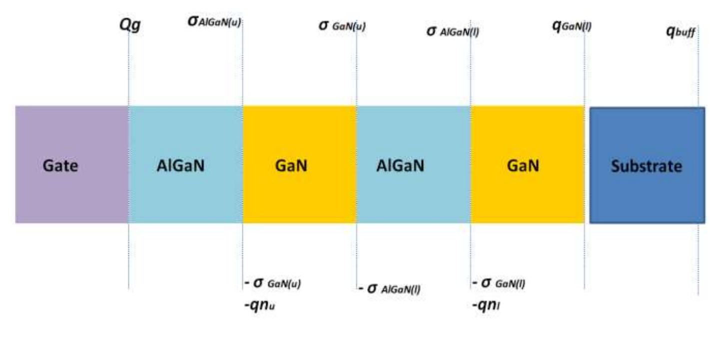

(b)

Fig. 4.1(a). Schematic of the DCHEMT used in this study. (b) Charges at interfaces according to charge neutrality model.

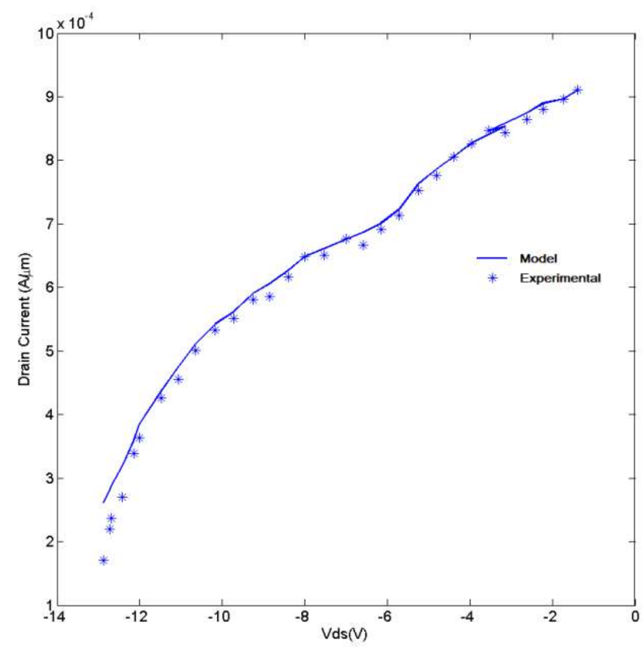

(a)

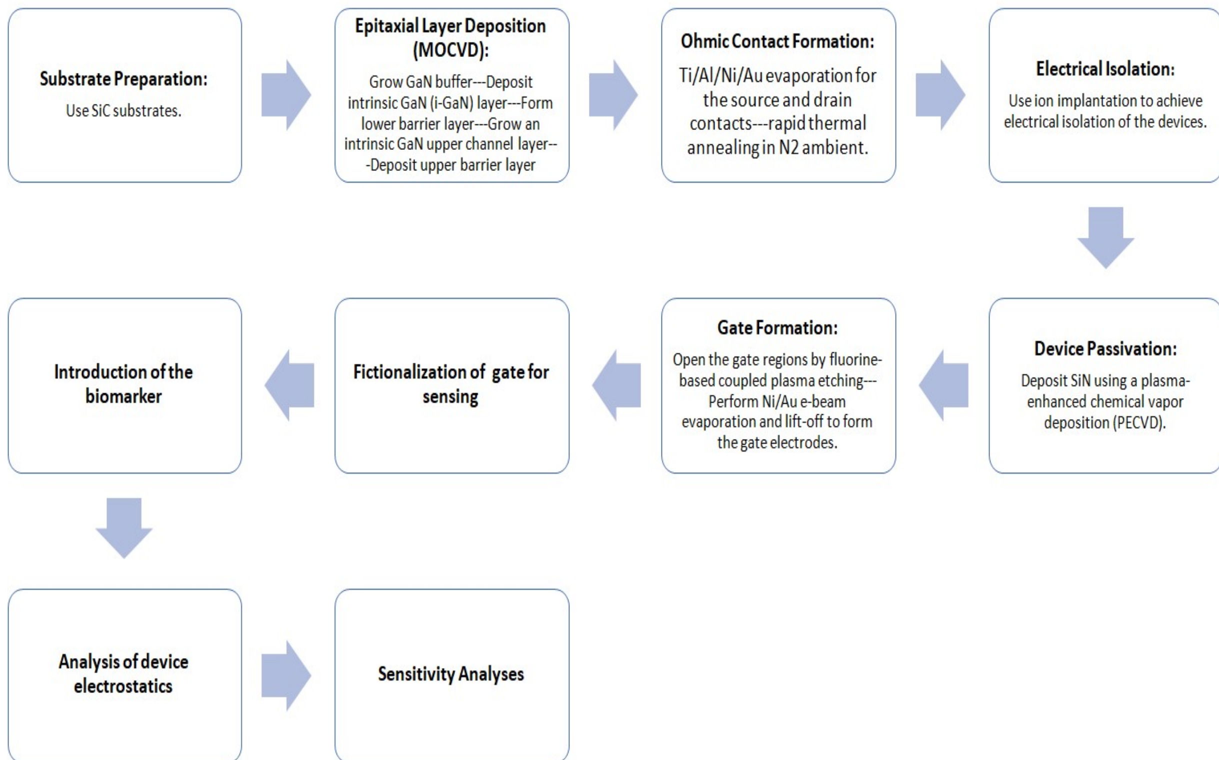

(b)

Fig. 4.2 a.Alignment of the models (lines) with the corresponding experimental results (marks) , b. Process flow diagram for potential device fabrication and analyzing sensitivity .

The structure used for this study is depicted in figure 4.1(a). Figure 4.1(b) depicts the charge distribution along vertical cross-section based on charge neutrality model. This configuration is typically grown epitaxially on a sapphire substrate using either Organometallic Vapor-Phase Epitaxy (OMVPE) or Metalorganic Chemical Vapor Deposition (MOCVD) [234], [235]. The configuration utilizes a sapphire substrate, on which undoped GaN layers (lower channel) are deposited with an AlN insertion layer. The growth sequence is followed by a undoped GaN(lower) layer (that serve as lower channel), a $Al_xGa_{(1-x)}N$(lower)barrier layer(lower barrier), a second undoped GaN(upper) layer(upper channel), and ultimately capping it with $Al_xGa_{(1-x)}N$(upper)barrier layer (upper barrier). The procedural schematic for possible device construction and sensitivity evaluation is shown in Figure 4.2b. The parameter values presented in

Table 4.1 which are derived from experimental and simulation studies referenced in the literature.

Parameter	Value
Source Length	0.5μm
Source-gate spacing	1.5μm
Gate Length	2μm
Gate-drain spacing	1.5μm
Drain Length	0.5μm
Upper AlGaN barrier	30nm
Upper GaN Channel	100 nm
Lower AlGaN barrier	25nm
Lower GaN Channel	800 nm
AlN	50nm

Table 4.1: Dimensions of the device taken into account in this modeling

The source drain contact involves a multi-layer metal stack, Ti/Al/Ni/Au. Typically, Ti/Al layers lowers contact resistance by forming low work function Ti-N and Al–Ti–N layers and creating of numerous N vacancies acting as donors. Au is chosen to prevent oxidation and minimize the overall contact resistance. Ni restricts interdiffusion between Au and Al during Rapid Thermal Annealing (RTA). In this work, the source - drain contacts were characterized with work function (WF)-4eV, equivalent to Ti/Al/Ni/Au stackWF. The Schottky type gate is represented with WF5.15eV, corresponding to WFof Ni/Au [211]

Two triangular quantum wells are created within each of the GaN layers at the interfaces of $Al_xGa_{(1-x)}N$ /GaNowing to electrical confinement induced by the polarization vector in $Al_xGa_{(1-x)}N$. The proportion of Al in the $Al_xGa_{(1-x)}N$ composition is influenced by the growth temperature. As reported, the Al content is increased by approximately 0.24% per degree Celsius. The same is monitored using photoluminescence mapping, a non-destructive technique [236]. The piezoelectric polarization at $Al_xGa_{(1-x)}N$ /GaN induces an electric field that results narrower

confinement of triangular potential well at the hetero-interface. It also results upsurge in sheet carrier concentration [44]. The effect is even more appreciable in wurtzite group-III nitrides ensuing overall increase of polarization based effects in $Al_xGa_{(1-x)}N$ /GaN HEMTs. Thereafter, most of the physical parameters viz. lattice constants , elastic , spontaneous as well as piezoelectric coefficients, total polarization are linearly interpolated depending on the mole fraction [237].

According to the figure 4.1(b), for this $Al_xGa_{(1-x)}N$ (upper)/GaN(upper)/$Al_xGa_{(1-x)}N$ (lower)/GaN(lower) structure the charge neutrality expression along vertical direction is

$$Q_g = (-qn_u(y) - \sigma_{GaN(l)} - qn_l(y) - qn_{buff}) \tag{4.4}$$

Where, Q_g is the gate charge, $n_{u,l}(y)$ are charge density in respective layer which can be derived by applying Fermi-Dirac statistics with 2-D density of states (DOS) theory as [213]

$$n_{u,l}(y) = D_n kT ln[1 + exp(\frac{E_f(y) - \Delta E_c}{kT})] \tag{4.5}$$

Where in respective layer, E_f denotes the energy of sub-bands at the upper and lower quantum wells, ΔE_c is the difference between Fermi level and conduction band, D_n is the 2-D Density of States. Based on the DoS (Density of States) model for triangular well created at both channel , the sheet charge density in each layer can be derived using Fermi-Dirac statistics as

$$\begin{aligned} n_u(y) &= D_n kT ln\left[1 + exp\left(\begin{array}{c} \frac{q\varphi_{eff}^u(y)}{kT} + \frac{q(-qn_u(x_u) - \sigma_{GaN(l)} - qn_l(x_l) - qn_{buff})}{C_{AlGaN(u)}kT} \\ -\frac{\alpha}{kT}\left(\frac{q(-\sigma_{GaN(l)} - qn_l(x_l) - qn_{buff})}{\varepsilon_{GaN(u)}}\right)^{2/3} \end{array}\right)\right] \\ n_l(y) &= D_n kT ln\left[1 + exp\left(\begin{array}{c} \frac{qV_{eff}^l(y)}{kT} + \frac{q(-qn_u(x_u) - \sigma_{GaN(l)} - qn_l(x_l) - qn_{buff})}{C_{AlGaN(u)}kT} \\ + \frac{q(-\sigma_{GaN(l)} - qn_l(x_l) - qn_{buff})}{C_{AlGaN(l)}kT}\left(\frac{1}{C_{GaN}} + \frac{1}{C_{AlGaN(l)}}\right) \\ -\frac{\alpha}{kT}\left(\frac{q(qn_l(x_l) + qn_{buff})}{\varepsilon_{GaN(l)}}\right)^{2/3} \end{array}\right)\right] \end{aligned} \tag{4.6}$$

Where $\varphi_{eff}^u(y)$ is upper channel effective potential balancing the (i) Gate- $Al_xGa_{(1-x)}N$(upper) Schottky barriers, (ii) GaN(upper) Fermi level, (iii) GaN(upper) conduction-band-edge and (iv) conduction band offset at the $Al_xGa_{(1-x)}N$(upper) /GaN(upper) interface. φ_{eff}^l(y) is lower channel effective potential created by adding (i) GaN Fermi level (ii) conduction-band-edge and (iii) conduction band offset at the $Al_xGa_{(1-x)}N$(lower) / GaN(lower) interface. $\sigma_{AlGaN(u,l)}$ is the bound

sheet charge resulting from piezoelectric and spontaneous polarization , $n_{u,l}(x_{u,l})$is upper and lower channel sheet electron concentration, $\sigma_{GaN(u,l)}$ denotes bound sheet charge in upper and lower GaN channel from spontaneous polarization, n_{buff} is the intrinsic concentration is lower GaN buffer. C_{ox}, $C_{GaN(u,l)}$ and $C_{AlGaN(u,l)}$ are capacitances of respective layer whereas $\varepsilon_{GaN(u,l)}$ indicate permittivity of the layers.

Now as per section 4.2, DG (continuous) quantum potential (Bohm-like / DG form)

$$\Lambda_{DG} = -\gamma \frac{h^2 \nabla^2 \sqrt{n,p}}{6m\sqrt{n,p}} \tag{4.7}$$

In one direction (y)

$$\Lambda_{DG}(y) = -\gamma \frac{h^2 d^2 \sqrt{n_{u,l}(x_{u,l})}}{6m\sqrt{n_{u,l}(x_{u,l})}dy^2} \tag{4.8}$$

Effective potential after the potential correction is

$$\left[\varphi_{eff}{}^{u,l}(y)\right]_{i+1} = \left[\varphi_{eff}{}^{u,l}(y)\right]_i + \Lambda_{DG}(y)/q \text{ ..... i=number of iteration} \tag{4.9}$$

This corrected potential is then substituted into the charge density expressions for both the upper and lower channels, where the carrier concentration is a function of the local potential. By iteratively updating the potential and charge densities, the DG-corrected sheet charge densities are obtained, capturing the quantum confinement effects more accurately than classical models. This theoretical explanation clearly indicate interdependency of both channels and enormous impact of barrier composition.

Simulation Approach using Density Gradient Method

The inter-channel coupling in AlGaN/GaN double-channel HEMTs involves complex interactions that are challenging to capture through experimental methods alone. A validated simulation approach has potential to complement experimental data, offering a cost-effective and efficient way to explore a wide range of parameters and conditions.For analysis of the DCHEMT structure integrating quantization models, the present study employs SILVACO ATLAS TCAD.In this model, the linear as well as saturation characteristics (relation between drain current and drain voltage)

are regulated by low as well as high field mobility models. Therefore, both models have been incorporated for precise simulation.The low-field model, dependent on composition and temperature, has been implemented by defining FMCT.N and FMCT.P in the MOBILITY statement, where FMCT refers to Farahmand Modified Caughey Thomas. For elevated fields, a nitride-specific, field-dependent mobility model has been employed by specifying GANSAT.N and GANSAT.P in the MOBILITY statement. To consider additional factors like bandgap narrowing and Fermi-Dirac statistics etc, AUGER, SRH, and CONSRH models have been included. Model calibration is conducted against the experimental study by Gaska et al., establishing accurate agreement in current vs. drain-source voltage (I_d-V_{ds}) characteristics as depicted in fig. 4.2a .Throughout the analysis, the ambient temperature T=300 K is maintained, as this study does not encompass the self-heating effect. To account for quantum effects, Density Gradient (Quantum Moments Model) has been utilized in this simulation to account for HEMT confinement, considering the variation in locally generated potential. This also includes quantum adjustments to the carrier temperatures in the carrier current expression. To enable the quantum model, MODELS QUANTUM is included in the MODELS statement.'QFACTOR' parameter is employed to gradually introduce quantum moments, ensuring convergence on the moments function.As reported, $Al_{0.53}Ga_{0.47}N/Al_{0.38}/Ga_{0.62}N$ HEMTs demonstrated a peak drain current density of 114 mA mm−1, where, $Al_{0.85}Ga_{0.15}N/Al_{0.70}Ga_{0.30}N$ HEMTs, equipped with 80 nm gates, achieved 160 mA mm^{-1} [238], [239]. However, in this study, the mole fraction is varied uptosafe limit of 0.5 based on previous research on $Al_xGa_{(1-x)}N$ HEMTs which showcased a notable improvement device current drive while ensuring crystal stability [240].

In the context of biomolecule simulation, an interface charge model is employed to obtain sensitivity for healthy and diseased cells [22]. In an experimental setup, the recognition process involves the placement of a target biomolecule linker on the gate area, such as self-assembled thioglycolic acid ($HSCH_2COOH$) and the molecular linking of thiol -gold [241]. Upon immobilization, the charged biomolecules influence the channel through capacitive coupling. Hence, in the simulation model, to replicate this, the net interface charge is applied at the gate electrode. When the immobilized charge is negative, electrons from the channel are repelled, resulting in a reduction in the drain current. Here, biomarker-induced equivalent interface charge has been included in the modeling through the 'interface' charge statement following the reported data . It is worth noting

that we have incorporated lower values of the clinical concentration of C-erbB-2 in saliva into our model to validate the device's effectiveness and response to C-erbB-2.

Medium – Saliva	Healthy Condition	Diseased Condition
C-erbB-2 Clinical concentration (μg/ml)	4 – 6	9 – 13
**Equivalent induced interface charge ($10^{14}/m^2$)*	-0.63 to -0.948	-1.42 to -2.05

Table 4.2: Interface charges associated with C-ERB2 biomolecules investigated in the current study

Results and Discussions

Figure 4.3 depicts energy band diagram in vertical cross section for variations of mole fractions of upper and lower channel (x_u and x_l respectively). The plots indicate creation of triangular quantum wells in both upper and lower $Al_xGa_{(1-x)}N$ /GaN interfaces. Raising $x_u$cause dipsnot only the upper, but also lower channels energy bands, indicating the presence of inter-channel coupling. The reason can be attributed to the polarization model as explained in section II. The GaN(upper) is electrically as well as structurally confined by $Al_xGa_{(1-x)}N$(upper) and $Al_xGa_{(1-x)}N$(lower) layer resulting direct impact of both layers. On the contrary, the GaN(lower) experiences an indirect influence from the $Al_xGa_{(1-x)}N$(upper) but a more direct impact from the $Al_xGa_{(1-x)}N$(lower). Owing to this, lower barrier mole fractions does not produce visible shifts in conduction and valence band offsets come out for different $x_l$values.

From the neutrality model as described in figure 4.1(b), the gate charge density is distributed through oxide interface charge density, upper channel 2DEG density $n_u(x)$, $Al_xGa_{(1-x)}N$(upper)interface charge, lower channel 2DEG density $n_l(x)$, $Al_xGa_{(1-x)}N$(lower)interface charge density and bulk charges. Consequently, the electric field at upper channel and lower becomes a function of $n_l(x)$and $n_u(x)$respectivelyand the Fermi-level to conduction band difference in each layer carries cumulative impact of $n_u(x)$and$n_l(x)$ and vice versa. The energy band's slope signifies quasi-constant electric fields. Hence, an intricately interdependent system is established, intertwining both channels. The changes in quantum well barrier height and well depth alters 2DEG density as depicted in Figure 4.4 (a-c). Furthermore, it is noted that with increasing mole fractions, charge density declines rapidly in regard of vertical distance. This restricts carriers

along the surface, ensuring superior confinement within the quantum well.

The variation of maximum carrier concentration in the upper and lower channels of the AlGaN/GaN double-channel HEMT is shown in figure 4.4 (d). The results obtained without DG correction overestimate the charge density in both channels, as the quantum confinement effect is neglected. When the DG correction is incorporated, the charge density decreases and shows better agreement with the simulated results. A notable observation is that the lower channel consistently exhibits a higher carrier concentration compared to the upper channel. This behavior can be attributed to the stronger electrostatic confinement and polarization-induced charge accumulation at the lower AlGaN/GaN interface. The upper channel, being closer to the gate, experiences enhanced quantum confinement and field screening, which reduce its effective 2DEG density. The inclusion of the DG correction thus provides a more realistic representation of charge distribution across the double-channel structure, highlighting the inter-channel coupling effect and the role of quantum mechanical corrections in accurate HEMT modeling.

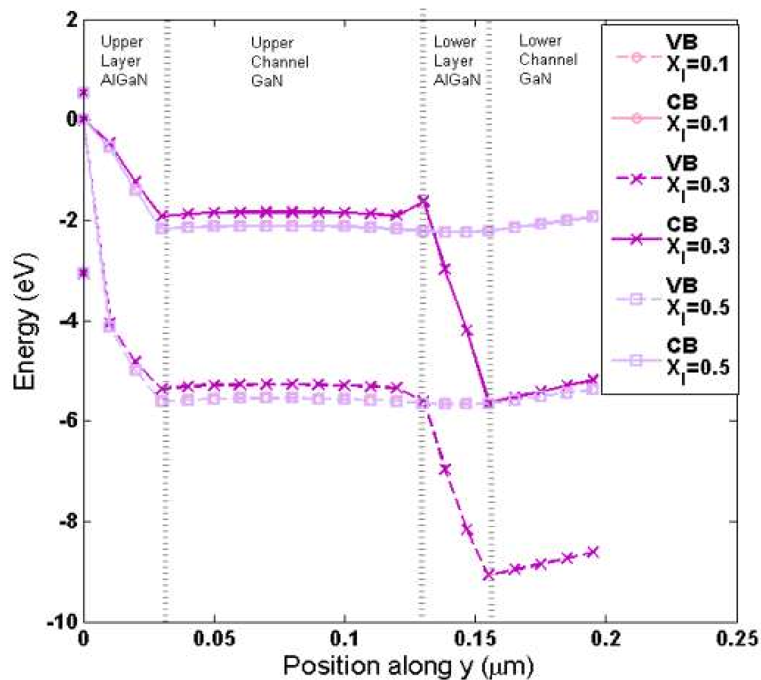

(a) X_u=0.1

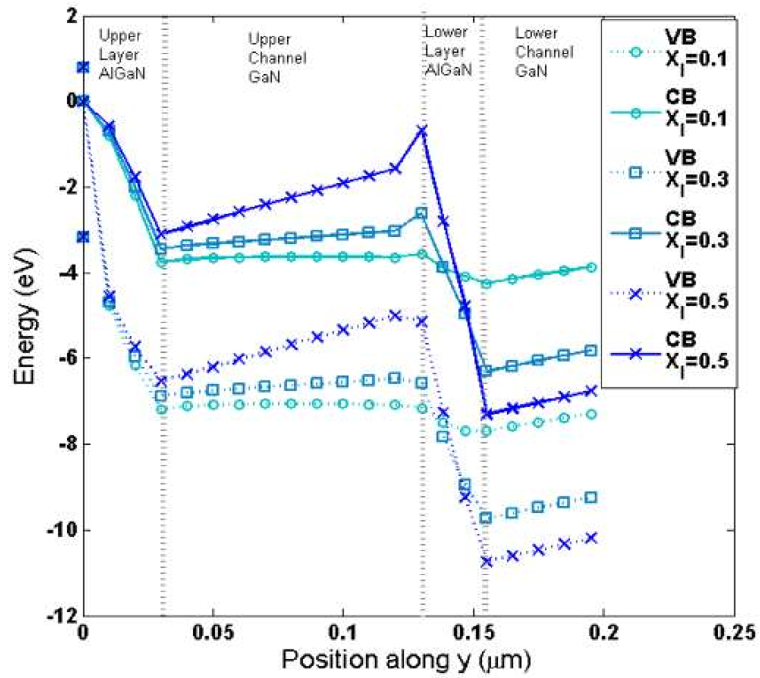

(b) X_u=0.3

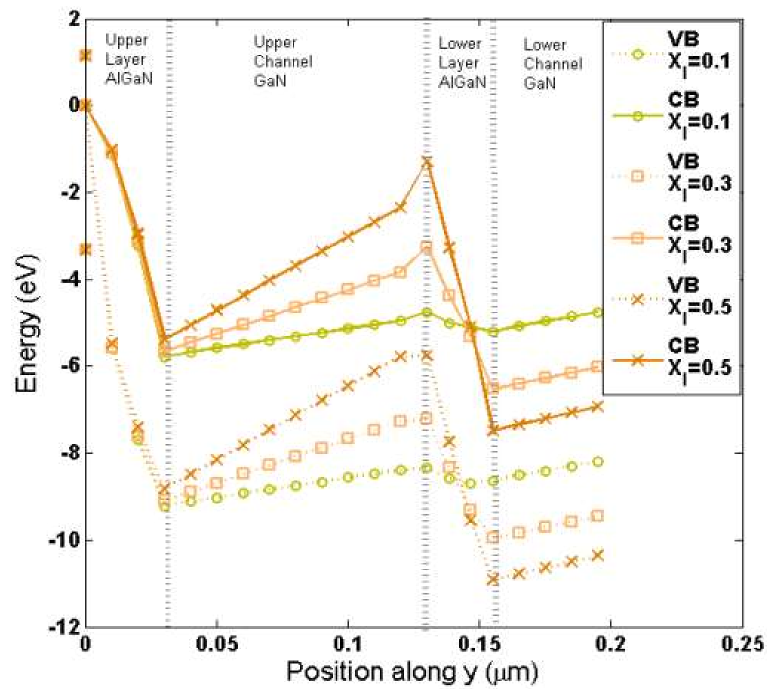

(c) X_u=0.5

Fig 4.3. Plot of energy band diagram along device thickness for x_u=0.1, 0.3, 0.5, each plot corresponds to change in x_l=0.1, 0.3, 0.5.

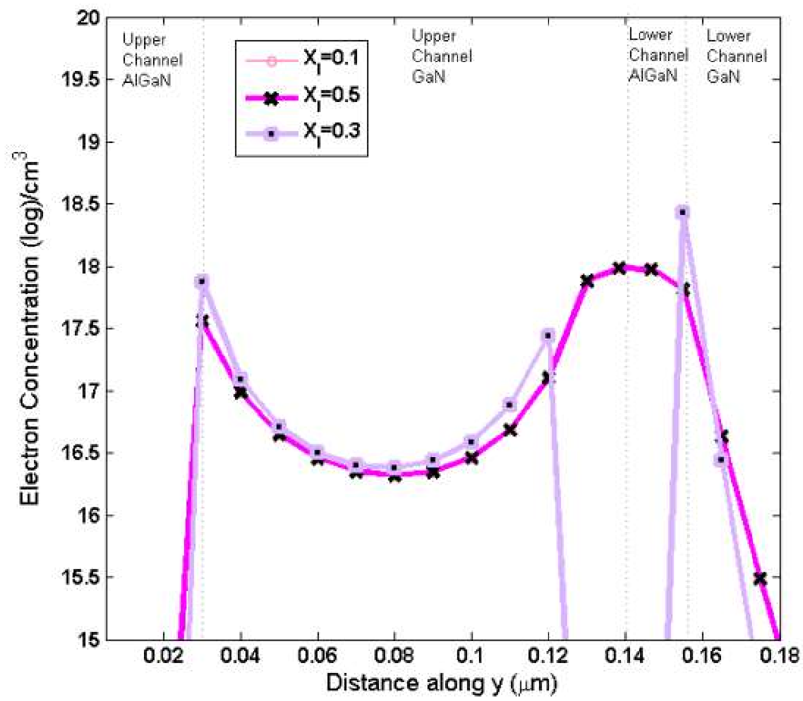

(a) X_u=0.1

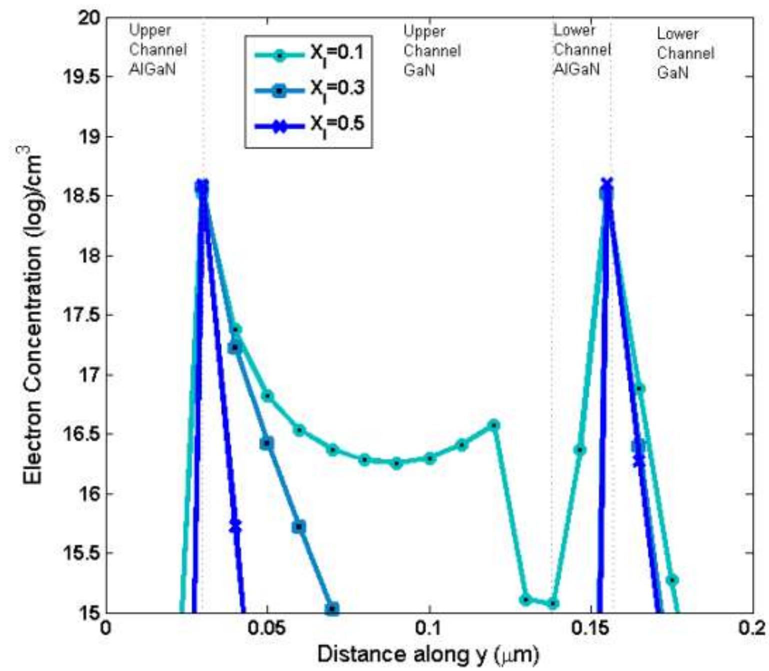

(b) X_u=0.3

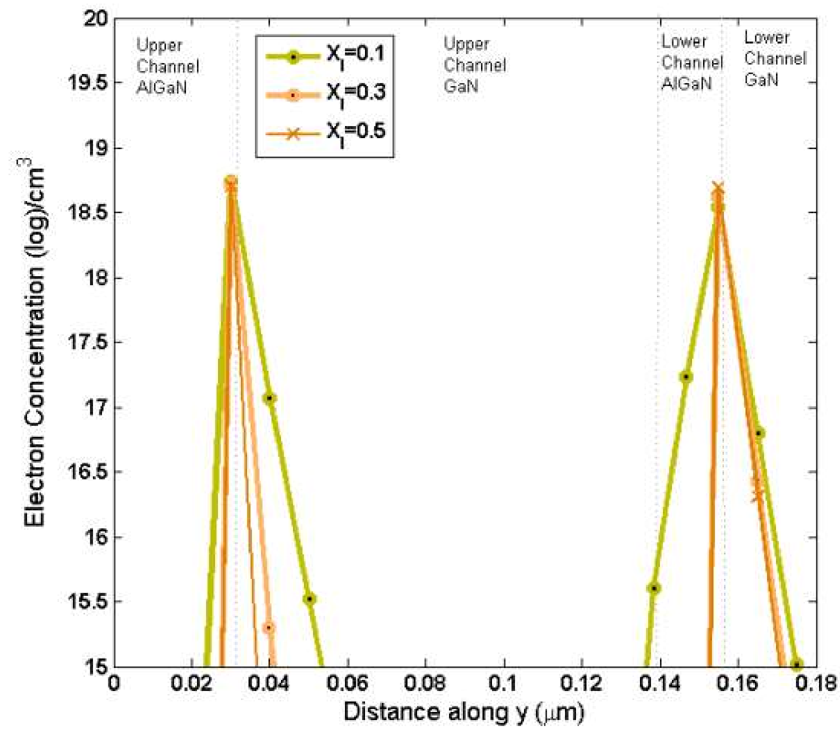

(c) X_u=0.5

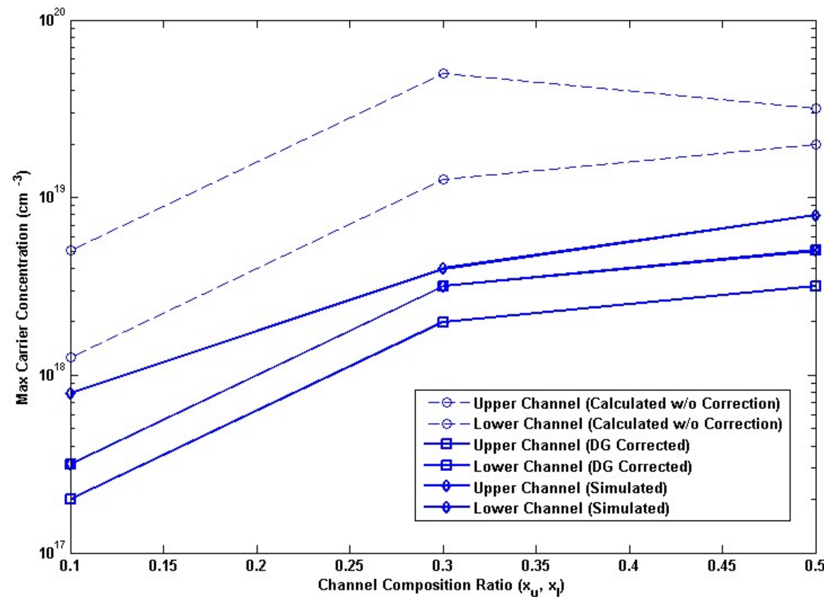

(d)

Fig 4.4. (a-c) Distribution of electron concentration profiles across the device's thickness illustrating the impact of different mole fractions (d) Comparison of maximum carrier concentration in upper and lower channels of the AlGaN/GaN double-channel HEMT obtained from analytical calculation (with and without Density Gradient correction) and numerical simulation.

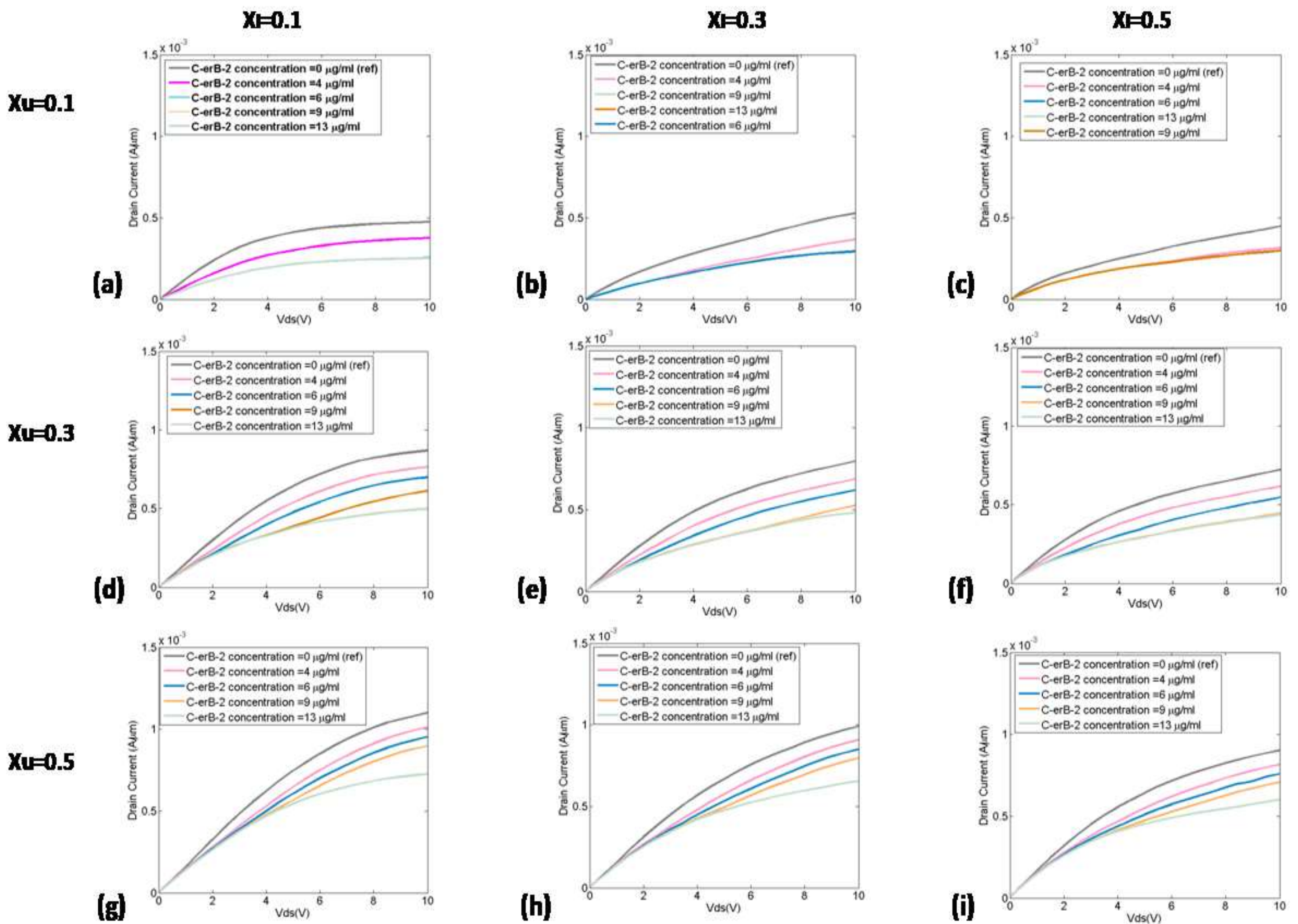

Fig. 4.5.Comparison of drain current vs. drain-source voltage (Id-Vds) characteristics. Marker for no biomarker condition (Iref), c-erB-2 concentration 4 μg/ml, 6 μg/ml, 9μg/ml, 13 μg/ml.

Figures 4.5 depicts overlays of drain current vs drain to source voltage characteristics for combinations of $x_{u,l}$where each plot displays drive current (i) the absence of a biomarker (I_{ref}), (ii) at applied c-erB-2 concentration of 4 μg/mland (iii) at applied c-erB-2 concentration of 13 μg/ml. Notably, the application of biomarkers results in a reduction in drive current due to the negative charge induced by the biomarker, as indicated by the solid lines.

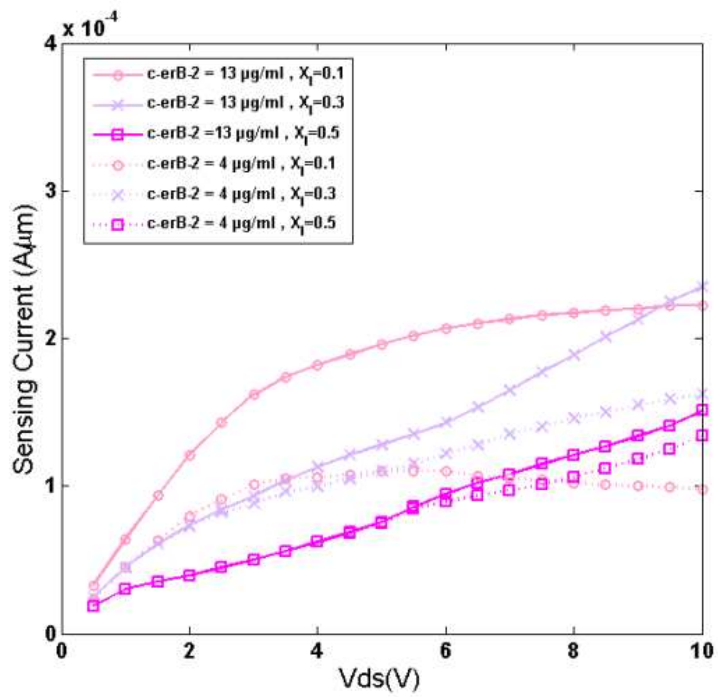

(a) X_u=0.1

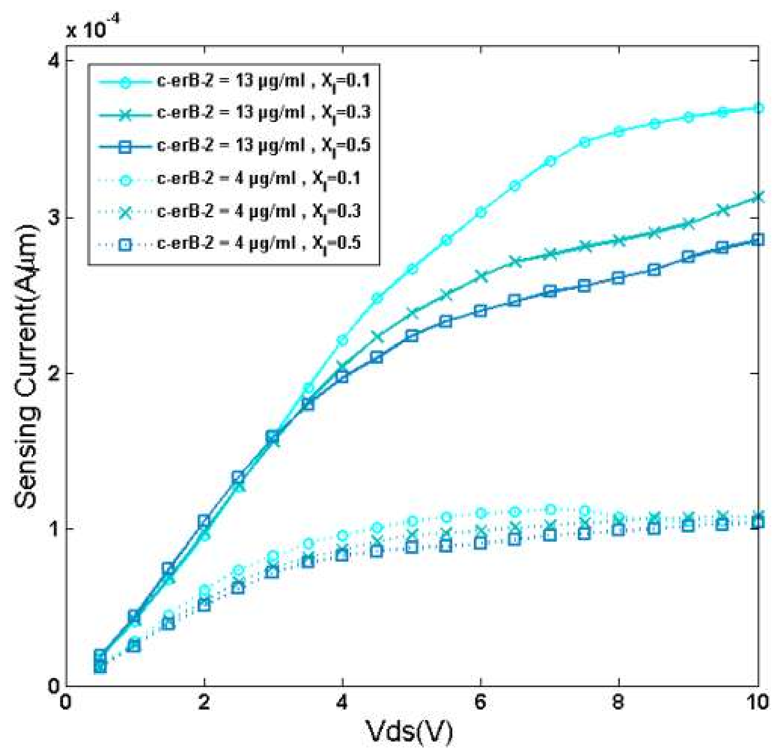

(b) X_u=0.3

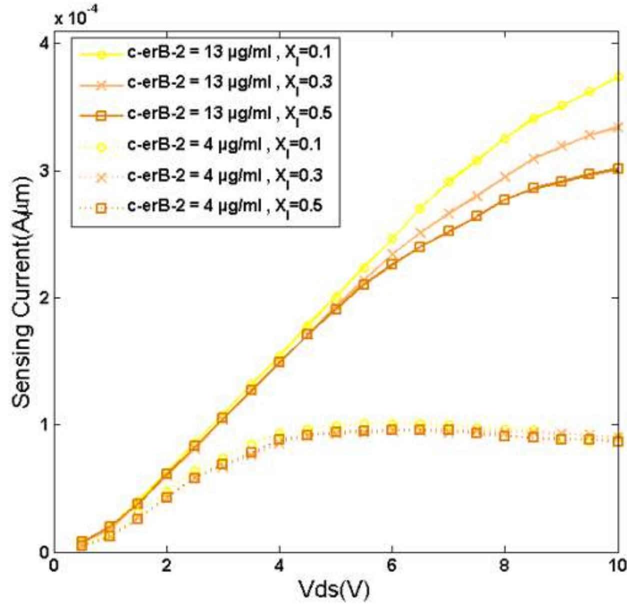

(c) X_u=0.5

Fig.4. 6.Comparison of Sensing Current for increasing both channel mole fraction. Solid lines and dotted lines indicate Sensing Current c-erB-2 concentration 4 μg/ml (indicating healthy condition) and c-erB-2 concentration 13 μg/ml(indicating diseased condition) for x_u=0.1, 0.3, 0.5, with each plot corresponding to variations in x_l=0.1, 0.3, 0.5.

A higher concentration of c-erB2 (associated with disease) generates higher sensing current due to even greater reduction in drive current, illustrated by the dotted lines.For each of these scenarios, the influence of both x_u and x_l is analyzed and plotted. It is observed that elevating $x_u$results an increase in drive current due to the heightened carrier density peak (as shown in Figure 4.4). Conversely, increasing the $x_l$adversely impacts the charge density in upper channel closer to sensing surfaces due to inverse polarization, leading to a decrease in sensing current. In figure 4.6 it is observed that in all conditions, the sensing current decreases as the x_u and $x_l$increase. However, the rate of decrease is markedly higher for lower c-erB2 concentrations when compared to higher concentrations. This differential rate of decrease gives rise to distinct sensitivities associated with variations in both x_u and x_l, as depicted below. Figure 4.7 illustrates that, with a fixed x_l, sensitivity amplifies as $x_u$increases due to sharper confinement achieved through an increased energy band offset, explained in Figure 4.3.

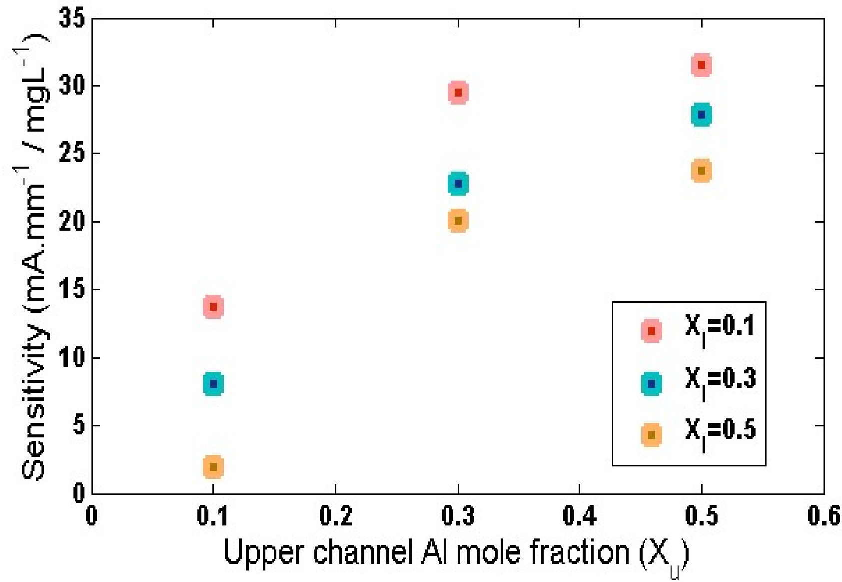

Fig. 4.7. The sensitivity of drain current is analyzed for different values of x_u =0.1, 0.3, 0.5 and x_l =0.1 , 0.3, 0.5.

Quantitatively, for $x_l = 0.1$, sensitivity increases from 13.77mA/mm per mg/L to 29.55mA/mm per mg/L to 31.55mA/mm per mg/L for rise of $x_u$from 0.1 to 0.3 to 0.5 indicating an increase of 129% in sensitivity. Whereas, rise of $x_l$leads to higher barrier above lower channel which lower impact and control of gate electrostatics, hence leads to poor sensitivity.For a given x_u, sensitivity diminishes with increasing $x_l$also due to the heightened negative polarization within the GaN channel between two barrier layers [50].At $x_u = 0.1$, Sensitivity falls 86% from 13.77 to 1.9 for rise of $x_l$from 0.1 to 0.5, while the rate is 31% and 24.8% for $x_u = 0.3$ and $x_u = 0.5$. It is noteworthy that for Al-rich $Al_xGa_{(1-x)}N$ at x=0.5, a dip in sensitivity is observed due to the composition and doping-dependent mobility models used in the work.

Table 4.3 illustrates a comparative analysis of sensitivity offered by the DCHEMT with different biomarkers under analogous conditions. The sensitivity data has been obtained based on the shift in device electrostatics in response of induced negative interface charge as reported by [241] . It is noted that the device is capable to offer significant sensitivity over wide range of biomarkers with similar trend.

Bio-sensing application for detecting	Equivalent interface charge (*10^{14} /m^2) [R13]		Sensitivity at x_u = 0.3, and x_l =0.1.	Sensitivity at x_u = 0.5, and x_l =0.1.
	Healthy limit	Diseased limit		
MIG	-2.42	4100	36.2 mA/(ng/ml)	39.1 mA/(ng/ml)
c-erbB-2	-0.63	-2.05	29.5 mA/(mm/mgL)	31.5 mA/(mm/mgL)
PSA	-2.65	26.5	32.5 mA/(μg/l)	337 mA/(μg/l)
KIM-I	-0.72	5.06	33.6 mA/(ng/ml)	34.8 mA/(ng/ml)

Table 4.3: Comparison of the sensitivity data with the double channel HEMTs used for other sensing applications [241].

In conclusion, the study analyzes the impact of inter-channel coupling in $Al_xGa_{(1-x)}N$ /GaN Double Channel HEMT on C-ERB2 sensing applications and its dependence on mole fraction through calibrated simulation. The intricate interdependence between both channels is established, influencing the quantum well barrier height, well depth, and 2DEG density. Increasing mole fractions result in a rapid charge density decline with vertical distance, ensuring superior carrier confinement within the quantum wells. The reduction in drive current in the presence of biomarkers is evident, and the sensitivity analysis with Al content variation highlights the potential sensitivity achievable from DCHEMT in C-ERB2 detection.

An increase in Al composition at the upper layer leads to enhanced sensitivity, while an increase in Al composition at the lower layer diminishes sensitivity due to higher negative polarization within the GaN channel. The sensor holds significant potential in real-world applications for early cancer diagnosis with high sensitivity. It can monitor disease progression by analyzing the levels

of C-ERB2 over time. This provides valuable information on the effectiveness of treatments and the progression of the disease to personalized medicine. However, the practical challenges in deploying the biosensors in clinical settings include ensuring device stability, sensitivity, and specificity. Assessing the impact of material compositions, device dimensions, and doping concentrations on performance and optimizing these parameters can lead to further improvements. Additionally, the use of DCHEMTs in various sensing applications under different environmental conditions, experimental validation, and 3D simulation models can be explored to capture the complex inter-channel dynamics and electrostatics in greater detail.

4.5. Conclusion and Future Work

In this chapter, we have explored the application of the Density Gradient (DG) or Quantum Moments Model in High-Electron-Mobility Transistors (HEMTs) for biosensing, specifically in the context of AlGaN/GaN Double Channel HEMTs (DC-HEMTs). By studying the deep inter-channel coupling within the AlGaN/GaN structure, we have developed a better understanding of the quantum mechanical interactions that influence the device's sensitivity and performance in biosensing applications.

The coupling of the two channels in the AlGaN/GaN HEMT structure was found to play a significant role in enhancing the sensitivity and the response of the device to external stimuli, such as biomolecular interactions. The application of the DG model provided a deeper insight into the behavior of the 2DEG (Two-Dimensional Electron Gas) under varying conditions, elucidating how the channel characteristics are altered upon the binding of target molecules. The model demonstrated that the coupled channels offer a robust platform for improving the selectivity and sensitivity of biosensors, particularly in the detection of complex biomarkers such as C-ERB2 proteins. The simulation and analysis of the device behavior through the DG model have shown how quantum effects, including the electron density modulation, affect the biosensing performance. Moreover, the incorporation of quantum corrections and the analysis of the DG method have proven to be crucial for the design of more efficient and precise biosensing devices. The use of this advanced modeling technique has revealed the potential of HEMTs to operate with improved performance in environments with low signal-to-noise ratios and complex biomolecular

interactions. In the specific application of C-ERB2 biomarker sensing, the DG model's approach allowed us to model the binding interactions in real-time, providing significant insights into the performance of AlGaN/GaN DC-HEMTs. This makes the study of DG a powerful tool in biosensing, especially for high-sensitivity applications where the detection of minuscule molecular interactions is required.

While this study has provided valuable insights into the use of the Density Gradient (DG) model for AlGaN/GaN HEMT biosensors, several areas remain open for further exploration:

: Future work can focus on developing advanced surface modification techniques to enhance receptor binding, reduce non-specific adsorption, and expand detection to multiple biomarkers beyond C-ERB2.

Further optimization of channel geometries, doping levels, and heterostructures can maximize inter-channel coupling, improving sensitivity and overall device performance.

Incorporating quantum mechanical principles, particularly in ultra-nanoscale regimes, can enhance sensitivity and reduce noise, enabling the development of next-generation quantum-based biosensors.

Development of multi-channel or array-based HEMTs can enable simultaneous detection of multiple biomarkers, improving throughput and diagnostic efficiency.

Combining HEMTs with microfluidics can allow real-time, portable, and highly sensitive detection for applications in personalized medicine and environmental monitoring.

In conclusion, the application of the DG model in AlGaN/GaN Double Channel HEMTs has shown strong potential for highly sensitive and selective biosensing. Addressing challenges in surface functionalization, channel design, quantum integration, and system-level incorporation can pave the way for next-generation biosensors with unprecedented sensitivity, accuracy, and real-world applicability.

Chapter 5:

Analytical and BQP (Bohm Quamtm Potential) based Quantum Analysis of Tunnel Field-Effect Transistors

5.1. *Introduction to TFETs*

5.2. *Quantum Effects in TFETs*

5.3. *Quantum Analytical Modeling of Very Low-Dimensional Dual Metal Double Gate TFET*

5.4. *Impact of Bohm Quantum Potential on SiGe-Based Heterojunction Tunnel FET Biosensors: Modeling and Comparative Analysis*

5.5. *Conclusion and Future Work*

5.1. Introduction to Tunnel Field-Effect Transistors (TFETs)

Tunnel Field-Effect Transistors (TFETs) represent a promising class of next-generation semiconductor devices that exploit quantum tunneling for charge transport, distinguishing them from traditional Metal-Oxide-Semiconductor Field-Effect Transistors (MOSFETs). The fundamental advantage of TFETs lies in their ability to achieve steep subthreshold slopes, a feature that theoretically enables them to operate with significantly reduced power consumption compared to conventional MOSFETs. This makes them highly suitable for applications in areas such as ultra-low

power electronics, IoT devices, and even wearable technologies, where power efficiency is a critical factor [242], [243], [244].

In order to understand the significance of TFETs, it is important to first revisit the operation of traditional MOSFETs. In a MOSFET, current conduction occurs via thermal excitation, where charge carriers (electrons or holes) gain enough energy to overcome the energy barrier at the source-channel junction and flow through the channel. However, as device dimensions shrink to the nanoscale, traditional MOSFETs encounter a phenomenon known as the *short-channel effect*, where control over the channel current by the gate becomes increasingly less effective, leading to high subthreshold slopes and increased leakage currents at low voltages. This not only limits the performance of MOSFETs but also hinders their ability to meet the power and performance requirements of modern electronic systems [245], [246], [247], [248].

The advent of TFETs, with their quantum tunneling-based operation, provides a potential solution to these challenges. In a TFET, the current conduction is governed by the band-to-band tunneling (BTBT) mechanism, in which charge carriers pass through a potential barrier even though they do not possess the requisite thermal energy to surmount the barrier classically [249], [250]. This quantum effect is a direct consequence of the wave-like nature of electrons at the nanoscale and is most noticeable in semiconductors with a significant bandgap, such as silicon and germanium, where the tunneling process can be controlled through gate voltage modulation.

A typical TFET consists of a source, a drain, a gate, and a channel. The source region is heavily doped to create a large concentration of charge carriers, while the channel, which is usually undoped or lightly doped, lies between the source and drain. The gate electrode is placed on top of the channel and modulates the energy alignment between the source and the channel. Under the influence of a gate voltage, the potential energy profile in the channel is altered, and for sufficiently large gate voltages, electrons (or holes, depending on the type of TFET) can tunnel from the source to the channel, enabling current conduction.

One of the most significant features of TFETs is their *steep subthreshold slope*—the rate at which the current increases as the gate voltage exceeds the threshold voltage [251], [252], [253]. In an ideal MOSFET, the subthreshold slope is 60 mV/decade at room temperature, meaning that for

every 60 mV increase in gate voltage, the current increases by a factor of ten. This steepness limit is dictated by the thermionic emission process and represents a theoretical lower bound for subthreshold behavior in classical devices. In contrast, TFETs can, in theory, achieve a subthreshold slope as low as 30 mV/decade or even below, depending on the material and device structure, providing a significant advantage in low-power operation.

The ability of TFETs to achieve such low subthreshold slopes is due to the quantum tunneling phenomenon, which allows for current conduction even at very small gate voltages. As a result, TFETs exhibit reduced power dissipation compared to conventional MOSFETs, making them highly attractive for low-power digital circuits, memory devices, and analog applications. Moreover, the inherent scalability of TFETs, particularly in their ability to maintain a low subthreshold slope as device dimensions are reduced, ensures that they can continue to perform effectively at the nanoscale, addressing some of the limitations of MOSFETs as transistor sizes shrink.

Despite their advantages, TFETs face several challenges that must be addressed before they can be fully realized in commercial applications. One of the primary hurdles is the lower *drive current* of TFETs compared to MOSFETs [254]. While TFETs offer steep subthreshold slopes, the tunneling current is inherently lower than the thermionic current in MOSFETs. This can limit the switching speed and overall performance of TFETs, particularly in high-frequency applications. Researchers are exploring various ways to enhance the drive current, such as optimizing the doping concentration in the source region, engineering the bandgap of the material used in the channel, and developing novel TFET architectures that can improve carrier transport efficiency.

Another challenge is the *temperature sensitivity* of TFETs [255]. The tunneling process is highly dependent on the electric field and the alignment of energy bands in the device, which can fluctuate with changes in temperature. This makes TFETs more susceptible to performance degradation at high temperatures compared to MOSFETs. To mitigate this issue, advancements in material science, such as the development of novel high-k dielectrics and low-temperature processing techniques, are being investigated.

Furthermore, while TFETs exhibit reduced leakage currents and lower power consumption in the subthreshold region, their *on-state performance* (when the device is fully switched on) is often not as competitive as that of MOSFETs [256]. As a result, TFETs may need to be hybridized with MOSFETs or incorporated into complementary logic circuits to achieve optimal performance across both the on- and off-states. Researchers are actively exploring new device structures, such as *heterojunction TFETs* and *vertical TFETs*, to improve the on-state current while maintaining the low power dissipation characteristic of TFETs in the subthreshold regime [257], [258].

In addition to the traditional silicon-based TFETs, alternative materials such as germanium, III-V compounds (e.g., GaAs, InAs) [259], [260], [261], and two-dimensional (2D) materials [262] , [263] are being considered to overcome some of the limitations of conventional semiconductor materials. These materials offer superior carrier mobility and can enable faster tunneling processes, potentially leading to TFETs with improved drive currents and reduced temperature sensitivity. 2D materials, in particular, hold great promise for TFETs due to their excellent electrical properties and the ability to engineer their bandgap through structural modifications.

The *Bohm Quantum Potential (BQP)* approach is one of the quantum mechanical tools that has been used to gain deeper insights into the behavior of TFETs, [264]. The BQP is derived from the quantum hydrodynamic equations and allows for the inclusion of quantum effects that influence carrier transport, such as wave-particle duality and interference phenomena. This potential helps in modeling quantum tunneling processes more accurately than classical approaches, offering a more precise description of charge transport in TFETs at the nanoscale. By applying the BQP model, researchers can gain a better understanding of the role of quantum mechanics in TFET operation and design more efficient devices that harness these effects.

The study of TFETs using quantum mechanical approaches like BQP is crucial for advancing the development of these devices, as it provides a more detailed and accurate representation of their behavior. The insights gained from such studies can guide the optimization of TFET parameters, leading to the realization of high-performance, low-power devices suitable for the demands of modern electronics. In the following sections, we will delve deeper into the quantum mechanical

modeling of TFETs using the BQP approach, exploring the key factors that govern their performance and how they can be optimized for future applications.

5.2. Quantum Effects in TFETs

In the context of the chapter, i.e., *Bohm Quantum Potential (BQP) based Quantum Analysis of Tunnel Field-Effect Transistors (TFETs)*, the study of quantum transport phenomena—such as band-to-band tunneling, subband quantization, and confinement-induced energy modulation—forms the physical foundation for the inclusion of the BQP model. As TFETs scale to sub-20 nm dimensions, classical electrostatics fail to capture carrier behavior accurately due to the emergence of discrete energy states and wavefunction interference along the channel. In advanced architectures like dual-metal double-gate TFETs, the formation of quantum wells and tunneling barriers under gate regions introduces strong confinement and alters the transmission probabilities of charge carriers. Full quantum modeling using self-consistent Schrödinger–Poisson equations and Landauer-based transport analysis provides a rigorous description of these effects but at a high computational cost.

Tunnel Field-Effect Transistors (TFETs) operate based on quantum mechanical effects, primarily quantum tunneling, which distinguishes them from traditional MOSFETs [265], [266], [267], [268]. While classical devices depend on thermionic emission for charge transport, TFETs utilize quantum tunneling to facilitate current conduction even when the gate voltage is below the threshold voltage. The incorporation of quantum effects is critical in understanding the behavior and performance of TFETs, especially as the device dimensions shrink to the nanoscale. This section explores the significant quantum effects in TFETs, including band-to-band tunneling, quantum confinement, and subband quantization, focusing on their role in TFETs, particularly in advanced structures like dual metal double gate TFETs.

The most dominant quantum effect in TFETs is band-to-band tunneling (BTBT), a quantum mechanical phenomenon where charge carriers (electrons or holes) tunnel from the valence band in the source region to the conduction band in the channel region. This occurs because, at the

nanoscale, the carriers behave as quantum wavefunctions, which can penetrate through potential barriers even when they lack the classical energy required to overcome them [269].

Quantum confinement becomes particularly significant as the device dimensions shrink to the nanoscale. In conventional TFETs, carriers are confined within the channel, and their motion is restricted in the direction perpendicular to the channel. This confinement alters the density of states (DOS) and the energy spectrum of the device, leading to changes in the tunneling characteristics. As the channel length and width are reduced, the energy levels of the carriers become quantized, and the behavior of the carriers is no longer described by classical physics but by quantum mechanics.

In TFETs, quantum confinement can affect both the transverse (across the channel thickness) and longitudinal (along the channel length) directions. In the transverse direction, the reduction in channel thickness leads to discrete subband energy levels that influence the tunneling current. In the longitudinal direction, the length of the channel also plays a critical role, as the confinement in this direction can affect the electron wavefunctions and modify the tunneling probability. The interplay between these two types of confinement is crucial for the device's performance, especially in advanced TFET structures like dual metal double gate TFETs.

The literature on quantum confinement effects in tunnel field-effect transistors (TFETs) has evolved significantly over the years, addressing various aspects of device performance and modeling. Vandenberghe et al. (2011) explored the impact of field-induced quantum confinement on tunneling currents and subthreshold behavior in silicon TFETs [270]. Padilla et al. (2012) presented a simplified approach to integrating quantum confinement effects (QCEs) into TCAD simulations, emphasizing double-gate TFETs [271]. In 2013, the same group extended their work, analyzing the influence of QCEs on band-to-band tunneling (BTBT) and gate threshold voltages. Walke et al. (2013) examined the onset voltage shifts caused by field-induced quantum confinement in n-type line TFETs [272]. Smets et al. (2014) provided experimental validation of delayed onset tunneling behavior due to quantum confinement effects [273]. More recently, Najam et al. (2019) investigated BTBT in L-shaped TFETs under the influence of QCEs [274], while Thai et al. (2025) proposed a practical methodology for studying QCEs' impact on TFET electrical

characteristics, highlighting their dependence on body thickness [268]. Collectively, these studies underscore the critical role of quantum confinement in optimizing TFET design and performance.

In addition to confinement along the thickness, quantum effects also influence the electron wavefunctions along the length of the channel. This form of confinement becomes important in devices with very short channel lengths. In such devices, the wavefunction of the carriers is spread across the channel length, leading to discrete energy levels that influence the current conduction. Here, the BQP formalism effectively captures such confinement-induced potential variations by introducing a quantum correction term derived from the curvature of carrier density, thereby serving as a computationally tractable bridge between fully quantum mechanical and drift–diffusion-based device models.

The next section is device-oriented, focusing on the fundamental analytical modeling of quantum effects in advanced TFET architectures through self-consistent Schrödinger–Poisson-based formulations, highlighting confinement-induced quantization, tunneling dynamics, and electrostatic control. The later section transitions toward an application-oriented study, employing the BQP framework to analyze strain-engineered SiGe heterojunction TFETs for biosensing applications, emphasizing the role of quantum potential, strain coupling, and material composition on sensitivity and selectivity. Together, these sections bridge the gap between fundamental quantum transport theory and its practical implementation in nanoscale sensing devices.

5.3. Quantum Analytical Modeling of Very Low-Dimensional Dual Metal Double Gate TFET

Quantum effects in TFETs, such as band-to-band tunneling, quantum confinement, and subband quantization, play a pivotal role in determining the performance of these devices. As the channel dimensions shrink, the quantum behavior of the carriers becomes more pronounced, leading to the formation of discrete energy levels that influence the tunneling process. Advanced TFET structures, such as dual metal double gate TFETs, offer further control over the tunneling

characteristics by manipulating the potential well and barrier under the gates. These quantum effects enable TFETs to achieve superior subthreshold performance and low-power operation, making them promising candidates for future electronic devices. However, the trade-off between steep subthreshold slopes and on-current remains a challenge that requires ongoing optimization and innovation in device design.

In advanced TFET structures such as dual metal double gate TFETs, where the potential well is created under the first gate and the potential barrier is created under the second gate, this confinement along the length of the channel becomes particularly relevant. The quantum well under the first gate enhances the tunneling probability by lowering the energy barrier for electrons in the channel. Meanwhile, the potential barrier created by the second gate modifies the tunneling characteristics by controlling the alignment of the energy bands and the confinement of the carriers.

We present a novel and comprehensive quantum analytical modeling of a sub-20 nm Dual Metal Double Gate (DMDG) Tunnel Field Effect Transistor (TFET) for the first time in literature. Owing to structural confinement at sub-20 nm regime, the energy states at channel are quantized and carrier propagation is regulated by quantum transport. We address such quantization aspects (viz. subband quantization, bandgap shifting, tunneling through barrier etc.) and incorporate them in analytical modeling using self-consistent solution of Schrödinger-Poisson's equation. As a result of work function difference at gate, we observe creation of quantum well, followed by a tunneling barrier, along the channel. Energy states in the quantum well are derived from Schrodinger equation, whereas, transmission coefficients are derived for each tunneling barrier. Finally, current density is obtained using 'Landauer formula for quantum transport'. We methodically study the effects of structural confinement on device performances and observe significant shift from classical counterpart. Moreover, we note that quantization in DMDG TFET can be optimized that will lead to superior device performance. The results are verified with simulation data in each occasion to substantiate analytical models.

Device Structure

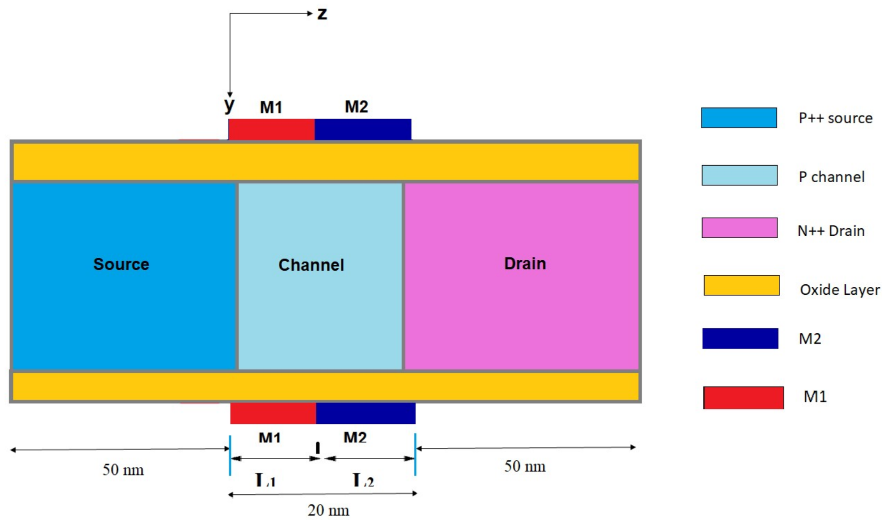

Fig. 5.1. Device structure of the Dual Material Double Gate tunnel FET.

The Dual Material Double Gate TFET structure (as deployed for analytical modeling) is depicted in figure 5.1. The front gate is divided in 2 parts viz. M_1 and M_2 of length L_1 and L_2 respectively. The back gate is also a dual material gate consisting M_1 and M_2 of length L_1 and L_2 respectively, where, total gate length (i.e., L_1+L_2) is taken to be ≤20nm throughout the model. Work function of M_1 (ϕ_{M1}) is kept lower than Work function of M_2 (ϕ_{M2}) (i.e., $\phi_{M1} < \phi_{M2}$) such that a potential barrier could be formed near drain end of the channel to reduce ambipolarity . The channel is uniformly doped and effects of fixed oxide charges are not considered. The typical parameter values used in the model are listed below

TABLE 5.1

TYPICAL PARAMETER VALUES

Parameter	Value
Front Gate Oxide thickness (t_{oxf})	1 nm
Back Gate Oxide thickness (t_{oxb})	1 nm
Film thickness (t_{si})	5 nm
Channel Doping Concentration(N_{Ch})	$2x10^{15}$ cm^{-3}
Source Doping Concentration (N_A)	$5x10^{21}$ cm^{-3}
Drain Doping Concentration (N_D)	$5x10^{21}$ cm^{-3}

Analytical Models

A. Surface Potential and Electric Field

To find the quantized energy states in the channel, Poisson and Schrödinger equations must be solved self consistently. The 2-D Poisson equation is given by

$$\frac{\partial^2\varphi(\mathrm{y,z})}{\partial y^2}+\frac{\partial^2\varphi(\mathrm{y,z})}{\partial z^2}=\frac{qN_{Ch}}{\varepsilon_{Si}} \tag{5.1}$$

Where, $\varphi(\mathrm{y,z})=\varphi_S(\mathrm{z})+P_1(\mathrm{z})y+P_2(\mathrm{z})y^2$ (5.2)

φ *(y, z)* is the 2-D potential profile in the channel given by K.K. Young [275] N_{Ch} is uniform channel concentration, ε_{Si} is dielectric constant of silicon, $\varphi_S(z)$ is the surface potential along length; P_1, P_2 are z-dependent coefficient.

The front gate consists of two metals (M_1 and M_2) for regions 0< z < L_1 and L_1 < z < L_2 respectively. Thus, the surface potentials for regions 0< z < L_1 and L_1 < z < L_2 are denoted as $\varphi_{S1}(z)$ and $\varphi_{S2}(z)$ respectively and expressed as :

$$\begin{aligned}\varphi_1(\mathrm{y,z})&=\varphi_{S1}(\mathrm{z})+P_{11}(\mathrm{z})y+P_{12}(\mathrm{z})y^2 \text{ for } 0\le z\le L_1, 0\le y\le t_{Si}\\ \varphi_2(\mathrm{y,z})&=\varphi_{S2}(\mathrm{z})+P_{21}(\mathrm{z})y+P_{22}(\mathrm{z})y^2 \text{ for } L_1\le z\le L, 0\le y\le t_{Si}\end{aligned} \tag{5.3}$$

All the arbitrary coefficients (P_{11}, P_{12}, P_{21}, P_{22}) are unknown variables and their values can be obtained by applying the boundary conditions for front gate and back gate. When all the coefficients are substituted in (5.2), we get

$$\begin{aligned}\frac{d^2\varphi_{S1}(\mathrm{z})}{dz^2}-\alpha\varphi_{S1}(\mathrm{z})&=\beta_1\\ \frac{d^2\varphi_{S2}(\mathrm{z})}{dz^2}-\alpha\varphi_{S2}(\mathrm{z})&=\beta_2\end{aligned} \tag{5.4}$$

Where,

$$\alpha=2\left[1+\frac{C_{oxf}}{C_{Si}}+\frac{C_{oxf}}{C_{oxb}}\right]\Big/t_{Si}^2\left(1+\frac{2C_{Si}}{C_{oxb}}\right),$$

$$\beta_1=\frac{qN_{Ch}}{\varepsilon_{Si}}-2V_{G1}^{'}\left[\frac{C_{oxf}}{C_{oxb}}+\frac{C_{oxf}}{C_{Si}}+1\right]\Big/t_{Si}^2\left(1+\frac{2C_{Si}}{C_{oxb}}\right),$$

$$\beta_2=\frac{qN_{Ch}}{\varepsilon_{Si}}-2V_{G2}^{'}\left[\frac{C_{oxf}}{C_{oxb}}+\frac{C_{oxf}}{C_{Si}}+1\right]\Big/t_{Si}^2\left(1+\frac{2C_{Si}}{C_{oxb}}\right),$$

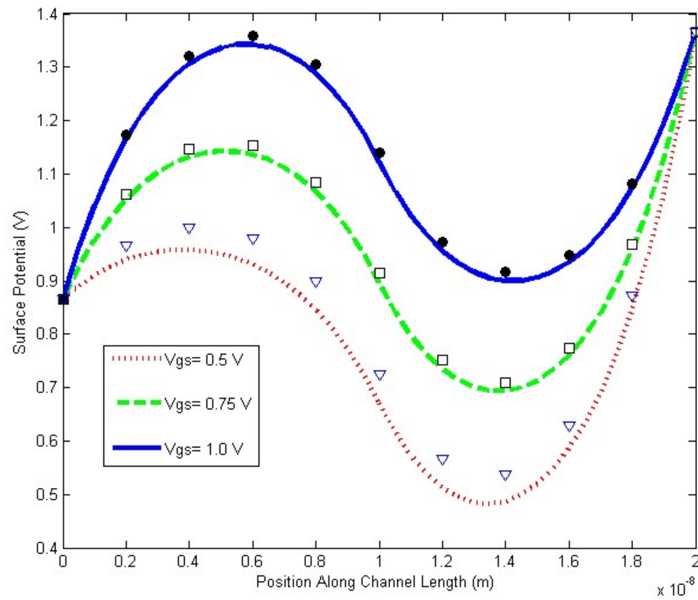

Fig. 5.2. Surface potential profile along the channel with Vds = 0.5 V and varying Vgs.= 0.5V, 0.7V and 1.0V. Symbols: Simulation values from ATLAS.

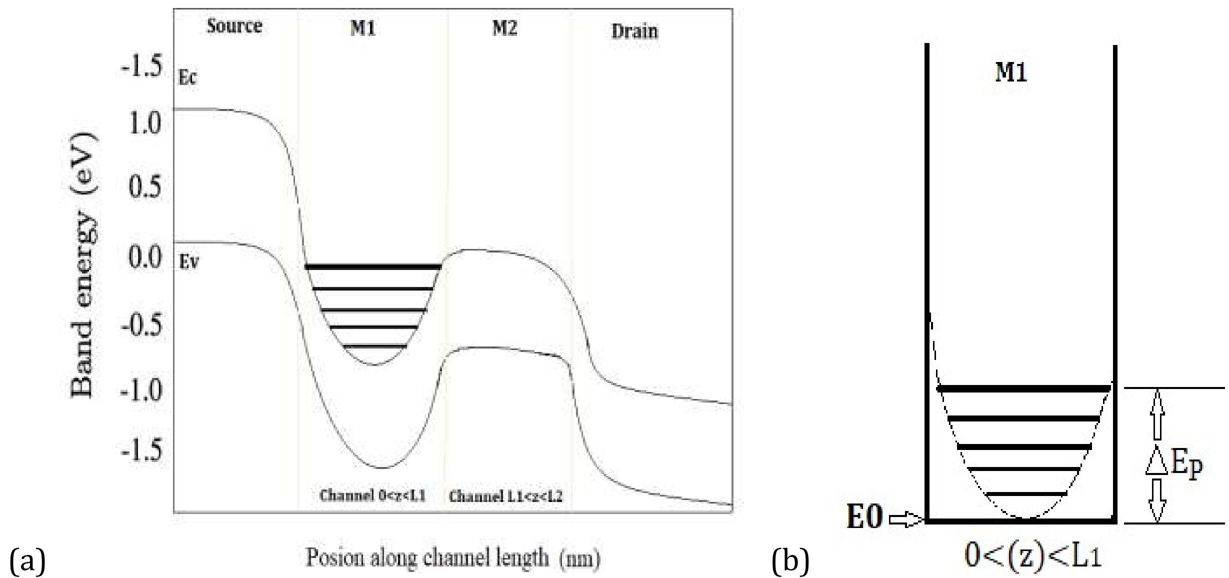

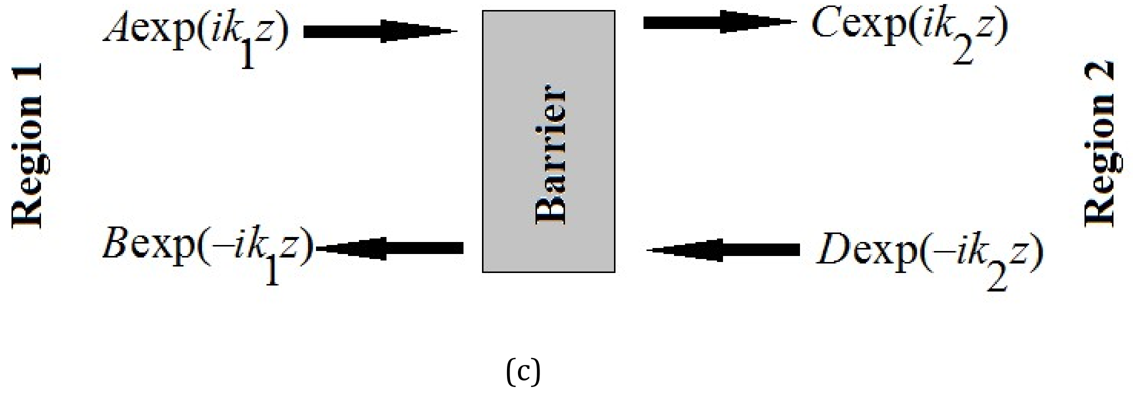

(c)

Fig. 5.3. (a) Formation of potential well and potential barrier along the channel at on state (b) Approximated rectangular potential well under M_1 with perturbation. (c) Quantum transport of electron from region1(channel $0<z<L_1$) to region2(drain) through potential barrier (channel $L_1 < z < L_2$).

$$C_{oxf} = \varepsilon_{oxf}/t_{oxf}, \; C_{Si} = \varepsilon_{Si}/t_{Si}, \; C_{oxb} = \varepsilon_{oxb}/t_{oxb},$$

$$V'_{G1} = V_{gs} - V_{FB1}, \; V_{FB1}/q = \phi_{M1} - \left[\chi + E_g/2q + kT/q \ln\left(N_{Ch}/n_i\right)\right],$$

$$V'_{G2} = V_{gs} - V_{FB2}, \; V_{FB2}/q = \phi_{M2} - \left[\chi + E_g/2q + kT/q \ln\left(N_{Ch}/n_i\right)\right].$$

C_{oxf}, C_{oxb}, and C_{Si} are respectively front gate, back gate and channel capacitances with dielectric constants ε_{oxf}, ε_{oxb} and ε_{Si}. Vgs is gate to source voltage, V_{FB1} and V_{FB2} are flat band voltages as expressed above. χ is the Si affinity, E_g is Si bandgap and n_i is the intrinsic concentration of Si.

Thus, solving (5.4), the surface potentials $\varphi_{S1}(z)$ and $\varphi_{S2}(z)$, for regions $0< z < L_1$ and $L_1 < z < L_2$, are found as

$$\varphi_{S1}(\mathrm{z}) = ae^{\eta z} + be^{-\eta z} - \frac{\beta_1}{\alpha}$$
$$\varphi_{S2}(\mathrm{z}) = ce^{\eta(z-L_1)} + de^{-\eta(z-L_1)} - \frac{\beta_2}{\alpha} \tag{5.5}$$

Where,

$$a=\begin{bmatrix}\left(V_{bi}+V_{ds}+\sigma_2\right)-\left(V_{bi}+\sigma_1\right)e^{-\eta L}\\+\left(\sigma_1-\sigma_2\right)\cosh\left(\eta L_2\right)\left\{\dfrac{e^{-\eta L}}{1-e^{-2\eta L}}\right\}\end{bmatrix},b=\begin{bmatrix}\dfrac{\left(V_{bi}+\sigma_1\right)-\left(V_{bi}+V_{ds}+\sigma_2\right)e^{-\eta L}}{1-e^{-2\eta L}}\\-\dfrac{\left(\sigma_1-\sigma_2\right)\cosh\left(\eta L_2\right)e^{-\eta L}}{1-e^{-2\eta L}}\end{bmatrix},$$

$$c=ae^{\eta L_1}-\frac{\left(\sigma_1-\sigma_2\right)}{2},d=be^{-\eta L_1}-\frac{\left(\sigma_1-\sigma_2\right)}{2},\sigma_1=\frac{\beta_1}{\alpha},\sigma_2=\frac{\beta_2}{\alpha},\eta=\sqrt{\alpha},$$

From (5.5), we find the complete nature of the potential profile as plotted in figure 5.2. As $\phi_{M1} < \phi_{M2}$, the difference results formation of two distinguished region along the channel. The plot forms the base of analytical modelling towards derivation of electric field, potential well-barrier, tunneling coefficient & current density.

The corresponding electric fields for regions $0 < z < L_1$ and $L_1 < z < L_2$ can be derived from (5.5) as

$$F_{S1}(\mathrm{z})=-\left\{a\eta e^{\eta z}-b\eta e^{-\eta z}\right\}$$
$$F_{S2}(\mathrm{z})=-\left\{c\eta\left(z-L_1\right)e^{\eta(z-L_1)}-d\eta\left(z-L_1\right)e^{-\eta(z-L_1)}\right\} \tag{5.6}$$

Now, the energy bands along the channel are shifted according to surface potentials by an amount ($\Delta E(z)$) as follows

$$\Delta E(z)|_{\varphi_{S1}(\mathrm{z})}=-kT\ln\left(\frac{p_{\varphi_{S1}(\mathrm{z})}}{n_i}\right) \text{for region } 0<z<L_1$$
$$\Delta E(z)|_{\varphi_{S2}(\mathrm{z})}=-kT\ln\left(\frac{p_{\varphi_{S2}(\mathrm{z})}}{n_i}\right) \text{for region } L_1<z<L_2 \tag{5.7}$$

$$p_{\varphi_{S1}(\mathrm{z})}=n_i\exp\left[{q\left(\varphi_i-\varphi_{S1}(\mathrm{z})\right)}/{kT}\right],p_{\varphi_{S2}(\mathrm{z})}=n_i\exp\left[{q\left(\varphi_i-\varphi_{S2}(\mathrm{z})\right)}/{kT}\right]$$

$p_{\phi_{S1}(\mathrm{z})}$ and $p_{\phi 2(\mathrm{z})}$ denote effective surface carrier concentration corresponding to potential $\varphi_{S1}(\mathrm{z})$ and $\varphi_{S2}(\mathrm{z})$. φ_i is the surface potential for the condition $\phi_{M1}=\phi_{M2}$ (also obtained from 5).

We find that rise of surface potential at $0 < z < L_1$ pushes the energy bands down, whereas, drop in surface potential at $L_1 < z < L_2$ uplifts the energy bands. Successive decrease and increase of energy bands along the channel creates a well at $0 < z < L_1$ and a barrier at $L_1 < z < L_2$ (figure 5.3(a)).

Now, width of the well (at $0 < z < L_1$) being sub-10nm, it is subjected to quantum/structural confinement and available energy states are quantized into subbands. While, the barrier at $L_1 < z <$

L_2, also being sub-10 nm, becomes thin enough to allow tunneling through it. The comprehensive effect is that, an electron tunnels from source to permissible subbands of quantum well then again tunnels through the quantum barrier to reach the drain. The corresponding energy states at quantum well and tunneling coefficient at quantum barrier are derived in next section.

B. Energy States in quantum well

To observe device characteristics in presence of quantization, we need to determine permissible energy states in the quantum well which an electron can acquire during propagation through the channel. The well formed in the region $0<z<L_1$ is approximated to be rectangular in nature for analytical modeling with height V_0 [determined from (5.5) and (5.7)] and energy states E_q^i. The schematic of band diagram of the device is depicted in figure 5.3(a) and 5.3(b) along the plane parallel to direction of tunneling. The height V_0 is calculated at $z=L_1$ (i.e., at edge of quantum well) as

$$V_0 = \left[\Delta E(z)|_{\varphi_{S2}(z)}\right]_{Z=L_1} - \left[\Delta E(z)|_{\varphi_{S1}(z)}\right]_{Z=L_1} \quad (5.8)$$

With these approximations, we rewrite the Schrödinger equation for the approximated potential well with height V_0 and discretized energies E_q^i as

$$-\frac{\hbar^2}{2m^*}\frac{\partial^2\psi}{\partial z^2} - V_0\psi_i = E_q^i\psi_i \quad (5.9)$$

By employing effective mass approximation, we have taken into account all six <100> oriented silicon conduction band valleys, out of which four are transverse and two are longitudinal in nature. Effective masses of all these six valleys are incorporated in the temperature-dependent electron 'density-of-states effective mass' $m^*=1.08m_e$.

$m_{e,dos}^* = (m_l\, m_t\, m_t)^{1/3} = (6)^{2/3}\ (0.89 \times 0.19 \times 0.19)^{1/3}\ m_0 = 1.08\ m_0$.

Ψ_i, the wave function associated with i^{th} energy level. The allowed energy states E_q^i for transmission through shallow-narrow quantum well are given by

$$E_q^i = E_0 + \frac{\hbar^2\pi^2 i^2}{2qm^* L_1^2} - V_0 \quad (5.10)$$

E_0 is the bottom of conduction band of Si at $0<z<L_1$ at 300K obtained from literature

Now, for the changing nature of surface potential with external voltages, we need to add 1st order perturbation (ΔE_P) which is dependent on bias conditions and position(z). Thus, effective

energy states ($E_q^{\sim i}$) become

$$E_q^{\sim i} = E_q^i + \Delta E_P \text{ (i=1,2,3...n, number of subbands)} \tag{5.11}$$

$\Delta E_P = <\Psi_i^*|H|\Psi_i>$, where, $H=-q(C_{11}z+C_{12}z^2)$ is the perturbation Hamiltonian operator, Ψ_i^* is the complex conjugate of Ψ_i, calculated from (5.9). Thus, we get

$$\begin{aligned} E_q^{\sim i} &= E_0 + \frac{\hbar^2 \pi^2 i^2}{2qm^* L_1^2} - V_0 + \Delta E_P \\ &= E_0 + \frac{\hbar^2 \pi^2 i^2}{2qm^* L_1^2} - \left\{ \left[\Delta E(z)|_{\varphi_{S2}(z)} \right]_{Z=L_1} - \left[\Delta E(z)|_{\varphi_{S1}(z)} \right]_{Z=L_1} \right\} \\ &\quad + \left[< \Psi_i^* \left| q\left(C_{11} y + C_{12} y^2 \right) \right| \Psi_i > \right] \end{aligned} \tag{5.12}$$

In addition to the energy quantization, the charge density also undergoes quantum mechanical shifts from their classical counterpart. Due to confinement along the length, the charge density resembles step like 2DEG model instead of continuous 3D/classical model. The density of electrons in a 2D subband starting at $E_q^{\sim i}$ is given by

$$\begin{aligned} n^j{}_{2D}(E_q^{\sim i} - E) &= \frac{m^*}{\pi \hbar^2} \int_{Ej}^{\infty} f(E, E_q^{\sim i}) dE \\ &= \frac{m^* kT}{\pi \hbar^2} \ln \left[1 + \exp\left(\frac{E_q^{\sim i} - E}{kT} \right) \right] \end{aligned} \tag{5.13}$$

B. Quantum Transport Though Barriers

In our model, the electrons (bearing the properties of wave) need to impinge from source to quantum well ($0<z<L_1$) and then pass through the tunneling barrier ($L_1 < z < L_2$) towards the drain to generate effective drain current. Thus, we observe two tunneling probability coefficient $T_1(E)$ (source to channel) and $T_2(E)$ (channel to drain).

Firstly, when an electrons tunnels from source to potential well, we consider the tunneling probability [$T_1(E)$] identical to the tunneling probability through a delta barrier

$$T_1(\mathrm{E}) = \left(1 + \frac{mS^2}{2\hbar^2 E} \right) \tag{5.14}$$

S is a specified constant for delta barrier equal to barrier's width-height product [$S=WV_0$]. Here, the width ('W') is the minimum tunnel path and height (V_0) is expressed in (5.8). Secondly, due to the formation of tunneling barrier in channel under M_2 [as depicted in figure 5.3], the charge carriers are confronted to a filtering wall which helps to reduce the ambipolar transport. To find

the tunneling probability coefficient $T_2(E)$(channel to drain), a 1-D transmission model (as depicted below) is considered (figure 5.4) with suitable boundary conditions.

In the system depicted at figure 5.3(c), the incoming and outgoing waves in both sides of the potential barrier are expressed using Schrödinger equation as

$$\Psi_{12}(z) = \begin{Bmatrix} A\exp(ik_1 z) + B\exp(-ik_1 z) \\ C\exp(ik_2 z) + D\exp(-ik_2 z) \end{Bmatrix}, \quad (5.15)$$

$$k_1^2 = 2m^* E/\hbar^2, \; k_2^2 = 2m^*(E - V_0)/\hbar^2$$

A, B, C, D are transmission constants, k_1, k_2 are wave numbers in region 1 and 2 respectively, m* is effective mass, E is energy of penetrating electron, V_0 is barrier height from (5.8).

We concentrate on the flux transmission coefficient which is best expressed in terms of transfer or T-matrix as

$$\begin{pmatrix} C \\ D \end{pmatrix} = T_2(k)\begin{pmatrix} A \\ B \end{pmatrix}, T_2(k) = T(k_2, k_1) = \frac{1}{2k_2}\begin{pmatrix} (k_2+k_1) & (k_2-k_1) \\ (k_2-k_1) & (k_2+k_1) \end{pmatrix}$$

After various multiplication and using boundary conditions, transmission flux coefficient $[T_2(E)]$ is defined as

$$T_2(k) = \left|t^2\right| = \frac{4k_1^2 k_2^2}{4k_1^2 k_2^2 + (k_1^2 + k_2^2)^2 \sinh^2 k_2 L_2}$$

Replacing values of k_1 and k_2

$$T_2(k) = \left[1 + \frac{V_0^2}{4E(V_0 - E)}\sinh^2 k_2 L_2\right]^{-1}$$

Now, considering $k_2 L_2$ is large and using (5.12), we get

$$T_2(E) \approx (16E/V_0)\exp(-2L_2\sqrt{2m(E - V_0)/\hbar^2}) \quad (5.16)$$

C. Current Density

In this section, the analytical model of current voltage relationship has been derived using generalized Landauer quantum transport theory. According to Landauer theory, the tunneling current density through a barrier is

$$J = \frac{e}{h}\int_{E_L}^{\infty}\left[n_{2D}(E_L - E)\right]T(E)dE \tag{5.17}$$

In general, $n_{2D}(E)$ is the charge density of electrons having energy E over a range of dE. E_L is topmost energy level at left side of the barrier. $T(E)$ is transmission coefficient through the barrier. For our model, tunneling occurs two times, (i) from source to quantum well created in channel at $0<z<L_1$ and (ii) from said quantum well to drain through potential barrier created at $L_1 < z < L_2$. Initially, the electrons tunnel from filled valanced band of source to permissible sub-bands of potential well (at $0<z<L_1$) crossing the tunneling barrier having transmission coefficient $T_1(E)$. Due to discrete nature of energy states in quantum well [vide (5.12)], current density takes a different form in comparison to classical model and is expressed by

$$J_1(E) = \frac{e}{h}\sum_{i=1,2,3\ldots n}\int_{E_{\mu L}}^{E_q^{\sim i}}\left[n_{2D}(E_{\mu L} - E)\right]T_1(E)dE \tag{5.18}$$

$E_{\mu L}$ indicates top of valance band at source at 300K obtained from literature , $E_q^{\sim i}$, $n_{2D}(E_{\mu L} - E)$, $T_1(E)$ are defined at (5.12), (5.13) and (5.14) respectively.

So, we have

$$J_1(E) = \frac{e}{h}\sum_{i=1,2,3\ldots n}\int_{E_{\mu L}}^{E_q^{\sim i}}\frac{m^* kT}{\pi\hbar^2}\ln\left[1+\exp\left(\frac{E_q^{\sim i} - E}{kT}\right)\right]\left(1+\frac{mS^2}{2\hbar^2 E}\right)dE \tag{5.19}$$

Due to positive bias at drain at on state, the tunneled electrons in quantum well instantly sweep through region $0<z<L_1$. Subsequently, they reach drain through potential barrier ($L_1 < z < L_2$) having tunneling coefficient $T_2(E)$ [vide (5.16)]. So the final current density can be written as

$$J = \int_{E_q^{\sim i}}^{E_{\mu R}} J_1(E)T_2(E)dE \tag{5.20}$$

$E_{\mu R}$ indicates bottom of conduction band at drain at 300K obtained from literature [271]. Substituting all variables, we get,

$$J = \sum_{i=1,2,3\ldots n} \int_{\tilde{E}_q^i}^{E_{\mu R}} J_1(E)(16E/V_0)\exp(-2L_2\sqrt{2m\left(E_q^{\sim i} - V_0\right)/\hbar^2})\,dE$$

$$= \sum_{i=1,2,3\ldots n} \int_{\tilde{E}_q^i}^{E_{\mu R}} \left\{ \begin{matrix} \left[\dfrac{e}{h} \int_{E_{\mu L}}^{\tilde{E}_q^i} \begin{matrix} \dfrac{m^* k_B T}{\pi \hbar^2}\left(1 + mS^2/2\hbar^2 E\right) \\ \ln\left[1 + \exp\left(\dfrac{E_{\mu L} - E}{k_B T}\right)\right] dE \end{matrix} \right] \\ (16E/V_0)\exp(-2L_2\sqrt{2m\left(E - V_0\right)/\hbar^2})\,dE \end{matrix} \right\} \quad (5.21)$$

$$= \frac{e}{h}(16/V_0)\frac{m^* k_B T}{\pi \hbar^2} \sum_{i=1,2,3\ldots n} \int_{\tilde{E}_q^i}^{E_{\mu R}} \left\{ \begin{matrix} \left[\int_{E_{\mu L}}^{\tilde{E}_q^i} \begin{matrix} \left[\ln(2) + \left(\dfrac{E_{\mu L} - E}{2k_B T}\right)\right] \\ \left(1 + mS^2/2\hbar^2 E\right) dE \end{matrix} \right] \\ \mathrm{E}\left[1 - 2L_2\sqrt{2m\left(E - V_0\right)/\hbar^2}\right] dE \end{matrix} \right\}$$

After expanding into Taylor series and necessary simplifications, we obtain the current density as written underneath in equation (5.19) which is computed over available energy values $E_q^{\sim i}$ (i=1,2,3…n).

$$J = \frac{16e}{hV_0}(J')\frac{m^* k_B T}{\pi\hbar^2} \sum_{i=1,2,3\ldots n} \left[\begin{matrix} \dfrac{1}{2}(\tilde{E}_q^i)^2 - \sqrt{2m/\hbar^2}\,2L_2 \\ \left\{ \dfrac{2}{5}\left(\tilde{E}_q^i - V_0\right)^{\frac{5}{2}} - \dfrac{2V_0}{3}\left(E_{\mu R} - V_0\right)^{\frac{3}{2}} \right\} \end{matrix} \right] \quad (5.22)$$

$$\text{where} \quad J' = \int_{E_{\mu L}}^{\tilde{E}_q^i} \left[\begin{matrix} \left\{ \ln(2) + \left(\dfrac{E_{\mu L}}{2k_B T}\right) - \left(\dfrac{mS^2}{2\hbar^2 2k_B T}\right) \right\} \\ -\dfrac{E}{2k_B T} + \dfrac{1}{E}\left\{ \dfrac{\ln(2) mS^2}{2\hbar^2} + \dfrac{E_{\mu L} mS^2}{2\hbar^2 2k_B T} \right\} \end{matrix} \right] dE$$

(5.23)

$$= \sum_{\substack{i=1,2,3... \\ number\ of \\ subbands}} \frac{\left[\begin{array}{l} \left\{ \ln(2) + \left(\dfrac{E_{\mu L}}{2k_B T} \right) - \left(\dfrac{mS^2}{2\hbar^2 2k_B T} \right) \right\} \tilde{E}_q^{\,i} \\ - \dfrac{\tilde{E}_q^{\,i\,2}}{4k_B T} + \ln(\tilde{E}_q^{\,i}) \left\{ \dfrac{\ln(2) mS^2}{2\hbar^2} + \dfrac{E_{\mu L} mS^2}{2\hbar^2 2k_B T} \right\} \end{array} \right] -}{\left[\begin{array}{l} \left\{ \ln(2) + \left(\dfrac{E_{\mu L}}{2k_B T} \right) - \left(\dfrac{mS^2}{2\hbar^2 2k_B T} \right) \right\} E_{\mu L} \\ - \dfrac{E_{\mu L}^{\,2}}{4k_B T} + \ln(E_{\mu L}) \left\{ \dfrac{\ln(2) mS^2}{2\hbar^2} + \dfrac{E_{\mu L} mS^2}{2\hbar^2 2k_B T} \right\} \end{array} \right]}$$

Result and Discussion

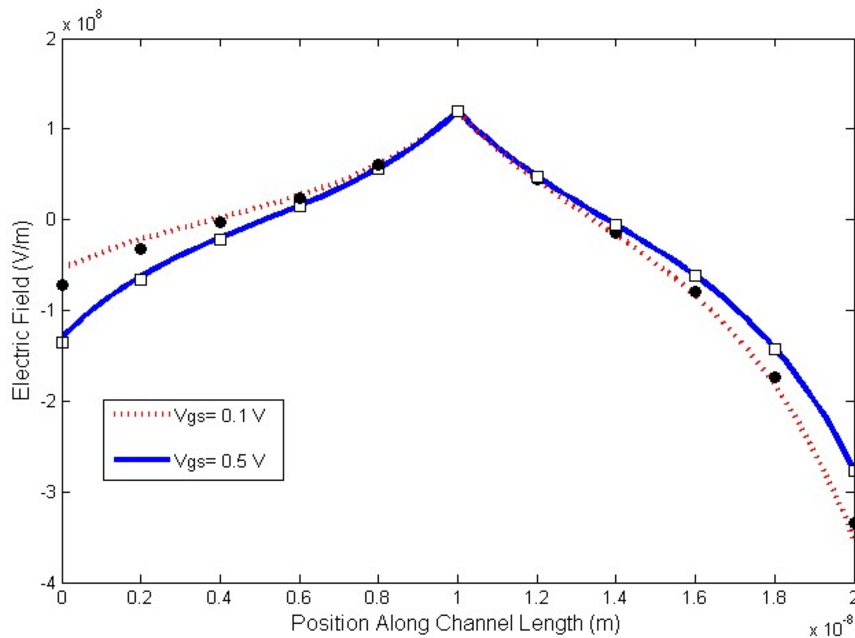

Fig. 5.4. Electric Field along the channel with Vgs =0.1V and 0.5V at Vds = 0.5 V. Symbols: ATLAS.

The results obtained from our proposed analytical models are presented and analyzed in this section. For verification, we used SILVACO Non-Equilibrium Green's Function (NEGF) solver (suitable for ballistic transport) using rectangular geometry in ATLAS. The simulation model has been calibrated according to the quantum model presented by Padilla et al. for 20 nm channel

TFET. As quantum analytical model is formulated on local BTBT model (Landauer theory), Hurkx's local Band-to-Band Model is referred while comparing with classical model.

Figure 5.2 presents the effect of drain voltage (Vds) on surface potential at Vgs=0.5V. As Vds increases, surface potential at source side remains almost unaffected. Thus, tunneling junction is screened from drain electric field and SCEs are eliminated to great extent.

Figure 5.4 plots electric field along the channel length for Vds = 0.5V with Vgs (=0.1V, 0.5V). Introduction of two different work functions at gate generates abrupt change in the conduction band energy and creates an electric-field peak at the middle of the channel. Relatively higher electric field at source-channel junction enhance controllability of gate, increased band bending & induce higher tunneling Generation rate [28]. Whereas, substantially lower electric field at drain-channel junction reduces the possibility of hot carrier generation (which happens in high electric field at drain). Thus, possibility of interface and oxide trapped charges reduces & performance degradation is prevented [5-6, 27-29].

Figure 5.5 analyses tunneling occurring from source to quantum well generating the current density J_1 [refer (18)].

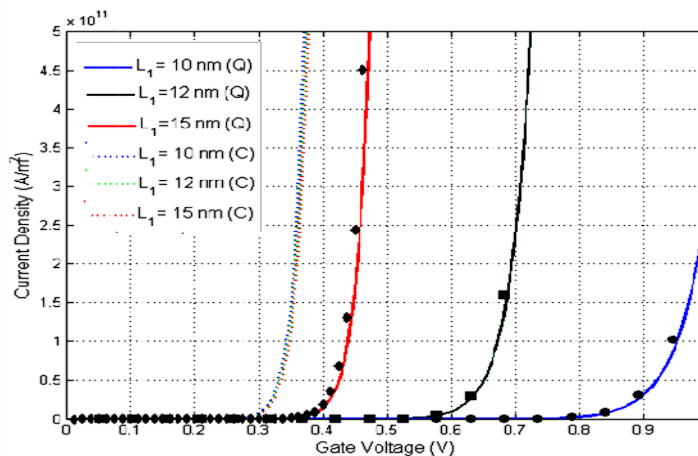

Fig. 5.5. Current density vs gate voltage with scaling (L_1) at Vds=0.5V.

Q: Quantum, C: Classical, Marks: Simulation.

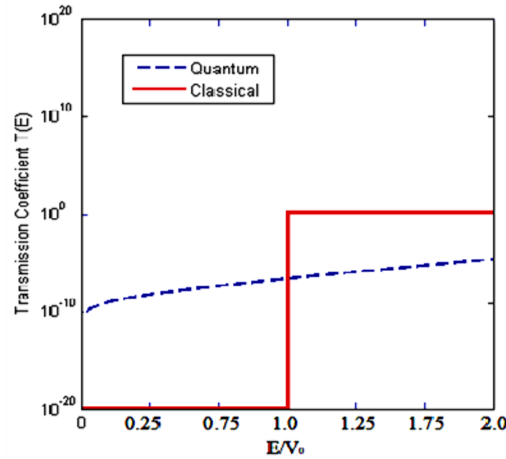

Fig. 5.6. An exploratory comparison of transmission coefficientT(E)-vs engergy between classical tunneling and quantum tunneling.

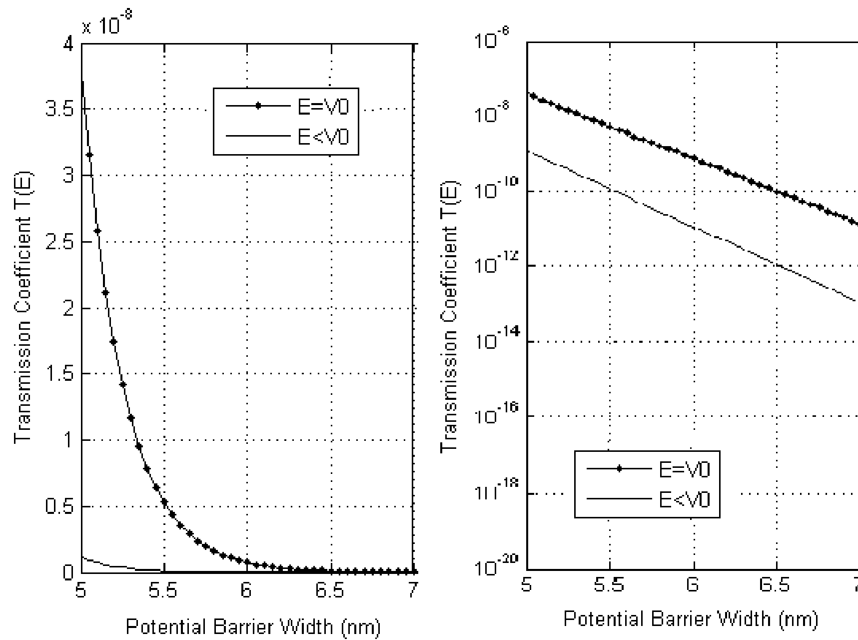

Fig.5.7. (a) Quantum transmission coefficient of an electron, having energy (E), tunneling through potential barrier (V_0) under M_2, (a) Linear, (b) semi-log

The plot (current density vs gate voltage at Vds=0.5V) depict that as L_1 reduces, threshold voltage increases and on state current density decreases. With reduction of L_1, quantum well ($0<z<L_1$) becomes narrower & conduction sub-bands separates even more. First permissible subband shifts upward further from classical position & effective bandgap increases. Hence, to reach threshold

criteria , more gate voltage is required and this elevates threshold voltage. Besides, lesser number of subbands are accommodated in narrower well, which lowers total density of states [vide (23)] and reduces current density. Whereas, such consequence of dimensional scaling (i.e., increase of threshold voltage & reduction of current density) is not observed in classical model.

Quantum model differs from classical model in treatment of tunneling barrier present in device channel. Figure 5.6 illustrates that 'quantum tunneling coefficient' possess non-zero value even when electron energy (E) < barrier height (V_0). Whereas, 'classical tunneling coefficient' reaches 1 from 0 at $E=V_0$. Nature of 'quantum tunneling coefficient' is further studied in figure 5.7(a) and 5.7(b) which show strong dependency of transmission coefficient on potential barrier width.

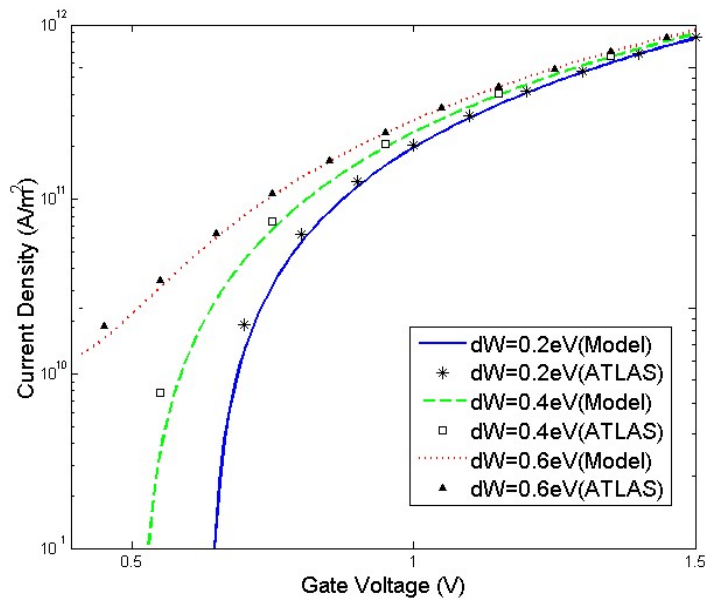

Fig. 5.8. Current density against gate voltage with varying work function difference ($dW=\phi_{M2}-\phi_{M1}$) in gate materials.

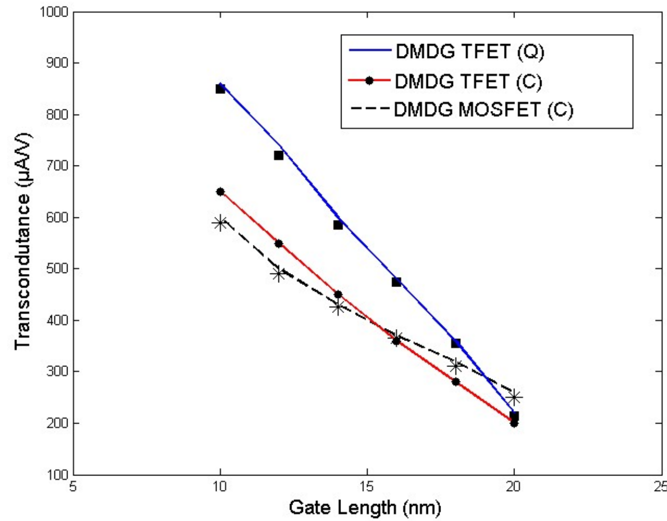

Fig. 5.9. Transconductance against gate length for Vgs =1V to 1.05V and Vds =0.75V. Q: Quantum, C: Classical, Marks: Simulation.

The impact of work function on device characteristics is studied in figure 5.8 at Vds=0.5 V L_1/L_2=1 and L_1+L_2=20nm). Work function of M_2 is kept fixed while work function of M_1 is decreased. With increasing work function difference (dW= ϕ_{M2} - ϕ_{M1}), deeper potential well develops under M_1 . Thus, smaller gate voltage is required to trigger tunneling and threshold voltage reduces. Nevertheless, with further increment of dW, current-voltage characteristics deteriorates, marking limit on work function difference in gate materials. Thus, a trade-off is observed between L(channel length) and dW(work function difference) towards optimization of device performance. The transconductance values per unit area for DMDG TFET quantum model are plotted in figure 5.9 and compared with DMDG TFET classical model & DMDG MOSFET. The transconductance values are extracted from J-Vgs characteristics between Vgs =0.95V to 1.00V, with a typical value of Vds=0.75V. At lower dimension, highest transconductance is offered by DMDG TFET quantum model. Transconductance from quantum model decreases with increased gate length & meet classical model values in higher dimensions as quantization fades off at higher dimension.

Quantization aspects on a sub-20 nm DMDG TFET are explored by analytical modeling in this work. It demonstrates presence of quantum well and tunneling barrier in channel due to structural confinement. With dimensional downscaling, narrower quantum well is formed, which

results to steeper subthreshold slope and higher threshold voltage. Whereas, such increase of threshold voltage is found to be reversed with suitable choice of gate metals. These properties have not been observed in classical model which prove the necessity of quantum modeling in very low dimension. By optimization of quantum well depth-width, excellentl device characteristics [on state current density(J_{on}) 6 .2064 $\times 10^{13}$ A/m^2, off state current density(J_{off}) 2.4102 $\times 10^{-6}$ A/m^2, $J_{on}/J_{off} \sim 10^{18}$, average subthreshold slope 26 mV/dec with Mo (~4.6eV) as M_1 & Au (5.1 eV) as M_2] can be achieved. Such analytical results are found to be at par with previous simulation results. This work give fundamentals of quantization phenomena in low dimensional TFET and can be enriched with detailing in future research. The preceding section presented the analytical modeling of a Dual Metal Double Gate (DMDG) TFET, emphasizing the role of structural confinement and gate work function engineering in inducing a lengthwise potential well within the sub-20 nm channel. Such potential modulation governs the quantization of energy states and directly influences the tunneling probability through band alignment control. Considering this quantum analytical foundation, the subsequent section extends the discussion toward a more generalized and physically inclusive approach using the Bohm Quantum Potential (BQP) framework. While the analytical model captures discrete quantization and resonant tunneling in idealized structures, the BQP-based formulation enables semi-classical incorporation of quantum confinement and strain coupling effects in practical heterojunction TFETs, particularly for biosensing applications.

5.4. Impact of Bohm Quantum Potential on SiGe-Based Heterojunction Tunnel FET Biosensors: Modeling and Comparative Analysis

SiGe-based TFETs are ideal for low-power logic circuits, enabling significant energy savings in portable and battery-operated devices. Their high-speed operation and low noise make them suitable for RF, microwave, and wireless communication and sensing applications [276], [277], [278], . Additionally, they enhance CMOS performance by reducing power dissipation, improve non-volatile memory devices with faster operations, and support photonic applications like optical

communication through high-speed optoelectronic integration.

SiGe heterojunction Tunnel Field Effect Transistors (HJ-TFETs) exhibit significant potential for sensor applications, leveraging band-to-band tunneling (BTBT) mechanisms to achieve enhanced sensitivity and efficiency. The reduced bandgap of SiGe facilitates superior tunneling efficiency, enabling high on currents and low operating voltages, critical for low-power sensing. Tajima et al. reported the thermoelectric properties of RF-sputtered SiGe thin films, highlighting their potential for hydrogen gas sensing applications due to their excellent material properties [279]. Dash et al. demonstrated the enhanced sensitivity of a hetero-gate dielectric SiGe/Si tunnel FET when used as a hydrogen gas sensor, showcasing its effectiveness in detecting gas concentrations [280]. Similarly, Hirphaa et al. investigated the role of SiGe pocket integration in various TFET structures, revealing its significant impact on improving gas sensing performance, further emphasizing the versatility of SiGe-based materials in advanced sensing technologies [281]. In biosensing application, Biomolecular interactions at the sensing interface modulate local electric fields and dielectric properties, inducing shifts in threshold voltage and drain current for precise detection of analytes [282], [283]. Key advantages of SiGe include tunable bandgap sensitivity, energy-efficient operation at low voltages, rapid response times due to the low effective mass of carriers, and suitability for label-free detection[284], [285], [286], [287], [288], [289] . These features position SiGe HJ-TFETs for diverse applications, including biosensors for medical diagnostics, chemical sensors for pollutant detection, and integrated IoT-enabled systems.

SiGe-based Heterojunction Tunnel FETs (HJ-TFETs) exploit material bandgap engineering to enhance tunneling efficiency and device performance [290]. The Ge Source–SiGe Channel–Si Drain configuration benefits from the Ge source's low bandgap, reducing tunneling distance and enabling high on currents with minimal off leakage, ideal for high-performance logic circuits [291], [292], [293]. The SiGe Source–Si Channel–Si Drain structure leverages the intermediate bandgap of SiGe at the source to balance tunneling efficiency and switching speed, providing optimized performance for low-power and high-speed applications [294], [295]. The Si Source–SiGe Pocket–Si Channel–Si Drain introduces a SiGe pocket between the source and channel, inducing localized strain that enhances charge modulation and significantly improves on current and subthreshold swing [296], [297], [298], [299]. These configurations demonstrate the potential

of SiGe-based HJ-TFETs in advancing energy-efficient and high-speed semiconductor technologies [300].

Silicon-germanium (SiGe) heterostructure Tunnel Field Effect Transistors (TFETs) is likely to be profoundly influenced by quantum effects due to the unique material properties and device architecture [301]. The band-to-band tunneling mechanism, central to TFET operation, as well as bandgap engineering alongwith operation at lower voltages can contribute to quantum effects. Additionally, quantum confinement at nanoscale dimensions modifies energy landscapes, resulting in discrete energy levels that enhance tunneling currents. However, the impact of Quantum Potential, particularly in different SiGe-based nanosensors, remains underexplored. This work aims to address this research gap by analyzing and quantifying the differential behaviors of such systems, advancing the understanding of quantum effects in TFET sensing applications.

This work investigates the impact of Bohm Quantum Potential (BQP) on the performance of SiGe-based heterojunction Tunnel Field Effect Transistor (TFET) biosensors through analytical modeling and comparative analysis. Sensitivity and selectivity metrics were evaluated for three configurations: (a) Ge Source–SiGe Channel–Si Drain, (b) SiGe Source–Si Channel–Si Drain, and (c) Si Source–SiGe Pocket–Si Channel–Si Drain, under classical and quantum frameworks. The results reveal that quantum confinement effects, as introduced by BQP, significantly suppress sensitivity and selectivity, with varying degrees depending on the material properties and structural design. The Ge Source configuration demonstrates minimal quantum suppression due to strong tunneling effects, while the SiGe Source configuration shows the highest suppression, attributed to moderate confinement and the absence of strain-enhanced modulation. The SiGe Pocket configuration achieves the highest classical selectivity and maintains moderate quantum sensitivity due to strain-induced charge modulation effects. These findings underscore the critical role of material choice, strain engineering, and quantum effects in designing high-performance TFET biosensors, providing valuable insights into their optimization for next-generation sensing applications.

Device Structure

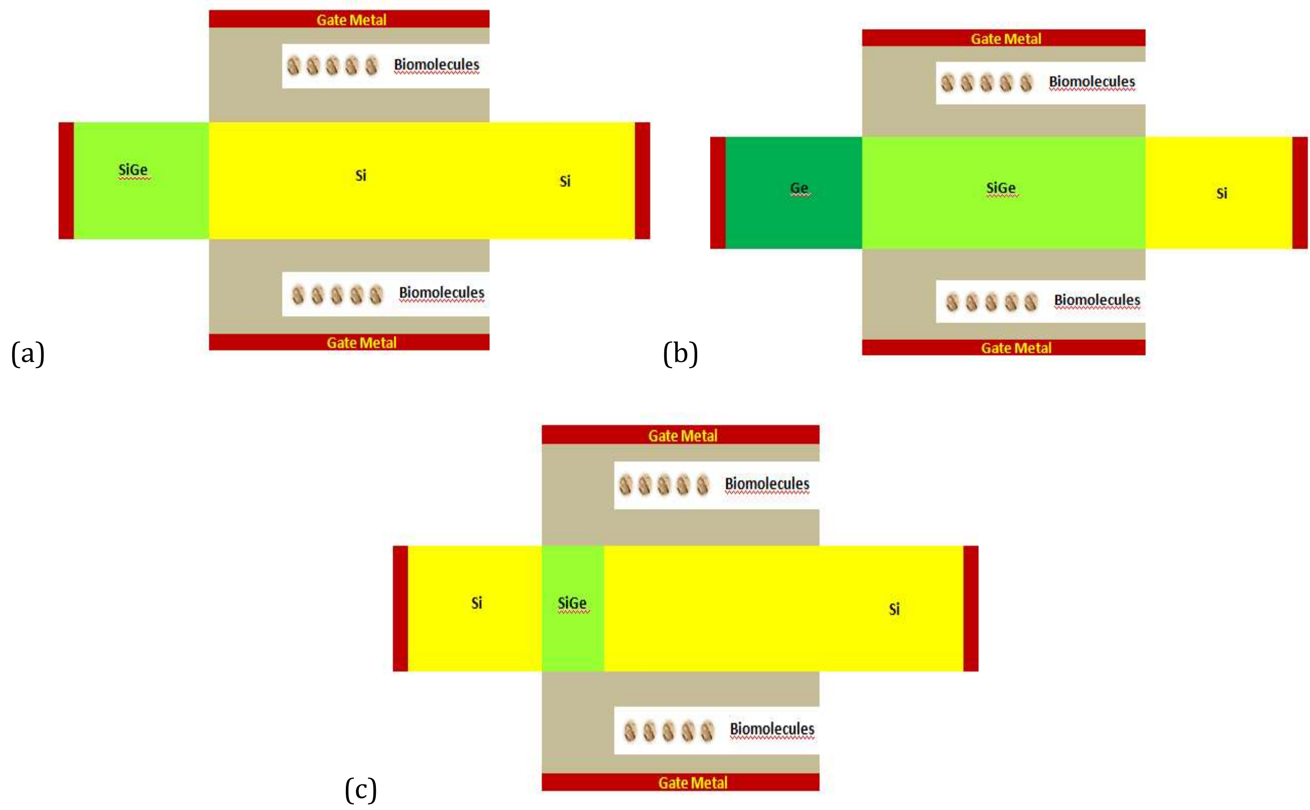

Fig.5.10. Heterojunction TFET with (a)SiGe Source, Si Channel, and Si Drain , (b) Ge Source, SiGe Channel and Si Drain configurations (c) Si source SiGe Pocket Si channel and Si drain

The proposed TFET architectures are designed with a source length of 10 nm, an intrinsic channel length of 15 nm, and a drain length of 10 nm. The channel thickness varies across configuration is 10 nm, while the oxide layer thickness is fixed at 2 nm, and the cavity thickness is 4 nm. The device width is maintained at 20 nm, with a gate metal work function of 4.45 eV. Doping concentrations are set at 10^{19} cm^{-3} (p-type) for the source region, 10^{16} cm^{-3} (p-type) for the intrinsic channel, and 10^{19} cm^{-3} (n-type) for the drain. These architectures include: (a) a SiGe source, Si channel, and Si drain TFET leveraging bandgap discontinuities for enhanced tunneling; ((b) a Ge source, SiGe channel, and Si drain TFET exploiting Ge's narrow bandgap for efficient carrier injection and reduced strain-induced defects, c) a SiGe Pocket TFET optimizing band-to-band tunneling (BTBT) and electrostatic control.

From fabrication aspect, Heterojunction SiGe Source TFET starts with a Si substrate, where a gate structure comprising a dielectric layer (e.g., SiO_2 or high-k) and a gate electrode is defined

using photolithography and etching. An undoped SiGe layer with an initial Ge concentration of less than ~30% is grown epitaxially in the source region, partially extending beneath the gate dielectric. A doped SiGe layer with a higher Ge concentration (above ~30%) is deposited over the undoped layer, followed by thermal annealing. The source, drain, and electrical contacts are patterned and metallized, resulting in a structure optimized for tunneling through the SiGe/Si heterojunction. The SiGe Pocket TFET uses a p-type Si substrate, where LOCOS and p-well implantation isolate active regions. The p+ source region is formed by ion implantation, and an n+ ultra-shallow pocket is introduced using Ge ion pre-amorphization and arsenic implantation, followed by spike annealing to create a strained, high-concentration pocket at the source-channel interface. A thin oxide layer and polysilicon are deposited using LPCVD to form the gate stack, which overlaps with the source for vertical tunneling. Spacer formation isolates the source and drain, and metallization completes the device. Cross-sectional HRTEM and EDX mapping ensure precise control of the pocket's position and strain. Whereas, in Ge Source TFET fabrication begins with depositing an intrinsic Si layer on a SiO_2 substrate, followed by thermal oxidation to grow a passivating oxide layer. Doping for the pocket and drain regions is done via diffusion and drive-in processes. A Ge layer is deposited on the patterned Si substrate using LPCVD to form the source, doped with p+ dopants for high conductivity. The gate oxide, typically high-k materials like HfO_2, is deposited using ALD, and a metal gate is formed by sputtering. Spacers are added using Si_3N_4 deposited through LPCVD or PECVD, completing the device. An alternate method involves selective etching of the substrate to integrate the Ge source, with Al_2O_3 layers used for passivation and dielectric functionality.Each fabrication method aligns with the unique design requirements of the respective TFET architecture.

Simulation Aspect

In simulation environment, a semi-classical solution is obtained. Then, the BQP equation is solved separately using a Gummel iteration to determine Q_{eff} at each node in the device. The semi-classical potential is adjusted by incorporating the value of Q_{eff} at every node, and the set of semi-classical equations is solved to convergence using a Newton or block iterative scheme. This process is repeated: solving the BQP equation to convergence, adjusting the semi-classical potential, and resolving the semi-classical equations until self-consistency is achieved between the

BQP solution and the semi-classical equations.

To evaluate the device characteristics, simulations were conducted using the ATLAS framework in Silvaco. The modeling incorporated various physical phenomena, including the local band-to-band tunneling (BTBT) model, Fermi-Dirac (FD) statistics, drift-diffusion (DD) carrier transport, Shockley-Read-Hall (SRH) recombination, and bandgap narrowing effects. To examine device behavior at scaled dimensions and to assess the impact of quantum mechanical effects, the Effective Bohm Quantum Potential (BQP) model was utilized.

The BQP model provides notable advantages over conventional methods such as the Schrödinger-Poisson (SP) solver and the Density Gradient (DG) model. It integrates Fermi-Dirac statistics, which are critical for accurately representing carrier distributions in semiconductor devices, particularly under quantum confinement in low-dimensional structures. With only two fitting parameters, the BQP model enables precise calibration for a variety of semiconductor materials (including non-silicon options) and device architectures.

Kane's model was employed to compute the band-to-band tunneling generation rate under a uniform electric field, where the tunneling parameter P was set to 2.5 for indirect tunneling. Calibration of parameters A and B for the Ge-$Si_{0.8}Ge_{0.2}$ junction was performed to ensure alignment with experimental data and simulation accuracy.

Theory, Result and Discussion

The results and discussion section begins by presenting a theoretical analysis that supports the simulation findings.

In a double gate structure, the 2-D Poisson equation is as follows :

$$\frac{\partial^2 \varphi(x.y)}{\partial x^2} + \frac{\partial^2 \varphi(x.y)}{\partial y^2} = \frac{qN}{\epsilon_{Ge/SiGe}}, \quad (5.24)$$

$\varphi(x.y)$ is the two dimensional potential, N is the carrier density. By Young's Parabolic approximation

$$\varphi(x, y) = \varphi_s(x) + y a_1(x) + y_2 a_2(x) \tag{5.25}$$

Where $\varphi_i(x, y)$ *is* 2-D potential profile , $a_i(x)$ is one dimensional potential along length. To calculate a_0, a_{1i} *and* a_{2i} we apple the boundary conditions as:-

1. The source end potential is the build in potential V_{bi_S}
2. Drain end potential is bildin in potential at drain V_{bi_D} added with applied drain Voltage
3. $\left.\frac{\partial \varphi_i(x,y)}{\partial y}\right|_{y=0} = a_{1i}(x)$
4. $\left.\frac{\partial \varphi \;\; (x,y)}{\partial y}\right|_{y=t(Si_{(1-mf)}Ge_{(mf)})} = a_1(x) + 2t_{Si_{(1-mf)}Ge_{(mfi)}} a_2(x)$ (5.26)

$\varphi_S(x)$ is the surface potential, $t_{\left(Si_{(1-mf)}Ge_{(mf)}\right)}$ is the thickness of the channel. *'mf'* denotes the Germanium mole fraction in Silicon in each region.

Solving,

$$a_2(x) = \frac{C_{ox}[V_{GS} - V_{FBi} - \varphi_S]}{t_{Si_{(1-mf)}Ge_{(mf)}} \epsilon_{Ge/Si_{(1-mf)}Ge_{(mf)}}},$$

$$a_1(x) = \frac{-C_{ox}[V_{GS} - V_{FBi} - \varphi_{S,}]}{t_{Si_{(1-mf)}Ge_{(mf)}} \epsilon_{Ge/Si_{(1-mf)}Ge_{(mf)}}} \tag{5.27}$$

VGS is the gate to source voltage, V_{FBi} is the flat-band voltage corresponding to every region, ε is the permittivity. C_{ox} is the oxide capacitance . Now 1-D equation takes the form,

$$\frac{\partial^2 \varphi_{s,i}(x)}{\partial x^2} - \frac{\varphi_{s,i}(x) - (V_{GS} - V_{fbi})}{\lambda^2} = \frac{qN_i}{\epsilon_{Ge/Si_{(1-mf)}Ge_{(mf)}}} \tag{5.28}$$

λ is the characteristics length given by, $\lambda = \sqrt{\frac{t_{Ge/Si_{(1-mfi)}Ge_{(mfi)}} \varepsilon_{Si_{(1-mfi)}Ge_{(mfi)}}}{2C_{HfO2}}}$

(5.29)

Here, 2/π is multiplied in the denominator to consider fringing field effects.

The general solution of the above differential equation,

$$\varphi_S(x) = P \exp\left(\frac{x}{\lambda}\right) + Q \exp\left(-\frac{x}{\lambda}\right) + \sigma \;\; , \tag{5.30}$$

Where, $\sigma \quad = V_{GS} - V_{fb} - \frac{qN_i}{\epsilon_{Ge/Si_{(1-m)}Ge_{(mf)}}}\lambda^2$, (5.31)

$V_{bs} = V_s - V_t \log\left(\frac{N_S}{n_i}\right)$

and $N_S = N - \frac{\varepsilon_{Ge}}{q\lambda^2}(V_{GS} - V_{FB} - V_{bs})$ (5.32)

It is pertinent to mention here that for different composition of SiGe in the different regions of channel, the surface potential is to be derived separately maintaining the boundary conditions of Potential continuity and Field continuity at the junction of different region are used .Thus the general classical potential is

$$\varphi(x,y) = \frac{qN_S}{2\varepsilon_{Ge}}(x+L)^2 + V_{bs} + y\frac{-C_{ox}\left[V_{GS} - V_{FB} - \varphi_s\right]}{t_{Si_{(1-mf)}Ge_{(mf)}}\varepsilon_{Ge/Si_{mf}Ge_{(mf)}}} + y^2\frac{C_{ox}\left[V_{GS} - V_{FB} - \varphi_s\right]}{t_{Si_{(1-mf)}Ge_{(mf)}}\varepsilon_{\frac{Ge}{Si_{(1-mf)}Ge_{(mf)}}}} \tag{5.33}$$

At scaled dimension, the device potential consists of the classical and quantum potential adds a position-dependent quantum potential, *Qeff*, to the carrier's potential energy, derived from Bohm's interpretation of quantum mechanics (BQP). The general form of Schrödinger equation is

$$-\frac{\hbar^2}{2m^*(x)}\frac{\partial^2\psi}{\partial x^2} + \varphi(x,y)\psi = i\hbar\frac{\partial\psi}{\partial t}, \tag{5.34}$$

is the wave function, $\hbar$ is the reduced Planck constant, m^* is the mass of the particle, and $\varphi(x,y)$ is the potential of that region. To derive the BQP, we express the wavefunction ψ in its polar form [302]

$$\psi = \sqrt{n}e^{iS/\hbar} \tag{5.35}$$

where '*n*' is the probability density and *S* is the phase of the wavefunction.

In this representation, the Schrödinger equation can be reformulated. Substituting this into the Schrödinger equation and separating the real and imaginary parts, we obtain two coupled equations. The real part of the equation represents the continuity equation, ensuring the conservation of probability density. The imaginary part ensures the conservation of total energy , which is the sum of Potential energy , Kinetic energy and Quantum potential which reflects quantum mechanical effects. The continuity equation is the partial derivative of probability of

carrier density with respect to time and distance. Whereas, the Quantum Hamilton-Jacobi Equation takes the form

$$\frac{\partial S}{\partial t}+\frac{1}{2m^*}\left(\frac{\partial S}{\partial x}\right)^2+\varphi(x,y)+Q_{eff}=0$$, where

$$Q_{eff}=\frac{\hbar^2\nabla\left(m^{*-1}\nabla(n^{\alpha})\right)\gamma}{2n^{\alpha}} \tag{5.36}$$

m^{*-1} is the inverse effective mass tensor, *'n'* is the carrier concentration, α , γ are adaptable parameters.

The following equations couple the BQP equation with Poisson's equation through the carrier concentration term *'n'*

$$n = N_c \exp\left(-\frac{(E_c+qQ_{eff})}{kT}\right) \tag{5.37}$$

To determine the values of the fitting parameters numerically, a close agreement between the BQP model and the results from Schrödinger-Poisson (S-P) calculations for any given class of device should be achieved. Thus the quantum potential takes the form in initial condition

$$Q_{eff}=\frac{\hbar^2\nabla\begin{pmatrix}\left(m_0*(1-\beta\ x\ Ge_{mf})\right)^{-1}\\ \nabla((N_c\exp\left(-\frac{(E_c+qQ_{eff}}{kT}\right))^{\alpha})\end{pmatrix}\gamma}{2(\ N_c\exp\left(-\frac{(E_c+qQ_{eff}}{kT}\right))^{\alpha}} \tag{5.38}$$

The parameters and the quantum potential (Q_{eff}) depend on the device structure and the applied bias. However, in our approach, we treat them as constant values determined through a fitting process with calibration with Schrodinger-Poisson simulation model. This significantly simplifies the calculation of the quantum potential, avoiding the need to directly solve the Schrödinger equation every time. When the system is out of equilibrium, the occupation factor is a function of position. After incorporation of BQP, the cumulative potential is

$$\varphi_{BQP}(x,y)=\varphi(x,y)+Q_{eff}(x) \tag{5.39}$$

From with maximun electric field approximation, which allows non-local calculation to be framed in local model, the tunneling current density is

$$I = A\frac{qVE_f^{\max}}{E_g^{1/2}}\exp(-B\frac{E_g^{3/2}}{E_f^{\max}}) \tag{5.40}$$

$$I = A\frac{qV\left[\sqrt{\left(\frac{d\varphi_{BQP}(x,y)}{dx}\right)^2+\left(\frac{d\varphi_{BQP}(x,y)}{dy}\right)^2}\right]_{\max}}{E_g^{1/2}}\exp(-B\frac{E_g^{3/2}}{\left[\sqrt{\left(\frac{d\varphi_{BQP}(x,y)}{dx}\right)^2+\left(\frac{d\varphi_{BQP}(x,y)}{dy}\right)^2}\right]_{\max}})$$

Where V is the bias, $E_f^{\max}$ is the max value of electric field obtained from $\varphi_{BQP}(x,y)$, A and B are two fitting parameters. If the varying electric filed is considered, the current is to be calculated as

$$I = q\iint A\frac{qV_a\sqrt{\left(\frac{d\varphi_{BQP}(x,y)}{dx}\right)^2+\left(\frac{d\varphi_{BQP}(x,y)}{dy}\right)^2}}{E_g^{1/2}}\exp(-B\frac{E_g^{3/2}}{\sqrt{\left(\frac{d\varphi_{BQP}(x,y)}{dx}\right)^2+\left(\frac{d\varphi_{BQP}(x,y)}{dy}\right)^2}})dxdy \tag{5.41}$$

It may be noted also that for the drift diffusion transport in the channel, the Quantum potential is incorporated in continuity equations . The results and discussion is based on electostatics and biosensing capabilities of each device mentioned above for varying dielectric constant values (k = 1, 2, 4, 6, 9, 12), which correspond to biomolecules such as air, biotin, ferro-cytochrome, bacteriophage T7 and keratin [303]. In all simulations, $Si_{0.8}Ge_{0.2}$ has been employed to align with previously reported results [304], [305], [306], [307]. The simulation model has been calibrated using where they modeled $Si_{0.8}Ge_{0.2}$ source TFET with DFT [304]. The results and discussion is based on electrostyatics and biosensing capabilities of each device mentioned above for varying dielectric constant values (k = 1, 2, 4, 6, 9, 12), which correspond to biomolecules such as air, biotin, ferro-cytochrome, bacteriophage T7 and keratin [303]. In absence of biomolecule , the potential profile (contour) of the proposed structures reveals the electrostatic landscape across the device region in figure 5.11. This serves as a foundation for understanding carrier transport mechanisms, which are further explored through the quantum potential profile presented in the subsequent analysis.

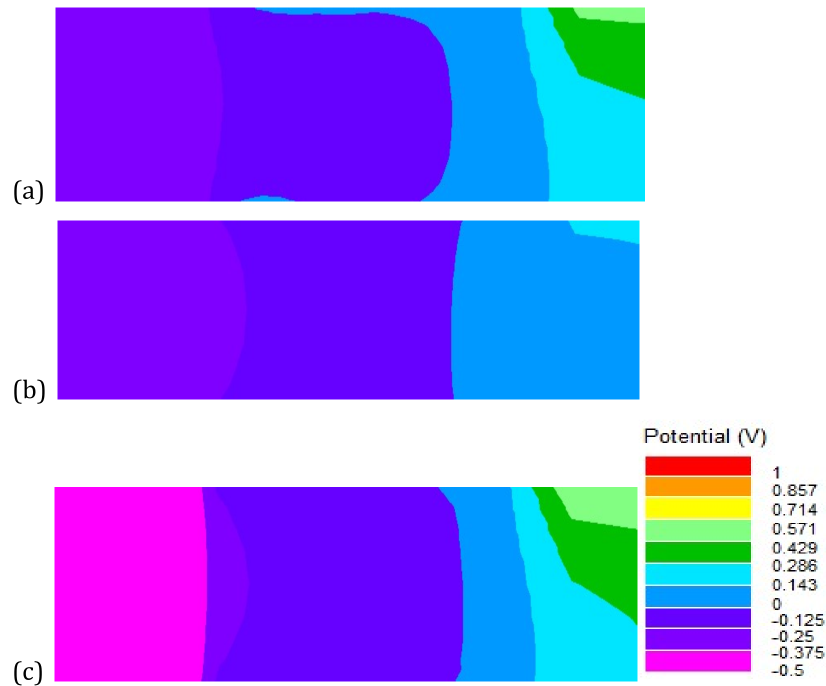

Fig. 5.11 Contour plots illustrating the classical potential profiles for the three TFET architectures: (i) SiGe Source-Si Channel-Si Drain, (ii) Ge Source-SiGe Channel-Si Drain, and (iii) Si Source-SiGe Pocket-Si Channel-Si Drain.

The contour plot of the classical potential for the proposed TFET structures reveals distinct characteristics for each configuration. Among the three configurations, the Ge Source–SiGe Channel–Si Drain (ii) structure exhibits the least potential variation along the source–channel–drain region due to its smooth band alignment and minimal lattice mismatch between Ge and SiGe. The smaller bandgap difference (Ge: 0.66 eV, $Si_{0.8}Ge_{0.2}$: ~1.0 eV) ensures gradual band transitions and uniform electrostatic potential distribution, minimizing abrupt field changes. In contrast, the SiGe Source–Si Channel–Si Drain (i) structure shows a moderate potential variation because of the larger band offset between SiGe and Si, which increases the conduction-band discontinuity and strengthens the field at the source–channel interface. The Si Source–SiGe Pocket–Si Channel–Si Drain (iii) configuration demonstrates the highest potential variation, as the embedded SiGe pocket introduces localized bandgap narrowing and strain-induced modulation, forming a confined potential well that enhances quantum confinement effects and electrostatic perturbations along the channel.

Electron quantum potential is generated in SiGe heterojunction tunnel field-effect transistors (TFETs) due to the electric field distributions and potential profiles established by the

heterojunction's band alignment. When the Bohm Quantum Potential (BQP) models are activated, they account for quantum effects that arise from the wave-like behavior of carriers at nanoscale dimensions.

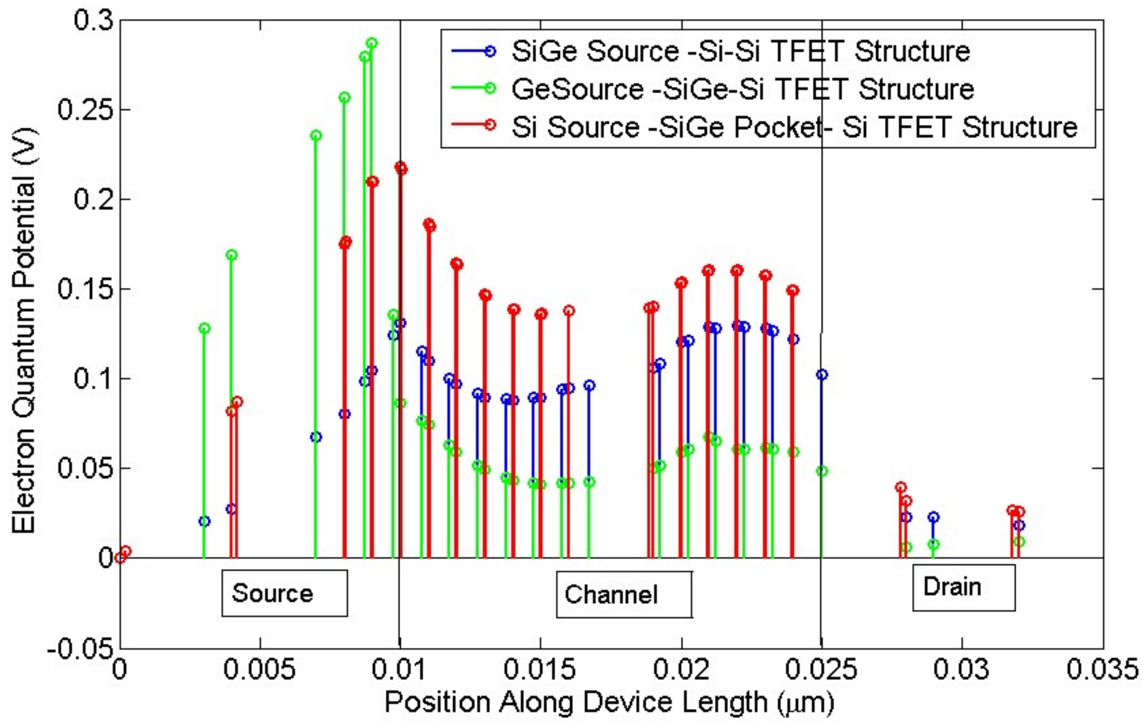

(a)

(b)

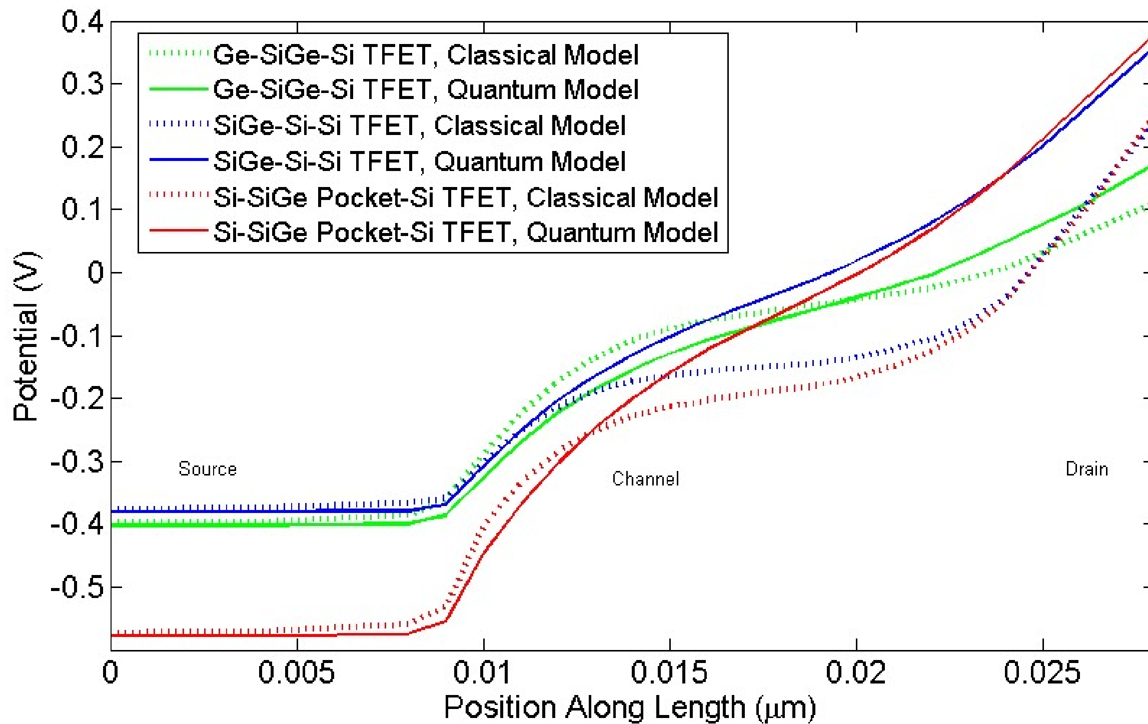

Fig. 5.12. (a) electron quantum potential and (b) overall potential for the three TFET architectures: (i) Ge Source-SiGe Channel-Si Drain, (ii) SiGe Source-Si Channel-Si Drain, and (ii) Si Source-SiGe Pocket-Si Channel-Si Drain with and without quantum effects.

In the Ge source-SiGe channel-Si drain configuration, the electron quantum potential is highest near the source-channel interface due to Ge's narrow bandgap (0.66 eV), resulting in strong quantum confinement and enhanced tunneling. The transition from Ge to SiGe introduces strain and band alignment effects, while the Si drain's larger bandgap (1.12 eV) creates sharp potential transitions. In the SiGe source-Si channel-Si drain configuration, the quantum potential is lowest at the source-channel junction, with minimal bandgap variation and band structure, leading to weaker quantum effects and reduced quantum confinement, but increases at channel due to Si's intermediate bandgap and effective mass compared to SiGe. Whereas, in the Si source-SiGe pocket-Si channel-Si drain configuration, the quantum potential is moderate in the source –channel junction , but highest in the channel region due to additional quantum effects incorporated by SiGe pocket.

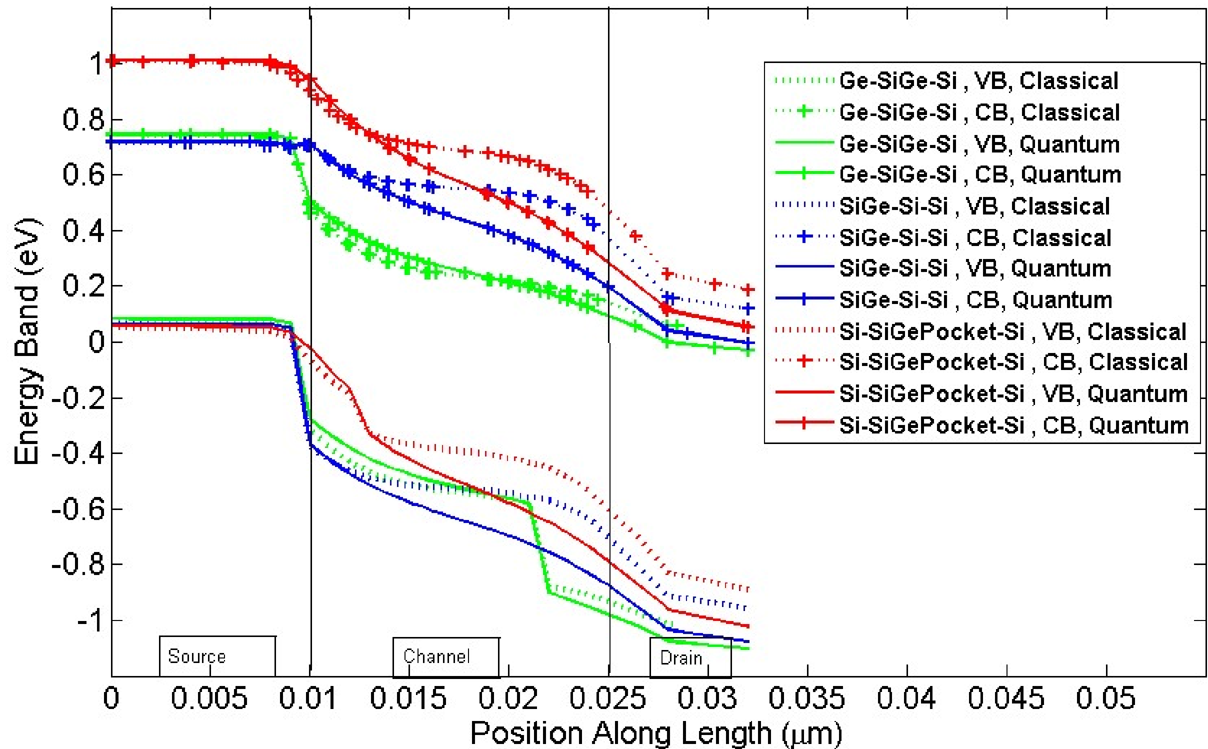

Fig 5.13. Energy band diagrams for (i) Ge Source-SiGe Channel-Si Drain, (ii) Si Source-SiGe Pocket-Si Channel-Si Drain, and (iii) SiGe Source-Si Channel-Si Drain configurations with and without quantum effects.

The overall impact of BQP on the energy band is depicted in figure 5.13 where we can find that BQP corrections refine the wavefunction behavior at the drain significantly at a lower drain voltage at 0.2V, reducing the classical approximation of the energy band. This refinement alters the band profile more significantly, especially in the depletion region near the channel-drain junction. The greater Impact on the Drain Side Than at the Source-Channel Junction can be attributed to the fact that the source is the region of carrier injection, where band bending and tunneling dominate. These effects are already steep and well-defined due to the material properties (e.g., Ge or SiGe at the source). BQP introduces corrections at the source channel junction too, but the changes are less pronounced because the quantum tunneling effects are already significant without additional modifications.

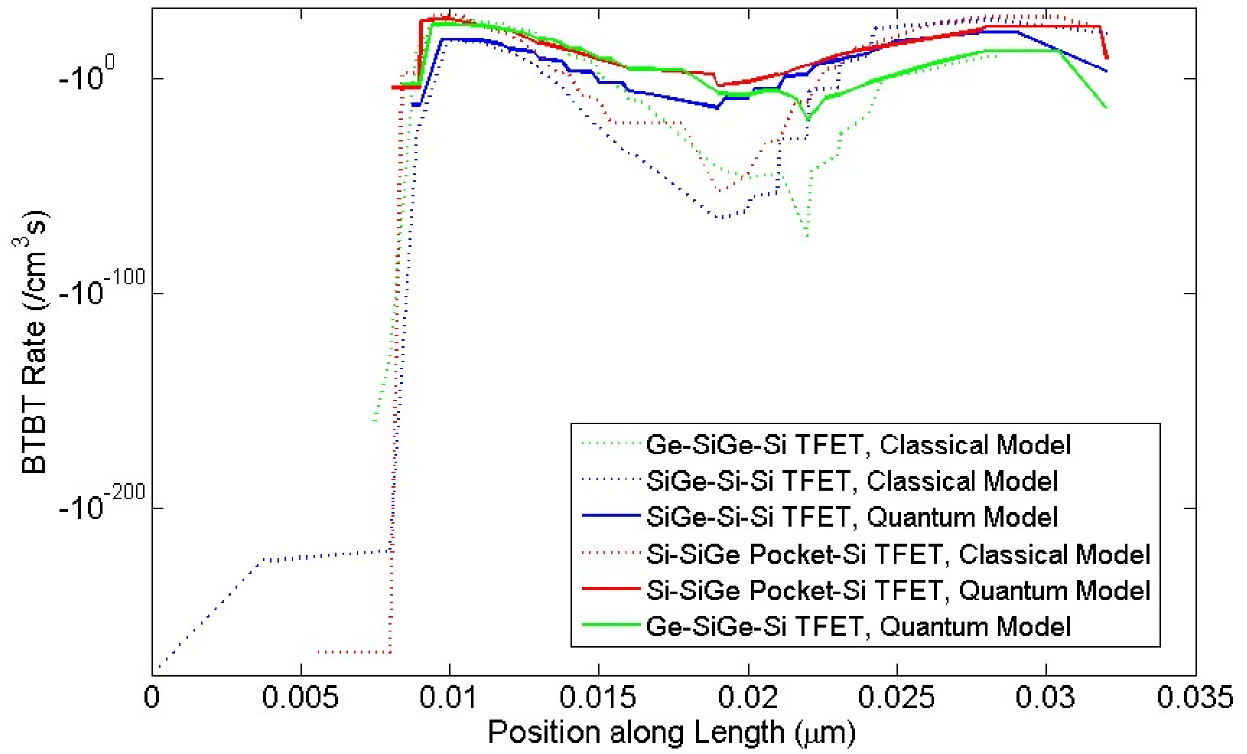

Fig.5.14 BTBT for (i) Ge Source-SiGe Channel-Si Drain, (ii) Si Source-SiGe Pocket-Si Channel-Si Drain, and (iii) SiGe Source-Si Channel-Si Drain configurations with and without quantum effects.

As explained in figure 5.13, the BQP modifies the classical potential by incorporating the quantum mechanical contributions of electron wavefunction curvature, effectively reducing the barrier width and altering the energy profile. This modification enhances tunneling probabilities by increasing wavefunction overlap across the tunneling barrier. In all three configurations, the enhanced localization of the wavefunction near the source interface, as modeled by BQP, results in a higher BTBT rate by more accurately capturing the narrow and sharp energy transitions.

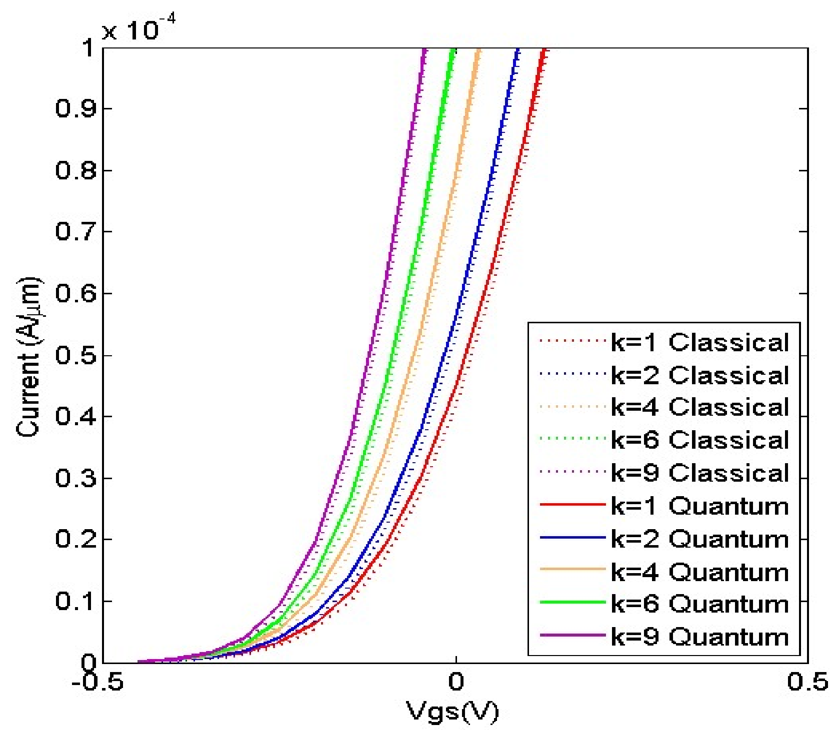

(a)

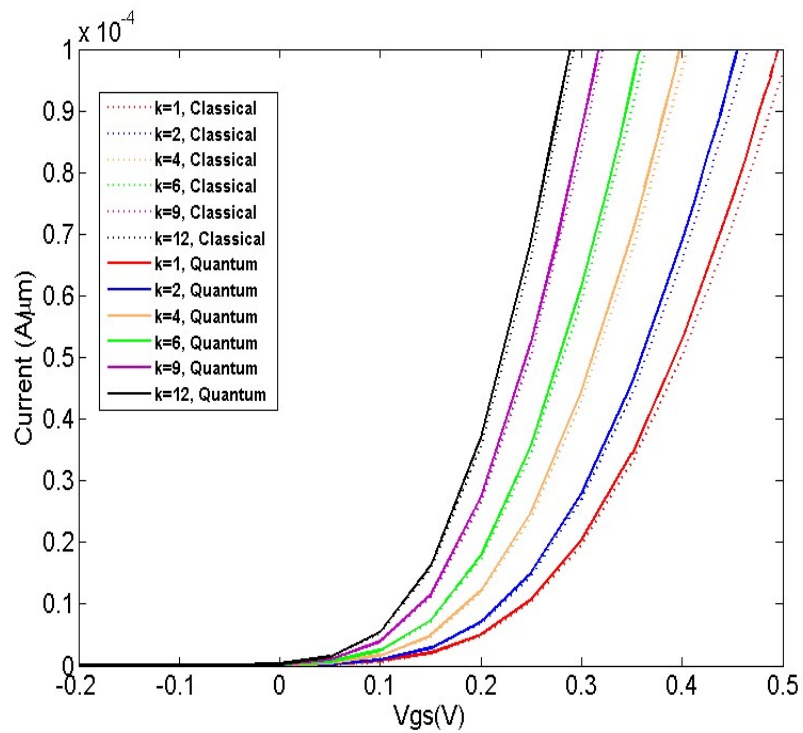

(b)

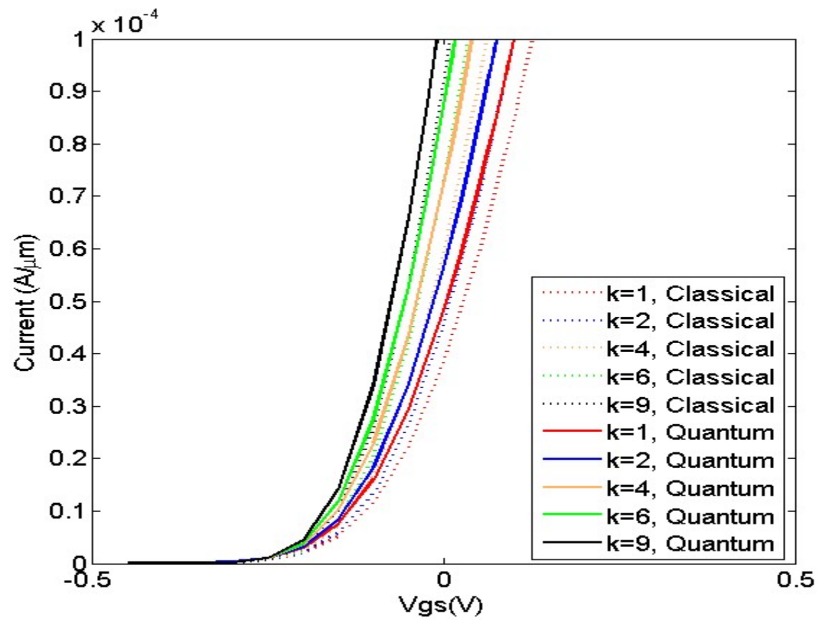

(c)

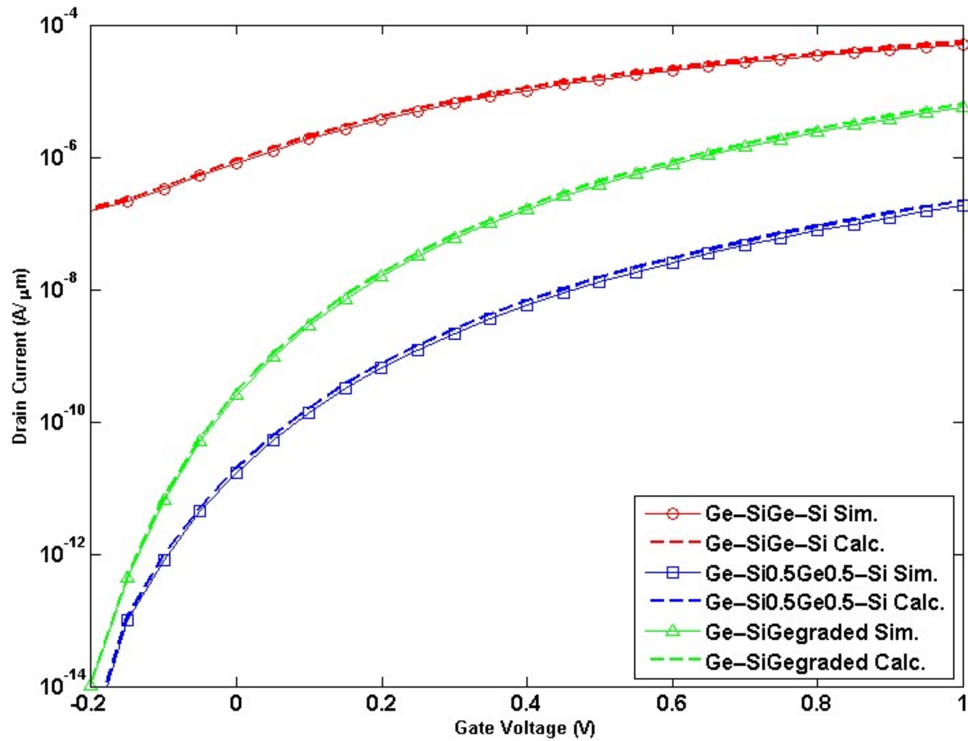

(d)

Fig.515. Id-Vg for (a) Ge Source-SiGe Channel-Si Drain, (b) SiGe Source-Si Channel-Si Drain and (c) Si Source-SiGe Pocket-Si Channel-Si Drain configurations with and without quantum effects (d) Drain current vs Gate Voltage Characteristics for Different TFET Configurations comparing the analytical model(calc.) and simulation results(Sim.).

The drain current gate voltage characteristics of the three TFET configurations in figure 5.15 reveal an increasing impact of quantization as we move from (a) Ge Source–SiGe Channel–Si Drain to (b) SiGe Source–Si Channel–Si Drain, and finally to (c) Si Source–SiGe Pocket–Si Channel–Si Drain. In (a), the strong tunneling at the Ge source with minimal quantization effects results in higher current and reduced suppression in the quantum model. In (b), the SiGe source introduces moderate quantization effects due to its intermediate bandgap, leading to a noticeable reduction in current as quantum effects begin to dominate. In (c), the SiGe pocket significantly enhances quantum confinement and strain effects, resulting in the most pronounced suppression of current in the quantum model.

Sensitivity is quantified as the ratio of the change in current caused by the presence of a biomolecule in the cavity to the drain current measured under conditions where no biomolecule is present, typically corresponding to air with a dielectric constant k=1.

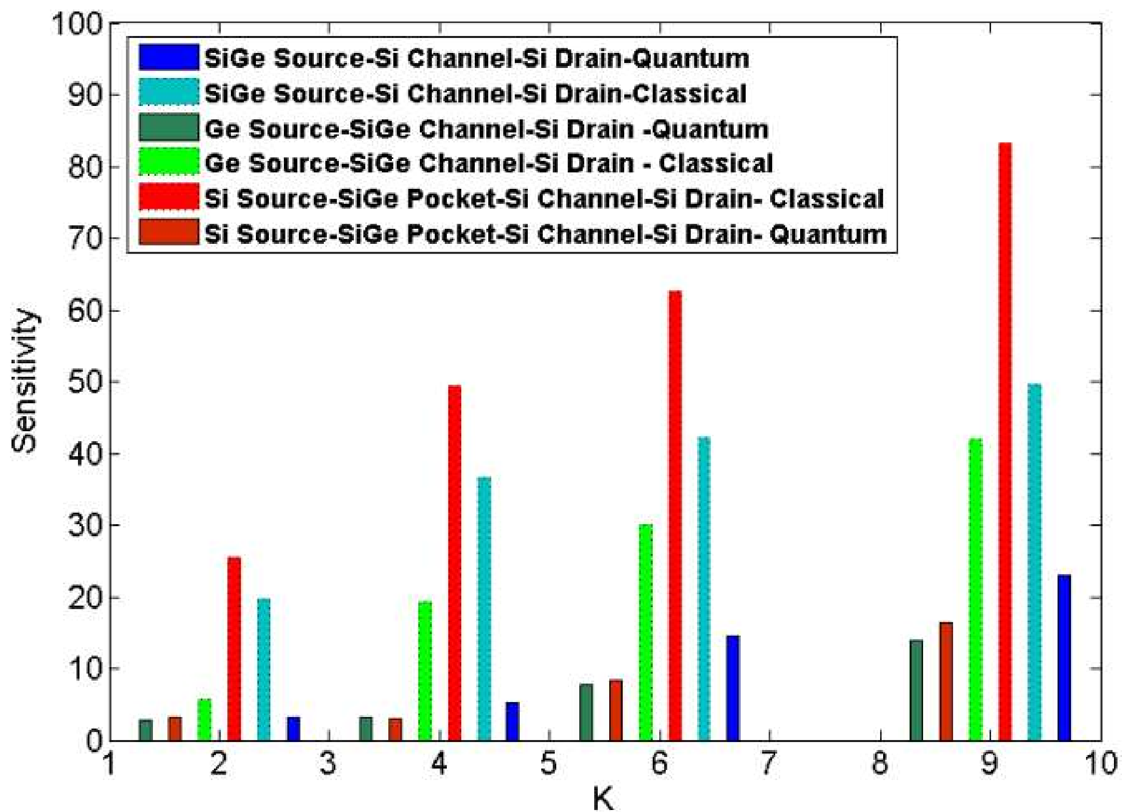

Fig 5.16. On state current sensitivity for (i) Ge Source-SiGe Channel-Si Drain, (ii) SiGe Source-Si Channel-Si Drain and (iii) Si Source-SiGe Pocket-Si Channel-Si Drain configurations with and without quantum effects.

The sensitivity data in figure 5.16 highlights the differences between classical and quantum (Bohm Quantum Potential, BQP) models for three TFET configurations, underscoring the role of quantum confinement and tunneling effects. Sensitivity in the quantum model is significantly lower due to BQP-induced wavefunction effects and reduced charge modulation, particularly in tunneling-dominant regions. For the Ge Source–SiGe Channel–Si Drain configuration, classical sensitivity ranges from 5.57 to 41.94, while quantum sensitivity spans 2.68 to 13.84, reflecting strong confinement and amplified tunneling effects due to Ge's narrow bandgap. The SiGe Source–Si Channel–Si Drain configuration shows higher sensitivity (classical: 19.63–49.52, quantum: 3.25–22.93) due to a moderate bandgap and balanced effects, whereas the Si Source–SiGe Pocket–Si Channel–Si Drain configuration exhibits the highest classical sensitivity (25.40–83.28), sharply reduced in the quantum model (3.21–16.36) due to localized quantum effects in the pocket. The BQP reduces sensitivity by accounting for quantum wavefunction spreading and decreased mobility, with Ge-based configurations experiencing stronger quantum suppression and SiGe-pocket configurations demonstrating the highest classical sensitivity but significant quantum dampening.

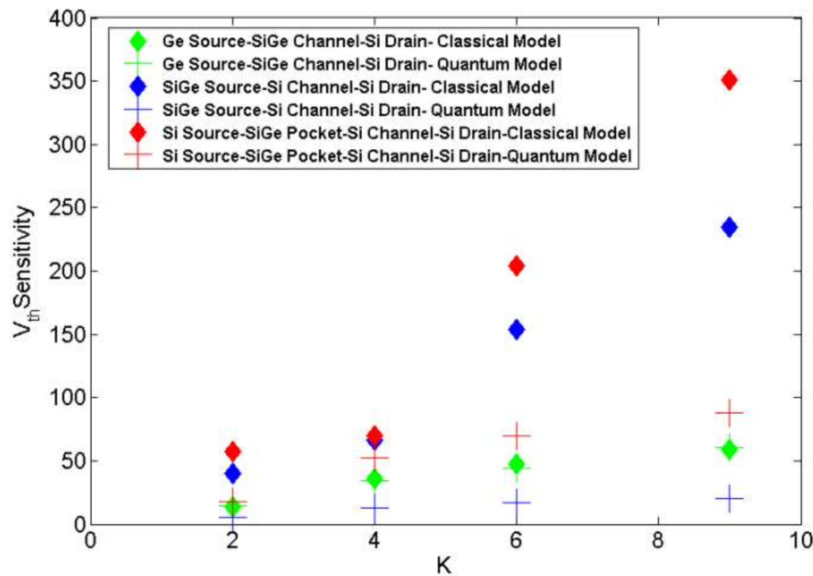

Fig.5.17. Threshold voltage sensitivity for (i) Ge Source-SiGe Channel-Si Drain, (ii) SiGe Source-Si Channel-Si Drain and (iii) Si Source-SiGe Pocket-Si Channel-Si Drain configurations with and without quantum effects.

The threshold voltage (Vth) sensitivity data in figure 5.17 for three Tunnel FET (TFET) configurations highlights the interplay between quantum effects, material properties, and structural designs under classical and Bohm Quantum Potential (BQP) models. For the Ge Source–SiGe Channel–Si Drain configuration, sensitivity remains comparable across models (13.85–59.29 in classical vs. 14.10–60.55 in quantum) due to strong tunneling effects and low effective mass at the Ge source, minimizing quantum suppression. In the SiGe Source–Si Channel–Si Drain, sensitivity drops significantly in the quantum model (39.79–234.29 in classical vs. 5.22–19.96 in quantum) due to moderate confinement and limited charge modulation from strain absence. For Si Source–SiGe Pocket–Si Channel–Si Drain, classical sensitivity is highest (57.10–351.11), while quantum suppression is moderate (18.05–87.75) due to enhanced modulation by strain in the SiGe pocket, partially counteracting quantum effects. These trends emphasize the dominant role of material selection and heterostructure design in shaping Vth sensitivity under quantum confinement.

In terms of selectivity, the following trnd has been observed for highest k value biomolecule in this study (Keratin), with respect to lowest k value biomolecule, Biotin. Here's a table summarizing the selectivity data and its analysis:

Configuration	**Selectivity (Classical)**	**Selectivity (Quantum)**	**Observation**
Ge Source–SiGe Channel–Si Drain	429.26	427.87	Minimal difference between classical and quantum due to strong tunneling effects at the Ge source.
SiGe Source–Si Channel–Si Drain	588.76	382.20	Significant suppression in quantum due to moderate quantum confinement and lack of strain-enhanced modulation.
Si Source–SiGe Pocket–Si Channel–Si Drain	614.86	486.22	Moderate suppression in quantum, but strain effects in the pocket region preserve higher sensitivity.

Table. 5.2. Comparison of selectivity data between classical and quantum models

The study highlights the significant influence of Bohm Quantum Potential (BQP) on the electrostatic and biosensing capabilities of three distinct SiGe-based heterojunction Tunnel Field Effect Transistor (TFET) biosensor configurations, namely Ge Source-SiGe Channel-Si Drain, SiGe Source-Si Channel-Si Drain, and Si Source-SiGe Pocket-Si Channel-Si Drain. Through an analysis of the sensitivity and threshold voltage characteristics under classical and quantum models, the impact of quantum effects on the performance of these devices is quantified. The inclusion of BQP led to a notable reduction in sensitivity across all configurations. Specifically, for the Ge Source-SiGe Channel-Si Drain configuration, sensitivity decreased by approximately 52% (from 41.94 to 13.84), reflecting the strong quantum confinement due to Ge's narrow bandgap. The SiGe Source-Si Channel-Si Drain configuration showed a more moderate decrease in sensitivity, around 53% (from 49.52 to 22.93), due to moderate quantum confinement effects. However, the Si Source-SiGe Pocket-Si Channel-Si Drain configuration exhibited the largest relative reduction in sensitivity, with a 62% drop (from 83.28 to 16.36), demonstrating that the localized strain and quantum confinement in the SiGe pocket region significantly dampen charge modulation and wavefunction behavior. Among the three configurations, the Si Source-SiGe Pocket-Si Channel-Si Drain is most prone to quantum effects, with the highest sensitivity drop, indicating that quantum confinement in the pocket region plays a dominant role in influencing the overall device performance. This is also evident in the threshold voltage sensitivity, where the SiGe Source-Si Channel-Si Drain configuration experienced a significant drop in sensitivity (by 94% from 234.29 to 19.96) due to reduced charge modulation and quantum suppression. The findings underscore the importance of considering quantum effects, especially at nanoscale dimensions, for accurate device modeling and biosensor performance prediction. Future studies could explore the integration of alternative materials with different bandgap characteristics, such as transition metal dichalcogenides (TMDs), to potentially mitigate quantum suppression and enhance the biosensing performance in TFETs. Further research could also investigate the impact of higher-level quantum corrections, such as including scattering effects in quantum transport models, and the exploration of multi-material heterostructures to optimize sensitivity and selectivity for specific biomolecule detection applications.

5.5. Conclusion and Future work

This chapter demonstrated the importance of Bohm Quantum Potential (BQP)-based quantum analysis in understanding and optimizing Tunnel Field-Effect Transistors (TFETs) for low-power electronics and biosensing. Quantum effects, such as tunneling and confinement, were shown to be critical for TFET performance, especially in dual-metal double-gate architectures and SiGe-based heterojunctions. The study highlighted the potential of TFETs in biosensing, leveraging enhanced tunneling effects and quantum-aware models to achieve high sensitivity and low power consumption. The BQP framework proved superior in capturing these effects, offering valuable insights into carrier dynamics and device behavior that traditional models often overlook.

Future work will focus on advancing BQP-based methodologies by incorporating higher-order quantum effects and integrating them with frameworks like NEGF or density functional theory for multi-scale modeling. Exploring novel materials, such as 2D semiconductors and heterostructures, alongside innovative device geometries like nanowires and vertical TFETs, will further enhance performance. In biosensing, optimizing surface functionalization and developing multi-analyte detection capabilities will broaden TFET applications. Experimental validation of the proposed models, along with scalability for mass production, will be key to transitioning TFETs from theoretical research to practical use in next-generation electronics and diagnostics.

Chapter 6:

Quantum correction models and Parabolic Quantum Well Model

6.1. Introduction to Parabolic Quantum Well Model and Multi-Well Photodetectors

6.2. Device structure, Simulation of $In_{(1-x)}Ga_xAs_yP_{(1-y)}$/InP **wideband Multi-Well Photodetectors** *using k.p Method*

6.3. Other Quantum correction models

6.4. Conclusion and Future Work

6.1. Introduction to Parabolic Quantum Well Model and Multi-Well Photodetectors

Quantum wells are structures where charge carriers are confined in one dimension, allowing motion in the other two dimensions.

In a typical quantum well, charge carriers are confined between two barriers made from materials with a wider bandgap than the well material itself. This creates discrete energy states, which the carriers occupy according to their quantum mechanical properties. The size of the quantum well, often in the range of a few nanometers, determines the energy spacing between these levels. The smaller the quantum well, the greater the spacing between energy levels, and this quantization affects the absorption and emission of light.

In photodetectors, quantum wells enhance the interaction between light and the semiconductor material. When photons of a specific energy are incident on the photodetector, they excite charge carriers in the quantum wells. These carriers then move through the device, generating an electrical current that can be measured. The quantum well structure is advantageous because it provides a higher absorption cross-section and more efficient carrier collection than bulk materials. Additionally, the discrete energy states in the quantum well lead to more precise control over the absorption spectrum, allowing the device to be tuned to specific wavelengths of light.

Wideband photo detectors are vital elements in contemporary communication sys- tems, as they enable the reception of a wide array of optical signals. This functionality allows them to adeptly manage multiple wavelengths, which is essential for systems employing wavelength division multiplexing (WDM) [308]. The capability to detect light across an extensive frequency range markedly boosts data transmission speeds. Wideband photodetectors can proficiently capture rapidly fluctuating optical signals, which is crucial for high-speed applications in optical fiber networks [309], [310].

. Various types of quantum wells can be used in multi-well photodetectors, depending on the desired properties of the device. The most common types of quantum wells used in these devices include:

Type-I Quantum Wells: In these wells, both electrons and holes are confined in the same material, resulting in a direct bandgap. This configuration is ideal for applications such as light absorption and emission, as the electron-hole pairs (excitons) are tightly bound and easily recombine to emit light.

Type-II Quantum Wells: In these wells, the electrons and holes are confined in different materials, leading to an indirect bandgap. Type-II quantum wells can be used in devices that require carrier separation, as the spatial separation of electrons and holes reduces recombination and enhances carrier transport. This is advantageous for photodetectors, where efficient charge collection is essential.

Unlike traditional single-layer photodetectors, multi-well structures offer superior quantum efficiency and faster response times. By incorporating multiple quantum wells, they boost light absorption and reduce surface recombination losses, resulting in higher sensitivity and faster operation—critical for high-speed communication applications.

While single quantum well (SQW) photodetectors have demonstrated promising results, multi-quantum-well (MQW) structures offer notable advantages in performance, tunability, and efficiency. In MQW photodetectors, several quantum wells are vertically stacked and separated by barrier layers, forming a periodic heterostructure that enhances optical absorption and carrier dynamics compared to single-well devices.

Enhanced Absorption Efficiency:

Multiple wells allow greater interaction with incident photons, increasing total absorption and enabling detection over a broader spectral range. This is particularly beneficial for optical communication and spectroscopy, where wide spectral sensitivity is essential.

Improved Carrier Collection:

Multi-well structures facilitate efficient carrier transfer between wells through tunneling or thermal excitation, minimizing recombination losses and improving photocurrent collection compared to single-well configurations.

Higher Quantum Efficiency:

The probability of photon absorption and carrier generation increases with the number of wells, leading to higher quantum efficiency (QE)—the ratio of photo-generated carriers to incident photons.

Wavelength Tunability:

By adjusting well width, barrier thickness, and composition, MQW photodetectors can be spectrally tuned. This tunability enables multi-wavelength or broadband detection, crucial for systems employing dense wavelength division multiplexing (DWDM) and emerging LiFi technologies.

Designing MQW photodetectors requires precise control of material composition, layer thickness, and interface quality. Growth techniques such as Molecular Beam Epitaxy (MBE) and Metal-Organic Chemical Vapor Deposition (MOCVD) are typically employed to ensure atomic-scale precision.

Barrier materials with wider bandgaps confine carriers within the wells, and their thickness critically affects quantum confinement, tunneling probability, and energy level spacing. Therefore, careful optimization of well–barrier parameters is essential to achieve desired spectral and transport properties.

MQW photodetectors find extensive use in high-speed optical communication, infrared imaging, LiFi, and spectral sensing. Their enhanced responsivity and tunability make them ideal for detecting signals across diverse wavelengths, improving the bandwidth and sensitivity of communication networks and optoelectronic sensors.

The performance of MQW photodetectors is governed by the dynamics of carrier generation, transport, recombination, and scattering, which are inherently more complex than in SQW devices due to inter-well interactions.

Carrier Injection:

Photon absorption excites electrons from the valence to conduction band within the wells. The efficiency of injection depends on the optical transition matrix elements and alignment of subband energies with the incident photon energy.

Carrier Transport:

Carriers traverse multiple wells either by quantum tunneling or thermionic emission, depending on barrier height and spacing. Optimally designed barriers balance confinement and inter-well coupling, enhancing overall carrier mobility and collection efficiency.

Carrier Recombination:

Recombination reduces the available carrier population for current generation. In MQW systems, recombination occurs within wells and at interfaces. Reducing recombination is possible through type-II band alignment or spatial separation of electrons and holes, which extends carrier lifetime.

Scattering Mechanisms:

Carrier mobility is influenced by phonon, impurity, and carrier–carrier scattering. These processes, sensitive to temperature and material quality, can limit response speed and efficiency. High-quality epitaxial growth and optimized layer design help mitigate scattering losses.

The behavior of carriers in MQW photodetectors is dominated by quantum confinement, which quantizes energy levels within each well. Modeling these effects using parabolic or square quantum well approximations enables analytical derivation of subband energies, wavefunctions, and transition probabilities. These models form the theoretical foundation for understanding responsivity, absorption spectra, and carrier transport mechanisms in multi-well structures.

Tbale 6.1. Key Differences of Single and Multiple Qunatum Well

Parameter	Single Quantum Well (SQW) Photodetector	Multiple Quantum Well (MQW) Photodetector
Structure	Contains a single quantum well between two barrier layers.	Consists of several quantum wells separated by barrier layers, forming a periodic heterostructure.
Absorption Efficiency	Limited absorption due to a single active layer interacting with photons.	Enhanced absorption as multiple wells interact with the incident light, increasing optical path and quantum efficiency.
Spectral Response	Typically narrowband, sensitive to specific photon energies corresponding to discrete subband transitions.	Broad or tunable spectral response due to different well thicknesses or compositions allowing absorption across wider wavelengths.
Carrier Collection	Carriers may recombine before reaching contacts, reducing collection efficiency.	Improved carrier transport through tunneling and coupling between wells, enhancing collection efficiency.
Quantum Efficiency (QE)	Lower QE since fewer photons are absorbed and converted to carriers.	Higher QE because multiple wells increase the probability of photon absorption and carrier generation.
Carrier Recombination	Fewer recombination pathways, but efficiency limited by single absorption region.	Higher recombination possibilities between wells; mitigated through design optimization and type-II structures.
Wavelength Tunability	Limited; fixed by the dimensions and material of the single well.	Highly tunable through variation in well thickness, barrier height, or alloy composition across multiple wells.

6.2. Optimization and Simulation of $In_{(1-x)}Ga_xAs_yP_{(1-y)}/InP$ wideband Multi-Well Photodetectors for Communication Systems using k.p Method

Wideband photo detectors are critical components in modern com- munication systems, enabling high-speed data transmission and improved signal fidelity. This section presents a study on the simulation and optimization aspects of InGaAsP/InP multi-well photo detectors, focusing on their application in communication systems wavelength range ~1000 nm to ~2000 nm,. InGaAsP/InP multi-well photodetectors leverage the unique properties of multi-quantum wells (MQWs) to enhance optical detection and performance. These devices utilize the bandgap engineering flexibility of $In_{(1-x)}Ga_xAs_yP_{(1-y)}/InP$ materials to achieve efficient light absorption across specific wavelength ranges while maintaining high speed and sensitivity [311], [312]. The composition of InGaAsP can be tailored by adjusting the ratios of indium, gallium, arsenic, and phosphorus, enabling tunable electronic and optical properties crucial for photodetectors operating across diverse wavelengths, particularly in communication systems [313], [313]. Studies have shown that the growth temperature significantly influences the composition of InGaAsP films grown by MOVPE, with temperature-dependent variations in photoluminescence wavelength and lattice mismatch, especially in quaternary alloys with shorter bandgap wavelengths [314]. Another investigation focused on developing high-power 890 nm semiconductor laser pump sources for 3.9 μm mid-infrared fiber lasers by optimizing the epitaxial growth of 10-layer InGaAs/GaAsP quantum wells, improving gain and conduction band step height [315]. Wang et al. explored the tunable bandgap and photoemissive properties of quaternary $In_{(1-x)}Ga_xAs_yP_{(1-y)}$ demonstrating its superiority over GaAs and InGaAs for extending spectral response and enhancing sensitivity at 1.06 μm wavelengths [316]. Malik et al. proposed an efficient tapered coupling mechanism for monolithic integration on $In_{(1-x)}Ga_xAs_yP_{(1-y)}$ /InP quantum well structures, achieving significant reductions in coupling and insertion losses through impurity-free QW intermixing and optimized epitaxial designs [317]. Increasing the indium content lowers the bandgap, enabling longer wavelength detection suitable for applications like telecommunications, but higher mole fractions can increase defect densities and dark currents, impacting performance in sensitive applications. An optimized mole fraction enhances light absorption in the active layer, improving overall

photodetector performance, which is critical for high-speed optical communication [318]. Changes in mole fraction can also lead to thermal stability issues and variations in lattice parameters, affecting structural integrity [319], [320]. Maintaining lattice matching with the InP substrate through precise mole fraction control reduces stress and potential defects during fabrication. Additionally, design optimizations that minimize recombination losses further enhance device efficiency, vital for fast-readout applications such as real-time interactive communications [321], [322], [323]. We investigate the properties of $In_{(1-x)}Ga_xAs_yP_{(1-y)}$/InP photo detectors with change in mole fraction of As as it influences device performance, such as well and barrier energy gap, dark current and photo current. Using simulation tools, we model the electronic band structure and carrier transport mechanisms within the photo detectors, employing the k•p method and quantum well models. We ex- plore various optimization metrics including responsively, quantum efficiency, bandwidth, and noise analysis.

Device Structure

Fig 6.1: Schematic of the device used in simulation.

This device , as depicted in figure 6.1., The device structure begins with a top contact made of $In_{(1-x)}Ga_xAs_\gamma P_{(1-y)}$, approximately 100 nm thick and heavily doped n-type (1.2×10^{18} cm^{-3}), which serves as the top electrical contact for efficient carrier collection and ensures good ohmic contact due to its high doping. Beneath this lies Barrier 1, composed of ~50 nm of nearly intrinsic InP (~1×10^{11} cm^{-3}), providing confinement between the contact and the first quantum well. The first quantum well consists of ~4 nm of $In_{(1-x)}Ga_xAs_\gamma P_{(1-y)}$, n-type doped ($1.2\times10^{18}$ cm^{-3}), which acts as the first active region where photon absorption excites carriers between discrete subbands. Barrier 2, another ~50 nm layer of intrinsic InP, separates the first and second quantum wells to maintain discrete energy levels. The second quantum well mirrors the first in composition and thickness (~4 nm of n-type $In_{(1-x)}Ga_xAs_\gamma P_{(1-y)}$) and contributes to enhanced absorption and device responsivity. Following this, Barrier 3, again ~50 nm of intrinsic InP, provides confinement between the second and third wells. The third quantum well, similar in structure (~4 nm n-type $In_{(1-x)}Ga_xAs_\gamma P_{(1-y)}$), further improves bandwidth and absorption efficiency. Below the wells, Barrier 4 (~50 nm of intrinsic InP) isolates the active regions from the bottom contact, which is composed of ~100 nm of n-type $In_{(1-x)}Ga_xAs_\gamma P_{(1-y)}$ (1.2×10^{18} cm^{-3}) and collects carriers, serving as the bottom electrode. Overall, this layered configuration ensures efficient carrier confinement, absorption, and collection, optimizing the device's optical and electrical performance. This structure approximates the conditions studied by [320] .

The core concept of Multiple Quantum Well (MQW) photodetectors revolves around employing multiple thin semiconductor layers that generate distinct quantum states due to quantum confinement effects. When light interacts with these quantum wells, photons can elevate electrons from their initial ground state to higher energy levels. Once in these excited states, the electrons can either contribute to photocurrent or recombine with holes, enabling the detection of infrared radiation. MQW photodetectors take advantage of inter-subband transitions, where electrons are excited between different quantized energy levels within the conduction band. This adaptability allows photodetectors to be engineered for sensitivity to specific wavelengths by modifying the band structure through variations in the composition and thickness of the quantum wells. Additionally, n-doping fills the ground state of the quantum wells with electrons, ensuring effective detection as photons are absorbed.

Simulation methodology

The simulation uses a mesh specification with fine granularity, particularly in the active region, to accurately model the potential and carrier distribution. Regions are defined for the top contact, barriers, wells, and bottom contact, each with specific material compositions. Doping concentrations are adjusted to ensure minimal artifacts in the potential over the active region. Below is the summery of the models and methods used for the simulation.

Table. 6.2. Summary of models used in the simulation

Parameter	**Model**	**Purpose**
Band Structure	ZB.TWO or WZ.KP	Multi-band (k.p) band coupling (light, heavy holes, conduction).
Quantum Confinement	KP.FEM.LAGRANGE or KP.FEM.HERMITE	FEM solution of Schrödinger eqn.
Wavefunction Penetration	WELL.MARGIN	Allows wavefunction overlap into barriers.
Capture–Escape	WELL.CAPT	Coupled 2D–3D carrier dynamics.
Self-Consistent Quantum Correction	WELL.SELFCON	Couples quantum charge with Poisson.
Superlattice Effects	SLATT, SL.GEOM, SL.NUMBER	Quantum coupling of multiple wells (minibands).
Optical Absorption	beam qwip tr.matrix	Transfer-matrix–based optical generation.
Recombination	SRH, Radiative, Auger (if declared)	Non-radiative loss modeling.

The parabolic quantum well model calculates bound state energies, which are used to study optoelectronic properties like gain, radiative recombination, and absorption. These energies are obtained by solving the Schrödinger equation along discrete slices in the quantization direction. Effective masses and band-edge parameters come from k·p-based models which correspond to zincblende and wurtzite materials and the number of valence bands used.

This model assumes the effective mass approximation, but its accuracy decreases away from the Brillouin zone center due to intermixing of hole states. While it provides quick results by solving in momentum space, its optical response is less reliable for regions with large mass variations

between the well and barriers. Advanced k·p models offer better accuracy but are computationally more intensive.

The quantum well model is activated using the QWELL parameter in the REGION or MODELS statement. The solver orientation (1DY by default) can be changed using the SP.GEOMETRY parameter. Adjacent quantum wells with the same orientation are merged into one unless separated using the QWNUM parameter.

The model expands the Schrödinger solution domain into neighboring regions to capture wavefunction penetration into barriers, controlled by the WELL.MARGIN parameter (default: 0.01 microns). Overlapping wavefunctions are allowed, and barrier bands are adjusted to avoid bound states at the edges during calculations.

Parameters such as WELL.GAMMA0 and WELL.TAUN are used to define the broadening of Lorentzians and the capture lifetime of carriers by the wells, respectively.

Models including Fermi-Dirac statistics, temperature effects, and the k.p method are specified. The k·p method relies on perturbation theory to approximate the band struc- ture near a specific point in the Brillouin zone—most commonly at the Γ point (k = 0), which is the center of the Brillouin zone. The calculation is executed based on Bloch theorem that guarantees that the single-electron eigenstates in the crystal have a periodic form. The electronic states at the Γ point serve as a basis for expanding the band structure to other points in the Brillouin zone. First the k·p method approximates the wavefunctions along with expansion coefficients by which the band structure is expanded in terms of the wavevector k in matrix equations and defines a Hamiltonian matrix, where each element represents interactions between different bands. This matrix depends on both the momentum operator (p) and the wavevector (k). At the Γ point, the Hamiltonian is diagonal, meaning each band is independent. However, as k increases (i.e., away from the Γ point), off-diagonal terms appear, representing coupl- ing between the bands. Since an exact solution would require infinite states, a per- turbation approximation (Löwdin perturbation method) is applied. This approximation reduces the problem by focusing on a small set of energy bands near the band gap, decoupling them from the other, higher-energy bands. This perturbation expands

the Hamiltonian in powers of k, limiting the area of the Brillouin zone that can be cov- ered, but allowing for a computationally efficient solution.

To represent the coupled quantum wells, the **SLATT** parameter in the REGION statement has been used to group adjacent regions into a single superlattice domain. To separate regions into different superlattice domains, the **SL.NUMBER** parameter has been used. The direction of the Schrödinger solver is specified with **SL.GEOM**.

Here the same band structure is formed as the quantum well model.

The collective states of the superlattice are determined using the Quantum Transmitting Boundary Method (QTBM), which solves a nonlinear Schrödinger equation while accounting for open-boundary conditions. Based on the wavefunction's spatial distribution and energy relative to the band edge, eigenstates are categorized as either bound (localized) or traveling (propagating).

The Quantum Transmitting Boundary Method (QTBM) is employed specifically for analyzing ballistic transport and is mathematically equivalent to the Non-Equilibrium Green's Function (NEGF) approach under the ballistic regime. In this framework, the wave function Ψ\PsiΨ represents the coefficient describing carrier states within the device, from which all measurable quantities — such as charge density and current density — are obtained. In general, QTBM solves the steady-state Schrödinger equation for an open system:

At the contacts, QTBM assumes that the wavefunction is a sum of incoming and outgoing (transmitted/reflected) plane waves. Inside the device, the potential is arbitrary (e.g., due to wells and barriers), and the wavefunction is solved numerically. Thus, instead of confining the wavefunction, QTBM transmits it through the structure, simulating realistic current flow.

The simulation turns couples the capture-escape and drift-diffusion models for a self- consistent solution. Bound states in each well are computed, allowing for up to two states to confirm only one bound state exists. The x and y compositions are defined in the REGION statement using the Y.COMP parameters. The relationship between x and y that fulfills this condition is expressed as follows:

$$x = \frac{0.1896 * Y.COMP}{0.4176 - (0.0125 * Y.COMP)}$$

The simulation method uses Newton's method with specified error tolerance to solve the system equations. An optical source is defined using the transfer matrix method for multiple reflections and coherent light propagation within the active layer. Initial solutions are calculated, and the dark current is evaluated by stepping the collector voltage from 0 to 1V. The system is reset for optical response calculations, and inter- subband spectra are obtained at various collector voltages. Spectral response is analyzed over a wavelength range from 1 to 2 micrometers.

6.3.1. Result and Discussions

7. The variation of arsenic (As) mole fraction in the $In_{(1-x)}Ga_xAs_yP_{(1-y)}$/InP multiple quantum well (MQW) structure has been shown in figure 6.2. As experimentally validated by Sten Seifert [324], the lattice-matched As mole fractions of 0.24, 0.42 and 0.69 has been studied. The variation has a significant effect on the electron concentration (figure 6.2(a), 6.2(b)), dark current(figure 6.3, photocur- rent(figure 6.4), quantum efficiency, and spectral characteristics.
8. As shown in figure 6.2(a) and 6.2(b) the overall electron concentration in an $In_{(1-x)}Ga_xAs_yP_{(1-y)}$/InP multiple quantum well (MQW) structure decreases with in- creasing arsenic (As) mole fraction due to several interconnected factors involving band structure, density of states, carrier dynamics, and quantum confinement effects. The incorporation of deep-level defects linked to arsenic can generate confined ener- gy states inside the bandgap, limiting the population of electrons thermally excited for conduction in the conduction band. Consequently, this reduces the total effective car- rier density. The addition of arsenic (As) may also result in a compensatory decline in electron density due to a higher concentration of acceptor-like states caused by misfit dislocations or point defects. These states tend to trap free electrons, thereby reducing the number of carriers available for conduction. Although it might seem logical to expect that increasing dopants would boost carrier concentration, the dynamics in As- rich alloys complicate this interaction, frequently leading to a net reduction in free carrier density as the As content rises.

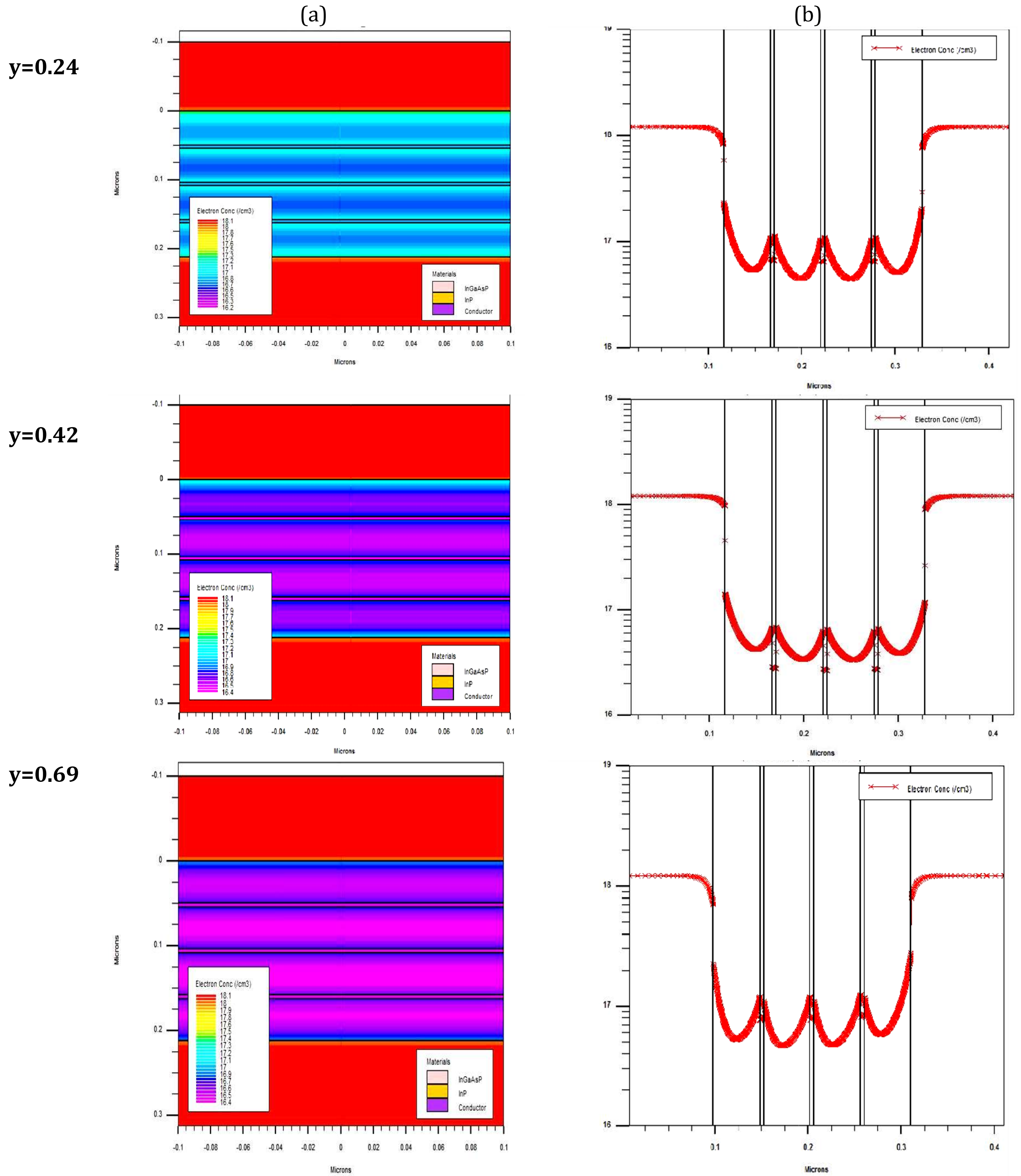

Fig.6.2. Impact of varying As mole fraction in $In_{(1-x)}Ga_xAs_yP_{(1-y)}$ /InP MQW structure on electron concentration (2a, 2b).

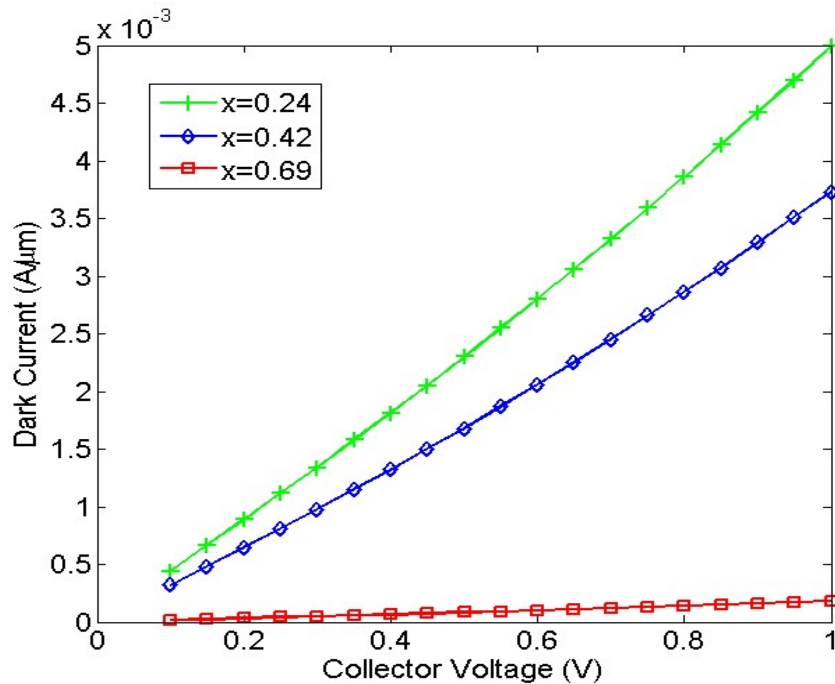

Fig.6.3. Impact of varying As mole fraction in $In_{(1-x)}Ga_xAs_yP_{(1-y)}$ /InP MQW structure on dark current.

When the As mole fraction increases from 0.24 to 0.69, the dark current decreases from 0.000665A to 0.00018A, as depicted in figure 6.3. This is a direct result of the bandgap widening as the As mole fraction increases. A wider bandgap reduces the number of thermally excited carriers, which in turn reduces the dark current. The decrease in electron concentration is con- sistent with this observation since fewer carriers are thermally excited across the larg- er bandgap into the conduction band. For y = 0.24, the bandgap is narrower, allowing more electrons to be thermally excited into the conduction band, leading to higher dark current. As y increases, the bandgap widens, leading to lower thermal carrier generation and thus lower dark current and electron concentration. The photocurrent (figure 6.4)) shows a similar trend, decreasing from 0.000665A at y = 0.24 to 0.00018A at y = 0.69. The calculation of quantum efficiency presents a performance analysis of a photodetector under varying optical wavelengths (λ) and collector current conditions (y=0.24, y=0.42 and y=0.69) with a constant light intensity of 1.00×103.

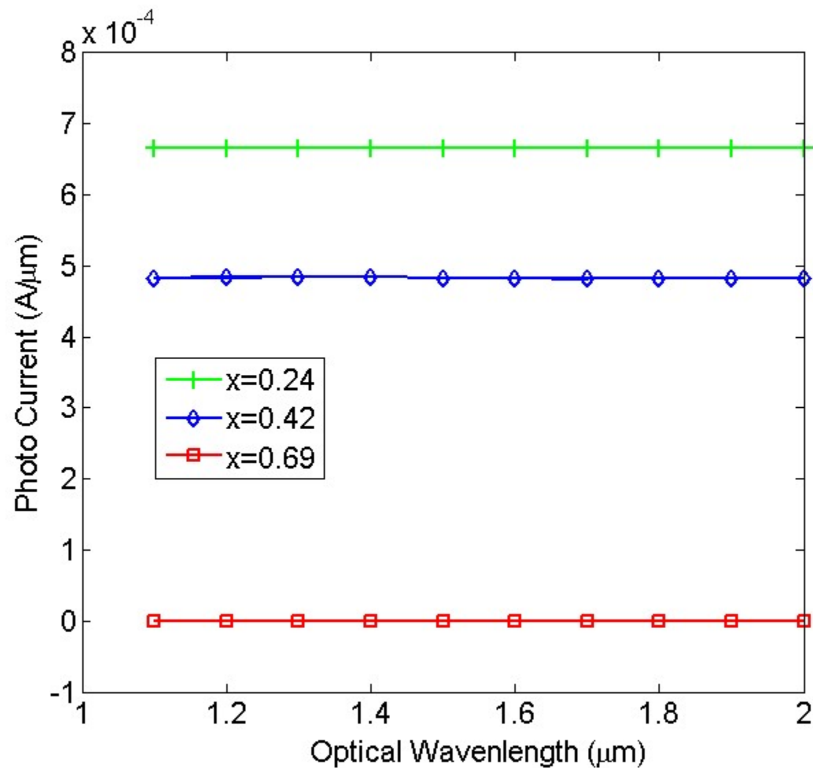

Fig.6.4. Impact of varying As mole fraction in $In_{(1-x)}Ga_xAs_yP_{(1-y)}$/InP MQW structure on photocurrent.

The responsivity, calculated as photocurrent divided by optical power, shows values of 6.65, 4.84, and 1.90 at y=0. 24, y=0.42, and y=0.69 respectively, for all wavelengths. Quantum efficiency (η) [derived using the formula (Responsivity*h*c)/(q*wavelength), with responsively=(photocurrent/optical power)], decreases with increasing wavelength, indicating reduced sensitivity at longer wavelengths. For y=0.24, η decreases from 8.24 to 4.12; for y=0.42, from 6.01 to 2.99; and for y=0.69, from 2.36 to 1.12, showing a consistent trend. These results demonstrate the dependence of responsivity and quantum efficiency on the optical wavelength and collector current. This performance is significantly higher than that of SiGe/Si MQW photodetectors, which achieve around 0.1% at 1.3 μm and up to 20% at 0.95 μm [325]. While HgCdTe-based photodetectors exhibit quantum efficiencies

exceeding 70%, our results are promising, especially considering the trade-offs between material composition and performance [326]. Furthermore, our quantum efficiency surpasses GaN-based MQW photo- detectors, which report external quantum efficiencies of 5% to 8%, particularly within a broad temperature range [327]. This highlights the potential of our $In_{(1-x)}Ga_xAs_yP_{(1-y)}$/InP MQW structures for applications requiring high efficiency across a wide wave- length spectrum, making them a strong candidate for next-generation communication systems.

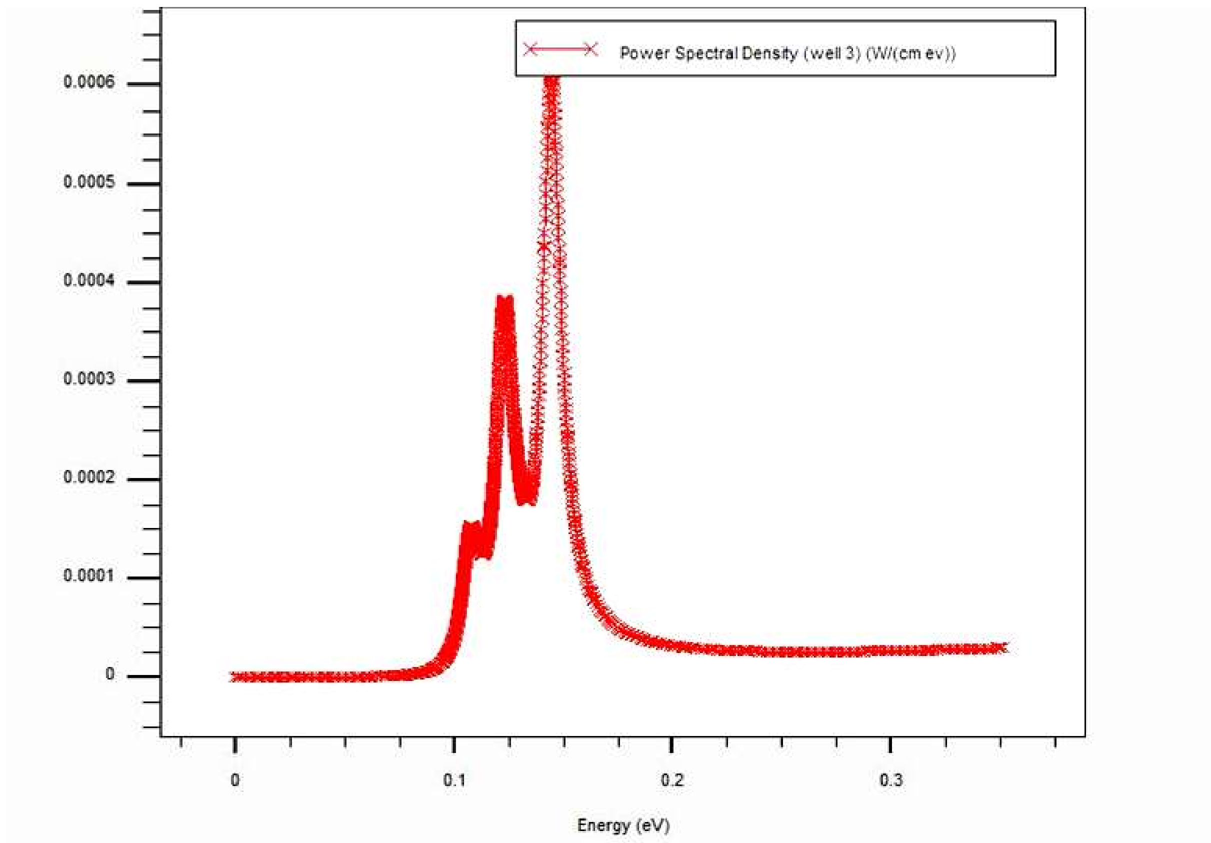

(a)

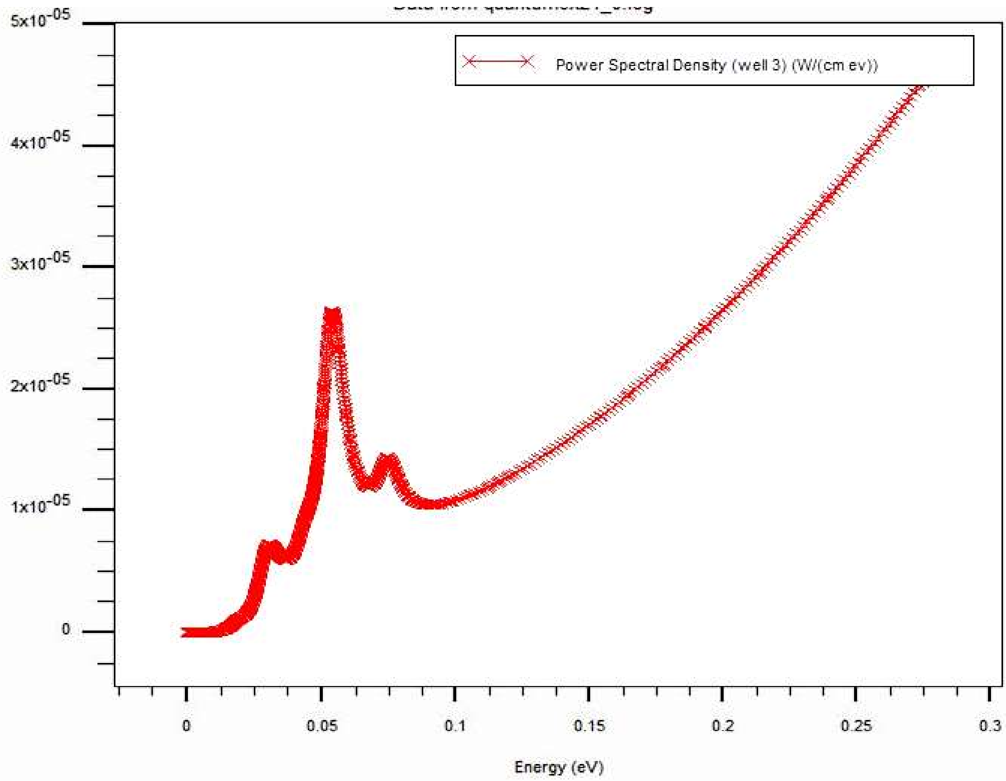

(b)

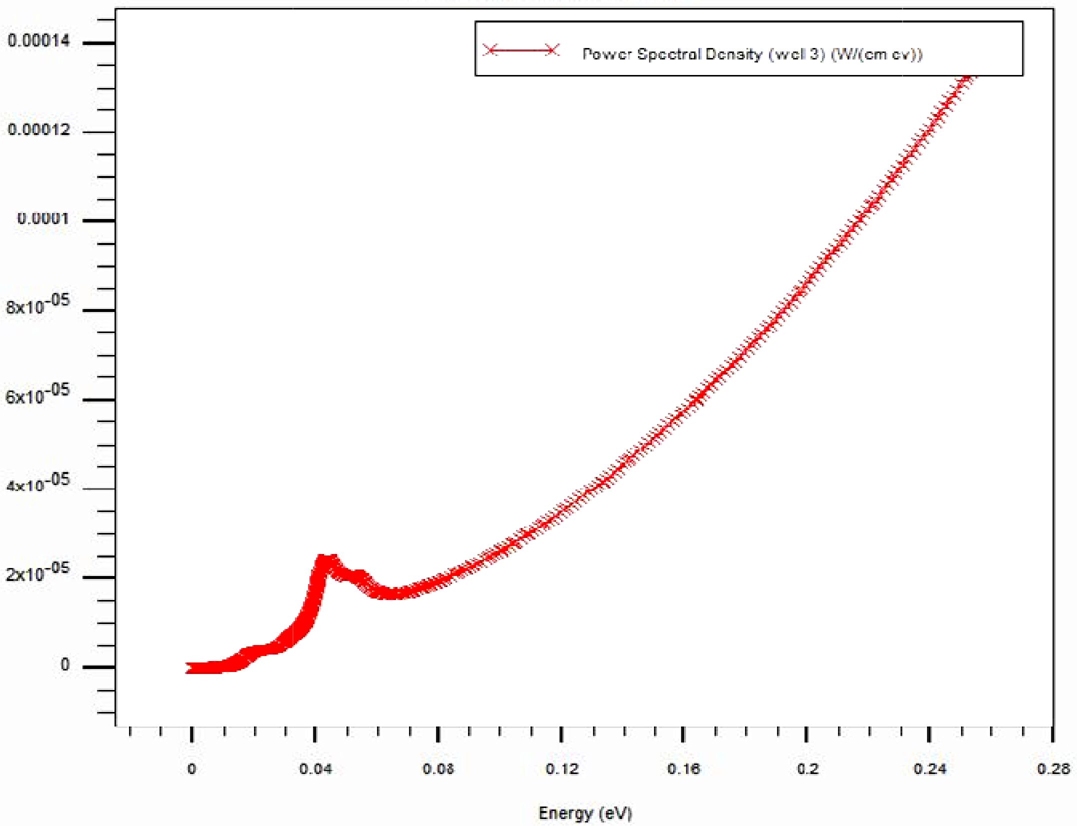

(c)

Fig 6.5. Power Spectral Density at (a) y=0.24 (b) y=0.42 and (c) y=0.69.

The bandwidth-efficiency trade-off in InGaAsP/InP multiwell photodetectors in figure 6.5 arises from quantum confinement effects and material properties. Increasing the As mole fraction widens the bandgap, resulting in lower quantum efficiency due to fewer electron transitions across the bandgap. However, this wider bandgap enhances response time, allowing the photodetector to operate at higher frequencies (larger bandwidth).

At lower As mole fractions (y=0.24), the quantum efficiency is higher due to a greater density of states near the band edge, but the bandwidth is limited by slower carrier dynamics. In contrast, at higher As mole fractions (y=0.69), faster carrier dynamics reduce the density of states, increasing bandwidth but lowering quantum efficiency. This trade-off between quantum efficiency and bandwidth reflects the interplay between material properties and carrier behavior in such multiwell structures.

Our study of an $In_{(1-x)}Ga_xAs_yP_{(1-y)}$/InP multiwell photodetector using k.p model shows that increasing the As mole fraction leads to lower dark current, lower photocurrent, and a broadening of the power spectral density (PSD). As the As mole fraction increases, the PSD exhibits both a shift and a rise. The broader PSD is attributed to a combination of reduced low-frequency noise, dominated by 1/f noise (flicker noise), and increased high-frequency noise, primarily from shot noise and thermal noise. The narrowing bandgap with higher As mole fractions enhances quantum confinement effects, which in turn increase scattering rates and reduce carrier mobility, leading to higher overall noise levels.

At lower As mole fractions (narrower bandgap), thermally excited carriers and recombination rates are higher, contributing to increased 1/f noise and low-frequency shot noise. Conversely, at higher As mole fractions, the wider bandgap suppresses low-frequency noise due to reduced dark current and electron concentration. However, high-frequency noise becomes more prominent as faster carrier dynamics and scattering rates dominate.

For y=0.69, the photodetector shows significantly amplified high-frequency noise components due to its faster response time. This leads to an elevated noise floor across the spectrum, with the PSD shifting towards higher frequencies as low-frequency noise

diminishes. The results highlight the critical balance required between sensitivity and noise performance, as the magnitude and distribution of noise in the PSD are strongly influenced by the As mole fraction.

6.3 Other Quantum correction models

While advanced quantum transport frameworks such as NEGF and QTBM explicitly solve for quantum states, and DG and BQP models approximate confinement effects through potential-based corrections, the previous sections primarily focused on quantum transport formalism in multi-quantum-well structures, where carrier tunneling, coupling, and quantized states dominate the optical and electronic behavior.

However, in nanoscale MOS and heterostructure devices, quantum mechanical confinement near the gate oxide interface gives rise to the formation of a two-dimensional electron gas (2DEG), whose effects are not adequately captured by these models. To address this, several semi-empirical quantum correction approaches have been developed to incorporate confinement-induced band-edge shifts within classical device simulators. Among them, the Van Dort and Hänsch models are particularly important, as they provide simplified yet physically meaningful ways to account for quantum confinement and carrier redistribution in regions where 2DEG formation occurs—offering a computationally efficient alternative to full quantum transport calculations.

Van Dort Model:[328], [329]

The Van Dort model accounts for quantum mechanical effects by widening the energy bandgap (ΔE) in the inversion channel of MOSFETs, specifically addressing the reduction in the density of states caused by quantum confinement. This model adjusts the conduction band edge as a function of the perpendicular electric field near the gate oxide interface. The formula:

$$\Delta \mathrm{E} = (\mathrm{B.DORT}).\beta.\left(\frac{\varepsilon}{4\mathrm{qk_B T_L}}\right)^{1/3} (E_{\downarrow} - E_C)^{\alpha} g(y) \tag{6.1}$$

Where

ΔE	Quantum confinement–induced change in energy bandgap,
β	Empirical fitting parameter (Van Dort parameter)
(q)	Electron charge
(k_B)	Boltzmann constant
(T)	Absolute temperature
ε	Permittivity of silicon
(L)	Characteristic length or inversion layer width
(g(y))	Field-dependent correction function, typically related to $(E_{\downarrow} - E_C)^{\alpha}$
$E_{\downarrow}$	Perpendicular electric field component
E_C	Conduction band edge
α	Empirical exponent (~1/3 or 1/2 depending on calibration)

corrects for quantum mechanical carrier behavior, but it occasionally results in unphysical outcomes, such as an excess of electron concentration near the oxide interface. Despite this limitation, the Van Dort model is valuable for modeling capacitance-voltage (C–V) characteristics in nanoscale devices.

Hansch Model:[330]

The Hansch model, originally developed for quantitative structure-activity relationship (QSAR) analysis in medicinal chemistry, is a mathematical approach that helps relate chemical structure to biological activity. In the context of semiconductor device physics, its adaptation provides a way to incorporate quantum mechanical corrections into simulations of charge transport and device behavior at the nanoscale. This extension of the Hansch model helps better account for the quantum confinement effects in modern semiconductor devices, like MOSFETs, where the classical models struggle.

In semiconductor devices at the nanoscale, quantum effects become prominent due to the confinement of electrons and the formation of quantum wells. Classical models tend to overestimate carrier densities near the interface of semiconductors and insulators (like

Si/SiO_2 in MOSFETs). The Hansch model corrects this by introducing quantum mechanical considerations. The confinement causes quantization of energy levels, leading to a modified density of states and an effective increase in the bandgap energy. The Hansch model accounts for these shifts to make the simulated behavior closer to reality.
In the adaptation of the Hansch model to semiconductors, certain quantum descriptors are utilized. These quantum descriptors are metrics that characterize the quantum mechanical nature of the system, such as :

- Electron wavefunctions in confined structures (quantum wells)
- Energy eigenstates of the carriers (electrons/holes) within the semiconductor
- Carrier concentration near interfaces, where the quantum confinement is strongest

While the exact mathematical form of the Hansch model in semiconductor physics may differ depending on the specific application, the general approach involves modifying the classical drift-diffusion equations by adding corrections based on quantum mechanical principles.

For example, in the context of a MOSFET, the quantum correction factor introduced by the Hansch model would modify the electron density profile near the gate oxide interface [89-91]:

$$n_q(z) = n_c(z) \times exp(-\frac{E_g{}^q(z)}{k_B T}) \tag{6.2}$$

$n_q(z)$ is the quantum-corrected electron density at position z, $n_c(z)$) is the classically predicted electron density, $E_g{}^q$ is the quantum-corrected bandgap energy, which depends on factors like gate electric field and oxide thickness, k_B is Boltzmann's constant, T is the temperature [331].

Table. 6.3. Summary of Comparison of quantum correction models

Aspect	Van Dort Model	Hänsch Model
Primary Focus	Quantum confinement in inversion	Quantum transport and tunneling
Complexity	Low	Moderate to High
Scope	Narrow	Moderate
Strength	Easy integration with classical models	Includes broader quantum effects
Limitation	Limited to confinement effects	Computationally intensive

Each model serves specific aspects of quantum modeling and is selected based on the physical phenomena of interest and the computational resources available.

6.4 Conclusion and Future Work

The analysis of $In_{(1-x)}Ga_xAs_yP_{(1-y)}$/InP materials and the corresponding multi-well photodetector design highlights several critical factors that contribute to the enhanced performance of these devices. The wideband nature of the photodetectors is achieved by tailoring the material composition of the wells to create energy band alignments that are optimal for broad-spectrum light absorption. The ability to tune the material properties through the $In_{(1-x)}Ga_xAs_yP_{(1-y)}$/InP alloy system allows for precise control over the photodetector's absorption spectrum, making it suitable for a wide range of optical communication applications. This flexibility is one of the key strengths of the multi-well photodetector design and makes it highly adaptable for future communication systems.

One of the major achievements in this study is the demonstration of improved carrier dynamics in multi-well structures. Quantum confinement effects in the individual wells, along with the ability to engineer barriers between wells, facilitate better carrier transport, lower recombination rates, and enhanced overall device efficiency. By simulating and optimizing the carrier dynamics within the multi-well system, we can ensure that the photodetector exhibits high quantum efficiency, reduced dark current, and fast response times, all essential features for next-generation high-speed communication systems.

The k·p method simulations allow for the fine-tuning of the quantum well parameters and material compositions to achieve a desired performance, and the insights gained from these simulations help to inform experimental designs. The model also proves instrumental in understanding the effects of multi-well interactions, providing a detailed analysis of carrier transport and recombination across the stacked quantum wells. This detailed understanding aids in improving photodetector reliability, efficiency, and adaptability to changing environmental conditions, making these devices robust for real-world applications.

Overall, this study underscores the importance of material optimization, carrier dynamics control, and quantum confinement effects in the design of high-performance multi-well photodetectors for communication systems. The successful simulation and optimization of $In_{(1-x)}Ga_xAs_yP_{(1-y)}/InP$ multi-well structures using the k·p method offer a clear path forward for the development of photodetectors capable of supporting the bandwidth and speed requirements of modern communication technologies.

While this study has provided valuable insights into the design and optimization of multi-well photodetectors, there remain several opportunities for future research and development to further enhance the performance of these devices and push the boundaries of their application in communication systems.

Although the k·p method has proven to be an effective tool for simulating the electronic structure of multi-well photodetectors, future work could explore the integration of more advanced simulation techniques to model additional phenomena that may impact device performance. One promising avenue is the use of non-equilibrium Green's function (NEGF) methods to simulate quantum transport in multi-well structures more accurately. The NEGF approach can capture the quantum mechanical nature of electron transport in greater detail, especially for devices operating in the ballistic or quasi-ballistic regimes, where scattering and other non-thermal effects become more pronounced. By combining

k·p and NEGF methods, a more complete and accurate model for carrier transport in multi-well photodetectors can be developed.

Additionally, integrating Monte Carlo simulations could further enhance the accuracy of modeling carrier dynamics and recombination processes. The combination of these techniques would enable researchers to better predict the behavior of photodetectors under different operational conditions, including varying temperatures and optical input powers.

Another critical area for future work is the exploration of new material systems that go beyond the traditional $In_{(1-x)}Ga_xAs_yP_{(1-y)}$ /InP alloys. Although this material system is well-suited for multi-well photodetectors, there are emerging materials that may offer even better performance, such as two-dimensional (2D) materials or perovskite-based materials. 2D materials, such as graphene or transition metal dichalcogenides (TMDs), have unique electronic properties that could be leveraged to improve the quantum efficiency and response speed of multi-well photodetectors. The integration of these materials into multi-well photodetector designs would require a detailed understanding of their electronic band structures and their interactions with the quantum wells.

Chapter 7:

Conclusion and Future Work

7.1 Conclusion

7.2 Future Work

Conclusion

The present thesis, titled *"Semiclassical and Quantum Modeling of Low-Dimensional Devices and Sensors,"* systematically investigates the intricate interplay between transport mechanisms, material physics, and device architecture in nanoscale sensing technologies. With the continuous downscaling of device dimensions, quantum mechanical phenomena such as tunneling, confinement, and quantization increasingly dominate carrier transport behavior, necessitating a transition from classical to semiclassical and fully quantum mechanical modeling. Through a sequence of studies employing calibrated TCAD simulations and analytical frameworks — including Bohm Quantum Potential (BQP), Schrödinger–Poisson self-consistent models, and Non-Equilibrium Green's Function (NEGF) formalisms — the thesis provides an in-depth understanding of the electrostatics and transport phenomena shaping device operation in low-dimensional sensors.

The chapter 3 of this work presents a p-type $MoTe_2$-based PMOSFET hydrogen sensor featuring charge-plasma-based source and drain formation using palladium electrodes. The elimination of physical doping in $MoTe_2$ through charge plasma engineering simplifies fabrication while simultaneously enlarging the effective sensing area at both terminals. The NEGF-based quantum transport simulation reveals that below the 10 nm regime, quantum confinement and tunneling strongly influence carrier dynamics, leading to non-classical potential profiles and density of states modulation. The results confirm that palladium-induced plasma formation effectively enhances sensitivity by modulating surface charge

density in the presence of H_2 molecules. Furthermore, the analysis underscores that device dimension scaling — particularly the reduction of channel length and oxide thickness — is crucial for optimizing gate control and improving transconductance response. The study thus establishes a quantum-aware design framework for next-generation TMD-based CMOS-compatible hydrogen sensors.

The investigation in chapter 4 focuses on the $Al_xGa_{1-x}N$/GaN Double Channel High Electron Mobility Transistor (DCHEMT) structure, examining inter-channel coupling effects and their influence on C-ERB2 biomarker detection. The simulation results, calibrated against experimental mobility and polarization models, demonstrate that inter-channel electrostatic coupling significantly alters quantum well depth, barrier height, and 2DEG distribution, which in turn govern biosensor sensitivity. Variation of the Al mole fraction modifies spontaneous and piezoelectric polarization fields, thereby tailoring carrier confinement. Higher Al concentration in the upper channel enhances the electric field coupling, improving sensitivity, while excessive Al composition in the lower channel induces adverse polarization, reducing net response. The study quantitatively correlates mole fraction variations with sensitivity metrics and drain current modulation, illustrating the delicate balance between electrostatic control and quantum well engineering. This work provides a critical foundation for designing polarization-controlled biosensors capable of early cancer diagnostics through detection of biomarkers such as C-ERB2, while outlining challenges like stability, selectivity, and material uniformity for practical biomedical deployment.

In the chapter 5, a detailed analysis of strain-engineered SiGe heterojunction Tunnel Field-Effect Transistors (TFETs) is conducted to explore the impact of Bohm Quantum Potential (BQP) and Schrödinger–Poisson calibrated modeling on biosensor performance. Three device configurations — Ge Source–SiGe Channel–Si Drain, SiGe Source–Si Channel–Si Drain, and Si Source–SiGe Pocket–Si Channel–Si Drain — were examined to capture strain-modulated variations in electrostatic potential and tunneling probability. The inclusion of quantum corrections revealed sensitivity suppression up to 62% and notable threshold voltage modulation due to enhanced carrier localization and reduced band-to-band

tunneling (BTBT) transparency. The SiGe pocket configuration, while classically exhibiting high selectivity, showed significant degradation under quantum confinement, emphasizing the need to balance strain engineering and quantum correction effects. This part of the study establishes a clear link between quantum potential-induced electrostatic distortion and device-level sensing degradation, contributing to a more accurate predictive modeling of TFET-based biosensors operating in the deep nanometer regime.

The chapter 6 investigates $In_{(1-x)}Ga_xAs_YP_{(1-Y)}/InP$ multi-quantum well (MQW) photodetectors, employing the k·p method to capture band structure evolution and optical transition behavior in the 1000–2000 nm wavelength range, relevant for optical communication and LiFi applications. The simulation results indicate that increasing arsenic (As) mole fraction reduces dark current and thermal noise by widening the bandgap, but simultaneously decreases photocurrent and quantum efficiency due to diminished carrier excitation probability. The spectral response narrowing observed with higher As composition reveals a fundamental bandwidth–efficiency trade-off, where enhanced high-speed response comes at the expense of reduced photon-to-electron conversion. This analysis underscores the necessity of band structure tuning for achieving optimal balance between responsivity, bandwidth, and noise, marking a significant step toward quantum-efficient, wideband photonic sensors.

Collectively, these four investigations reinforce a unifying theme: transport modeling serves as the fundamental bridge between material physics and device functionality in low-dimensional systems.

Each study demonstrates that semi-classical frameworks (Density Gradient, Energy Balance) provide computationally efficient insights into intermediate regimes, while fully quantum mechanical models (NEGF, BQP, Schrödinger–Poisson) are indispensable for capturing confinement, tunneling, and carrier correlation effects in ultra-scaled devices.

Moreover, by incorporating structural engineering principles—including charge plasma doping, inter-channel coupling, strain modulation, and quantum well band engineering—the thesis establishes a multi-scale modeling approach that holistically describes

electrostatics, transport, and sensitivity across diverse device architectures. The consistent use of TCAD-based modeling underlines the adaptability of available frameworks to explore a broad range of transport regimes even without access to specialized quantum solvers.

Future Scope

Building upon the simulation-driven insights and transport-based analyses presented in this thesis, several future research directions are envisioned to further advance the understanding and application of quantum and semiclassical transport in low-dimensional sensors:

1. Deeper Exploration of Device Physics:

Future work will delve more deeply into the underlying physics of carrier transport, quantum confinement, and tunneling mechanisms, extending beyond numerical simulation to develop rigorous physics-based analytical models. These models will provide closed-form relations linking material properties, electrostatics, and quantum effects to observable sensing characteristics such as current modulation, sensitivity, and response time.

2. Analytical Modeling for Quantum and Semiclassical Sensors:

Building on the existing NEGF and BQP simulation framework, the goal is to derive analytical formulations that capture the essential device physics of TMD MOSFETs, TFETs, and quantum well photodetectors. Such analytical models will not only enhance theoretical understanding but also serve as compact models for circuit-level integration and co-design of sensor interfaces.

3. Sensor Array and Network Integration:

With increasing interest in smart sensing systems, the next stage of this research will involve the extension of single-device models to sensor arrays and networks. The integration of multiple low-dimensional sensors into interconnected platforms will allow investigation of collective response, power, interference, and calibration strategies under

practical operating conditions. These studies will support the design of multi-sensor quantum-aware networks for Internet of Things (IoT) and cyber-physical applications.

4. Experimental Validation and Prototype Development:

A key objective is to translate the simulated device structures into experimental prototypes through collaboration with fabrication and characterization facilities. Emphasis will be placed on validating the NEGF and BQP-based predictions via electrical, optical, and spectroscopic measurements. This will include benchmarking sensor performance under real environmental and biochemical conditions, bridging the gap between theoretical prediction and physical realization.

5. Inclusion of Scattering, Phonon, and Trap Effects:

The current simulations assume coherent transport conditions. Future studies will incorporate phonon interactions, surface roughness, impurity scattering, and defect states, thereby enhancing the physical accuracy of the quantum transport models and making them more reflective of realistic operational scenarios.

6. Progression Toward Quantum-Enabled Sensing and Single-Photon Detection:

Finally, the long-term vision includes extending the developed models toward quantum sensors, particularly single-photon detection devices and quantum dot-based architectures. These systems represent the ultimate limit of sensing performance, where quantum coherence and discrete energy states govern detection dynamics. Modeling and experimentally realizing such devices will represent a natural evolution of the current work toward the quantum limit of sensitivity.

In summary, the future direction of this research emphasizes a transition from simulation-based modeling to physics-grounded analytical frameworks, supported by experimental validation and network-level implementation. By integrating analytical theory, fabrication insights, and multi-sensor architectures, the next phase aims to establish a comprehensive physics-to-system approach for quantum and semiclassical sensors, ultimately guiding the development of next-generation intelligent and quantum-enabled sensor technologies.

References

[1] C. A. Mack, “Fifty Years of Moore’s Law,” *IEEE Trans. Semicond. Manuf.*, vol. 24, no. 2, pp. 202–207, May 2011, doi: 10.1109/TSM.2010.2096437.

[2] R. R. Schaller, “Moore’s law: past, present and future,” *IEEE Spectr.*, vol. 34, no. 6, pp. 52–59, Jun. 1997, doi: 10.1109/6.591665.

[3] P. A. Gargini, “The IRDS is paving the way for chips acts around the world,” in *International Conference on Extreme Ultraviolet Lithography 2023*, K. G. Ronse, P. A. Gargini, P. P. Naulleau, and T. Itani, Eds., Monterey, United States: SPIE, Dec. 2023, p. 31. doi: 10.1117/12.2685867.

[4] M. L. Pedersen, M. J. Frank, and G. Biele, “The drift diffusion model as the choice rule in reinforcement learning,” *Psychon. Bull. Rev.*, vol. 24, no. 4, pp. 1234–1251, Aug. 2017, doi: 10.3758/s13423-016-1199-y.

[5] D. Fudenberg, W. Newey, P. Strack, and T. Strzalecki, “Testing the drift-diffusion model,” *Proc. Natl. Acad. Sci.*, vol. 117, no. 52, pp. 33141–33148, Dec. 2020, doi: 10.1073/pnas.2011446117.

[6] R. Pinnau, “A REVIEW ON THE QUANTUM DRIFT DIFFUSION MODEL,” *Transp. Theory Stat. Phys.*, vol. 31, no. 4–6, pp. 367–395, Jan. 2002, doi: 10.1081/TT-120015506.

[7] N. Briggs *et al.*, “A roadmap for electronic grade 2D materials,” *2D Mater.*, vol. 6, no. 2, p. 022001, Jan. 2019, doi: 10.1088/2053-1583/aaf836.

[8] S. Alam, M. Asaduzzaman Chowdhury, A. Shahid, R. Alam, and A. Rahim, “Synthesis of emerging two-dimensional (2D) materials – Advances, challenges and prospects,” *FlatChem*, vol. 30, p. 100305, Nov. 2021, doi: 10.1016/j.flatc.2021.100305.

[9] M. Chhowalla, Z. Liu, and H. Zhang, “Two-dimensional transition metal dichalcogenide (TMD) nanosheets,” *Chem. Soc. Rev.*, vol. 44, no. 9, pp. 2584–2586, 2015, doi: 10.1039/C5CS90037A.

[10] J. Köster *et al.*, “Evaluation of TEM methods for their signature of the number of layers in mono- and few-layer TMDs as exemplified by MoS2 and $MoTe_2$,” *Micron*, vol. 160, p. 103303, Sep. 2022, doi: 10.1016/j.micron.2022.103303.

[11] O. Hayden, R. Agarwal, and W. Lu, “Semiconductor nanowire devices,” *Nano Today*, vol. 3, no. 5–6, pp. 12–22, Oct. 2008, doi: 10.1016/S1748-0132(08)70061-6.

[12] J. Appenzeller, J. Knoch, M. T. Bjork, H. Riel, H. Schmid, and W. Riess, “Toward Nanowire Electronics,” *IEEE Trans. Electron Devices*, vol. 55, no. 11, pp. 2827–2845, Nov. 2008, doi: 10.1109/TED.2008.2008011.

[13] S.-W. Chung, J.-Y. Yu, and J. R. Heath, “Silicon nanowire devices,” *Appl. Phys. Lett.*, vol. 76, no. 15, pp. 2068–2070, Apr. 2000, doi: 10.1063/1.126257.

[14] H.-E. Jung and M. Shin, “Surface-Roughness-Limited Mean Free Path in Si Nanowire FETs,” Apr. 20, 2013, *arXiv*: arXiv:1304.5597. doi: 10.48550/arXiv.1304.5597.

[15] M. A. U. Khan, A. Srivastava, C. Mayberry, and A. K. Sharma, “Analytical Current Transport Modeling of Monolayer Molybdenum Disulfide-Based Dual Gate Tunnel Field Effect Transistor,” *IEEE Trans. Nanotechnol.*, vol. 19, pp. 620–627, 2020, doi: 10.1109/TNANO.2020.3012772.

[16] D. A. B. Miller, “QUANTUM WELL OPTOELECTRONIC SWITCHING DEVICES,” *Int. J. High Speed Electron. Syst.*, vol. 01, no. 01, pp. 19–46, Mar. 1990, doi: 10.1142/S0129156490000034.

[17] T. H. Wood, “Multiple quantum well (MQW) waveguide modulators,” *J. Light. Technol.*, vol. 6, no. 6, pp. 743–757, Jun. 1988, doi: 10.1109/50.4063.

[18] H. C. Liu, “Chapter 3 Quantum Well Infrared Photodetector Physics and Novel Devices,” in *Semiconductors and Semimetals*, vol. 62, Elsevier, 1999, pp. 129–196. doi: 10.1016/S0080-8784(08)60306-3.

[19] R. Abdel-Karim, Y. Reda, and A. Abdel-Fattah, “Review—Nanostructured Materials-Based Nanosensors,” *J. Electrochem. Soc.*, vol. 167, no. 3, p. 037554, Jan. 2020, doi: 10.1149/1945-7111/ab67aa.

[20] M. Javaid, A. Haleem, R. P. Singh, S. Rab, and R. Suman, “Exploring the potential of nanosensors: A brief overview,” *Sens. Int.*, vol. 2, p. 100130, 2021, doi: 10.1016/j.sintl.2021.100130.

[21] J. Riu, A. Maroto, and F. Rius, “Nanosensors in environmental analysis,” *Talanta*, vol. 69, no. 2, pp. 288–301, Apr. 2006, doi: 10.1016/j.talanta.2005.09.045.

[22] Y. Kim *et al.*, “Recent Advances in Functionalization and Hybridization of Two-Dimensional Transition Metal Dichalcogenide for Gas Sensor,” *Adv. Eng. Mater.*, vol. 26, no. 1, p. 2301063, Jan. 2024, doi: 10.1002/adem.202301063.

[23] N. N. Reddy and D. K. Panda, “A Comprehensive Review on Tunnel Field-Effect Transistor (TFET) Based Biosensors: Recent Advances and Future Prospects on Device Structure and Sensitivity,” *Silicon*, vol. 13, no. 9, pp. 3085–3100, Sep. 2021, doi: 10.1007/s12633-020-00657-1.

[24] D. Vook, M. Cao, P. J. Vande Voorde, R. W. Dutton, Z. Yu, and M. G. Ancona, “Density-gradient analysis of MOS tunneling,” *IEEE Trans. Electron Devices*, vol. 47, no. 12, pp. 2310–2319, Dec. 2000, doi: 10.1109/16.887013.

[25] D. Connelly, Zhiping Yu, and D. Yergeau, “Macroscopic simulation of quantum mechanical effects in 2-D MOS devices via the density gradient method,” *IEEE Trans. Electron Devices*, vol. 49, no. 4, pp. 619–626, Apr. 2002, doi: 10.1109/16.992871.

[26] G. Baccarani, E. Gnani, A. Gnudi, S. Reggiani, and M. Rudan, “Theoretical foundations of the quantum drift-diffusion and density-gradient models,” *Solid-State Electron.*, vol. 52, no. 4, pp. 526–532, Apr. 2008, doi: 10.1016/j.sse.2007.10.051.

[27] M. G. Ancona, “Density-gradient theory: a macroscopic approach to quantum confinement and tunneling in semiconductor devices,” *J. Comput. Electron.*, vol. 10, no. 1–2, pp. 65–97, Jun. 2011, doi: 10.1007/s10825-011-0356-9.

[28] A. Forghieri, R. Guerrieri, P. Ciampolini, A. Gnudi, M. Rudan, and G. Baccarani, “A new discretization strategy of the semiconductor equations comprising momentum and energy balance,” *IEEE Trans. Comput.-Aided Des. Integr. Circuits Syst.*, vol. 7, no. 2, pp. 231–242, Feb. 1988, doi: 10.1109/43.3153.

[29] Y. Omura, “An improved analytical solution of energy balance equation for short-channel SOI MOSFET’s and transverse-field-induced carrier heating,” *IEEE Trans. Electron Devices*, vol. 42, no. 2, pp. 301–306, Feb. 1995, doi: 10.1109/16.370065.

[30] M. Rudan, R. Brunetti, and S. Reggiani, Eds., *Springer handbook of semiconductor devices*. in Springer handbooks. Cham: Springer, 2023.

[31] J. T. Cushing, A. Fine, and S. Goldstein, Eds., *Bohmian mechanics and quantum theory: an appraisal*. in Boston studies in the philosophy of science, no. Volume 184. Dordrecht: Springer Science+Business Media, 1996.

[32] M. Lundstrom, *Fundamentals of nanotransistors*. in Lessons from nanoscience: a lecture notes series, no. vol. 6. New Jersey: World Scientific, 2018.

[33] M. J. Kumar, R. Vishnoi, and P. Pandey, *Tunnel field-effect transistors (TFET): modelling and simulations*, First edition. Hoboken: Wiley, 2017.

[34] T. R. Lenka and H. P. T. Nguyen, Eds., *HEMT technology and applications*. in Springer tracts in electrical and electronics engineering. Singapore: Springer, 2023.

[35] B. R. Nag, *Physics of Quantum Well Devices*. in Solid-State Science and Technology Library, no. v. 7. Dordrecht: Springer Netherlands, 2001.

[36] R. J. Martín-Palma and J. M. Martínez-Duart, “Semiconductor Quantum Nanostructures, Multiple Quantum Wells, and Superlattices,” in *Nanotechnology for Microelectronics and Photonics*, Elsevier, 2017, pp. 107–131. doi: 10.1016/B978-0-323-46176-4.00005-5.

[37] P. Kumar Nayak, Ed., *Two-dimensional Materials: Synthesis, Characterization and Potential Applications*. Erscheinungsort nicht ermittelbar: IntechOpen, 2016.

[38] “A theory of electrons and protons”.

[39] M. Mamone Capria (ed.), *Physics before and after Einstein*. Erscheinungsort nicht ermittelbar: IOS Press, 2005.

[40] J.-P. Vigier, “Louis de Broglie—Physicist and thinker,” *Found. Phys.*, vol. 12, no. 10, pp. 923–930, Oct. 1982, doi: 10.1007/BF01889266.

[41] H. H. Martens, “The uncertainty principle,” 1991, *Technische Universiteit Eindhoven*. doi: 10.6100/IR348359.

[42] H. Kragh, “A quantum discontinuity: The Schrödinger–Bohr dialogue,” in *ESI Lectures in Mathematics and Physics*, 1st ed., vol. 9, W. L. Reiter and J. Yngvason, Eds., EMS Press, 2013, pp. 135–151. doi: 10.4171/121-1/7.

[43] J. Gerratt, “General Theory of Spin-Coupled Wave Functions for Atoms and Molecules,” in *Advances in Atomic and Molecular Physics*, vol. 7, Elsevier, 1971, pp. 141–221. doi: 10.1016/S0065-2199(08)60360-7.

[44] F. Szmulowicz, “Kronig - Penney model: a new solution,” *Eur. J. Phys.*, vol. 18, no. 5, pp. 392–397, Sep. 1997, doi: 10.1088/0143-0807/18/5/015.

[45] K. Blotekjaer, “Transport equations for electrons in two-valley semiconductors,” *IEEE Trans. Electron Devices*, vol. 17, no. 1, pp. 38–47, Jan. 1970, doi: 10.1109/T-ED.1970.16921.

[46] G. Wachutka, “Consistent treatment of carrier emission and capture kinetics in electrothermal and energy transport models,” *Microelectron. J.*, vol. 26, no. 2–3, pp. 307–315, Mar. 1995, doi: 10.1016/0026-2692(95)98933-I.

[47] B. L. Hammond, P. J. Reynolds, and W. A. Lester, *Monte Carlo methods in ab initio quantum chemistry*. in World Scientific lecture and course notes in chemistry, no. v. 1. Singapore River Edge, N.J: World Scientific Pub. Co, 1994.

[48] M. Ryzhii, V. Ryzhii, and World Scientific (Firm), Eds., *Physics and modeling of tera-and nano-devices*. in Selected topics in electronics and systems, no. v. 47. Singapore Hackensack, N.J: World Scientific Pub. Co, 2008.

[49] M. Pourfath, *The Non-Equilibrium Green’s Function Method for Nanoscale Device Simulation*. in Computational Microelectronics Ser. Vienna: Springer Wien, 2014.

[50] D. Sholl, J. A. Steckel, and Sholl, *Density Functional Theory: a Practical Introduction*. Somerset: Wiley, 2011.

[51] D. A. Neamen, *Semiconductor physics and devices: basic principles*, 3rd ed. Boston: McGraw-Hill, 2003.

[52] A. Erlebach, K. H. Lee, and F. M. Bufler, “Empirical ballistic mobility model for drift-diffusion simulation,” in *2016 46th European Solid-State Device Research Conference (ESSDERC)*, Lausanne, Switzerland: IEEE, Sep. 2016, pp. 420–423. doi: 10.1109/ESSDERC.2016.7599675.

[53] D. Long and J. Myers, “Ionized-Impurity Scattering Mobility of Electrons in Silicon,” *Phys. Rev.*, vol. 115, no. 5, pp. 1107–1118, Sep. 1959, doi: 10.1103/PhysRev.115.1107.

[54] R. L. Boylestad and L. Nashelsky, *Electronic devices and circuit theory*, 3rd ed. Englewood Cliffs, N.J: Prentice-Hall, 1982.

[55] W. Hänsch, *The Drift Diffusion Equation and Its Applications in MOSFET Modeling*. in Computational Microelectronics Ser. Vienna: Springer Wien, 1991.

[56] S. Y. Kim *et al.*, “Design and Analysis of Sub-10 nm Junctionless Fin-Shaped Field-Effect Transistors,” *JSTSJournal Semicond. Technol. Sci.*, vol. 14, no. 5, pp. 508–517, Oct. 2014, doi: 10.5573/JSTS.2014.14.5.508.

[57] T. S. A. Samuel, Y. S. Song, S. Tayal, P. Vimalā, and S. B. Rahi, Eds., *Tunneling field effect transistors: design, modeling and applications*. in Materials, devices, and circuits. Boca Raton: CRC Press, 2023.

[58] I. Prigogine and S. A. Rice, Eds., *Advances in Chemical Physics*, 1st ed., vol. 25. in Advances in Chemical Physics, vol. 25. Wiley, 1974. doi: 10.1002/9780470143773.

[59] K. M. Schep, P. J. Kelly, and G. E. W. Bauer, “Ballistic transport and electronic structure,” *Phys. Rev. B*, vol. 57, no. 15, pp. 8907–8926, Apr. 1998, doi: 10.1103/PhysRevB.57.8907.

[60] S. Veeraraghavan and J. G. Fossum, “Short-channel effects in SOI MOSFETs,” *IEEE Trans. Electron Devices*, vol. 36, no. 3, pp. 522–528, Mar. 1989, doi: 10.1109/16.19963.

[61] T. H. Ning and C. T. Sah, “Theory of Scattering of Electrons in a Nondegenerate-Semiconductor-Surface Inversion Layer by Surface-Oxide Charges,” *Phys. Rev. B*, vol. 6, no. 12, pp. 4605–4613, Dec. 1972, doi: 10.1103/PhysRevB.6.4605.

[62] K. Yamasue and Y. Cho, “Spatial scale dependent impact of non-uniform interface defect distribution on field effect mobility in SiC MOSFETs,” *Microelectron. Reliab.*, vol. 114, p. 113829, Nov. 2020, doi: 10.1016/j.microrel.2020.113829.

[63] B. M. Tenbroek, M. S. L. Lee, W. Redman-White, J. T. Bunyan, and M. J. Uren, “Self-heating effects in SOI MOSFETs and their measurement by small signal conductance techniques,” *IEEE Trans. Electron Devices*, vol. 43, no. 12, pp. 2240–2248, Dec. 1996, doi: 10.1109/16.544417.

[64] N. Ben Abdallah, F. Méhats, and N. Vauchelet, “Analysis of a Drift-Diffusion-Schrödinger–Poisson model,” *Comptes Rendus Mathématique*, vol. 335, no. 12, pp. 1007–1012, Nov. 2002, doi: 10.1016/S1631-073X(02)02612-2.

[65] A. Wettstein, A. Schenk, and W. Fichtner, “Quantum device-simulation with the density-gradient model on unstructured grids,” *IEEE Trans. Electron Devices*, vol. 48, no. 2, pp. 279–284, Feb. 2001, doi: 10.1109/16.902727.

[66] Y. Li and S.-M. Yu, “A study of threshold voltage fluctuations of nanoscale double gate metal-oxide-semiconductor field effect transistors using quantum correction simulation,” *J. Comput. Electron.*, vol. 5, no. 2–3, pp. 125–129, Jul. 2006, doi: 10.1007/s10825-006-8831-4.

[67] R. C. Miller, A. C. Gossard, D. A. Kleinman, and O. Munteanu, "Parabolic quantum wells with the G a A s − Al x Ga 1 − x As system," *Phys. Rev. B*, vol. 29, no. 6, pp. 3740–3743, Mar. 1984, doi: 10.1103/PhysRevB.29.3740.

[68] M. Pourfath, *The Non-Equilibrium Green's Function Method for Nanoscale Device Simulation*. in Computational Microelectronics. Vienna: Springer Vienna, 2014. doi: 10.1007/978-3-7091-1800-9.

[69] N. Sano, K. Matsuzawa, M. Mukai, and N. Nakayama, "On discrete random dopant modeling in drift-diffusion simulations: physical meaning of `atomistic' dopants," *Microelectron. Reliab.*, vol. 42, no. 2, pp. 189–199, Feb. 2002, doi: 10.1016/S0026-2714(01)00138-X.

[70] R. Pinnau, "A REVIEW ON THE QUANTUM DRIFT DIFFUSION MODEL," *Transp. Theory Stat. Phys.*, vol. 31, no. 4–6, pp. 367–395, Jan. 2002, doi: 10.1081/TT-120015506.

[71] K. Konno, O. Matsushima, D. Navarro, and M. Miura-Mattausch, "Limit of validity of the drift-diffusion approximation for simulation of photodiode characteristics," *Appl. Phys. Lett.*, vol. 84, no. 8, pp. 1398–1400, Feb. 2004, doi: 10.1063/1.1650033.

[72] C. De Falco, E. Gatti, A. L. Lacaita, and R. Sacco, "Quantum-corrected drift-diffusion models for transport in semiconductor devices," *J. Comput. Phys.*, vol. 204, no. 2, pp. 533–561, Apr. 2005, doi: 10.1016/j.jcp.2004.10.029.

[73] N. Felekidis, A. Melianas, and M. Kemerink, "Nonequilibrium drift-diffusion model for organic semiconductor devices," *Phys. Rev. B*, vol. 94, no. 3, p. 035205, Jul. 2016, doi: 10.1103/PhysRevB.94.035205.

[74] D. Rossi, F. Santoni, M. Auf Der Maur, and A. Di Carlo, "A Multiparticle Drift-Diffusion Model and its Application to Organic and Inorganic Electronic Device Simulation," *IEEE Trans. Electron Devices*, vol. 66, no. 6, pp. 2715–2722, Jun. 2019, doi: 10.1109/TED.2019.2912521.

[75] A. Leone, A. Gnudi, and G. Baccarani, "Hydrodynamic simulation of semiconductor devices operating at low temperature," *IEEE Trans. Comput.-Aided Des. Integr. Circuits Syst.*, vol. 13, no. 11, pp. 1400–1408, Nov. 1994, doi: 10.1109/43.329268.

[76] H. Wang, W.-K. Shih, S. Green, S. Hareland, C. M. Maziar, and Al. F. Tasch, "Hydrodynamic (HD) Simulation of *N* -Channel MOSFET'swith a Computationally Efficient Inversion LayerQuantization Model," *VLSI Des.*, vol. 8, no. 1–4, pp. 423–428, Jan. 1998, doi: 10.1155/1998/19078.

[77] F. M. Bufler, A. Schenk, and W. Fichtner, "Monte Carlo, Hydrodynamic and Drift-Diffusion Simulation of Scaled Double-Gate MOSFETs," *J. Comput. Electron.*, vol. 2, no. 2–4, pp. 81–84, Dec. 2003, doi: 10.1023/B:JCEL.0000011403.57401.55.

[78] R. Granzner *et al.*, "Simulation of nanoscale MOSFETs using modified drift-diffusion and hydrodynamic models and comparison with Monte Carlo results," *Microelectron. Eng.*, vol. 83, no. 2, pp. 241–246, Feb. 2006, doi: 10.1016/j.mee.2005.08.003.

[79] Y. Apanovich, E. Lyumkis, B. Polsky, A. Shur, and P. Blakey, “Steady-state and transient analysis of submicron devices using energy balance and simplified hydrodynamic models,” *IEEE Trans. Comput.-Aided Des. Integr. Circuits Syst.*, vol. 13, no. 6, pp. 702–711, Jun. 1994, doi: 10.1109/43.285243.

[80] D. C. Kerr, N. Goldsman, and I. D. Mayergoyz, “Three-Dimensional Hydrodynamic Modelingof MOSFET Devices,” *VLSI Des.*, vol. 6, no. 1–4, pp. 261–265, Jan. 1998, doi: 10.1155/1998/60859.

[81] Z. Butkovic and A. Baric, “Energy balance simulation of submicrometer Si n-MOSFETs,” in *MELECON ’98. 9th Mediterranean Electrotechnical Conference. Proceedings (Cat. No.98CH36056)*, Tel-Aviv, Israel: IEEE, 1998, pp. 354–357. doi: 10.1109/MELCON.1998.692425.

[82] R. Van Leeuwen, N. E. Dahlen, G. Stefanucci, C.-O. Almbladh, and U. Von Barth, “Introduction to the Keldysh Formalism,” in *Time-Dependent Density Functional Theory*, vol. 706, M. A. L. Marques, C. A. Ullrich, F. Nogueira, A. Rubio, K. Burke, and E. K. U. Gross, Eds., in Lecture Notes in Physics, vol. 706. , Berlin, Heidelberg: Springer Berlin Heidelberg, 2006, pp. 33–59. doi: 10.1007/3-540-35426-3_3.

[83] C. A. Polanco, “Nonequilibrium Green’s functions (NEGF) in vibrational energy transport: a topical review,” *Nanoscale Microscale Thermophys. Eng.*, vol. 25, no. 1, pp. 1–24, Jan. 2021, doi: 10.1080/15567265.2021.1881193.

[84] N. Mingo and L. Yang, “Phonon transport in nanowires coated with an amorphous material: An atomistic Green’s function approach,” *Phys. Rev. B*, vol. 68, no. 24, p. 245406, Dec. 2003, doi: 10.1103/PhysRevB.68.245406.

[85] T. Yamamoto and K. Watanabe, “Nonequilibrium Green’s Function Approach to Phonon Transport in Defective Carbon Nanotubes,” *Phys. Rev. Lett.*, vol. 96, no. 25, p. 255503, Jun. 2006, doi: 10.1103/PhysRevLett.96.255503.

[86] J. Dai and Z. Tian, “Rigorous formalism of anharmonic atomistic Green’s function for three-dimensional interfaces,” *Phys. Rev. B*, vol. 101, no. 4, p. 041301, Jan. 2020, doi: 10.1103/PhysRevB.101.041301.

[87] R. Ravishankar, G. Kathawala, U. Ravaioli, S. Hasan, and M. Lundstrom, “Comparison of Monte Carlo and NEGF Simulations of Double Gate MOSFETs,” *J. Comput. Electron.*, vol. 4, no. 1–2, pp. 39–43, Apr. 2005, doi: 10.1007/s10825-005-7104-y.

[88] A. Martinez *et al.*, “A Self-Consistent Full 3-D Real-Space NEGF Simulator for Studying Nonperturbative Effects in Nano-MOSFETs,” *IEEE Trans. Electron Devices*, vol. 54, no. 9, pp. 2213–2222, Sep. 2007, doi: 10.1109/TED.2007.902867.

[89] N. Neophytou, S. Ahmed, and G. Klimeck, “Non-equilibrium Green’s function (NEGF) simulation of metallic carbon nanotubes including vacancy defects,” *J. Comput. Electron.*, vol. 6, no. 1–3, pp. 317–320, Sep. 2007, doi: 10.1007/s10825-006-0116-4.

[90] H. R. Khan, D. Mamaluy, and D. Vasileska, "3D NEGF quantum transport simulator for modeling ballistic transport in nano FinFETs," *J. Phys. Conf. Ser.*, vol. 107, p. 012007, Mar. 2008, doi: 10.1088/1742-6596/107/1/012007.

[91] M. D. Ganji, Z. Sohbatzadeh, and A. Khosravi, "Spin-dependent transport characteristics of Fe met-cars," *Struct. Chem.*, vol. 25, no. 2, pp. 551–559, Apr. 2014, doi: 10.1007/s11224-013-0328-8.

[92] D. Munteanu, J. L. Autran, M. Moreau, and M. Houssa, "Electron transport through high-κ dielectric barriers: A non-equilibrium Green's function (NEGF) study," *J. Non-Cryst. Solids*, vol. 355, no. 18–21, pp. 1180–1184, Jul. 2009, doi: 10.1016/j.jnoncrysol.2009.03.006.

[93] N. Seoane, A. Martinez, A. R. Brown, J. R. Barker, and A. Asenov, "Current Variability in Si Nanowire MOSFETs Due to Random Dopants in the Source/Drain Regions: A Fully 3-D NEGF Simulation Study," *IEEE Trans. Electron Devices*, vol. 56, no. 7, pp. 1388–1395, Jul. 2009, doi: 10.1109/TED.2009.2021357.

[94] E. Dastjerdy, R. Ghayour, and H. Sarvari, "3D quantum mechanical simulation of square nanowire MOSFETs by using NEGF method," *Open Phys.*, vol. 9, no. 2, pp. 472–481, Apr. 2011, doi: 10.2478/s11534-010-0097-6.

[95] X. Ji, J. Zhang, Y. Wang, H. Qian, and Z. Yu, "A theoretical model for metal–graphene contact resistance using a DFT–NEGF method," *Phys. Chem. Chem. Phys.*, vol. 15, no. 41, p. 17883, 2013, doi: 10.1039/c3cp52589a.

[96] W. Wang *et al.*, "Transport study of gate and channel engineering on the surrounding-gate CNTFETs based on NEGF quantum theory," *J. Comput. Electron.*, vol. 13, no. 1, pp. 192–197, Mar. 2014, doi: 10.1007/s10825-013-0499-y.

[97] M. Syaputra, S. A. Wella, T. D. K. Wungu, A. Purqon, and Suprijadi, "Study on transport properties of silicene monolayer under external field using NEGF method," presented at the THE 5TH INTERNATIONAL CONFERENCE ON MATHEMATICS AND NATURAL SCIENCES, Bandung, Indonesia, 2015, p. 080012. doi: 10.1063/1.4930743.

[98] M. Mahdi, Md. A. Hossain, and J. K. Saha, "Performance Analysis of an Empirical Model of Carbon Nanotube Field Effect Transistor," in *2018 International Conference on Innovation in Engineering and Technology (ICIET)*, Dhaka, Bangladesh: IEEE, Dec. 2018, pp. 1–6. doi: 10.1109/CIET.2018.8660775.

[99] J. Pang *et al.*, "DFT coupled with NEGF study of ultra-sensitive HCN and HNC gases detection and distinct *I* – *V* response based on phosphorene," *Phys. Chem. Chem. Phys.*, vol. 19, no. 45, pp. 30852–30860, 2017, doi: 10.1039/C7CP03941G.

[100] W. Zhou *et al.*, "DFT coupled with NEGF study of a promising two-dimensional channel material: black phosphorene-type GaTeCl," *Nanoscale*, vol. 10, no. 7, pp. 3350–3355, 2018, doi: 10.1039/C7NR08252E.

[101] R. Sellers *et al.*, “Optimization of HgCdTe nBn photodetectors utilizing a superlattice barrier,” *J. Appl. Phys.*, vol. 137, no. 8, p. 084502, Feb. 2025, doi: 10.1063/5.0245126.

[102] L. S. J. Wilson, J. R. Barker, and A. E. Martinez, “DFT/NEGF study of discrete dopants in Si/III–V 3D FET,” *J. Phys. Condens. Matter*, vol. 31, no. 14, p. 144003, Apr. 2019, doi: 10.1088/1361-648X/aaffb2.

[103] M. G. Pala and D. Esseni, “Quantum transport models based on NEGF and empirical pseudopotentials for accurate modeling of nanoscale electron devices,” *J. Appl. Phys.*, vol. 126, no. 5, p. 055703, Aug. 2019, doi: 10.1063/1.5109187.

[104] A. Martinez, A. Price, R. Valin, M. Aldegunde, and J. Barker, “Impact of phonon scattering in Si/GaAs/InGaAs nanowires and FinFets: a NEGF perspective,” *J. Comput. Electron.*, vol. 15, no. 4, pp. 1130–1147, Dec. 2016, doi: 10.1007/s10825-016-0851-0.

[105] X. Hu *et al.*, “DFT coupled with NEGF study of the electronic properties and ballistic transport performances of 2D $SbSiTe_3$,” *Nanoscale*, vol. 12, no. 18, pp. 9958–9963, 2020, doi: 10.1039/D0NR01838D.

[106] E. Pavarini, E. Koch, Institute for Advanced Simulation, and Forschungszentrum Jülich, Eds., *Simulating correlations with computers*. in Schriften des Forschungszentrums Jülich Reihe Modeling and Simulation, no. Band/volume 11. Jülich: Forschungszentrum Jülich, Zentralbibliothek, Verlag, 2021.

[107] A. Raman, D. Shekhar, and N. Kumar, *Sub-Micron Semiconductor Devices: Design and Applications*, 1st ed. Boca Raton: CRC Press, 2022. doi: 10.1201/9781003126393.

[108] A. Thakur and N. Sarkar, “A tutorial on the NEGF method for electron transport in devices and defective materials,” *Eur. Phys. J. B*, vol. 96, no. 8, p. 113, Aug. 2023, doi: 10.1140/epjb/s10051-023-00580-5.

[109] P. Poobalan, Y. Wong, N. E. Alias, S. Isaak, and M. L. P. Tan, “Quantum transport properties of AB bilayer graphene via tight-binding approach with NEGF formalisms,” *Appl. Phys. A*, vol. 130, no. 8, p. 561, Aug. 2024, doi: 10.1007/s00339-024-07695-1.

[110] S. Agrawal, A. Srivastava, and G. Kaushal, “Performance metrics of doped graphene nanoribbons based nanoscale interconnects: DFT and NEGF analysis,” *Solid State Commun.*, vol. 380, p. 115389, Mar. 2024, doi: 10.1016/j.ssc.2023.115389.

[111] M.-Q. Zhu and X.-F. Wang, “High-performance heavy metal sensor based on GeS monolayer: A DFT-NEGF study,” *Chem. Phys. Lett.*, vol. 876, p. 142236, Oct. 2025, doi: 10.1016/j.cplett.2025.142236.

[112] M. R. Munna and M. Alam, “Bismuthene nanoribbon topological field-effect transistor: a DFT-NEGF-based study,” *New J. Phys.*, vol. 27, no. 7, p. 073505, Jul. 2025, doi: 10.1088/1367-2630/adf13f.

[113] A. Sakthi Balaji, A. Ramasamy, K. Janani Sivasankar, H. Rajalakshmi Mohanraj, and D. John Thiruvadigal, “Low lattice thermal conductance of buckled GeTe/antimonene vdW interface device: A

DFT + NEGF study,” *Comput. Mater. Sci.*, vol. 252, p. 113784, Apr. 2025, doi: 10.1016/j.commatsci.2025.113784.

[114] P. Acharya, N. Kumar, A. Dixit, J. Lee, and V. Georgiev, “Impact of interface roughness correlation on resonant tunnelling diode variation,” *Sci. Rep.*, vol. 15, no. 1, p. 26815, Jul. 2025, doi: 10.1038/s41598-025-07720-0.

[115] A. Raman, R. Sachdeva, P. Kumar, and P. Singh, “Effect of SiGe-Composite Placement on Quantum Effects of a Nanowire FET Using NEGF,” *Silicon*, vol. 17, no. 2, pp. 259–266, Jan. 2025, doi: 10.1007/s12633-024-03197-0.

[116] A. Afzalian, “Ab-initio-NEGF Fundamental Roadmap for Carbon-Nanotube and Two-Dimensional-Material MOSFETs at the Scaling and VDD Limit,” 2025, *arXiv*. doi: 10.48550/ARXIV.2507.00599.

[117] L.-T. Wu and J.-C. Jiang, “Designing highly selective NO_2 and SO_3 sensors *via* doped and substituted polythiophene: a DFT, NEGF, and microkinetic study,” *J. Mater. Chem. A*, vol. 13, no. 38, pp. 32331–32343, 2025, doi: 10.1039/D5TA04096E.

[118] D. Vook, M. Cao, P. J. Vande Voorde, R. W. Dutton, Z. Yu, and M. G. Ancona, “Density-gradient analysis of MOS tunneling,” *IEEE Trans. Electron Devices*, vol. 47, no. 12, pp. 2310–2319, Dec. 2000, doi: 10.1109/16.887013.

[119] A. Wettstein, A. Schenk, and W. Fichtner, “Quantum device-simulation with the density-gradient model on unstructured grids,” *IEEE Trans. Electron Devices*, vol. 48, no. 2, pp. 279–284, Feb. 2001, doi: 10.1109/16.902727.

[120] A. Asenov, A. R. Brown, and J. R. Watling, “Quantum corrections in the simulation of decanano MOSFETs,” *Solid-State Electron.*, vol. 47, no. 7, pp. 1141–1145, Jul. 2003, doi: 10.1016/S0038-1101(03)00030-3.

[121] S. Jin, Y. J. Park, and H. S. Min, “A numerically efficient method for the hydrodynamic density-gradient model,” in *International Conference on Simulation of Semiconductor Processes and Devices, 2003. SISPAD 2003.*, Boston, MA, USA: IEEE, 2003, pp. 263–266. doi: 10.1109/SISPAD.2003.1233687.

[122] R.-C. Chen and J.-L. Liu, “A quantum corrected energy-transport model for nanoscale semiconductor devices,” *J. Comput. Phys.*, vol. 204, no. 1, pp. 131–156, Mar. 2005, doi: 10.1016/j.jcp.2004.10.006.

[123] V. Lashkaryov Institute of Semiconductor Physics, NAS of Ukraine, 41, prospect Nauky, 03028 Kyiv, Ukraine and A. V. Naumov, “Self-heating effects in AlGaN/GaN HEMT heterostructures: Electrical and optical characterization,” *Semicond. Phys. Quantum Electron. Optoelectron.*, vol. 18, no. 4, pp. 396–402, Dec. 2015, doi: 10.15407/spqeo18.04.396.

[124] H. Morris and A. Limon, “Quantum corrections: a multilevel solver for the density-gradient equation,” *Int. J. Comput. Sci. Eng.*, vol. 2, no. 3/4, p. 119, 2006, doi: 10.1504/IJCSE.2006.012763.

[125] F. M. Bufler, R. Hudé, and A. Erlebach, “On a simple and accurate quantum correction for Monte Carlo simulation,” *J. Comput. Electron.*, vol. 5, no. 4, pp. 467–469, Dec. 2006, doi: 10.1007/s10825-006-0038-1.

[126] A. R. Brown *et al.*, “Use of density gradient quantum corrections in the simulation of statistical variability in MOSFETs,” *J. Comput. Electron.*, vol. 9, no. 3–4, pp. 187–196, Dec. 2010, doi: 10.1007/s10825-010-0314-y.

[127] G. Baccarani, E. Gnani, A. Gnudi, S. Reggiani, and M. Rudan, “Theoretical foundations of the quantum drift-diffusion and density-gradient models,” *Solid-State Electron.*, vol. 52, no. 4, pp. 526–532, Apr. 2008, doi: 10.1016/j.sse.2007.10.051.

[128] D. Gambacurta and F. Catara, “Second random phase approximation studies in metallic clusters,” *Phys. Rev. B*, vol. 79, no. 8, p. 085403, Feb. 2009, doi: 10.1103/PhysRevB.79.085403.

[129] A. R. Brown, A. Martinez, N. Seoane, and A. Asenov, “Comparison of Density Gradient and NEGF for 3D Simulation of a Nanowire MOSFET,” in *2009 Spanish Conference on Electron Devices*, Santiago de Compostela, Spain: IEEE, Feb. 2009, pp. 140–143. doi: 10.1109/SCED.2009.4800450.

[130] A. R. Brown *et al.*, “Use of density gradient quantum corrections in the simulation of statistical variability in MOSFETs,” *J. Comput. Electron.*, vol. 9, no. 3–4, pp. 187–196, Dec. 2010, doi: 10.1007/s10825-010-0314-y.

[131] A. J. Garcia-Loureiro *et al.*, “Implementation of the Density Gradient Quantum Corrections for 3-D Simulations of Multigate Nanoscaled Transistors,” *IEEE Trans. Comput.-Aided Des. Integr. Circuits Syst.*, vol. 30, no. 6, pp. 841–851, Jun. 2011, doi: 10.1109/TCAD.2011.2107990.

[132] N. Pons *et al.*, “Density Gradient calibration for 2D quantum confinement: Tri-Gate SOI transistor application,” in *2013 International Conference on Simulation of Semiconductor Processes and Devices (SISPAD)*, Glasgow, United Kingdom: IEEE, Sep. 2013, pp. 184–187. doi: 10.1109/SISPAD.2013.6650605.

[133] A. Gaurav, S. S. Gill, N. Kaur, and M. Rattan, “Density gradient quantum corrections based performance optimization of triangular TG bulk FinFETs using ANN and GA,” in *2016 20th International Symposium on VLSI Design and Test (VDAT)*, Guwahati, India: IEEE, May 2016, pp. 1–5. doi: 10.1109/ISVDAT.2016.8064854.

[134] S.-M. Hong, “Compact Charge Modeling of Double-Gate MOSFETs Considering the Density-Gradient Equation,” *IEEE J. Electron Devices Soc.*, vol. 7, pp. 409–416, 2019, doi: 10.1109/JEDS.2019.2903854.

[135] T. Dutta, C. Medina-Bailon, N. Xeni, V. P. Georgiev, and A. Asenov, “Density Gradient Based Quantum-Corrected 3D Drift-Diffusion Simulator for Nanoscale MOSFETs,” in *2021 IEEE 16th Nanotechnology Materials and Devices Conference (NMDC)*, Vancouver, BC, Canada: IEEE, Dec. 2021, pp. 1–4. doi: 10.1109/NMDC50713.2021.9677480.

[136] C. D. S. Soares, G. Furtado, A. C. J. Rossetto, G. I. Wirth, and D. Vasileska, "3D Quantum-Corrected Monte Carlo Device Simulator of n-FinFETs," Aug. 09, 2023, *In Review*. doi: 10.21203/rs.3.rs-3229583/v1.

[137] S. Rhee, D. Kim, K. Kim, S. Choi, B.-G. Park, and Y. J. Park, "Extension of the DG Model to the Second-Order Quantum Correction for Analysis of the Single-Charge Effect in Sub-10-nm MOS Devices," *IEEE J. Electron Devices Soc.*, vol. 8, pp. 213–222, 2020, doi: 10.1109/JEDS.2020.2971426.

[138] X. Li, S. Huang, J. Wang, L. Wang, and L. Li, "Fundamental understanding of quantum confinement effect on gate oxide reliability for gate-all around field-effect transistor," *J. Appl. Phys.*, vol. 136, no. 23, p. 235701, Dec. 2024, doi: 10.1063/5.0229625.

[139] D. Bohm and B. J. Hiley, "Measurement understood through the quantum potential approach," *Found. Phys.*, vol. 14, no. 3, pp. 255–274, Mar. 1984, doi: 10.1007/BF00730211.

[140] Y. Aharonov and D. Bohm, "Further Considerations on Electromagnetic Potentials in the Quantum Theory," *Phys. Rev.*, vol. 123, no. 4, pp. 1511–1524, Aug. 1961, doi: 10.1103/PhysRev.123.1511.

[141] G. Dennis, M. A. De Gosson, and B. J. Hiley, "Bohm's quantum potential as an internal energy," *Phys. Lett. A*, vol. 379, no. 18–19, pp. 1224–1227, Jun. 2015, doi: 10.1016/j.physleta.2015.02.038.

[142] Z. Moldabekov, T. Schoof, P. Ludwig, M. Bonitz, and T. Ramazanov, "Statically screened ion potential and Bohm potential in a quantum plasma," *Phys. Plasmas*, vol. 22, no. 10, p. 102104, Oct. 2015, doi: 10.1063/1.4932051.

[143] S. A. Hojman and F. A. Asenjo, "Classical and Quantum Dispersion Relations," *Phys. Scr.*, vol. 95, no. 8, p. 085001, Aug. 2020, doi: 10.1088/1402-4896/ab986b.

[144] R. Mauri and M. Giona, "A Covariant Non-Local Model of Bohm's Quantum Potential," *Entropy*, vol. 25, no. 6, p. 915, Jun. 2023, doi: 10.3390/e25060915.

[145] G. A. Nemnes, A. Palici, and A. Manolescu, "Transparent boundary conditions for time-dependent electron transport in the R -matrix method with applications to nanostructured interfaces," *Comput. Phys. Commun.*, vol. 208, pp. 109–116, Nov. 2016, doi: 10.1016/j.cpc.2016.08.007.

[146] R. Kosik, J. Cervenka, and H. Kosina, "Numerical constraints and non-spatial open boundary conditions for the Wigner equation," *J. Comput. Electron.*, vol. 20, no. 6, pp. 2052–2061, Dec. 2021, doi: 10.1007/s10825-021-01800-w.

[147] R. R. Nimje and A. Mahajan, "Analytical estimation of lifetime of quasi-bound states in III -v semiconductors quantum well," *Phys. Scr.*, vol. 98, no. 9, p. 095014, Sep. 2023, doi: 10.1088/1402-4896/acea03.

[148] A. Sarkar and A. Deyasi, Eds., *Low-dimensional nanoelectronic devices: theoretical analysis and cutting-edge research*, First edition. Palm Bay, FL: Apple Academic Press, Inc., USA, 2023.

[149] T. Krishnamohan, D. Kim, and K. C. Saraswat, “Properties and Trade-Offs of Compound Semiconductor MOSFETs,” in *Fundamentals of III-V Semiconductor MOSFETs*, S. Oktyabrsky and P. Ye, Eds., Boston, MA: Springer US, 2010, pp. 7–27. doi: 10.1007/978-1-4419-1547-4_2.

[150] K. Biswas and A. Sarkar, Eds., *Advanced nanoscale MOSFET architectures: current trends and future perspectives*. Hoboken, New Jersey: Wiley, 2024.

[151] X. Duan and H. Zhang, “Introduction: Two-Dimensional Layered Transition Metal Dichalcogenides,” *Chem. Rev.*, vol. 124, no. 19, pp. 10619–10622, Oct. 2024, doi: 10.1021/acs.chemrev.4c00586.

[152] H. Chen *et al.*, “The Recent Progress of Two-Dimensional Transition Metal Dichalcogenides and Their Phase Transition”.

[153] M. Heyns and W. Tsai, “Ultimate Scaling of CMOS Logic Devices with Ge and III–V Materials,” *MRS Bull.*, vol. 34, no. 7, pp. 485–492, Jul. 2009, doi: 10.1557/mrs2009.136.

[154] C. Claeys, J. Mitard, G. Eneman, M. Meuris, and E. Simoen, “Si versus Ge for future microelectronics,” *Thin Solid Films*, vol. 518, no. 9, pp. 2301–2306, Feb. 2010, doi: 10.1016/j.tsf.2009.08.027.

[155] S. Datta, “Non-equilibrium green’s function (NEGF) method: a different perspective,” in *2015 International Workshop on Computational Electronics (IWCE)*, West Lafayette, IN, USA: IEEE, Sep. 2015, pp. 1–6. doi: 10.1109/IWCE.2015.7301951.

[156] K. Y. Camsari, S. Chowdhury, and S. Datta, “The Nonequilibrium Green Function (NEGF) Method,” in *Springer Handbook of Semiconductor Devices*, M. Rudan, R. Brunetti, and S. Reggiani, Eds., in Springer Handbooks. , Cham: Springer International Publishing, 2023, pp. 1583–1599. doi: 10.1007/978-3-030-79827-7_44.

[157] A. Thakur and N. Sarkar, “A tutorial on the NEGF method for electron transport in devices and defective materials,” *Eur. Phys. J. B*, vol. 96, no. 8, p. 113, Aug. 2023, doi: 10.1140/epjb/s10051-023-00580-5.

[158] C. Sahu and J. Singh, “Charge-Plasma Based Process Variation Immune Junctionless Transistor,” *IEEE Electron Device Lett.*, vol. 35, no. 3, pp. 411–413, Mar. 2014, doi: 10.1109/LED.2013.2297451.

[159] Z. Ramezani, A. A. Orouji, S. A. Ghoreishi, and I. S. Amiri, “A Nano junctionless Double-Gate MOSFET by Using the Charge Plasma Concept to Improve Short-Channel Effects and Frequency Characteristics,” *J. Electron. Mater.*, vol. 48, no. 11, pp. 7487–7494, Nov. 2019, doi: 10.1007/s11664-019-07559-y.

[160] W. Wan, H. Lou, Y. Xiao, and X. Lin, “Source/Drain Engineered Charge-Plasma Junctionless Transistor for the Immune of Line Edge Roughness Effect,” *IEEE Trans. Electron Devices*, vol. 65, no. 5, pp. 1873–1879, May 2018, doi: 10.1109/TED.2018.2812241.

[161] S. I. Amin and R. K. Sarin, "Charge-plasma based dual-material and gate-stacked architecture of junctionless transistor for enhanced analog performance," *Superlattices Microstruct.*, vol. 88, pp. 582–590, Dec. 2015, doi: 10.1016/j.spmi.2015.10.017.

[162] N. Trivedi, M. Kumar, S. Haldar, S. S. Deswal, M. Gupta, and R. S. Gupta, "Charge plasma technique based dopingless accumulation mode junctionless cylindrical surrounding gate MOSFET: analog performance improvement," *Appl. Phys. A*, vol. 123, no. 9, p. 564, Sep. 2017, doi: 10.1007/s00339-017-1176-y.

[163] J. P. Colinge *et al.*, "Junctionless Nanowire Transistor (JNT): Properties and design guidelines," *Solid-State Electron.*, vol. 65–66, pp. 33–37, Nov. 2011, doi: 10.1016/j.sse.2011.06.004.

[164] D. Singh, S. Pandey, K. Nigam, D. Sharma, D. S. Yadav, and P. Kondekar, "A Charge-Plasma-Based Dielectric-Modulated Junctionless TFET for Biosensor Label-Free Detection," *IEEE Trans. Electron Devices*, vol. 64, no. 1, pp. 271–278, Jan. 2017, doi: 10.1109/TED.2016.2622403.

[165] B. Sharma and J.-S. Kim, "MEMS based highly sensitive dual FET gas sensor using graphene decorated Pd-Ag alloy nanoparticles for H_2 detection," *Sci. Rep.*, vol. 8, no. 1, p. 5902, Apr. 2018, doi: 10.1038/s41598-018-24324-z.

[166] Y. Ma *et al.*, "Black Phosphorus Field-Effect Transistors with Work Function Tunable Contacts," *ACS Nano*, vol. 11, no. 7, pp. 7126–7133, Jul. 2017, doi: 10.1021/acsnano.7b02858.

[167] Q. Hu, P. Solomon, L. Österlund, and Z. Zhang, "Nanotransistor-based gas sensing with record-high sensitivity enabled by electron trapping effect in nanoparticles," *Nat. Commun.*, vol. 15, no. 1, p. 5259, Jun. 2024, doi: 10.1038/s41467-024-49658-3.

[168] A. I. Osman *et al.*, "Hydrogen production, storage, utilisation and environmental impacts: a review," *Environ. Chem. Lett.*, vol. 20, no. 1, pp. 153–188, Feb. 2022, doi: 10.1007/s10311-021-01322-8.

[169] K. Zhang *et al.*, "Effect of ignition, initial pressure and temperature on the lower flammability limit of hydrogen/air mixture," *Int. J. Hydrog. Energy*, vol. 47, no. 33, pp. 15107–15119, Apr. 2022, doi: 10.1016/j.ijhydene.2022.02.224.

[170] A. Hinojo, E. Lujan, M. Nel-lo, S. Colominas, and J. Abella, "BaCe0.6Zr0.3Y0.1O3-α electrochemical hydrogen sensor for fusion applications," *Fusion Eng. Des.*, vol. 188, p. 113452, Mar. 2023, doi: 10.1016/j.fusengdes.2023.113452.

[171] A. Kumar, "Palladium-based trench gate MOSFET for highly sensitive hydrogen gas sensor," *Mater. Sci. Semicond. Process.*, vol. 120, p. 105274, Dec. 2020, doi: 10.1016/j.mssp.2020.105274.

[172] "A New Gas Sensor Based on MOSFET Having a Horizontal Floating-Gate," *IEEE Electron Device Lett.*, vol. 35, no. 2, pp. 265–267, Feb. 2014, doi: 10.1109/LED.2013.2294722.

[173] G. C. Mutinati *et al.*, "CMOS-integrable Ultrathin SnO2 Layer for Smart Gas Sensor Devices," *Procedia Eng.*, vol. 47, pp. 490–493, 2012, doi: 10.1016/j.proeng.2012.09.191.

[174] M. Graf, *CMOS hotplate chemical microsensors*. in Microtechnology and MEMS. Berlin: Springer, 2007.

[175] H.-J. Kim and J.-H. Lee, “Highly sensitive and selective gas sensors using p-type oxide semiconductors: Overview,” *Sens. Actuators B Chem.*, vol. 192, pp. 607–627, Mar. 2014, doi: 10.1016/j.snb.2013.11.005.

[176] S. Ahmed and S. K. Sinha, “Studies on nanomaterial-based p-type semiconductor gas sensors,” *Environ. Sci. Pollut. Res.*, vol. 30, no. 10, pp. 24975–24986, Jun. 2022, doi: 10.1007/s11356-022-21218-6.

[177] J. Gu *et al.*, “Cryogenic Transport Characteristics of P-Type Gate-All-Around Silicon Nanowire MOSFETs,” *Nanomaterials*, vol. 11, no. 2, p. 309, Jan. 2021, doi: 10.3390/nano11020309.

[178] C. Qin, Z. Wei, B. Wang, and Y. Wang, “Sn and Mn co-doping synergistically promotes the sensing properties of Co3O4 sensor for high-sensitive CO detection,” *Sens. Actuators B Chem.*, vol. 390, p. 133930, Sep. 2023, doi: 10.1016/j.snb.2023.133930.

[179] S. Yang *et al.*, “Enhancing the Hydrogen-Sensing Performance of p-Type PdO by Modulating the Conduction Model,” *ACS Appl. Mater. Interfaces*, vol. 13, no. 44, pp. 52754–52764, Nov. 2021, doi: 10.1021/acsami.1c13034.

[180] S. Luan *et al.*, “The enhanced sensing properties of MOS-based resistive gas sensors by Au functionalization: a review,” *Dalton Trans.*, vol. 52, no. 25, pp. 8503–8529, 2023, doi: 10.1039/D3DT01078C.

[181] A. Paghi, S. Mariani, and G. Barillaro, “1D and 2D Field Effect Transistors in Gas Sensing: A Comprehensive Review,” *Small*, vol. 19, no. 15, p. 2206100, Apr. 2023, doi: 10.1002/smll.202206100.

[182] B. Wang *et al.*, “Gate-Modulated High-Response Field-Effect Transistor-Type Gas Sensor Based on the MoS_2 /Metal–Organic Framework Heterostructure,” *ACS Appl. Mater. Interfaces*, vol. 14, no. 37, pp. 42356–42364, Sep. 2022, doi: 10.1021/acsami.2c11359.

[183] M. Donarelli and L. Ottaviano, “2D Materials for Gas Sensing Applications: A Review on Graphene Oxide, MoS2, WS2 and Phosphorene,” *Sensors*, vol. 18, no. 11, p. 3638, Oct. 2018, doi: 10.3390/s18113638.

[184] D. Li, Y. Huang, Z. Li, L. Zhong, C. Liu, and X. Peng, “Deep eutectic solvents derived carbon-based efficient electrocatalyst for boosting H_2 production coupled with glucose oxidation,” *Chem. Eng. J.*, vol. 430, p. 132783, Feb. 2022, doi: 10.1016/j.cej.2021.132783.

[185] S. B. Mitta *et al.*, “Electrical characterization of 2D materials-based field-effect transistors,” *2D Mater.*, vol. 8, no. 1, p. 012002, Jan. 2021, doi: 10.1088/2053-1583/abc187.

[186] D. Sarkar, W. Liu, X. Xie, A. C. Anselmo, S. Mitragotri, and K. Banerjee, “MoS_2 Field-Effect Transistor for Next-Generation Label-Free Biosensors,” *ACS Nano*, vol. 8, no. 4, pp. 3992–4003, Apr. 2014, doi: 10.1021/nn5009148.

[187] A. De, S. Shee Kanrar, and S. K. Sarkar, “Investigation into $MoTe_2$ Based Dielectric Modulated AMFET Biosensor for Label-Free Detection of DNA Including Electric Variational Effects,” *Silicon*, vol. 14, no. 12, pp. 6787–6799, Aug. 2022, doi: 10.1007/s12633-021-01423-7.

[188] A. Rani, K. DiCamillo, M. A. H. Khan, M. Paranjape, and M. E. Zaghloul, “Tuning the Polarity of $MoTe_2$ FETs by Varying the Channel Thickness for Gas-Sensing Applications,” *Sensors*, vol. 19, no. 11, p. 2551, Jun. 2019, doi: 10.3390/s19112551.

[189] S. Luan *et al.*, “The enhanced sensing properties of MOS-based resistive gas sensors by Au functionalization: a review,” *Dalton Trans.*, vol. 52, no. 25, pp. 8503–8529, 2023, doi: 10.1039/D3DT01078C.

[190] Z. Feng *et al.*, “Enhanced Sensitivity of $MoTe_2$ Chemical Sensor through Light Illumination,” *Micromachines*, vol. 8, no. 5, p. 155, May 2017, doi: 10.3390/mi8050155.

[191] E. Wu *et al.*, “Specific and Highly Sensitive Detection of Ketone Compounds Based on p-Type $MoTe_2$ under Ultraviolet Illumination,” *ACS Appl. Mater. Interfaces*, vol. 10, no. 41, pp. 35664–35669, Oct. 2018, doi: 10.1021/acsami.8b14142.

[192] Z. Liu, Y. Gui, L. Xu, and X. Chen, “Adsorption and gas-sensing properties of Aun (n = 1–3) cluster doped $MoTe_2$ for NH3, NO2, and SO2 gas molecules,” *Surf. Interfaces*, vol. 30, p. 101883, Jun. 2022, doi: 10.1016/j.surfin.2022.101883.

[193] W. Cao, Q. Zhao, L. Yang, and H. Cui, “Enhanced NOx adsorption and sensing properties of $MoTe_2$ monolayer by Ni-doping: A first-principles study,” *Surf. Interfaces*, vol. 26, p. 101372, Oct. 2021, doi: 10.1016/j.surfin.2021.101372.

[194] M. J. Szary, D. M. Florjan, and J. A. Bąbelek, “Selective Detection of Carbon Monoxide on P-Block Doped Monolayers of $MoTe_2$,” *ACS Sens.*, vol. 7, no. 1, pp. 272–285, Jan. 2022, doi: 10.1021/acssensors.1c02246.

[195] D. Kwon *et al.*, “Efficient fusion of spiking neural networks and FET-type gas sensors for a fast and reliable artificial olfactory system,” *Sens. Actuators B Chem.*, vol. 345, p. 130419, Oct. 2021, doi: 10.1016/j.snb.2021.130419.

[196] Z. Chen, Z. Chen, Z. Song, W. Ye, and Z. Fan, “Smart gas sensor arrays powered by artificial intelligence,” *J. Semicond.*, vol. 40, no. 11, p. 111601, Nov. 2019, doi: 10.1088/1674-4926/40/11/111601.

[197] R. Duflou, G. Pourtois, M. Houssa, and A. Afzalian, “Fundamentals of low-resistive 2D-semiconductor metal contacts: an ab-initio NEGF study,” *Npj 2D Mater. Appl.*, vol. 7, no. 1, p. 38, May 2023, doi: 10.1038/s41699-023-00402-3.

[198] R. Lake, D. Jovanovic, and C. Rivas, “NON-EQUILIBRIUM GREEN’S FUNCTIONS IN SEMICONDUCTOR DEVICE MODELING,” in *Progress in Nonequilibrium Green’s Functions II*, Dresden, Germany: WORLD SCIENTIFIC, May 2003, pp. 143–158. doi: 10.1142/9789812705129_0013.

[199] N. Islam, M. F. P. Mohamed, M. F. A. J. Khan, S. Falina, H. Kawarada, and M. Syamsul, “Reliability, Applications and Challenges of GaN HEMT Technology for Modern Power Devices: A Review,” *Crystals*, vol. 12, no. 11, p. 1581, Nov. 2022, doi: 10.3390/cryst12111581.

[200] M. Haziq, S. Falina, A. A. Manaf, H. Kawarada, and M. Syamsul, “Challenges and Opportunities for High-Power and High-Frequency AlGaN/GaN High-Electron-Mobility Transistor (HEMT) Applications: A Review,” *Micromachines*, vol. 13, no. 12, p. 2133, Dec. 2022, doi: 10.3390/mi13122133.

[201] R. Thapa *et al.*, “Biofunctionalized AlGaN/GaN high electron mobility transistor for DNA hybridization detection,” *Appl. Phys. Lett.*, vol. 100, no. 23, p. 232109, Jun. 2012, doi: 10.1063/1.4727895.

[202] S. Zhang, M. C. Li, Z. H. Feng, B. Liu, J. Y. Yin, and L. C. Zhao, “High electron mobility and low sheet resistance in lattice-matched AlInN/AlN/GaN/AlN/GaN double-channel heterostructure,” *Appl. Phys. Lett.*, vol. 95, no. 21, p. 212101, Nov. 2009, doi: 10.1063/1.3264961.

[203] K. Drozdowska *et al.*, “The effects of gas exposure on the graphene/AlGaN/GaN heterostructure under UV irradiation,” *Sens. Actuators B Chem.*, vol. 381, p. 133430, Apr. 2023, doi: 10.1016/j.snb.2023.133430.

[204] P. L. Neumann, J. Radó, J. M. Bozorádi, and J. Volk, “AlGaN/GaN heterostructure based 3-dimensional force sensors,” *Micro Nano Eng.*, vol. 19, p. 100198, Jun. 2023, doi: 10.1016/j.mne.2023.100198.

[205] Z. Yan *et al.*, “A Novel AlGaN/GaN-Based Schottky Barrier Diode With Partial P-GaN Cap Layer and Semicircular T-Anode for Temperature Sensors,” *IEEE Trans. Electron Devices*, vol. 70, no. 10, pp. 5087–5091, Oct. 2023, doi: 10.1109/TED.2023.3306736.

[206] A. Kumar, A. Varghese, D. Kalra, S. Pancholi, and G. K. Sharma, “Optimizing Bio-Sensor Design With Support Vector Regression Technique for AlGaN/GaN MOS–HEMT,” *IEEE Sens. Lett.*, vol. 7, no. 9, pp. 1–4, Sep. 2023, doi: 10.1109/LSENS.2023.3307064.

[207] A. M. Bhat, C. Periasamy, R. Poonia, A. Varghese, N. Shafi, and S. Tripathy, “AlGaN/GaN HEMT Based pH Detection Using Atomic Layer Deposition of Al_2 O_3 as Sensing Membrane and Passivation,” *IEEE Trans. Nanotechnol.*, vol. 22, pp. 466–472, 2023, doi: 10.1109/TNANO.2023.3305360.

[208] P. Sriramani, N. Mohankumar, Y. Prasamsha, A. Sarkar, and M. Chanda, “Threshold and surface potential-based sensitivity analysis of symmetrical double gate AlGaN/GaN MOS-HEMT including capacitance effects for label-free biosensing,” *Phys. Scr.*, vol. 98, no. 11, p. 115036, Nov. 2023, doi: 10.1088/1402-4896/acff8e.

[209] Y. Zhang *et al.*, "Studies on the coupling correlation and strain state of AlGaN/GaN double channel heterostructures grown by metal organic chemical vapor deposition," *J. Alloys Compd.*, vol. 942, p. 169074, May 2023, doi: 10.1016/j.jallcom.2023.169074.

[210] S. Feng *et al.*, "Electroluminescence and Gate Carrier Dynamics in a Schottky-Type *p* -GaN Gate Double-Channel GaN HEMT," *IEEE Electron Device Lett.*, vol. 44, no. 10, pp. 1592–1595, Oct. 2023, doi: 10.1109/LED.2023.3301966.

[211] H. Liao *et al.*, "Normally-OFF p-GaN Gate Double-Channel HEMT With Suppressed Hot-Electron-Induced Dynamic ON-Resistance Degradation," *IEEE Electron Device Lett.*, vol. 43, no. 9, pp. 1424–1427, Sep. 2022, doi: 10.1109/LED.2022.3195489.

[212] L. Arivazhagan *et al.*, "Applicability of double Channel Technique in AlGaN/GaN HEMT for future biosensing applications," *Superlattices Microstruct.*, vol. 160, p. 107086, Dec. 2021, doi: 10.1016/j.spmi.2021.107086.

[213] R. R. Malik, M. A. Mir, Z. Bhat, A. Pampori, Y. S. Chauhan, and S. A. Ahsan, "Modeling and Analysis of Double Channel GaN HEMTs Using a Physics-Based Analytical Model," *IEEE J. Electron Devices Soc.*, vol. 9, pp. 789–797, 2021, doi: 10.1109/JEDS.2021.3108159.

[214] S. Heikman, S. Keller, D. S. Green, S. P. DenBaars, and U. K. Mishra, "High conductivity modulation doped AlGaN/GaN multiple channel heterostructures," *J. Appl. Phys.*, vol. 94, no. 8, pp. 5321–5325, Oct. 2003, doi: 10.1063/1.1610244.

[215] J. Ma, C. Erine, P. Xiang, K. Cheng, and E. Matioli, "Multi-channel tri-gate normally-on/off AlGaN/GaN MOSHEMTs on Si substrate with high breakdown voltage and low ON-resistance," *Appl. Phys. Lett.*, vol. 113, no. 24, p. 242102, Dec. 2018, doi: 10.1063/1.5064407.

[216] A. Li *et al.*, "Lattice-matched AlInN/GaN multi-channel heterostructure and HEMTs with low on-resistance," *Appl. Phys. Lett.*, vol. 119, no. 12, p. 122104, Sep. 2021, doi: 10.1063/5.0063638.

[217] R. Lingaparthi, N. Dharmarasu, K. Radhakrishnan, A. Ranjan, T. L. A. Seah, and L. Huo, "Source of two-dimensional electron gas in unintentionally doped AlGaN/GaN multichannel high-electron-mobility transistor heterostructures," *Appl. Phys. Lett.*, vol. 118, no. 12, p. 122105, Mar. 2021, doi: 10.1063/5.0045910.

[218] Y. Zhang *et al.*, "Studies on the coupling correlation and strain state of AlGaN/GaN double channel heterostructures grown by metal organic chemical vapor deposition," *J. Alloys Compd.*, vol. 942, p. 169074, May 2023, doi: 10.1016/j.jallcom.2023.169074.

[219] Y. Zhang *et al.*, "High performance InGaN double channel high electron mobility transistors with strong coupling effect between the channels," *Appl. Phys. Lett.*, vol. 113, no. 23, p. 233503, Dec. 2018, doi: 10.1063/1.5051685.

[220] H. Lu *et al.*, "AlN/GaN/InGaN Coupling-Channel HEMTs for Improved g_m and Gain Linearity," *IEEE Trans. Electron Devices*, vol. 68, no. 7, pp. 3308–3313, Jul. 2021, doi: 10.1109/TED.2021.3082104.

[221] Y. Zhang *et al.*, "High performance InGaN double channel high electron mobility transistors with strong coupling effect between the channels," *Appl. Phys. Lett.*, vol. 113, no. 23, p. 233503, Dec. 2018, doi: 10.1063/1.5051685.

[222] J. A. Goode, J. V. H. Rushworth, and P. A. Millner, "Biosensor Regeneration: A Review of Common Techniques and Outcomes," *Langmuir*, vol. 31, no. 23, pp. 6267–6276, Jun. 2015, doi: 10.1021/la503533g.

[223] K. S. Kim, H.-S. Lee, J.-A. Yang, M.-H. Jo, and S. K. Hahn, "The fabrication, characterization and application of aptamer-functionalized Si-nanowire FET biosensors," *Nanotechnology*, vol. 20, no. 23, p. 235501, Jun. 2009, doi: 10.1088/0957-4484/20/23/235501.

[224] J.-H. Ahn *et al.*, "Nanowire FET Biosensors on a Bulk Silicon Substrate," *IEEE Trans. Electron Devices*, vol. 59, no. 8, pp. 2243–2249, Aug. 2012, doi: 10.1109/TED.2012.2200105.

[225] Y.-T. Chen *et al.*, "High-field modulated ion-selective field-effect-transistor (FET) sensors with sensitivity higher than the ideal Nernst sensitivity," *Sci. Rep.*, vol. 8, no. 1, p. 8300, May 2018, doi: 10.1038/s41598-018-26792-9.

[226] P. Sriramani, N. Mohankumar, and Y. Prasamsha, "Drain current sensitivity analysis using a surface potential-based analytical model for AlGaN/GaN double gate MOS-HEMT," *Micro Nanostructures*, vol. 185, p. 207720, Jan. 2024, doi: 10.1016/j.micrna.2023.207720.

[227] G. Zhang *et al.*, "Study on the Thermal Conductivity Characteristics for Ultra-Thin Body FD SOI MOSFETs Based on Phonon Scattering Mechanisms," *Materials*, vol. 12, no. 16, p. 2601, Aug. 2019, doi: 10.3390/ma12162601.

[228] M. A. Khan, P. Kumar, G. Siddharth, M. Das, and S. Mukherjee, "Analysis of Drain Current in Polycrystalline MgZnO/ZnO and MgZnO/CdZnO HFET," *IEEE Trans. Electron Devices*, vol. 66, no. 12, pp. 5097–5102, Dec. 2019, doi: 10.1109/TED.2019.2947422.

[229] K. C. Oeffinger *et al.*, "Breast Cancer Screening for Women at Average Risk: 2015 Guideline Update From the American Cancer Society," *JAMA*, vol. 314, no. 15, p. 1599, Oct. 2015, doi: 10.1001/jama.2015.12783.

[230] I. Pant and S. Joshi, "Invasive papillary carcinoma of the male breast: Report of a rare case and review of the literature," *J. Cancer Res. Ther.*, vol. 5, no. 3, p. 216, 2009, doi: 10.4103/0973-1482.57132.

[231] S. A. Eccles, "[No title found]," *J. Mammary Gland Biol. Neoplasia*, vol. 6, no. 4, pp. 393–406, 2001, doi: 10.1023/A:1014730829872.

[232] K. H. Chen *et al.*, "c-erbB-2 sensing using AlGaN⁄GaN high electron mobility transistors for breast cancer detection," *Appl. Phys. Lett.*, vol. 92, no. 19, p. 192103, May 2008, doi: 10.1063/1.2926656.

[233] R. Kirste, N. Rohrbaugh, I. Bryan, Z. Bryan, R. Collazo, and A. Ivanisevic, "Electronic Biosensors Based on III-Nitride Semiconductors," *Annu. Rev. Anal. Chem.*, vol. 8, no. 1, pp. 149–169, Jul. 2015, doi: 10.1146/annurev-anchem-071114-040247.

[234] E. Österlund, S. Suihkonen, G. Ross, A. Torkkeli, H. Kuisma, and M. Paulasto-Kröckel, "Metalorganic chemical vapor deposition of aluminum nitride on vertical surfaces," *J. Cryst. Growth*, vol. 531, p. 125345, Feb. 2020, doi: 10.1016/j.jcrysgro.2019.125345.

[235] L. Aina, M. Mattingly, M. Serio, and E. Martin, "MOVPE of AlInAs HEMT structures," *J. Cryst. Growth*, vol. 107, no. 1–4, pp. 932–941, Jan. 1991, doi: 10.1016/0022-0248(91)90583-Q.

[236] X. Xu *et al.*, "Wafer-level MOCVD growth of AlGaN/GaN-on-Si HEMT structures with ultra-high room temperature 2DEG mobility," *AIP Adv.*, vol. 6, no. 11, p. 115016, Nov. 2016, doi: 10.1063/1.4967816.

[237] F. Bernardini, V. Fiorentini, and D. Vanderbilt, "Spontaneous polarization and piezoelectric constants of III-V nitrides," *Phys. Rev. B*, vol. 56, no. 16, pp. R10024–R10027, Oct. 1997, doi: 10.1103/PhysRevB.56.R10024.

[238] B. A. Klein *et al.*, "Saturation Velocity Measurement of Al0.7Ga0.3N-Channel High Electron Mobility Transistors," *J. Electron. Mater.*, vol. 48, no. 9, pp. 5581–5585, Sep. 2019, doi: 10.1007/s11664-019-07421-1.

[239] S. K. Jain *et al.*, "2D/3D Hybrid of MoS_2 /GaN for a High-Performance Broadband Photodetector," *ACS Appl. Electron. Mater.*, vol. 3, no. 5, pp. 2407–2414, May 2021, doi: 10.1021/acsaelm.1c00299.

[240] P. Tao *et al.*, "Crack-free Al 0.5 Ga 0.5 N epilayer grown on SiC substrate by in situ SiN x interlayer," *Mater. Sci. Semicond. Process.*, vol. 41, pp. 291–296, Jan. 2016, doi: 10.1016/j.mssp.2015.09.022.

[241] A. Varghese, C. Periasamy, and L. Bhargava, "Fabrication and Charge Deduction Based Sensitivity Analysis of GaN MOS-HEMT Device for Glucose, MIG, C-erbB-2, KIM-1, and PSA Detection," *IEEE Trans. Nanotechnol.*, vol. 18, pp. 747–755, 2019, doi: 10.1109/TNANO.2019.2928308.

[242] N. N. Reddy and D. K. Panda, "Nanowire gate all around-TFET-based biosensor by considering ambipolar transport," *Appl. Phys. A*, vol. 127, no. 9, p. 682, Sep. 2021, doi: 10.1007/s00339-021-04840-y.

[243] G. Nazir, A. Rehman, and S.-J. Park, "Energy-Efficient Tunneling Field-Effect Transistors for Low-Power Device Applications: Challenges and Opportunities," *ACS Appl. Mater. Interfaces*, vol. 12, no. 42, pp. 47127–47163, Oct. 2020, doi: 10.1021/acsami.0c10213.

[244] S. Falina *et al.*, "Ten Years Progress of Electrical Detection of Heavy Metal Ions (HMIs) Using Various Field-Effect Transistor (FET) Nanosensors: A Review," *Biosensors*, vol. 11, no. 12, p. 478, Nov. 2021, doi: 10.3390/bios11120478.

[245] F. Assad, Zhibin Ren, D. Vasileska, S. Datta, and M. Lundstrom, “On the performance limits for Si MOSFETs: a theoretical study,” *IEEE Trans. Electron Devices*, vol. 47, no. 1, pp. 232–240, Jan. 2000, doi: 10.1109/16.817590.

[246] D. J. Frank, R. H. Dennard, E. Nowak, P. M. Solomon, Y. Taur, and Hon-Sum Philip Wong, “Device scaling limits of Si MOSFETs and their application dependencies,” *Proc. IEEE*, vol. 89, no. 3, pp. 259–288, Mar. 2001, doi: 10.1109/5.915374.

[247] R. K. Ratnesh *et al.*, “Advancement and challenges in MOSFET scaling,” *Mater. Sci. Semicond. Process.*, vol. 134, p. 106002, Nov. 2021, doi: 10.1016/j.mssp.2021.106002.

[248] U. E. Avci, R. Rios, K. J. Kuhn, and I. A. Young, “Comparison of power and performance for the TFET and MOSFET and considerations for P-TFET,” in *2011 11th IEEE International Conference on Nanotechnology*, Portland, OR, USA: IEEE, Aug. 2011, pp. 869–872. doi: 10.1109/NANO.2011.6144631.

[249] R. Woo, H.-Y. S. Koh, C. Onal, P. B. Griffin, and J. D. Plummer, “BTBT Transistor Scaling: Can they be Competitive with MOSFETs?,” in *2008 Device Research Conference*, Santa Barbara, CA, USA: IEEE, Jun. 2008, pp. 75–76. doi: 10.1109/DRC.2008.4800741.

[250] M. Ehteshamuddin, A. G. Alharbi, and S. A. Loan, “Impact of interface traps on the BTBT-current in tunnel field effect transistors,” in *2018 5th International Conference on Electrical and Electronic Engineering (ICEEE)*, Istanbul: IEEE, May 2018, pp. 224–227. doi: 10.1109/ICEEE2.2018.8391335.

[251] L. Zhang, J. Huang, and M. Chan, “Steep Slope Devices and TFETs,” in *Tunneling Field Effect Transistor Technology*, L. Zhang and M. Chan, Eds., Cham: Springer International Publishing, 2016, pp. 1–31. doi: 10.1007/978-3-319-31653-6_1.

[252] U. E. Avci and I. A. Young, “Heterojunction TFET Scaling and resonant-TFET for steep subthreshold slope at sub-9nm gate-length,” in *2013 IEEE International Electron Devices Meeting*, Washington, DC, USA: IEEE, Dec. 2013, p. 4.3.1-4.3.4. doi: 10.1109/IEDM.2013.6724559.

[253] Y. Khatami and K. Banerjee, “Steep Subthreshold Slope n- and p-Type Tunnel-FET Devices for Low-Power and Energy-Efficient Digital Circuits,” *IEEE Trans. Electron Devices*, vol. 56, no. 11, pp. 2752–2761, Nov. 2009, doi: 10.1109/TED.2009.2030831.

[254] S. Mookerjea, R. Krishnan, S. Datta, and V. Narayanan, “Effective Capacitance and Drive Current for Tunnel FET (TFET) CV/I Estimation,” *IEEE Trans. Electron Devices*, vol. 56, no. 9, pp. 2092–2098, Sep. 2009, doi: 10.1109/TED.2009.2026516.

[255] N. Paras and S. S. Chauhan, “Temperature sensitivity analysis of vertical tunneling based dual metal Gate TFET on analog/RF FOMs,” *Appl. Phys. A*, vol. 125, no. 5, p. 316, May 2019, doi: 10.1007/s00339-019-2621-x.

[256] Lan Wei, S. Oh, and H.-S. P. Wong, “Performance benchmarks for Si, III–V, TFET, and carbon nanotube FET - re-thinking the technology assessment methodology for complementary logic

applications," in *2010 International Electron Devices Meeting*, San Francisco, CA, USA: IEEE, Dec. 2010, p. 16.2.1-16.2.4. doi: 10.1109/IEDM.2010.5703373.

[257] K. Vanlalawmpuia and B. Bhowmick, "Analysis of Hetero-Stacked Source TFET and Heterostructure Vertical TFET as Dielectrically Modulated Label-Free Biosensors," *IEEE Sens. J.*, vol. 22, no. 1, pp. 939–947, Jan. 2022, doi: 10.1109/JSEN.2021.3128473.

[258] M. R. Tripathy, A. K. Singh, K. Baral, P. K. Singh, and S. Jit, "III-V/Si staggered heterojunction based source-pocket engineered vertical TFETs for low power applications," *Superlattices Microstruct.*, vol. 142, p. 106494, Jun. 2020, doi: 10.1016/j.spmi.2020.106494.

[259] C. Convertino, C. B. Zota, H. Schmid, A. M. Ionescu, and K. E. Moselund, "III–V heterostructure tunnel field-effect transistor," *J. Phys. Condens. Matter*, vol. 30, no. 26, p. 264005, Jul. 2018, doi: 10.1088/1361-648X/aac5b4.

[260] G. Dewey *et al.*, "Fabrication, characterization, and physics of III–V heterojunction tunneling Field Effect Transistors (H-TFET) for steep sub-threshold swing," in *2011 International Electron Devices Meeting*, Washington, DC, USA: IEEE, Dec. 2011, p. 33.6.1-33.6.4. doi: 10.1109/IEDM.2011.6131666.

[261] U. E. Avci, S. Hasan, D. E. Nikonov, R. Rios, K. Kuhn, and I. A. Young, "Understanding the feasibility of scaled III–V TFET for logic by bridging atomistic simulations and experimental results," in *2012 Symposium on VLSI Technology (VLSIT)*, Honolulu, HI, USA: IEEE, Jun. 2012, pp. 183–184. doi: 10.1109/VLSIT.2012.6242522.

[262] H. Ilatikhameneh, Y. Tan, B. Novakovic, G. Klimeck, R. Rahman, and J. Appenzeller, "Tunnel Field-Effect Transistors in 2-D Transition Metal Dichalcogenide Materials," *IEEE J. Explor. Solid-State Comput. Devices Circuits*, vol. 1, pp. 12–18, Dec. 2015, doi: 10.1109/JXCDC.2015.2423096.

[263] S. Kanungo, G. Ahmad, P. Sahatiya, A. Mukhopadhyay, and S. Chattopadhyay, "2D materials-based nanoscale tunneling field effect transistors: current developments and future prospects," *Npj 2D Mater. Appl.*, vol. 6, no. 1, p. 83, Nov. 2022, doi: 10.1038/s41699-022-00352-2.

[264] S. Das, S. Tewari, and A. Chattopadhyay, "Impact of Technology Node on Low Power Analog Performance of AU-TFET: A Quantum-Inspired Study," in *Advances in Communication, Devices and Networking*, vol. 1243, S. Dhar, S. Mukhopadhyay, D.-T. Do, S. N. Sur, and A. L. Imoize, Eds., in Lecture Notes in Electrical Engineering, vol. 1243. , Singapore: Springer Nature Singapore, 2025, pp. 13–24. doi: 10.1007/978-981-97-6465-5_2.

[265] J. L. Padilla, F. Gamiz, and A. Godoy, "Impact of Quantum Confinement on Gate Threshold Voltage and Subthreshold Swings in Double-Gate Tunnel FETs," *IEEE Trans. Electron Devices*, vol. 59, no. 12, pp. 3205–3211, Dec. 2012, doi: 10.1109/TED.2012.2216531.

[266] F. Najam and Y. S. Yu, "Impact of Quantum Confinement on Band-to-Band Tunneling of Line-Tunneling Type L-Shaped Tunnel Field-Effect Transistor," *IEEE Trans. Electron Devices*, vol. 66, no. 4, pp. 2010–2016, Apr. 2019, doi: 10.1109/TED.2019.2898403.

[267] D. Esseni, M. Pala, P. Palestri, C. Alper, and T. Rollo, "A review of selected topics in physics based modeling for tunnel field-effect transistors," *Semicond. Sci. Technol.*, vol. 32, no. 8, p. 083005, Aug. 2017, doi: 10.1088/1361-6641/aa6fca.

[268] B. H. Thai, C.-H. Shih, and N. D. Chien, "A simple approach for integrating quantum confinement effects into TCAD simulations of tunnel field-effect transistors," *J. Comput. Electron.*, vol. 24, no. 1, p. 9, Feb. 2025, doi: 10.1007/s10825-024-02253-7.

[269] T. S. A. Samuel, Y. S. Song, S. Tayal, P. Vimalā, and S. B. Rahi, Eds., *Tunneling field effect transistors: design, modeling and applications*. in Materials, devices, and circuits. Boca Raton: CRC Press, 2023.

[270] W. G. Vandenberghe, B. Sorée, W. Magnus, G. Groeseneken, and M. V. Fischetti, "Impact of field-induced quantum confinement in tunneling field-effect devices," *Appl. Phys. Lett.*, vol. 98, no. 14, p. 143503, Apr. 2011, doi: 10.1063/1.3573812.

[271] J. L. Padilla, F. Gamiz, and A. Godoy, "Impact of Quantum Confinement on Gate Threshold Voltage and Subthreshold Swings in Double-Gate Tunnel FETs," *IEEE Trans. Electron Devices*, vol. 59, no. 12, pp. 3205–3211, Dec. 2012, doi: 10.1109/TED.2012.2216531.

[272] A. M. Walke *et al.*, "Part I: Impact of Field-Induced Quantum Confinement on the Subthreshold Swing Behavior of Line TFETs," *IEEE Trans. Electron Devices*, vol. 60, no. 12, pp. 4057–4064, Dec. 2013, doi: 10.1109/TED.2013.2287259.

[273] Q. Smets *et al.*, "Impact of field-induced quantum confinement on the onset of tunneling field-effect transistors: Experimental verification," *Appl. Phys. Lett.*, vol. 105, no. 20, p. 203507, Nov. 2014, doi: 10.1063/1.4902117.

[274] F. Najam and Y. S. Yu, "Impact of Quantum Confinement on Band-to-Band Tunneling of Line-Tunneling Type L-Shaped Tunnel Field-Effect Transistor," *IEEE Trans. Electron Devices*, vol. 66, no. 4, pp. 2010–2016, Apr. 2019, doi: 10.1109/TED.2019.2898403.

[275] K. K. Young, "Short-channel effect in fully depleted SOI MOSFETs," *IEEE Trans. Electron Devices*, vol. 36, no. 2, pp. 399–402, Feb. 1989, doi: 10.1109/16.19942.

[276] Q.-T. Zhao *et al.*, "Strained Si and SiGe Nanowire Tunnel FETs for Logic and Analog Applications," *IEEE J. Electron Devices Soc.*, vol. 3, no. 3, pp. 103–114, May 2015, doi: 10.1109/JEDS.2015.2400371.

[277] A. M. D. Azevedo, T. J. Lopes, D. D. Cardoso, S. N. Monterio, P. C. R. Silveira, and A. B.-H. D. S. Figueiredo, "SiGe semiconductor electronic component: a review on fundamentals and applications," *Obs. Econ. Latinoam.*, vol. 22, no. 12, p. e8370, Dec. 2024, doi: 10.55905/oelv22n12-219.

[278] D. Nirmal, J. Ajayan, and P. J. Fay, Eds., *Semiconductor devices and technologies for future ultra low power electronics*, First edition. Boca Raton, FL: CRC Press, Taylor & Francis Group, 2022.

[279] K. Tajima *et al.*, “Thermoelectric Properties of RF-Sputtered SiGe Thin Film for Hydrogen Gas Sensor,” *Jpn. J. Appl. Phys.*, vol. 43, no. 9R, p. 5978, Sep. 2004, doi: 10.1143/JJAP.43.5978.

[280] S. Dash, S. K. Mohanty, and G. P. Mishra, “Hetero-gate dielectric SiGe/Si tunnel FET: a hydrogen gas sensor with improved sensitivity,” *J. Comput. Electron.*, Dec. 2022, doi: 10.1007/s10825-022-01993-8.

[281] Y. G. Hirphaa, A. Singh, T. Hailu, and C. F. Wakweya, “Impact of SiGe pocket on different shape TFET structures for gas sensing application,” *Micro Nanostructures*, vol. 196, p. 207998, Dec. 2024, doi: 10.1016/j.micrna.2024.207998.

[282] W. Huang, A. K. Diallo, J. L. Dailey, K. Besar, and H. E. Katz, “Electrochemical processes and mechanistic aspects of field-effect sensors for biomolecules,” *J. Mater. Chem. C*, vol. 3, no. 25, pp. 6445–6470, 2015, doi: 10.1039/C5TC00755K.

[283] Y. Zhou *et al.*, “Recent Advances in Enhancing the Sensitivity of Biosensors Based on Field Effect Transistors,” *Adv. Electron. Mater.*, p. 2400712, Dec. 2024, doi: 10.1002/aelm.202400712.

[284] L. Zhang and T. Dong, “A Si/SiGe quantum well based biosensor for direct analysis of exothermic biochemical reaction,” *J. Micromechanics Microengineering*, vol. 23, no. 4, p. 045011, Apr. 2013, doi: 10.1088/0960-1317/23/4/045011.

[285] A. Lodhi, C. Rajan, A. K. Behera, D. P. Samajdar, D. Soni, and D. S. Yadav, “Sensitivity and sensing speed analysis of extended nano-cavity and source over electrode in Si/SiGe based TFET biosensor,” *Appl. Phys. A*, vol. 126, no. 11, p. 837, Nov. 2020, doi: 10.1007/s00339-020-04008-0.

[286] J. Singh and S. Singh, “Improvement in the sensing performance of SiGe pocket Si/Ge VTFET based biosensor using extended source electrode and nano-cavity length,” *Mater. Sci. Eng. B*, vol. 310, p. 117688, Dec. 2024, doi: 10.1016/j.mseb.2024.117688.

[287] M. K. Anvarifard, Z. Ramezani, I. S. Amiri, K. Tamersit, and A. M. Nejad, “Profound analysis on sensing performance of Nanogap SiGe source DM-TFET biosensor,” *J. Mater. Sci. Mater. Electron.*, vol. 31, no. 24, pp. 22699–22712, Dec. 2020, doi: 10.1007/s10854-020-04795-5.

[288] S. Kanungo, S. Chattopadhyay, P. S. Gupta, K. Sinha, and H. Rahaman, “Study and Analysis of the Effects of SiGe Source and Pocket-Doped Channel on Sensing Performance of Dielectrically Modulated Tunnel FET-Based Biosensors,” *IEEE Trans. Electron Devices*, vol. 63, no. 6, pp. 2589–2596, Jun. 2016, doi: 10.1109/TED.2016.2556081.

[289] N. Shafi, C. Sahu, and C. Periasamy, “Virtually doped SiGe tunnel FET for enhanced sensitivity in biosensing applications,” *Superlattices Microstruct.*, vol. 120, pp. 75–89, Aug. 2018, doi: 10.1016/j.spmi.2018.05.006.

[290] G. Nazir, A. Rehman, and S.-J. Park, “Energy-Efficient Tunneling Field-Effect Transistors for Low-Power Device Applications: Challenges and Opportunities,” *ACS Appl. Mater. Interfaces*, vol. 12, no. 42, pp. 47127–47163, Oct. 2020, doi: 10.1021/acsami.0c10213.

[291] R. Rooyackers *et al.*, “Ge-Source Vertical Tunnel FETs Using a Novel Replacement-Source Integration Scheme,” *IEEE Trans. Electron Devices*, vol. 61, no. 12, pp. 4032–4039, Dec. 2014, doi: 10.1109/TED.2014.2365142.

[292] S. H. Kim, S. Agarwal, Z. A. Jacobson, P. Matheu, C. Hu, and T.-J. K. Liu, “Tunnel Field Effect Transistor With Raised Germanium Source,” *IEEE Electron Device Lett.*, vol. 31, no. 10, pp. 1107–1109, Oct. 2010, doi: 10.1109/LED.2010.2061214.

[293] K. Vanlalawpuia and B. Bhowmick, “Investigation of a Ge-Source Vertical TFET With Delta-Doped Layer,” *IEEE Trans. Electron Devices*, vol. 66, no. 10, pp. 4439–4445, Oct. 2019, doi: 10.1109/TED.2019.2933313.

[294] M. K. Anvarifard and A. A. Orouji, “Energy Band Adjustment in a Reliable Novel Charge Plasma SiGe Source TFET to Intensify the BTBT Rate,” *IEEE Trans. Electron Devices*, vol. 68, no. 10, pp. 5284–5290, Oct. 2021, doi: 10.1109/TED.2021.3106891.

[295] N. Patel, A. Ramesha, and S. Mahapatra, “Drive current boosting of n-type tunnel FET with strained SiGe layer at source,” *Microelectron. J.*, vol. 39, no. 12, pp. 1671–1677, Dec. 2008, doi: 10.1016/j.mejo.2008.02.020.

[296] J. Talukdar, G. Rawat, and K. Mummaneni, “A Novel Extended Source TFET with δp+- SiGe Layer,” *Silicon*, vol. 12, no. 10, pp. 2273–2281, Oct. 2020, doi: 10.1007/s12633-019-00321-3.

[297] W. Li and J. C. S. Woo, “Vertical P-TFET With a P-Type SiGe Pocket,” *IEEE Trans. Electron Devices*, vol. 67, no. 4, pp. 1480–1484, Apr. 2020, doi: 10.1109/TED.2020.2971475.

[298] H. Xie and H. Liu, “Design and investigation of a dual source and U-shaped gate TFET with n buffer and SiGe pocket,” *AIP Adv.*, vol. 10, no. 5, p. 055125, May 2020, doi: 10.1063/5.0006510.

[299] S. Singh, R. Nr, G. Wadhwa, and S. Singh, “Linearly Work-Function Modulated Gate Metal For Hetero Gate Dielectric TFET with Si0.5Ge0.5-Pocket at Source/Channel Junction,” *Silicon*, vol. 14, no. 14, pp. 8475–8485, Sep. 2022, doi: 10.1007/s12633-021-01557-8.

[300] E. Kasper and D. J. Paul, “Silicon Quantum Integrated Circuits, Edition”.

[301] M. Myronov, “Molecular Beam Epitaxy of High Mobility Silicon, Silicon Germanium and Germanium Quantum Well Heterostructures,” in *Molecular Beam Epitaxy*, Elsevier, 2018, pp. 37–54. doi: 10.1016/B978-0-12-812136-8.00003-7.

[302] G. Iannaccone, G. Curatola, and G. Fiori, “Effective Bohm Quantum Potential for device simulators based on drift-diffusion and energy transport,” in *Simulation of Semiconductor Processes and*

Devices 2004, G. Wachutka and G. Schrag, Eds., Vienna: Springer Vienna, 2004, pp. 275–278. doi: 10.1007/978-3-7091-0624-2_64.

[303] S. Choudhury, K. L. Baishnab, K. Guha, Z. Jakšić, O. Jakšić, and J. Iannacci, “Modeling and Simulation of a TFET-Based Label-Free Biosensor with Enhanced Sensitivity,” *Chemosensors*, vol. 11, no. 5, p. 312, May 2023, doi: 10.3390/chemosensors11050312.

[304] N. Kumar Niranjan *et al.*, “2-D Si0.8Ge0.2 source double-gate pocket PTFET for low power application: Modeling and simulation,” *Mater. Sci. Eng. B*, vol. 303, p. 117290, May 2024, doi: 10.1016/j.mseb.2024.117290.

[305] T. Sakai *et al.*, “Photoemission Study on Si and Ge Segregation on Al/$Si_{0.8}$ $Ge_{0.2}$ Structures,” *ECS Trans.*, vol. 114, no. 2, pp. 177–183, Sep. 2024, doi: 10.1149/11402.0177ecst.

[306] Y.-C. Chang *et al.*, “Investigation of degradation behavior under negative bias temperature stress in Si/$Si_{0.8}$ $Ge_{0.2}$ metal-oxide-semiconductor capacitors,” *J. Phys. Appl. Phys.*, vol. 54, no. 47, p. 475103, Nov. 2021, doi: 10.1088/1361-6463/ac1bd2.

[307] N. K. Singh, R. Kar, D. Mandal, and D. Chowdhury, “Design and Temperature Analysis of Si0.8Ge0.2-Based Extended Gate Gate-All-Around TFET,” in *Micro and Nanoelectronics Devices, Circuits and Systems*, vol. 904, T. R. Lenka, D. Misra, and L. Fu, Eds., in Lecture Notes in Electrical Engineering, vol. 904. , Singapore: Springer Nature Singapore, 2023, pp. 31–39. doi: 10.1007/978-981-19-2308-1_4.

[308] H. Melchior, M. B. Fisher, and F. R. Arams, “Photodetectors for optical communication systems,” *Proc. IEEE*, vol. 58, no. 10, pp. 1466–1486, 1970, doi: 10.1109/PROC.1970.7972.

[309] R. Salama* and F. Al-Turjman, “An Overview of Long-Distance Optical Fiber Communication,” *J. Biomed. Res. Environ. Sci.*, vol. 5, no. 10, pp. 1306–1312, Oct. 2024, doi: 10.37871/jbres2018.

[310] D. Sahu and C. Kumar, “Performance analysis of optical amplifiers for Nyquist super channel transmission system,” *J. Opt.*, Dec. 2024, doi: 10.1007/s12596-024-02364-1.

[311] T. Bhowmick and U. Das, “Integrated MQW intermixed InGaAsP/InP waveguide photodiodes,” *Opt. Quantum Electron.*, vol. 42, no. 2, pp. 109–120, Jan. 2010, doi: 10.1007/s11082-010-9427-6.

[312] T. Bhowmick and U. Das, “Integrated MQW intermixed InGaAsP/InP waveguide photodiodes,” *Opt. Quantum Electron.*, vol. 42, no. 2, pp. 109–120, Jan. 2010, doi: 10.1007/s11082-010-9427-6.

[313] S. Sakai, M. Naitoh, M. Kobayashi, and M. Umeno, “InGaAsP/InP phototransistor-based detectors,” *IEEE Trans. Electron Devices*, vol. 30, no. 4, pp. 404–408, Apr. 1983, doi: 10.1109/T-ED.1983.21136.

[314] R. M. Lum, M. L. Mc Donald, E. M. Mack, Williams, F. G. Storz, and J. Levkoff, “Effect of temperature on InGaAsP alloy composition,” *J. Electron. Mater.*, vol. 24, no. 11, pp. 1577–1581, Nov. 1995, doi: 10.1007/BF02676814.

[315] J. Mu *et al.*, “Epitaxial growth conditions and interface quality of InGaAs/GaAsP multiple quantum wells,” *Mater. Sci. Semicond. Process.*, vol. 184, p. 108782, Dec. 2024, doi: 10.1016/j.mssp.2024.108782.

[316] Y. Wang, J. Li, J. Zhang, W. Sha, W. Zhang, and Y. Du, “First-principles study of InxGa1-xAs1-yPy with different compositions,” *Opt. Rev.*, vol. 29, no. 4, pp. 287–297, Aug. 2022, doi: 10.1007/s10043-022-00742-3.

[317] D. Malik and U. Das, “Design, optimization and characterization of InGaAsP/InP QW integrated tapered waveguides using QW intermixing,” *Opt. Quantum Electron.*, vol. 56, no. 8, p. 1280, Jul. 2024, doi: 10.1007/s11082-024-06793-x.

[318] Y. Gusakov, E. Finkman, G. Bahir, and D. Ritter, “The effect of strain in InP/InGaAs quantum-well infrared photodetectors on the operating wavelength,” *Appl. Phys. Lett.*, vol. 79, no. 16, pp. 2508–2510, Oct. 2001, doi: 10.1063/1.1408908.

[319] A. Kumari and R. K. Mishra, “Temperature dependence of optical gain in compressively strained InAsP/GaInAs based quantum well heterostructure for short wavelength infrared applications,” *Phys. B Condens. Matter*, vol. 677, p. 415701, Mar. 2024, doi: 10.1016/j.physb.2024.415701.

[320] Y. Yamazoe, T. Nishino, and Y. Hamakawa, “Electroreflectance study of InGaAsP quaternary alloys lattice matched to InP,” *IEEE J. Quantum Electron.*, vol. 17, no. 2, pp. 139–144, Feb. 1981, doi: 10.1109/JQE.1981.1071081.

[321] H. Chi, Y. Du, and G. Li, “Analysis of InGaN Multiple-Quantum-Well Photoelectric Device of Visible Light Communication,” *J. Nanoelectron. Optoelectron.*, vol. 15, no. 7, pp. 909–916, Jul. 2020, doi: 10.1166/jno.2020.2850.

[322] Z. Kourdi, H. E. Adardour, I. Four, and M. Khaouani, “Improved AlGaN–GaN MQW LED performance incorporating InAlN MLB and AlN back barrier: Li-Fi applications,” *Indian J. Phys.*, Jun. 2024, doi: 10.1007/s12648-024-03281-6.

[323] C.-L. Tsai *et al.*, “Underwater Optical Wireless Communications With InGaN LEDs Grown With an Asymmetric Multiple Quantum Well for Light Emission or Detection,” *IEEE Photonics J.*, vol. 14, no. 1, pp. 1–7, Feb. 2022, doi: 10.1109/JPHOT.2021.3130133.

[324] S. Seifert and P. Runge, “Revised refractive index and absorption of In_1-xGa_xAs_yP_1-y lattice-matched to InP in transparent and absorption IR-region,” *Opt. Mater. Express*, vol. 6, no. 2, p. 629, Feb. 2016, doi: 10.1364/OME.6.000629.

[325] B. Cheng *et al.*, “Normal-incident SiGe/Si MQW photodetectors operating at 1.3 µm,” presented at the International Symposium on Photonics and Applications, S. T. Ho, Y. Zhou, W. W. Chow, and Y. Arakawa, Eds., Singapore, Singapore, Nov. 1999, p. 326. doi: 10.1117/12.369415.

[324] S. Seifert and P. Runge, "Revised refractive index and absorption of In_1-xGa_xAs_yP_1-y lattice-matched to InP in transparent and absorption IR-region," *Opt. Mater. Express*, vol. 6, no. 2, p. 629, Feb. 2016, doi: 10.1364/OME.6.000629.

[325] B. Cheng *et al.*, "Normal-incident SiGe/Si MQW photodetectors operating at 1.3 µm," presented at the International Symposium on Photonics and Applications, S. T. Ho, Y. Zhou, W. W. Chow, and Y. Arakawa, Eds., Singapore, Singapore, Nov. 1999, p. 326. doi: 10.1117/12.369415.

[326] B. Kumari, S. Kattayat, S. Kumar, S. Kaya, A. Katti, and P. A. Alvi, "Improved and tunable optical absorption characteristics of MQW GaAs/AlGaAs nano-scale heterostructure," *Optik*, vol. 208, p. 164544, Apr. 2020, doi: 10.1016/j.ijleo.2020.164544.

[327] S. Madhusoodhanan *et al.*, "High-Temperature Analysis of GaN-Based MQW Photodetector for Optical Galvanic Isolations in High-Density Integrated Power Modules," *IEEE J. Emerg. Sel. Top. Power Electron.*, vol. 9, no. 4, pp. 3877–3882, Aug. 2021, doi: 10.1109/JESTPE.2020.2974788.

[328] M. Wagner, M. Karner, and T. Grasser, "Quantum Correction Models for Modern Semiconductor Devices".

[329] M. J. Van Dort, P. H. Woerlee, and A. J. Walker, "A simple model for quantisation effects in heavily-doped silicon MOSFETs at inversion conditions," *Solid-State Electron.*, vol. 37, no. 3, pp. 411–414, Mar. 1994, doi: 10.1016/0038-1101(94)90005-1.

[330] W. Hänsch, "Carrier Transport in an Inversion Channel," in *The Drift Diffusion Equation and Its Applications in MOSFET Modeling*, in Computational Microelectronics. , Vienna: Springer Vienna, 1991, pp. 111–141. doi: 10.1007/978-3-7091-9095-1_3.

[331] D. M. Ceperley, "Introduction to Quantum Monte Carlo Methods Ap- plied to the Electron Gas".

Sharmistha Shee Kanrar.
07/11/25